

Integrated Gallium Phosphide Photonics

Thèse N° 9250

Présentée le 4 avril 2019

à la Faculté des sciences de base

Laboratoire de photonique et mesures quantiques (SB/STI)

Programme doctoral en photonique

pour l'obtention du grade de Docteur ès Sciences

par

Katharina SCHMEING

Acceptée sur proposition du jury

Prof. R. Houdré, président du jury

Prof. T. Kippenberg, Dr P. F. Seidler, directeurs de thèse

Prof. A. Schliesser, rapporteur

Prof. E. Verhagen, rapporteur

Prof. N. Grandjean, rapporteur

2019



ÉCOLE POLYTECHNIQUE
FÉDÉRALE DE LAUSANNE

Nothing in life is to be feared, it is only to be understood.
Now is the time to understand more, so that we may fear less.
— Marie Curie

To my parents, who have given me the freedom to do whatever makes me happy.

To my husband Stephan, who went with me through the ups and downs of this work.

To my family, who always reminds me of what really matters in life.

To my friends, who balance my work with life.

Acknowledgements

I am very grateful that I had the chance to do my PhD at IBM Research - Zurich, which is a great place connecting fundamental research with the needs of industry. This opportunity I got to a large extent thanks to Paul Seidler. He trained me in the art of making silicon photonic crystals and together we learned how to use them for optomechanics. I've gotten to appreciate him as the most socially sensitive group leader who I have encountered in an academic environment so far. He knows how to read and guide people, which makes him a great group leader.

When it came to optomechanics, we got a lot of support from Prof. Tobias Kippenberg and his team at k-Lab. Liu Qiu, Ryan Schilling, Nicolas Piro and Dalziel Wilson regularly gave us advice on how to improve our measurements and what physical effects to look for.

The real adventure started when Paul and I decided to change our material system to gallium phosphide. We joined forces with Lukas Czornomaz and Yannick Baumgartner, who started with the material growth. This turned out to be especially tricky. Here Lukas with his great expertise on III-V materials patiently reassured everyone, that in the end it will work.

At this stage we got a lot of help from the two master students Tamara Aderneuer and Pol Welter. Tamara looked into the piezoelectric behavior of gallium phosphide, while Pol developed the dry etching and selective etching of gallium phosphide in the presence of GaP. It was a fun time with the two of them, where I encountered all stages from skepticism to great enthusiasm towards the project. At that time also Herwig Hahn was supporting us with his knowledge on III-V materials, coffee brewing and barefoot running.

A great milestone for the team was the move to our own lab with a big optical table and enough space for all our equipment. The best about it was though the ability to measure how often and how long we wanted, without having to assemble and disassemble the setup.

After approximately one year, the first Gap devices were ready and we were flooded with ideas on what to do with them. Luckily, Dal and Simon joined our team around that time. They took over the nonlinear optics and frequency comb project. From Dal I learned a lot about the view on life as a scientist. Simon and I often had differing opinions, but overall we complemented each other quite well.

Finally there was all the technical staff at IBM, who helped me with the daily challenges of a scientist: Heinz with his passion for vacuum chambers, Ute as the master of the ICP, Antonis as the one of the ebeam and Daniele who never gets tired of trying yet to bond another wafer. Besides all the people who supported me in my research, my husband Stephan was a great source of love and support during the past years. We got married during our PhD times and are now expecting our first child. Science has always had a place in our relationship, and this

Acknowledgements

is a great feeling.

Finally I want to thank my parents Doris and Manfred, as well as my siblings Heike, Nicole and Tobias. My family always supported me and gave me the freedom to pursue my own path in life. But I always knew that there was a place to go home to and be welcomed.

Zurich, 4 November 2018

K. S.

Abstract

The integration of new materials mediating light-matter interaction in nanoscale devices is a persistent goal in nanophotonics. One of these materials is Gallium phosphide, which offers an attractive combination of a high refractive index ($n=3.05$ at $\lambda = 1550$ nm) and a large bandgap ($E_g=2.26$ eV), enabling photonic devices with strongly confined light fields, not suffering from heating due to two-photon absorption at telecommunication wavelengths. Furthermore, due to its non-centrosymmetric crystal structure, it has a non-vanishing second-order susceptibility $\chi^{(2)}$ and is piezoelectric. Related to its large refractive index is a high third-order susceptibility $\chi^{(3)}$. Prior to this work the use of GaP for photonic devices was limited to individual non-integrated components, as GaP was not available on a substrate with substantially lower refractive index equivalent to SOI-wafers for silicon.

In this work a process was developed that allows the integration of GaP devices onto SiO₂. It exploits direct wafer bonding of a GaP/Al_xGa_{1-x}P/GaP heterostructure onto a SiO₂-on-Si wafer. After substrate removal, photonic devices are patterned by dry-etching in the top GaP device layer.

The GaP devices investigated here are used to explore nonlinear optics and optomechanics. In the area of nonlinear optics, second- and third-harmonic generation are observed. The Kerr coefficient is experimentally estimated as $n_2[1550\text{nm}] = 1.2(5) \times 10^{-17} \text{m}^2/\text{W}$, for the first time in a precision measurement at telecommunication wavelengths. Four-wave mixing is used for broadband frequency comb generation, where a power threshold as low as 3 mW is obtained. The combination of four-wave mixing and second-harmonic generation leads to frequency-doubled combs.

The optomechanical properties of GaP one-dimensional photonic crystal cavities are optimized by simulations and fabricated devices are characterized. Optical quality factors of $Q_o > 1 \times 10^5$ and optomechanical coupling strengths of $g_0/2\pi \approx 400$ kHz are measured. Dynamical backaction in the form of the spring effect and the parametric amplification are observed, as well as optomechanically induced transparency and absorption.

A device design for a microwave-to-optical transducer is developed, relying on the piezoelectricity of GaP. It combines electromechanical and optomechanical transduction. The predicted electromechanical coupling strength is in the MHz range.

Furthermore, photonic crystal cavity designs containing a slot at the center of the cavity are studied. According to simulations for slot widths below 30 nm, optomechanical coupling strengths $g_0/2\pi > 1$ MHz could be achieved. Fabricated silicon photonic crystal cavities show high quality factors of $Q_o \approx 8 \times 10^4$ while hosting a mechanical eigenmode with a frequency of

Acknowledgements

2.7 GHz. Because of process technology limitations, only slot widths ≥ 40 nm can be fabricated, the achieved $g_0/2\pi$ is limited to 300 kHz.

The new GaP-on-insulator material platform opens the door to integrated GaP devices. Frequency combs are of interest for soliton comb formation, mid-IR frequency combs, and ultra-broadband supercontinuum generation. Microwave-to-optical transducers are on the one hand desired for quantum information processing, on the other hand they are applicable as efficient modulators or detectors for classical signals.

Keywords: Gallium phosphide, optomechanics, nonlinear optics, integrated photonics, microwave-to-optical transduction, piezoelectricity, photonic crystal cavities, direct wafer bonding, III-V processing

Zusammenfassung

Die Integration neuer Materialien, die Licht-Materie-Wechselwirkungen in photonischen Komponenten auf Nanometerskala vermitteln, ist ein anhaltendes Ziel in der Nanophotonik. Eines dieser Materialien ist Galliumphosphid, das eine attraktive Kombination aus hohem Brechungsindex ($n = 3,05$ bei $\lambda = 1550$ nm) und großer Bandlücke ($E_g = 2,26$ eV) bietet. Dies ermöglicht photonische Bauelemente mit räumlich stark begrenzten Lichtfeldern und unterdrückt Erwärmung aufgrund von Zwei-Photonen-Absorption bei Telekommunikationswellenlängen. Aufgrund seiner nicht-zentrosymmetrischen Kristallstruktur hat es außerdem eine nicht verschwindende Suszeptibilität zweiter Ordnung $\chi^{(2)}$ und ist piezoelektrisch. Durch seinen großen Brechungsindex hat GaP auch eine hohe Suszeptibilität dritter Ordnung $\chi^{(3)}$. Vor dieser Arbeit war der Einsatz von GaP für photonische Bauelemente auf einzelne nicht integrierte Komponenten beschränkt, da GaP nicht auf einem Substrat mit wesentlich niedrigerem Brechungsindex verfügbar war.

In dieser Arbeit wurde ein Prozess entwickelt, der die Integration von GaP-Bauelementen auf SiO_2 ermöglicht. Er basiert auf direktem Waferbonden einer $\text{GaP}/\text{Al}_x\text{Ga}_{1-x}\text{P}/\text{GaP}$ -Heterostruktur auf einem SiO_2 -on-Si Wafer. Nach der Substratentfernung werden photonische Bauelemente mittels eines Trockenätzprozesses in die obere GaP-Schicht strukturiert.

Die hergestellten GaP-Bauelemente werden zur Erforschung nichtlinearer Optik und Optomechanik verwendet. Im Bereich der nichtlinearen Optik wird die Erzeugung der zweiten und dritten Harmonischen beobachtet. Der Kerr-Koeffizient wird zum ersten Mal in einer Präzisionsmessung experimentell auf $n_2[1550\text{nm}] = 1.2(5) \times 10^{-17} \text{m}^2/\text{W}$ geschätzt. Vier-Wellen-Mischung wird für die Breitband-Frequenzkammerzeugung mit einer unteren Leistungsschwelle von nur 3 mW verwendet.

Die optomechanischen Eigenschaften von Kavitäten in eindimensionalen photonischen Kristallen aus GaP werden durch Simulationen optimiert. Gefertigte Kristalle weisen optische Qualitätsfaktoren von $Q_o > 1 \times 10^5$ und optomechanische Kopplungsstärken von $g_0/2\pi \approx 400$ kHz auf. Dynamische Rückkopplung in Form des Federeffektes und der parametrischen Verstärkung, sowie optomechanisch induzierte Transparenz und Absorption werden beobachtet. Ein Design für einen Mikrowellen-zu-Licht Konverter wurde entwickelt, basierend auf der Piezoelektrizität von GaP. Es kombiniert elektromechanische und optomechanische Signalumwandlung. Die erwartete elektromechanische Kopplungsstärke ist im MHz-Bereich.

Darüberhinaus werden in dieser Arbeit photonische Kristalle mit einem Schlitz in der Mitte der Kavität untersucht. Für Schlitzbreiten unter 30 nm werden optomechanische Kopplungsstärken von $g_0/2\pi > 1$ MHz erwartet, aufgrund von prozesstechnologischen Einschränkungen

Acknowledgements

können nur Schlitzbreiten ≥ 40 nm hergestellt werden, was $g_0/2\pi$ auf 300 kHz begrenzt. Die neue GaP-auf-Isolator-Materialplattform ermöglicht integrierte photonische GaP-Bauteile. Frequenzkämme sind für Solitonerzeugung, Frequenzkämme im Infrarotbereich und Ultra-Breitband-Superkontinuums-Erzeugung von Interesse. Mikrowellen-zu-Licht Konverter werden zum einen für die Quanteninformatik benötigt, zum anderen können sie als effiziente Modulatoren oder Detektoren für klassische Signale dienen.

Stichwörter: Galliumphosphid, Optomechanik, nichtlineare Optik, integrierte Photonik, Mikrowellen-zu-Licht Konversion, Piezoelektrizität, photonische Kristalle, direktes Waferbonden

Résumé

L'intégration de nouveaux matériaux interagissant avec la lumière dans des dispositifs nano-métriques est un objectif constant de la nano-photonique. Parmi ces matériaux, le phosphure de gallium (GaP) offre la combinaison attrayante d'un indice de réfraction élevé ($n = 3,05$ à $\lambda = 1550$ nm) et d'une large bande interdite ($E_g = 2,26$ eV), ce qui permet de fabriquer des dispositifs photoniques opérant aux longueurs d'onde de télécommunication avec un fort confinement optique et sans problème d'échauffement induit par l'absorption à deux photons.

Par ailleurs, en raison de sa structure cristalline non centro-symétrique, le phosphure de gallium possède un terme de susceptibilité du second ordre $\chi^{(2)}$ et un effet piézoélectrique. Grâce à son indice de réfraction élevé, une forte susceptibilité du troisième ordre $\chi^{(3)}$ est également prédite. Avant ce travail, l'utilisation du GaP pour les dispositifs photoniques était limitée aux composants individuels non intégrés, car celui-ci n'était pas disponible sur un substrat à faible indice de réfraction.

Au cours de ce travail de thèse, un processus permettant l'intégration de dispositifs GaP sur SiO₂ a été développé. Celui-ci repose sur une technique de collage direct d'une hétérostructure GaP/Al_xGa_{1-x}P/GaP sur un wafer de silicium oxydé. Des dispositifs photoniques ont été fabriqués par gravure sèche de la couche de GaP.

Ils ont été utilisés pour explorer l'optique non linéaire et l'optomécanique. Dans le domaine de l'optique non linéaire, nous avons observé la génération de seconde et troisième harmoniques. Le coefficient de Kerr a été mesuré expérimentalement pour la première fois, $n_2[1550\text{nm}] = 1.2(5) \times 10^{-17} \text{m}^2/\text{W}$. Le mélange à quatre ondes a servi à la génération de peignes de fréquences à large bande, où un seuil de puissance aussi bas que 3 mW a été démontré.

Les propriétés optomécaniques des cristaux photoniques unidimensionnels de GaP ont été optimisées par des simulations. Des dispositifs fabriqués des facteurs de qualité optiques $Q_o > 1 \times 10^5$ et des forces de couplage optomécaniques de $g_0/2\pi \approx 400$ kHz. La rétroaction dynamique sous forme d'effet ressort ainsi que l'amplification paramétrique ont été observées. Le design d'un transducteur micro-ondes-optique a été développé à partir de l'effet piézoélectrique du GaP. Il combine l'électromécanique et l'optomécanique. Une force de couplage électromécanique dans la gamme du MHz est prédite.

Par ailleurs, des cavités à cristaux photoniques avec une fente au centre de la cavité a été étudié. Des forces de couplage optomécaniques $g_0/2\pi > 1$ MHz sont prédites pour des largeurs de fentes ≤ 30 nm. En raison des limites technologiques de fabrication, seuls des largeurs de

Acknowledgements

fentes ≥ 40 nm ont pu être fabriquées, ce qui a limité $g_0/2\pi$ à 300 kHz.

La nouvelle plateforme GaP-sur-isolant offre de nouvelles possibilités pour la fabrication de dispositifs GaP intégrés. Les peignes de fréquence sur GaP présentent un intérêt pour la génération de peignes à solitons, de peignes de fréquences s'étendant dans le moyen infrarouge et de supercontinuum à ultralarge bande spectrale. Les transducteurs micro-ondes-optiques sont d'une part désirés pour le traitement de l'information quantique, et peuvent être d'autre part directement employés en tant que modulateurs ou détecteurs efficaces pour traiter des signaux classiques.

Mots-clés : Phosphure de gallium, optomécanique, optique non linéaire, photonique intégrée, transduction micro-ondes-optique, piézoélectricité, cavités à cristaux photoniques, collage de wafers

Contents

Acknowledgements	v
Abstract (English/Français/Deutsch)	vii
List of figures	xvi
List of tables	xix
1 Introduction	1
2 Theory	11
2.1 Nonlinear optics	12
2.1.1 Second-harmonic generation	12
2.1.2 Third-harmonic generation	12
2.1.3 Intensity dependent refractive index	13
2.1.4 Four-wave mixing	14
2.1.5 Frequency comb generation via four-wave mixing in an optical resonator	14
2.2 Stimulated Raman scattering	15
2.3 Two-photon absorption	15
2.4 Optical resonators	16
2.4.1 Input output formalism of an optical cavity	17
2.4.2 Photothermal and Kerr shift	18
2.4.3 Ring resonators	19
2.4.4 Photonic crystal cavities	20
2.5 Cavity optomechanics	21
2.5.1 Optomechanical coupling	21
2.5.2 Calibration tone measurement	23
2.5.3 Optomechanically induced transparency and absorption	24
2.5.4 Dynamical backaction	25
2.6 Piezoelectric effect	25
2.6.1 Direct and inverse piezoelectric effect	26
2.6.2 Direction and magnitude of the piezoelectric effect	28
2.6.3 Electromechanical coupling strength	29
2.6.4 Quantum mechanical derivation of the electromechanical coupling rate	31

Contents

2.7	Microwave-to-optical transduction	32
3	Process development	35
3.1	Growth and direct wafer bonding	35
3.2	Wafer thinning and selective etching of GaP	36
3.2.1	Investigation of selective wet etching of GaP in the presence of $\text{Al}_x\text{Ga}_{1-x}\text{P}$	38
3.2.2	Thinning of the GaP substrate	38
3.2.3	Selective dry etching of GaP in the presence of $\text{Al}_x\text{Ga}_{1-x}\text{P}$	41
3.3	Removal of the $\text{Al}_x\text{Ga}_{1-x}\text{P}$ etch stop layer	44
3.4	Characterization of the GaP device layer	44
3.5	Dry etch for device patterning	45
3.5.1	Possible gases for ICP-RIE etching of GaP and their effects	45
3.5.2	Process development methodology	45
3.5.3	Influence of the BCl_3 to Cl_2 ratio	46
3.5.4	Influence of temperature and 'high-power' recipe	47
3.5.5	Etching of small openings	47
3.5.6	Influence of pressure	49
3.5.7	Passivation with CH_4 and 'low-power' recipe	50
3.6	Fabrication of waveguides, ring resonators and grating couplers	50
3.7	Fabrication of freestanding devices	51
3.8	Fabrication of photonic crystal cavities	51
3.9	Chip layout	54
4	Design of GaP devices for nonlinear optics	57
4.1	Waveguides	57
4.1.1	Single mode waveguides	57
4.1.2	Group index	59
4.2	Grating couplers	59
4.3	Ring resonators	61
5	Nonlinear optics	63
5.1	Experimental setup	63
5.2	Characterization of waveguides and grating couplers	64
5.3	Characterization of ring resonators	66
5.3.1	Ring resonators used for second- and third harmonic generation	66
5.3.2	Ring resonators used for frequency comb generation	68
5.4	Second- and third-harmonic generation	68
5.5	Measurement of the Kerr coefficient with a modulation-transfer technique	71
5.6	Confirmation of the simulated group velocity dispersion	72
5.7	Frequency comb generation	73
5.8	Frequency-doubled combs	77
5.9	Raman combs	77

6	Design of GaP devices for optomechanics and microwave-to-optical transduction	79
6.1	Design of photonic crystal cavities	79
6.1.1	Photoelastic coefficients of GaP	80
6.1.2	Simulation of design tolerances	81
6.2	Optimization of the piezoelectric coupling	83
6.2.1	Conditions for efficient actuation	83
6.2.2	Configuration with electrodes on the photonic crystal cavity	84
6.2.3	Configuration with electrodes separated laterally from the photonic crystal cavity	94
6.2.4	Expected performance of a microwave-to-optical transducer	95
7	Optomechanics with one-dimensional GaP photonic crystal cavities	99
7.1	Experimental setup	99
7.2	Optical spectroscopy	99
7.3	Thermomechanical radio frequency spectrum	102
7.4	Optomechanical vacuum coupling rate	103
7.5	Optomechanically induced transparency	106
7.6	Dynamical backaction	106
7.6.1	Determination of laser detuning for evaluation of dynamical backaction	107
8	Optomechanics with slotted one-dimensional silicon photonic crystal cavities	111
8.1	Exploiting the slot effect	111
8.2	Device design	112
8.3	Fabrication	113
8.4	Measurement setup	115
8.5	Device characterization	116
8.5.1	Optical transmission	116
8.5.2	Thermomechanical radio-frequency spectra	116
8.5.3	Optomechanical coupling rate	117
9	Summary and outlook	125
A	Processing manual GaP photonic devices	129
B	Processing manual Si photonic devices	131
C	Simulation of optomechanical coupling with COMSOL	133
D	Simulation of electromechanical coupling with COMSOL	139
E	Fully etched grating couplers with a Gaussian mode profile	141
F	Coplanar waveguide resonators made of Nb	149
	Bibliography	173

Contents

Abbreviations	175
Curriculum Vitae	177

List of Figures

1.1	Early GaP LED, commercially available green LED and GaP wafers.	2
1.2	GaP as a material for integrated nonlinear photonics	4
1.3	GaP as a material for integrated nonlinear photonics	6
1.4	GaP and Si photonic crystal cavities	9
2.1	Comparison of coupling schemes for optical resonators.	17
2.2	Four possible orientations of the piezoelectric effect.	28
2.3	Schematic representation of microwave-to-optical transduction involving optomechanical and piezoelectrical coupling.	33
2.4	Frequency scheme for the cavities involved in microwave-to-optical transduction.	33
3.1	Schematic of process flow for GaP-OI device fabrication.	35
3.2	Characterization of material growth	37
3.3	Etching GaP with aqua regia (HCl/HNO ₃ (3:1)) leads to circular etch pits.	39
3.5	Bonded wafer after substrate removal by grinding	40
3.6	XRD spectrum of a GaP-OI sample	44
3.7	Lithography mask for dry etch development.	46
3.8	Dependence of GaP etch rate and selectivity with respect to HSQ on BCl ₃ -to-Cl ₂ ratio.	47
3.9	Etch results for high-power recipe and low-power recipe.	48
3.10	Dependence of GaP etch rate and selectivity with respect to HSQ on ICP power	49
3.11	SEM images of fabricated photonic devices	50
3.12	AFM image of the GaP device layer after device fabrication.	51
3.13	Optical microscope image of released photonic crystal cavities (PhCs).	52
3.14	SEM images of a fabricated one-dimensional (1D) GaP PhC.	53
3.15	Challenges in photonic crystal cavity fabrication.	54
3.16	Typical chip layout of a 7 mm x 7 mm GaP-OI chip with photonic crystal cavities.	56
4.1	Band structure of a GaP-OI waveguide	58
4.2	Numerical simulations for the calculation of the group refractive index.	60
4.3	Simulated resonator dispersion for various waveguide widths.	62
5.1	Measurement setup used for transmission measurements, harmonic generation, comb generation and modulation transfer measurement.	65

List of Figures

5.2	Transmission spectra through a grating coupler and a ring resonator.	67
5.3	Transmission through ring resonator used for frequency comb generation . . .	68
5.4	Measurement of SHG and THG signal above ring resonator.	69
5.5	Grayscale images of second-harmonic generation from a ring resonator and a photonic crystal cavity (PhC) and camera image of the green third harmonic scattered by a ring resonator.	69
5.6	Measurement of SHG and THG signal above ring resonator.	70
5.7	Thermally shifting the SHG resonance.	71
5.8	Modulation transfer measurement to determine Kerr coefficient.	72
5.9	Comparison of measured and simulated dispersion.	73
5.10	Onset and power threshold for frequency comb generation.	74
5.11	Frequency comb generation above threshold power and SHG frequency combs.	75
5.12	Radiofrequency noise spectrum of Gap-OI frequency comb.	76
5.13	Measurement of cladded racetrack resonators.	78
6.1	Optimized PhC device design as obtained from numerical finite-element simulations.	80
6.2	Parameter sweeps for PhC dimensions performed in simulations with COMSOL	82
6.3	Desired GaP device orientation for piezoelectric actuation.	84
6.4	Sweep of the electrode position and resulting change in quality factor.	85
6.5	Evaluation of the coupling strength for the device design where the electrodes are at one end of the GaP beam.	86
6.6	Optimized device design for the piezoelectric actuation of the breathing mode of a GaP PhC.	88
6.7	Matching the applied electric potential to the potential created by the direct piezoelectric effect.	90
6.8	Optimized electrode position at an antinode of the eigenmode.	91
6.9	Effect of clamping by the electrodes on the electromechanical coupling strength.	91
6.10	Outward energy flux depending on electrode width for the optimized design.	92
6.11	Mechanical displacement for the devices design published by Bochmann et al.	92
6.12	Mechanical displacement and energy flux for the piezoelectrically actuated breathing mode of the optimized device design	93
6.13	Electromechanical coupling strength depending on electrode position.	94
6.14	Electric field for a configuration with electrodes separated laterally from the photonic crystal cavity.	95
6.15	Electromechanical coupling strength depending on lower electrode distance.	96
7.1	Schematic of the measurement apparatus for optomechanical characterization.	100
7.2	Analysis of optical transmission measurements with GaP photonic crystal cavities.	101
7.3	Optical resonance frequency as a function of sample temperature.	103
7.4	Thermomechanical radio frequency spectrum of a photonic crystal cavity	103
7.5	Calibration tone measurement to determine the optomechanical vacuum coupling rate.	104

7.6	OMIT and OMIA measured with a GaP photonic crystal cavity at room temperature	105
7.7	Dynamical backaction measurements with GaP photonic crystal cavities. . . .	108
7.8	Determination of the laser-cavity detuning for the measurement of dynamical backaction	109
8.1	Schematic of process flow for GaP-OI device fabrication.	113
8.2	Schematic of the process flow for SOI device fabrication.	114
8.3	SEM images of the freestanding photonic crystal nanobeam cavity on a silicon-on-insulator (SOI) wafer with a 40-nm slot.	115
8.4	Measurement setup for SOI device characterization.	115
8.5	Optical transmission through a silicon photonic crystal cavity.	117
8.6	Power spectral density of light transmitted through a slotted silicon PhC.	118
8.7	Calibration tone measurement for determining the optomechanical vacuum coupling rate.	119
8.8	Calibration of the phase modulator.	120
8.9	OMIA signals for devices with N=9 and N=10 holes.	122
8.10	Simulation of the expected coupling rate depending on slot width.	123
9.1	Envisioned fabrication scheme for the bottom electrode.	128
C.1	COMSOL model of 1D photonic crystal cavity.	134
C.2	Meshed model of an eighth of a PhC.	135
C.3	Settings for retaining the solution of the optical eigenfrequency study.	136
C.4	Structure of the program used for PhC design optimization.	137
E.1	Grating coupler design applied in our research group.	141
E.2	Considerations for the improvement of the grating coupler design.	143
E.3	Grating coupler efficiency versus coupler length.	144
E.4	Grating coupler efficiency versus focal point position.	145
E.5	Transmission profile of the optimized grating couplers.	146
E.6	Transmission through two couplers connected by a waveguide when tuning the left and right fiber position.	146
E.7	Improved design of fiber mount.	147
F.1	AFM and SEM images of sputtered Nb layer.	151
F.2	Fabricated Nb devices.	153
F.3	Four-point probe measurement for determining the critical temperature and the critical magnetic field for Nb electrodes.	154
F.4	Response curve of a Nb coplanar waveguide resonator in a reflection measurement.	155

List of Tables

1.1	Properties of current integrated nonlinear microresonator platforms operating at $\lambda = 1550$ nm.	3
1.2	Comparison of different RF to optical transducer concepts.	7
2.1	Material constants of GaP	11
2.2	Material coefficients for inverse and direct piezoelectric effect	27
2.3	Comparison of piezoelectric III-V materials	30
3.1	Etch tests for wet etching of GaP selective to $\text{Al}_x\text{Ga}_{1-x}\text{P}$	38
3.2	Etch tests of GaP and $\text{Al}_{0.18}\text{Ga}_{0.82}\text{P}$ with various sources of chlorine and fluorine species	42
3.3	Etch recipe for selective etching of GaP with respect to $\text{Al}_x\text{Ga}_{1-x}\text{P}$	42
3.4	Etch tests of GaP and $\text{Al}_{0.18}\text{Ga}_{0.82}\text{P}$ with a Cl_2/CF_4 plasma	43
3.5	Etch recipes for patterning of GaP	48
6.1	Expected performance of the microwave-to-optical transduction	97
A.1	Process flow for freestanding GaP-OI devices.	130
B.1	Process flow for freestanding Si-on-insulator devices.	132
E.1	Performance of published grating coupler designs.	142
E.2	Parameters for grating couplers for a transmitted field with a Gaussian profile.	142
E.3	Performance of conventional fully etched grating couplers fabricated with SOI in the BRNC.	144
F.1	Superconducting materials and their transition temperature and critical magnetic fields.	149
F.2	Process parameters for Nb magnetron sputtering.	150
F.3	ICP-RIE process for Nb etching.	152

1 Introduction

Gallium phosphide has played an important role in the photonics industry since the 1960s. Together with GaAsP, it has formed the basis for a range of light-emitting devices [1, 2] despite the fact that it has an indirect bandgap for the thermodynamically-favored cubic (zinc blende) crystal structure. Its bandgap is at 2.26 eV (549 nm), which lies in the visible (green) and leads to wafers being transparent for larger wavelengths as well as LEDs emitting green light ¹. More recently, efforts have been made to realize nanophotonic devices in GaP. The motivation is severalfold: First, GaP is nearly lattice-matched to silicon, in principle enabling waferscale production [6, 7]. Second, GaP has negligible two-photon absorption (TPA) for wavelengths above 1.1 μm , enabling high power operation over the full telecom band. Third, among visibly transparent III-V materials, GaP has the largest refractive index ($n_0 > 3$), enabling strong optical confinement and implying a large $\chi^{(3)}$ nonlinearity. Finally, the non-centrosymmetric crystal structure of GaP yields a nonzero piezoelectric effect and large $\chi^{(2)}$ nonlinearity. Starting from the year 2008, a range of nanophotonic devices exploiting these properties have been investigated. These include PhCs [8] and coupling of these cavities to emitters, such as fluorescent molecules [9] and nitrogen vacancy (NV) centers [10]. Nano-antennae for enhanced photoluminescence [11] as well as second-harmonic [12, 13] and sum-frequency generation [14] have also been demonstrated with PhCs. Microdisk resonators made of GaP have been coupled to NV centers [15], applied for telecom to optical wavelength conversion [16] and have been used to observe cavity optomechanics [17], where the low two-photon absorption at 1550 nm is assumed to produce reduced heating compared to Si devices [18, 19]. All of the nanophotonic devices mentioned above were fabricated on top of a sacrificial aluminum gallium phosphide ($\text{Al}_x\text{Ga}_{1-x}\text{P}$) layer, which was removed in the region under the device by wet etching. This approach is viable for free-standing structures which exploit the refractive index contrast between GaP and air; photonic devices such as waveguides, grating couplers or ring resonators cannot be realized in this manner. Fabrication of non-freestanding GaP photonic structures has been achieved utilizing liftoff and transfer onto diamond, where

¹The emission of undoped GaP LEDs is very inefficient (0.1%) because of the material's indirect bandgap. Even doped the emission in the green only approaches an efficiency of 3% [3]. More common for green LEDs is the usage of indium gallium nitride.

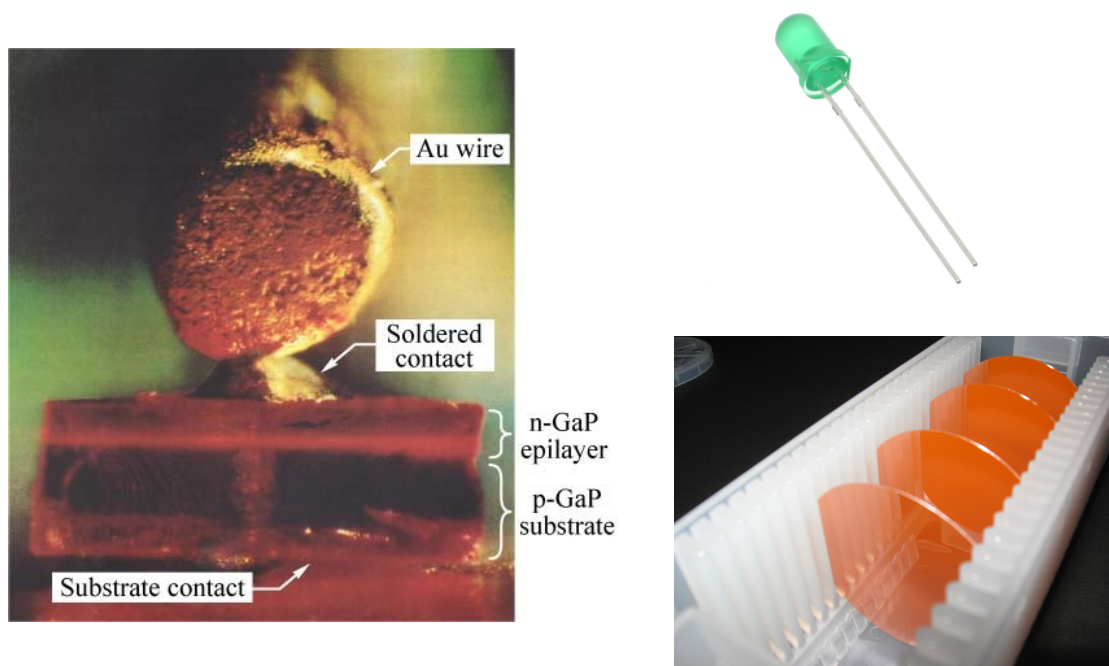


Figure 1.1 – (a) Zn- and O-doped p-n junction region of a GaP light-emitting diode developed by Pilkuhn, IBM, 1966 [1, p.12] (b) LEDs made of undoped GaP emit green light [4] (c) GaP wafers are transparent for wavelengths above the bandgap of 549 nm [5].

the specific aim was coupling to NV centers [15, 20, 21, 22]. In addition, a pick-and-place technique with a polymer-stamp was used to transfer GaP devices to a poly(methyl methacrylate) (PMMA) layer containing diamond nanocrystals [10]. Large-scale wafer-level fabrication is however not practicable with these techniques, and as such it is only sufficient for testing of single devices. Most recently, an approach has been demonstrated exploiting GaP films grown on silicon that are subsequently transferred to glass with an adhesive interlayer (SU-8 2002) [7]. Although this represents a step forward, the use of a polymer limits further processing because of thermal stability, and the process does not provide for full integration, for example with electronic circuitry.

Integrated GaP photonic devices

This thesis is based on the development of a scalable and manufacturable solution for fully integrated GaP photonic circuits, namely the first GaP photonic devices fabricated on SiO₂. It is in detail described in chapter 3 and has been published in 2018 [23]. The approach makes use of direct wafer bonding of a GaP/Al_xGa_{1-x}P/GaP layer structure onto a SiO₂-on-Si wafer. Direct wafer bonding is an established technique within the Binnig and Rohrer Nanotechnology Center (BRNC) for III-V materials such as InGaAs [24]. To enable the use

of this technique for GaP a recipe for metalorganic chemical vapor deposition (MOCVD) was developed which lead to surfaces sufficiently smooth for direct wafer bonding. The GaP substrate and the $\text{Al}_x\text{Ga}_{1-x}\text{P}$ stop layer are sequentially removed with selective dry- and wet-etch processes, leading to the desired gallium phosphide-on-insulator (GaP-OI) wafer. A major challenge was the development of an etch process for GaP selective to $\text{Al}_x\text{Ga}_{1-x}\text{P}$, which had only been shown by Epple et al. for what is now an obsolete reactive ion etching (RIE) tool [25]. A second dry-etch process was developed for anisotropic etching of high aspect-ratio structures, which is employed to pattern devices in the GaP top layer. Prior to this work, patterning of GaP has been performed for various purposes, but mainly optimized for high etch rates and surface morphology (for more details see section 3.5). The performance achieved in previously published results on two-dimensional (2D) PhCs was limited to quality factors ranging from 1 to 2×10^4 for wavelengths in the near infrared, which is a rather moderate value for PhCs, and could be significantly improved within this thesis. The final release step, which is accomplished by removing the underlying SiO_2 in buffered HF, is known from the release of silicon devices [26], but was optimized for GaP devices.

Based on this fabrication process for integrated GaP photonic devices, various fields of physics and related families of devices were explored as part of this thesis. They can be divided into two broad topics: nonlinear optics and microwave-to-optical transduction via an intermediate mechanical resonator. In the next paragraphs an overview over these fields is given.

material	n_0	n_2 $10^{-18}\text{m}^2/\text{W}$	$\chi^{(2)}$ pm/V	λ_{TPA} nm	A_{phys} μm^2	D_1 GHz	Q 10^6	P_{th} mW
Si	3.5	4	-	2250	-	-	-	-
$\text{Al}_{.38}\text{Ga}_{.17}\text{As}$	3.3	26	210	1540	0.2	995	0.1	3
$\text{In}_{.5}\text{Ga}_{.5}\text{P}$	3.12	6 ^a	220 ^b	1305 ^c	0.24	-	-	-
GaP	3.1	11(5)	82	1100	0.15	250	0.2	3
Diamond	2.4	0.082	-	450	0.81	925	1	20
GaN	2.3	3.4	16	730	-	-	-	-
AlN	2.1	0.23	0.43	440	2.3	435	0.8	200
Si_3N_4	2.0	0.25	-	460	1.8	200	36	0.3
Hydex	1.7	0.12	-	280	2.2	200	1	50
SiO_2	1.4	0.022	-	280	~ 30	33	270	1

Table 1.1 – Properties of current integrated nonlinear microresonator platforms operating at $\lambda = 1550$ nm. If P_{th} is given, frequency comb generation has been realized. Values are from [30] (Si), [31] ($\text{Al}_{.38}\text{Ga}_{.17}\text{As}$), [32] (InGaP), [33] (diamond), [34, 35] (GaN), [36] (AlN), [37] (Si_3N_4), [38] (Hydex), [39] (SiO_2)

^a[27]

^b[28]

^c[29]

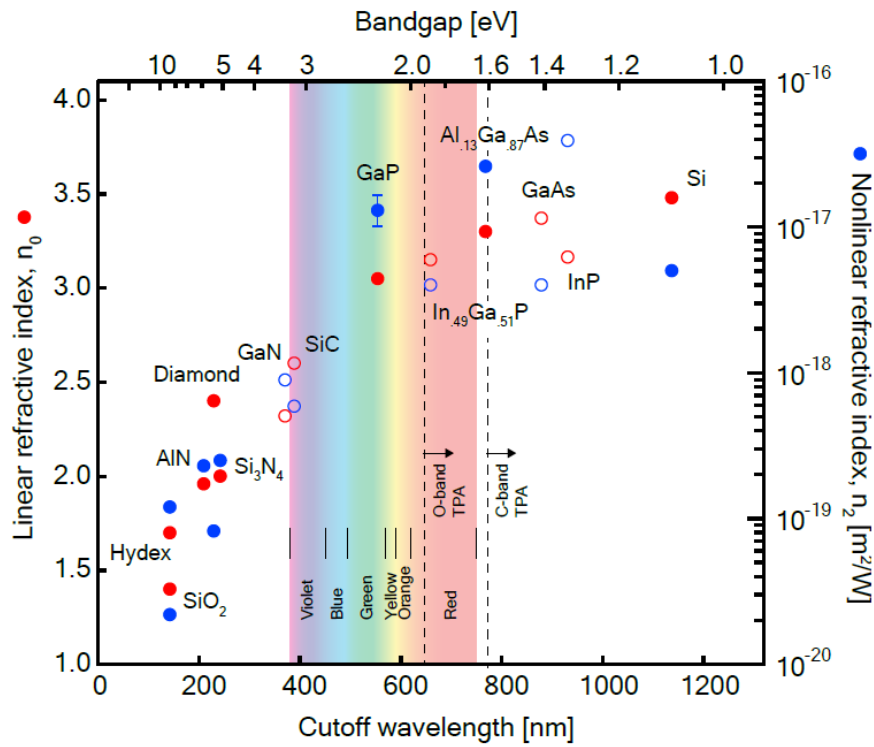


Figure 1.2 – GaP as a material for integrated nonlinear photonics. Linear (red) and nonlinear (blue) refractive indices of various integrated photonics materials, plotted versus bandgap energy and cutoff wavelength. Vertical lines denote cutoff wavelengths for TPA in the telecom O-band (1300-1350 nm) and C-band (1535-1575 nm). Solid circles denote materials with which microresonator frequency combs have been demonstrated. Values for materials other than GaP were taken from [31] (SiO_2 , Hydex, AlN, Diamond, Si_3N_4 , AlGaAs), [40] (SiC), [30] (Si), [41, 42] (GaN), [43] (InP), [27] (InGaP), and [44] (GaAs).

Nonlinear optics with GaP photonic devices

In the field of nonlinear optics, prior to this thesis GaP photonic devices have been used for second-harmonic [12, 13, 16] and sum-frequency generation [14]. Here, for the first time, third-harmonic and frequency comb generation, which rely on the Kerr coefficient, are shown. Additionally, the Kerr coefficient is measured.

There are other III-V material platforms with high second- and third-order susceptibility, for example InGaP-on-silicon dioxide [32] and AlGaAs-on-silicon dioxide [45], where integration of the nonlinear material was accomplished through a transfer technique with benzocyclobutene as an adhesive. A comparison to the device performance achieved with GaP-OI resonators is made in Table 1.1, the device performance is measured in terms of the power threshold to generate a frequency comb P_{th} .

The material and device parameters decisive for the efficiency of the presented devices are listed before the device performance. They are explained in detail in chapter 2 and shall be only briefly summarized here: To achieve a good confinement of an optical mode in a photonic device, a high-refractive index n_0 is desired to obtain high index contrast to the substrate or the surrounding air. The Kerr coefficient n_2 describes the efficiency of third-order nonlinear processes, such as four-wave mixing and frequency comb generation. In case of a non-centrosymmetric crystal structure second-order nonlinear effects can be observed, the strength of which is given by the second-order nonlinear susceptibility $\chi^{(2)}$. An undesired nonlinear process is TPA as it leads to heating of the devices. Therefore the threshold wavelength λ_{TPA} below which TPA becomes significant, which is given by the material's bandgap energy E_g , should be as low as possible. These four parameters are material dependent and the requirement of a large refractive index and a wide bandgap are inherently conflicting, which is illustrated in Figure 1.2. For a high refractive index, a material must have high polarizability at optical frequencies [46, p.67ff.], which is a property usually associated with rather weakly bound electrons. In contrast, a wide bandgap generally implies strong electronic bonds between atoms [47, p.167]. Gallium-containing compounds have a favorable tradeoff between n and E_g . GaP is especially appealing, as the cutoff wavelength for TPA lies at 1100 nm, which is below the standard telecommunication wavelengths of 1550 nm and 1300 nm.

Besides the material parameters, device parameters are decisive in determining the efficiency of a nonlinear optical process. As these scale with higher orders of the electric field strength it is important to confine the light both spatially and temporarily. This is accomplished by employing optical resonators. The spatial confinement is given by the mode volume $V = LA_{\text{eff}}$ (L is the optical path length and A_{eff} the effective mode area), the temporal confinement by the quality factor Q which is proportional to the lifetime of an optical mode in the resonator. The frequency separation between adjacent modes, which is called the free spectral range (FSR)= D_1 , is defined by the optical path length. The performance of a resonator is therefore governed by the device design and the quality of the resonator, which is often limited by fabrication capabilities. In the past years, great progress has been made in this respect, enabling the use of new materials and more efficient nonlinear optical processes.

Microwave-to-optical transduction

Research on systems that can coherently convert electrical signals at radio frequencies² (RF) to optical signals has recently gained interest because of the prospect of linking quantum computers based on superconducting microwave circuits over long distances, as is required for distributed quantum computing or remote access to quantum computers. Superconducting quantum circuits allow efficient and fast quantum operations based on the single-photon non-linearity at microwave frequencies of resonant circuits containing Josephson junctions. It is difficult though to transport quantum states at microwave frequencies over long distances, as they suffer from high attenuation and decoherence due to thermal noise at room temperature. The most robust carriers of quantum information over long distances are optical signals [50]. Therefore various platforms capable of transducing RF to optical photons have been proposed

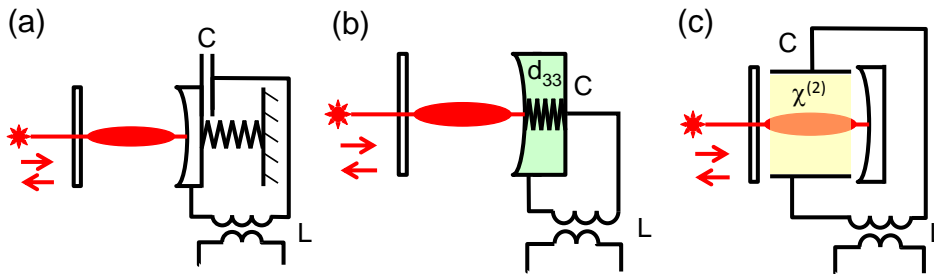


Figure 1.3 – Schematic illustration of alternative concepts for the transduction of RF photons to optical photons that are currently explored by various groups: a) Coupling of an optical cavity to an LC-circuit via a mechanical resonator. A capacitor plate of the LC-circuit is incorporated on the mechanical resonator. b) An optical resonator and an LC-circuit, where the mechanical resonator comprises a piezoelectric material also serving as the capacitor of the LC-circuit. c) Direct coupling of the electrical and the optical resonators via a second-order nonlinearity. A nonlinear material in the optical resonator is capacitively coupled to the LC-circuit.

and tested. Two key publications on transducers including an intermediate mechanical resonator are the following: Bochmann et al. [51] where the piezoelectric actuation of a photonic crystal beam is used to drive a stationary mechanical mode, which is in turn optomechanically coupled to a localized optical mode [51]; and Andrews et al. [52], where a Si_3N_4 membrane is placed in a Fabry-Pérot cavity. Part of the membrane is covered with an electrode serving as a capacitor plate coupled to a microwave circuit [52]. They represent two different concepts for performing microwave-to-optical transduction with an intermediate mechanical resonator: One makes use of piezoelectric actuation to realize electromechanical coupling [53, 54, 55, 56], the other uses capacitive coupling [57, 58, 59, 60, 61]. The two approaches

²The terms microwave and radio frequency are used equivalently in this work, although they actually refer to different frequency ranges: Microwaves are in the range of 300 MHz to 300 GHz and radio frequency signals are in the range of 20 kHz to 300 GHz. Of relevance for the discussed application as a transducer for signals used in quantum information processing in superconducting circuits is the frequency range used for qubits. For the often applied transmon qubit, this is a single-digit GHz frequency [48, 49]. The actual range of operation for the transducer is given by its bandwidth (see section 2.7)

are depicted schematically in Figure 1.3(a) and (b). These approaches stand in contrast to direct electro-optic conversion (Figure 1.3(c)), where no mechanical resonator is involved, but instead the $\chi^{(2)}$ nonlinearity provides the mechanism for modulation of the intracavity light through the Pockels effect [62, 63, 64, 65]. One promising example for this category is Fan et al. [66]. Here, the microwave resonator forms a capacitor, which creates an electric field overlapping with an optical resonator made of a nonlinear material, in this case AlN. Other systems, which have been proposed for microwave-to-optical transducers comprise intermediate collective spin excitations in atom ensembles [67], single-photon emitters on a mechanical resonator [68] and magnons in magneto-optics [69, 70].

The requirements for RF-to-optical transduction are described in detail in section 2.7. In order

parameter	capacitive coupling	piezoelectric coupling	direct electro-optic
	Andrews et al.	Vainsencher et al.	Fan et al.
$\omega_o/2\pi$ [Hz]	282×10^{12}	197×10^{12}	194×10^{12}
$\omega_e/2\pi$ [Hz]	7×10^9	3.78×10^9	8.31×10^9
$\Omega_m/2\pi$ [Hz]	560×10^3	3.78×10^9	-
$\kappa_o/2\pi$ [Hz]	1.65×10^6	15.2×10^9	$190 \& 480 \times 10^6$
$\kappa_e/2\pi$ [Hz]	1.59×10^6	<i>a</i>	0.55×10^6
$\kappa_m/2\pi$ [Hz]	4.0	5×10^6	-
Q_o	171×10^6	13.0×10^4	$1.0 \& 0.4 \times 10^6$
Q_e	4.4×10^3	<i>a</i>	-
Q_m	1.75×10^9	756	-
$g_{em}/2\pi$ [Hz]	2.1	?	-
$g_{om}/2\pi$ [Hz]	7	$115 \pm 15 \times 10^3$	-
$g_{eo}/2\pi$ [Hz]	-	-	310 ± 10
$C_{0,em}$	4.6×10^{-6}	<i>a</i>	-
$C_{0,om}$	3.2×10^{-4}	1.7×10^{-7}	-
$C_{0,eo}$	-	-	2.3×10^{-9}
$n_{cav,o}$	10^{6b}	9400 & 4900	$3.2 \pm 0.1 \times 10^7$
$n_{cav,e}$	10^7 to 10^9	-	-
$ t_{int} ^2$	~ 1	$0.4 \pm 0.2 \times 10^{-2}$	25.9 ± 0.3
$ t_{ext} ^2$	0.082 \pm 0.006	$1.3 \pm 0.6 \times 10^{-2}$	2.05 \pm 0.04
		$1.4 \pm 0.6 \times 10^{-4}$	
		$3.0 \pm 0.9 \times 10^{-4}$	

Table 1.2 – Comparison of different RF to optical transducer concepts. ω_i is the involved resonator's resonance frequency. The indices $i = o, e, m$ denote the optical, electrical or mechanical resonator. κ_i and Q_i are the resonator's linewidth and quality factor. g_{ij} is the coupling strength between the two relevant modes of the resonators, $C_{0,ij}$ the achieved single photon cooperativity. $n_{cav,i}$ is the number of photons in the resonator, $|t_{int}|$ and $|t_{ext}|$ are internal and external transduction efficiencies, which are defined in the text.

^aThis device did not include a microwave resonator. To my knowledge, no piezoelectric transducer including a microwave resonator has been published yet.

^bTaken from [71], the publication referenced for optical calibration.

to judge about the current state of the different transduction methods, the most important parameters are briefly explained in the following paragraph. For successful transduction, the information needs to be transferred faster from one domain to the other than the decay time of the resonators involved. This holds for the transduction through an intermediate mechanical resonator, as well as for the direct electro-optic conversion. This condition is expressed by the requirement that the cooperativity $C_{i,j} = \frac{n_{\text{cav},i} g_{0,ij}^2}{\kappa_i \kappa_j} > 1$. The indices $i = o, e, m$ denote the optical, electrical or mechanical resonator. $g_{0,ij}$ is the coupling rate between the involved resonator modes, $\kappa_{i,j}$ the linewidth of the two involved resonators and $n_{\text{cav},i}$ the number of photons in the input resonator. The conversion efficiency for direct electro-optic conversion is then given by $|t|^2 = \frac{4\eta_i \eta_j C_{ij}}{(1+C_{ij})^2}$ [66], and that for transduction through an intermediate mechanical resonator by $|t|^2 = \frac{4\eta_i \eta_k C_{ij} C_{jk}}{(1+C_{ij}+C_{jk})^2}$ [72, 73]. Here η_i and η_k are the input and output coupling efficiencies. The internal transduction efficiency neglects these coupling efficiencies. An overview over these parameters for the three examples presented in the previous section is given in Table 1.2, from which it can be seen how different the regimes are in which the transducers work: The capacitive coupling as well as the direct electro-optic conversion are non-resonant couplings in the sense that the frequencies of the involved signals differ by several orders of magnitude. Therefore the coupling rates $g_{0,em}$ and $g_{0,eo}$ are rather small. For the piezoelectric actuation, coupling rates above 1 MHz have been measured [74] and coupling rates of several 10 MHz have been predicted [75, 76] (not included in Table 1.2). In contrast, the linewidths of the resonators involved in the capacitive coupling and the direct electro-optic conversion are rather narrow and therefore lead to a high cooperativity and conversion efficiency. The linewidth of the resonators in Vainsencher et al. could in principle be improved, but because of fabrication limitations it will most probably not reach the performance of a Fabry-Pérot cavity with a membrane in the middle. Finally, the number of photons in a PhC is usually limited by heating effects. Therefore, the transduction through piezoelectric actuation must be carried out with two orders of magnitude less photons than the other approaches, which limits the attainable cooperativity. There are however other figures of merit to consider than just the transduction efficiency. Specifically, a large bandwidth and a low amount of added noise are desired, as discussed in section 2.7.

In order to achieve high cooperativities for a piezoelectric transducer the two stages of transduction can be optimized independently: The optomechanical conversion and on the electromechanical conversion. Both challenges have been addressed as part of this thesis. A design for optimized electromechanical coupling has been developed by numerical simulations as presented in section 6.2. PhCs made of the piezoelectric material GaP have been designed, fabricated and characterized for their optomechanical properties (section 6.1 and chapter 7), a fabricated GaP PhC is shown in Figure 1.4(a). GaP is a promising material for microwave-to-optical transduction compared to the currently used options GaAs [53, 77] and AlN [51, 54]. The piezoelectric constant of GaP ($e_{14} = -0.15 \text{ C/m}^2$ [78]) and GaAs ($e_{14} = 0.16 \text{ C/m}^2$ [79]) are quite similar. However, due to its lower bandgap, GaAs suffers from TPA (compare Figure 1.2) and therefore experiences substantial heating if too many intracavity photons n_{cav} are present. The piezoelectric constants of AlN ($e_{33} = 1.46 \text{ C/m}^2$ and $e_{31} = -0.60 \text{ C/m}^2$ [80]) are about an

order of magnitude higher than for GaP and also the bandgap is sufficiently large to prevent TPA. However, the photoelastic constants, which enter the optomechanical coupling rate based on the photoelastic effect (Equation 2.29) are about an order of magnitude smaller than for GaP [81], which leads to poor optomechanical coupling rates.

In the context of increasing the optomechanical coupling rate without relying on the photoelastic effect, but instead exploiting the moving boundary effect, design alternatives for PhCs have been tested as part of this thesis (chapter 8). A slotted design strongly confines the light and leads to an increased contribution of the moving boundary effect to the optomechanical coupling. This approach has been exploited by Leijssen et al. [82], where coupling strengths of $g_0/2\pi \approx 11.5$ MHz have been achieved, leading to a single-photon cooperativity of $C_0 = 0.16$. However, the optical quality factor was limited to $Q_o = 400$. In this thesis, the idea is to exploit the slot effect while at the same time maintaining a high optical quality factor. A fabricated slotted PhC made of Si is shown in Figure 1.4(b).

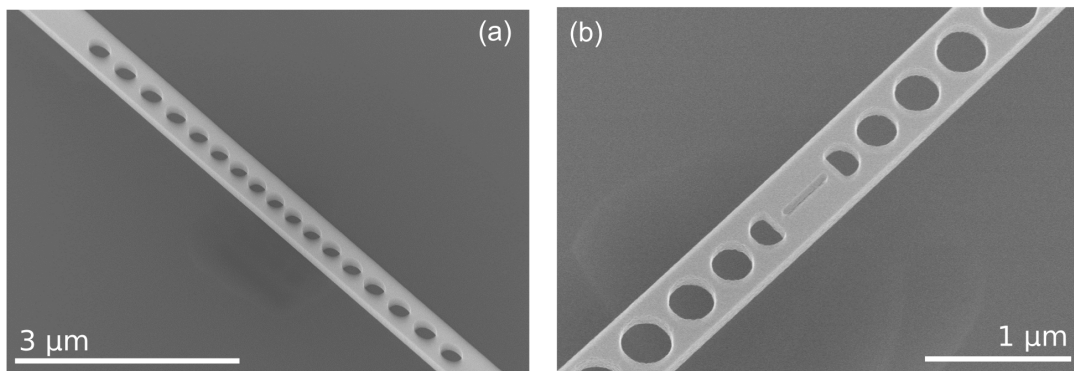


Figure 1.4 – Scanning electron microscope images of fabricated PhCs. (a) GaP PhC (b) Slotted Si PhC with a slot width of 40 nm.

Structure of the thesis

The structure of this thesis is as follows: In chapter 2 the fundamental concepts enabling the design and characterization of the nanophotonic devices are explained. This concerns the fields of optical resonators, nonlinear optics, optomechanics and piezoelectricity. Chapter 3 deals with the process development for GaP-OI devices, which is the fundamental achievement in this work enabling all following research. The topic of chapter 4 and 5 is nonlinear optics, where the former describes the design of the employed devices and the latter the measured effects as second- and third-harmonic generation and frequency comb generation. Chapter 6 and 7 treat the conducted research on optomechanics with 1D PhCs, where chapter 6 explains the design of the GaP-OI devices used for the optomechanical measurements and additionally the design optimization of an electrically actuated device meant for RF-to-optical transduction, which makes use of the piezoelectric properties of GaP. Chapter 7 treats the experimental characterization of the GaP-OI PhCs. Chapter 8 finally describes the work done with slotted PhCs made of silicon and their optomechanical properties.

2 Theory

Gallium phosphide is a non-centrosymmetric material, which makes it interesting for applications in the fields of nonlinear optics and piezoelectricity. In this work nonlinear optics appears as second- and third-harmonic generation, as well as frequency combs in ring resonators. Piezoelectrical coupling and optomechanical coupling can be combined in a 1D PhC to build a microwave-to-optical transducer. For this a microwave circuit is piezoelectrically connected to a mechanical resonator which in turn is optomechanically coupled to an optical resonator. The fundamental equations governing these topics are explained in this chapter. An overview of the relevant material constants for gallium phosphide (GaP) is given in Table 2.1.

Property	Material coefficient	Symbol	Value	Reference
General	Density	ρ	$4.138 \times 10^3 \text{ kg/m}^3$	[83]
	Lattice constant	a	5.45 \AA	[84]
	Band gap (indirect)	E_0	2.26 eV	[85]
Dielectric	Relative permittivity (1550 nm)	ϵ_r	9.33	
	Refractive index (1550 nm)	n	3.05	[86]
Elastic	Stiffness	c_{11}	$1.4050 \times 10^{11} \text{ Pa}$	[87]
		c_{12}	$0.6203 \times 10^{11} \text{ Pa}$	[87]
		c_{44}	$0.7033 \times 10^{11} \text{ Pa}$	[87]
Piezoelectric	Piezoelectric modulus	e_{14}	-0.15 C/m^2	[78]
Nonlinear optics	2nd order nonl. coeff.	$\chi_{14}^{(2)}$	164 pm/V	[88]
	Kerr coefficient	n_2	$1.1(5) \times 10^{-17}$	[89]
Optomechanics	photoelastic coeff. (632.8 nm)	p_{11}	-0.23	[90]
		p_{12}	-0.13	[90]
		p_{44}	-0.10	[90]

Table 2.1 – Material constants of GaP.

2.1 Nonlinear optics

In this section, the fundamentals of nonlinear optics are discussed, following the description in [91]. The dependence of the polarization of a medium $P(t)$ on the applied electric field $E(t)$ can be described as follows^{1,2}[91, p.2]:

$$\begin{aligned} P(t) &= \epsilon_0[\chi^{(1)}E(t) + \chi^{(2)}E(t)^2 + \chi^{(3)}E(t)^3 + \dots] \\ &= \chi_{\text{eff}}E(t) \\ &= P^{(1)}(t) + P^{(2)}(t) + P^{(3)}(t) + \dots \end{aligned} \tag{2.1}$$

The material properties $\chi^{(2)}$ and $\chi^{(3)}$ are known as the second-order and third-order susceptibility, which are third-rank and fourth-rank tensors. $P^{(2)} = \chi^{(2)}E(t)^2$ is called the second-order nonlinear polarization, $P^{(3)} = \chi^{(3)}E(t)^3$ the third-order nonlinear polarization. They both lead to their own set of physical effects, of which those relevant for this work will be discussed in the following paragraphs. Effects related to $\chi^{(2)}$ only occur in non-centrosymmetric materials, in which category gallium-phosphide belongs. Note also that χ_{eff} is related to the refractive index as $n = \sqrt{1 + \chi_{\text{eff}}}$ [91, p.208].

2.1.1 Second-harmonic generation

Second-harmonic generation is an example of a second-order nonlinear process. A laser creates an electric field $E(t) = E_0e^{-i\omega t} + c.c..$ The polarization within a medium with the second-order susceptibility $\chi^{(2)}$ is then [91, p.5]

$$P^{(2)}(t) = 2\epsilon_0\chi^{(2)}E_0E_0^* + (\epsilon_0\chi^{(2)}E_0^2e^{-2i\omega t} + c.c.) \tag{2.2}$$

In addition to a time-independent term, there is a contribution with a frequency of 2ω . This means that there will be radiation created at double the incoming frequency within the nonlinear medium. The strength of this signal is proportional to E_0^2 , so it increases quadratically incoming laser power.

2.1.2 Third-harmonic generation

Third-harmonic generation is an example of an effect occurring due to the third-order nonlinear polarization $P^{(3)} = \chi^{(3)}E(t)^3$. To simplify the derivation an electric field $E(t) = \mathcal{E} \cos \omega t$ is assumed. This leads, through the use of the identity $\cos^3 \omega t = \frac{1}{4} \cos 3\omega t + \frac{3}{4} \cos \omega t$ to a

¹An alternative definition, as found for example in [92], is $P(t) = \epsilon_0\chi^{(1)}E(t) + 2dE(t)^2 + 4\chi^{(3)}E(t)^3 + \dots$. Therefore the second-order nonlinear coefficient d is related to the second-order susceptibility as $d = 1/2\chi^{(2)}$.

²In the 2nd edition of Boyd's "Nonlinear optics" [93] the definition is in gaussian units for the nonlinear susceptibilities: $P(t) = \chi^{(1)}E(t) + \chi^{(2)}E(t)^2 + \chi^{(3)}E(t)^3 + \dots$

nonlinear polarization [91, p.11]

$$P^{(3)}(t) = \frac{1}{4}\epsilon_0\chi^{(3)}\mathcal{E}^3\cos 3\omega t + \frac{3}{4}\epsilon_0\chi^{(3)}\mathcal{E}^3\cos\omega t. \quad (2.3)$$

The first term on the right describes an electric field oscillating with the frequency 3ω . From three photons entering the medium with the frequency ω one photon with the frequency 3ω is generated. The strength of this signal is proportional to \mathcal{E}^3 , which means it grows cubically with the incident field.

The second part describes a nonlinear contribution to the field oscillating at the frequency of the incoming field ω and therefore leads to a nonlinear contribution to the refractive index. This intensity-dependent refractive index is discussed closer in the next paragraph.

2.1.3 Intensity dependent refractive index

The refractive index of a material is often described by the relation [91, p.207]

$$n = n_0 + n_2\langle E^2 \rangle = n_0 + 2n_2|E_0|^2 \quad (2.4)$$

with n_0 being the linear refractive index and n_2 the nonlinear refractive index or Kerr coefficient. The angular brackets denote a time average. This intensity dependent refractive index is due to the third-order nonlinear polarization $P^{(3)} = \epsilon_0\chi^{(3)}E(t)^3$, as shown in the previous paragraph. Taking into account that in general $n = \sqrt{1 + \chi_{\text{eff}}}$ and assuming an effective susceptibility $\chi_{\text{eff}} = \chi^{(1)} + 3\chi^{(3)}|E_0|^2$, the refractive index and the first-order susceptibility can be linked as

$$n_0 = \sqrt{1 + \chi^{(1)}} \quad (2.5)$$

and the Kerr coefficient to the third-order susceptibility as [91, p.208].

$$n_2 = \frac{3\chi^{(3)}}{4n_0}. \quad (2.6)$$

In literature the Kerr coefficient as well as the third-order susceptibility $\chi^{(3)}$ are used to describe the nonlinearity of materials. Equation 2.6 is derived for self-modulation. For cross-modulation a factor 2 must be added on the right side of Equation 2.6 (for details refer to [91, p.209]).

The derivation so far was held in SI-units (standard metric system of units). In this case n_2 is in units of V^2/W . In practice it is more convenient to write the intensity as $I = \frac{1}{2}\epsilon_0cn|E|^2$, where ϵ_0 is the vacuum permittivity and c the speed of light [94, p.447]. n_2 is then in units of m^2/W . For a waveguide made of a material with a third-order nonlinearity, the refractive index is then given by

$$n = n_0 + n_2 \frac{P}{A_{\text{eff}}}. \quad (2.7)$$

The field intensity is calculated as the guided power P per effective area A_{eff} . A_{eff} can be obtained by the approximate expression [94, p.44]

$$A_{\text{eff}} = \frac{(\int_{-\infty}^{\infty} \int_{-\infty}^{\infty} |E_0(x, y)|^2 dx dy)^2}{\int_{-\infty}^{\infty} \int_{-\infty}^{\infty} |E_0(x, y)|^4 dx dy}, \quad (2.8)$$

where $E_0(x, y)$ is the transverse field profile of the guided field.

The nonlinearity of a waveguide is often described by the nonlinearity parameter

$$\gamma_{\text{NL}} = \frac{\omega n_2}{A_{\text{eff}} c}. \quad (2.9)$$

2.1.4 Four-wave mixing

Another nonlinear optic effect caused by the third order susceptibility, is four-wave mixing (FWM), which enables the population of the lines of a frequency comb with photons. The third-order nonlinear polarization $P^{(3)} = \epsilon_0 \chi^{(3)} E(t)^3$, resulting from an incident field with three different frequency components $E(t) = E_1 e^{-i\omega_1 t} + E_2 e^{-i\omega_2 t} + E_3 e^{-i\omega_3 t} + c.c.$ includes 44 different frequency components. Some of them are described by the equation $\omega_4 = \omega_1 + \omega_2 - \omega_3$ and its permutations [91, p.12]. They can be rewritten in the form of $\omega_4 + \omega_3 = \omega_1 + \omega_2$. Considering this process on the level of individual photons, two photons of frequencies ω_1 and ω_2 are annihilated while two photons of the frequencies ω_3 and ω_4 are created. This process conserves the total energy of the system. Furthermore phase matching, i.e. momentum conservation, is required: $k_1 + k_2 = k_3 + k_4$, where $p = \hbar k$ is the magnitude of the momentum of the respective photon.

2.1.5 Frequency comb generation via four-wave mixing in an optical resonator

Cascaded FWM can be used to populate a frequency comb in an optical resonator. In order to make this process efficient, energy and momentum conservation has to be given. In a microresonator, the eigenmodes m have a discrete set of propagation constants $\beta_m = m \cdot L/2\pi$, with L being the length of the resonator. As a result the conversion of two pump photons with propagation constants β_m into symmetrically located modes β_{m-N}, β_{m+N} , $N=1,2,3\dots$ conserves momentum intrinsically [95]. Energy conservation though is not automatically given as the resonance frequencies are not evenly spaced due to both cavity and material dispersion. This challenge is addressed by dispersion engineering (subsection 2.4.3).

The first step of frequency comb generation is a degenerate FWM process, described by the equation $\omega_4 + \omega_3 = 2\omega_1$. To initiate the comb, the pump laser frequency is increased from the blue-side towards the cavity resonance. Starting from a certain detuning, the cavity frequency shifts due to the photothermal and Kerr-effect, leading to a stabilization of the detuning between pump laser and resonance (see subsection 2.4.2), which is referred to as photothermal locking. A comb forms if the pump power exceeds the threshold power

[95, 96, 89]

$$P_{\text{thresh}} = \frac{\pi}{4\eta} \frac{V_{\text{eff}}}{\lambda Q^2} \frac{n_g^2}{n_2}, \quad (2.10)$$

where η is the cavity coupling parameter (see subsection 2.4.1), Q is the quality factor of the cavity and $V_{\text{eff}} = A_{\text{eff}}L$ is the effective waveguide volume, L is the resonator length, λ the vacuum wavelength and n_g is the waveguide group index (see section 2.4).

2.1.5.1 Thermal and Kerr-nonlinear locking

The photothermal and the Kerr shift can be used to generate a stable laser-cavity detuning [97]. A change in the relative laser-cavity detuning would lead to a mismatch of pump frequency with respect to the resonator modes. To understand this lock we consider the case of a laser blue-detuned from the cavity resonance. The cavity frequency is already shifted from the "cold-cavity" frequency. If a fluctuation of the laser frequency occurs, the detuning can either increase or decrease. If the detuning is decreased, more light will enter the cavity, which enhances the photothermal and the Kerr-shift. The detuning will therefore go up again and be restored to its previous value. If the laser frequency fluctuation leads to a larger detuning, the intracavity photon number will go down, which pulls the resonance back again. Therefore, it is possible to achieve a stable detuning with thermal and Kerr-nonlinear locking.

2.2 Stimulated Raman scattering

A process, which can occur in competition to FWM in waveguides with normal or weak dispersion [98], is stimulated Raman scattering (SRS). In a classical picture it can be explained by the interaction of an optical field with a vibrational mode of the medium with resonance frequency Ω_v [91, p.479ff]. The optical polarization of the medium depends upon the internuclear separation. This will be modulated periodically in time for a given vibrational mode which leads to a variation of the refractive index. A laser beam passing through this medium will be phase modulated, which leads to frequency sidebands separated from the laser frequency by $\pm\Omega_v$. To achieve stimulated emission, this process has to be enhanced by the presence of the laser. The modulated laser at frequency ω_s can create a beat signal with the original laser field at frequency ω_L which leads to the creation of phonons at the frequency of the vibrational mode $\omega_L - \omega_s = \Omega_v$. This leads to stronger vibrations, which in turn will lead to a stronger Stokes field.

2.3 Two-photon absorption

An undesired nonlinear optical process in many devices is TPA, as it leads to heating. Described on the level of an individual atom, this makes a transition from its ground state to an excited state by the simultaneous absorption of two photons with frequency ω [91, p.16].

The absorption cross section for TPA is not constant, but scales linearly with laser intensity $\sigma = \sigma^{(2)}I$, where $\sigma^{(2)}$ is a material parameter describing the strength of the process. The transition rate of atoms from the ground to the excited state is given by $R = \frac{\sigma^{(2)}I^2}{\hbar\omega}$. The absorbed power is thus proportional to the square of the laser intensity, so the process becomes significant at high laser intensities.

In a semiconductor or insulator, TPA leads to the excitation of the material from a lower energy level into a higher one. This process can only occur if the photon energy is at least half the bandgap energy.

2.4 Optical resonators

For nonlinear optics as well as for optomechanics, it is important to confine the light to small mode volumes V to achieve high intracavity intensities. At the same time, long lifetimes of the optical modes are desired to increase light-matter interaction. For this reason optomechanics and nonlinear optics are often combined with optical resonators. There are various ways in which an optical resonator can be realized; the two applied in this thesis are ring resonators and PhCs. These resonators support a number of optical eigenmodes. The separation between two eigenmodes is designated the free spectral range (FSR) and is given by $\Delta_{\text{FSR}} = c/n_g L$, where n_g is the group refractive index, ω is the frequency, c is the speed of light and L is the length of the resonator. In the case of a ring resonator, $L = 2\pi r$, where r is the ring's radius. The group refractive index is given by

$$n_g = n_{\text{eff}} + \omega \frac{\partial n_{\text{eff}}}{\partial \omega} \quad (2.11)$$

where n_{eff} is the effective refractive index. As a function of the vacuum wavelength λ_0 , n_g is given by

$$n_g = n_{\text{eff}} - \lambda_0 \frac{\partial n_{\text{eff}}}{\partial \lambda_0}. \quad (2.12)$$

The FSR of a resonator is linked to its finesse \mathcal{F} as defined in Equation 2.13a.

$$\mathcal{F} = \frac{\Delta_{\text{FSR}}}{\kappa} \quad (2.13a)$$

$$\mathcal{F} = \frac{\pi}{2 \cdot \arcsin\left(\frac{1-\sqrt{p}}{2\sqrt[4]{p}}\right)} \approx \frac{\pi}{1-\sqrt{p}} \approx \frac{2\pi}{1-p} \quad (2.13b)$$

The finesse can be used to calculate the waveguide loss in a resonator, as it is connected to the fraction p of the circulating power which is left after one round-trip (see Equation 2.13b). In a ring resonator, $p = e^{\alpha L}$, where α is the waveguide loss.

In the following, the focus is on a single optical mode with the frequency ω_o .

2.4.1 Input output formalism of an optical cavity

Depending on the way a resonator is coupled, different types of resonators can be defined (see Figure 2.1): A single sided cavity has only one channel serving as input and output for light, e.g. a very antisymmetric 1D PhC. A double-sided cavity has two such channels, e.g. a Fabry-Pérot cavity. A ring resonator coupled to a bus waveguide also belongs in this category, if it is a bi-directional cavity, which means that coupling to the waveguide is possible in both directions of the bus waveguide. The loss channels of a resonator mode are internal scattering

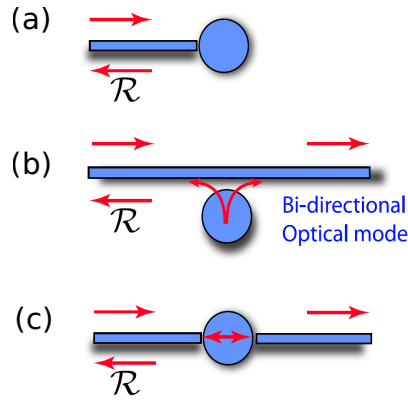


Figure 2.1 – Comparison of coupling schemes for optical resonators [99]. (a) A single-sided cavity coupled in reflection. (b) A bi-directional waveguide-coupled cavity, e.g. a ring resonator coupled to a bus waveguide. (c) A double sided cavity, e.g. a Fabry-Pérot cavity or a PhC, where reflection and transmission can be measured.

or absorption and coupling losses. They lead to an overall cavity decay rate $\kappa = \kappa_i + \kappa_e$ with the internal decay rate κ_i and external decay or coupling rate κ_e . Related to the decay rate is the optical quality factor $Q_o = \omega_o/\kappa$. $1/Q$ is a dimensionless decay rate and is equivalent to $1/Q = P_{\text{Out}}/(\omega_o U_{\text{cav}})$, where P_{Out} is the power leaving the resonator and U_{cav} is the intracavity energy.

To analyze the evolution of the photon population temporal coupled mode theory can be used. This is shown here for a double-sided cavity such as a PhC coupled to an input and an output waveguide [100]. An analogous derivation can be performed for a waveguide coupled bi-directional cavity, such as a ring resonator with a bus waveguide, which is not shown here. The rate equations describing a bidirectional cavity with two coupled waveguides $l = 1, 2$ is

$$\frac{dA}{dt} = -i(\omega - \omega_0)A - A/\tau_i - \sum_{l=1}^2 A/\tau_{e,l} + \sum_{l=1}^2 \sqrt{\frac{2}{\tau_{e,l}}} s_{l+}. \quad (2.14)$$

A is the intracavity amplitude of the electric field. A^2 is the electromagnetic energy in the cavity. Following the convention in [100, 99], τ is the decay time of the intracavity amplitude, where the indices e and i denote the loss mechanism. $\kappa = 2 \cdot 1/\tau$ is the decay rate of the intracavity energy. s_{l+} is the amplitude of the field entering through the respective waveguide.

Chapter 2. Theory

Assuming a symmetric cavity ($\tau_{e,1} = \tau_{e,2} = \tau_e$) and replacing the lifetimes with decay rates ($1/\tau = \kappa/2$), the derived transmission spectrum for this system is given by Equation 2.15a [100, p.210] which describes a Lorentzian transmission profile. The reflection spectrum is given by Equation 2.15b .

$$T(\omega) = \frac{\kappa_e^2/4}{(\omega - \omega_o)^2 + \kappa^2/4} \quad (2.15a)$$

$$R(\omega) = \frac{(\omega - \omega_o)^2 + (\kappa_i/2)^2}{(\omega - \omega_o)^2 + (\kappa_i/2 + \kappa_e)^2} \quad (2.15b)$$

In case of a PhC, couple with a tapered fiber, reflection and transmission spectrum are exchanged. The transmission on resonance is $T(\omega_o) = \kappa_e^2/\kappa^2 = \kappa_e^2/(\kappa_i + \kappa_e)^2$. This approaches 1 if $\kappa_e \gg \kappa_i$, which means that the cavity mode decays faster into the waveguide than into free space. The steady state photon population is given by [99, p.1396]

$$\bar{n}_{\text{cav}} = \frac{\kappa_e/2}{\Delta^2 + (\kappa/2)^2} \frac{P_{\text{In}}}{\hbar\omega_L}, \quad (2.16)$$

where P_{In} is the input power launched into the cavity and $\Delta = \omega_L - \omega_o$ is the laser-cavity detuning. The calculation of the intracavity power from the power leaving through one side of the symmetric cavity follows the equation

$$\bar{n}_{\text{cav}} = \frac{2P_{\text{Out}}Q_e}{\hbar\omega_o^2}, \quad (2.17)$$

which is apparent from the definition of the quality factor.

A cavity can be working in several regimes depending on the ratio of κ_e and κ_i . If $\kappa_e \approx \kappa \gg \kappa_i$ the system is called overcoupled. If $\kappa_i = \kappa_e$ this is called critical coupling. For a single-sided cavity, no light is reflected when critically coupled. The light is dissipated in the cavity with the same rate as it enters. The state where $\kappa_i \gg \kappa_e$ is referred to as undercoupling and is usually not favored in experiments, as it is basically a waste of cavity photons. A quantity sometimes used to describe the coupling regime is the cavity coupling parameter $\eta = \frac{\kappa_e}{\kappa}$, where $\eta = 1/2$ means critical coupling.

2.4.2 Photothermal and Kerr shift

The effective resonance frequency of the resonators employed in this work depends on the circulating intracavity power [97]. Absorption of the intracavity photons results in heating and changes the effective refractive index of the device. Another reason for a power dependent resonance frequency is the Kerr effect (subsection 2.1.3). When measuring the transmission through a device with a high quality factor, this leads to a triangular transmission profile instead of the expected Lorentzian resonance shape (see Figure 7.8(a)). The shape of the triangle depends on the sweep direction. This behavior has consequences for the experiments on cavity optomechanics and nonlinear optics in this work. For cavity optomechanics, this

property is generally detrimental, as it limits the number of intracavity photons for which operation at a desired laser-cavity detuning is possible. For frequency comb generation, this effect can be exploited to generate so-called self-locking.

2.4.2.1 Characterization of the photothermal shift

An important advantage of gallium phosphide is its large bandgap, as this prevents TPA at the telecommunication wavelengths used and therefore heating of the devices. To confirm this advantage, we compare the absorption losses of GaP devices to devices of materials showing TPA, for example silicon[97]. To obtain a more quantitative measure of the thermo-optic effect, we analyze the dependence of the optical resonance frequency on the power dissipated in the cavity $P_d = \kappa_i U_{\text{cav}}$ [101, 102], the derivative of which we define as the thermal susceptibility $\chi_{\text{th}} = \frac{d\omega}{dP_d}$. We are interested in the fraction ζ of the intrinsic loss rate of the cavity κ_i that comes from absorption and leads to heating of the device, namely $\kappa_{\text{abs}} = \zeta \kappa_i$. Assuming the frequency shift $d\omega$ is entirely due to thermo-optic effects, we can write $d\omega = \beta(\omega_o) \Delta T$, where $\beta(\omega_o)$ is a frequency-dependent coefficient incorporating both the thermo-refractive effect and thermal expansion, and ΔT is the local temperature increase. The power absorbed, $P_{\text{abs}} = \kappa_{\text{abs}} U_{\text{cav}}$, is also the heat flow through the device, and thus $\Delta T = R_{\text{th}} P_{\text{abs}}$, where R_{th} is the thermal resistance of the structure. Combining these equations gives

$$\kappa_{\text{abs}} = \frac{\kappa_i \chi_{\text{th}}}{\beta(\omega_o) R_{\text{th}}}. \quad (2.18)$$

The thermal resistance for a uniform beam can be calculated as $R_{\text{TH}} = \frac{L}{k_{\text{GaP}} A}$, where L is the length and A its cross section. For a more complicated connection between cavity and heat sink, e.g. a photonic crystal, numerical simulations can be performed to infer R_{TH} .

Making use of this result, we can as well estimate the frequency shift

$$d\omega = \beta(\omega_o) R_{\text{th}} \kappa_{\text{abs}} U_{\text{cav}}. \quad (2.19)$$

2.4.3 Ring resonators

Ring resonators present one of the simplest ways to create an optical cavity: A waveguide is routed in a circle or racetrack shape. It is important to consider the cross-section of the waveguide, as it will support modes of different polarization and frequency depending on its dimensions. The effective refractive index n_{eff} depends on the index of core and cladding, and the field distribution of the respective mode. The radius of the resonator together with the group refractive index determines the FSR (see section section 2.4). For frequency comb generation, care must be taken with the dispersion of the resonator, which will be addressed in the following section.

2.4.3.1 Dispersion in ring resonators

The dispersion of a ring resonator is a combination of material dispersion and geometric dispersion. It describes the frequency dependence of the effective refractive index $n_{\text{eff}}(\omega)$. Material dispersion is an intrinsic material property. For most materials the refractive index increases with frequency ($dn/d\omega > 0$), which is called normal dispersion. Geometric dispersion arises, because light takes different paths in a resonator depending on its frequency. Due to the different refractive indices of the core and the cladding, the position of reflection in the waveguide depends on the wavelength.

The dispersion of a microresonator can be characterized by the separation of the resonator modes [103].

$$\omega_m = \omega_0 + D_1 \cdot m + \frac{1}{2} D_2 \cdot m^2 + \dots \quad (2.20)$$

where ω_0 is the resonance frequency of the pump mode, $D_1/2\pi$ corresponds to the FSR of the resonator and

$$D_2/2\pi = D_1 \cdot \frac{\partial D_1}{\partial \omega} / 2\pi \quad (2.21)$$

to the difference of the FSRs between mode 0 and m . If $D_2 < 0$ this corresponds to a normal dispersion, if $D_2 > 0$ the dispersion is called anomalous. D_2 is related to the group velocity dispersion (GVD)[103]:

$$\beta_2 = -\frac{n_g}{c} \frac{D_2}{D_1^2} \quad (2.22)$$

The group velocity dispersion is defined as [94, p.9]

$$\beta_2 = \frac{1}{c} \left(2 \frac{dn_{\text{eff}}}{d\omega} + \omega \frac{d^2 n_{\text{eff}}}{d\omega^2} \right) = \frac{d}{d\omega} \left(\frac{1}{v_g} \right). \quad (2.23)$$

Here v_g denotes the group velocity and c is the speed of light. For generating a broad frequency comb a small, anomalous GVD is desirable [104]. For a low threshold, a large anomalous GVD is needed. With anomalous GVD phase matching can be achieved. Because the material dispersion for GaP, as for most materials, is normal, one has to design a waveguide resonator with an appropriate cross-section to achieve overall anomalous dispersion.

2.4.4 Photonic crystal cavities

Among the different types of existing optical cavities, a PhC is one of the most elegant ones. Its advantage compared to other cavities is its low mode volume. The figure of merit for the efficiency of most optical processes scales inversely with the mode volume. A way to decrease the mode volume further is to introduce a slot, as shown in chapter 8. For optomechanics, we benefit from tight confinement of the optical mode by colocalizing it with a mechanical

eigenmode, which greatly enhances the interaction between the two modes. A photonic crystal consists of a periodic arrangement of two different dielectrics. Depending on the periodicity, a photonic bandgap is created. Introducing a defect within this periodicity supporting an eigenmode with a frequency within the bandgap leads to spatial confinement of this mode. This way an optical cavity can be created. For the photonic crystal nanobeams, this technique traps the light in one dimension. In the other two dimensions the light is confined through total internal reflection. The exact device design can be quite complicated and is typically accomplished with numerical simulations combined with an optimization algorithm, as described in chapter 6.

2.5 Cavity optomechanics

This chapter provides the necessary theoretical background to understand and evaluate the measurements described in chapter 7. It is limited to the working regimes relevant for the 1D PhCs that are the subject of this thesis. Furthermore, the description is kept purely classical, as a quantum mechanical description is not required for the scope of this thesis.

2.5.1 Optomechanical coupling

Optomechanical coupling typically occurs between one mechanical mode with a resonance frequency Ω_m spatially overlapping with an optical eigenmode with a resonance frequency ω_o . The fundamental mechanism is momentum transfer from the photons to the mechanical mode, which is called radiation pressure. A model to describe optomechanical coupling is a Fabry-Pérot cavity, where one mirror is free to move. A displacement x of the mirror leads to a change of the optical resonance frequency $\omega_o(x) \approx \omega_o + x \cdot \partial\omega_o / \partial x + \dots$. For small displacements it is sufficient to consider the linear term. The frequency shift per displacement is called the optomechanical vacuum coupling rate $g_0/2\pi = \partial\omega_o / \partial x \cdot x_{zpf}$, where $x_{zpf} = \sqrt{\hbar/2m_{\text{eff}}\Omega_m}$ is the zero-point motion, m_{eff} is the effective mass discussed in the next paragraph, and \hbar the reduced Planck constant. In case of multiple photons exerting radiation pressure on the mechanical mode, the photon enhanced coupling rate $g = g_0\sqrt{\bar{n}_{\text{cav}}}$ determines the strength of the optomechanical coupling.

The potential energy of a certain mode with frequency Ω_m with the normalized displacement field $\mathbf{Q}(x)$ is given by

$$U = \frac{1}{2}\Omega_m^2 \int \rho(x)|\mathbf{Q}(x)|^2 dx, \quad (2.24)$$

where $\rho(x)$ is the material density as a function of position. For the same mode, the potential energy can also be expressed as

$$U = \frac{1}{2}m_{\text{eff}}\Omega_m^2 \alpha^2, \quad (2.25)$$

where an maximum displacement α of the mechanical motion has been defined. Comparing Equation 2.24 and Equation 2.25, leads to an effective mass

$$m_{\text{eff}} = \frac{\int \rho(x) |\mathbf{Q}(x)|^2 dx}{\alpha^2}, \quad (2.26)$$

The effective mass m_{eff} depends upon the choice of α , which is ambiguous. For some mechanical resonators there is an obvious choice for the definition of α (e.g. for a spherical pendulum the displacement of the center of mass could be used), but for the mechanical modes of a nanobeam there are sometimes several possible definitions. In the simulations for the devices presented in this work, the maximum displacement, that occurs anywhere in the displacement field $\mathbf{Q}(x)$ of the mode of interest was used.

2.5.1.1 Figures of merit for optomechanical systems

In addition to the vacuum coupling rate g_0 , the behavior of an optomechanical system is governed by its optical decay rate κ , which is related to the optical quality factor Q_o by $Q_o = \omega_o / \kappa$. A small decay rate can be advantageous for certain applications. For example, the ability to achieve ground-state cooling depends on the sideband suppression factor κ / Ω_m . Furthermore, for efficient transduction from individual phonons to photons, a high cooperativity $C = n_{\text{cav}} g_0^2 / \kappa \Gamma_m$ is required, Γ_m being the decay rate of the mechanical resonator.

2.5.1.2 Optomechanical coupling at the nanoscale

Various physical phenomena can produce optomechanical coupling [52, 105, 106]. At the nanometer scale, the most commonly considered mechanisms are the moving boundary effect [107] and the photoelastic effect [108]. The former occurs if a dielectric boundary moves through a region of non-zero electric field. The latter is induced by a change of the refractive index with strain. The overall coupling rate is described by the sum of the respective coupling rates for these effects, so that $g_0 = g_{0,\text{mb}} + g_{0,\text{pe}}$. From first-order perturbation theory, the optomechanical vacuum coupling rate g_0 can be described as [107]

$$g_0 = -\frac{\omega_o}{2} \frac{\int \mathbf{E} \frac{\partial \epsilon}{\partial x} \mathbf{E}^* dV}{\int \mathbf{E} \cdot \mathbf{D} dV}, \quad (2.27)$$

where \mathbf{E} is the electric field, \mathbf{D} is the electric displacement field and ϵ the material permittivity. In the case of the moving boundary contribution to the coupling, $g_{0,\text{mb}}$, this expression becomes

$$g_{0,\text{mb}} = -\frac{\omega_o}{2} \frac{\int (\mathbf{q} \cdot \hat{\mathbf{n}}) (\Delta \epsilon \mathbf{E}_{\parallel}^2 - \Delta \epsilon^{-1} \mathbf{D}_{\perp}^2) dS}{\int \mathbf{E} \cdot \mathbf{D} dV} \quad (2.28)$$

For the cavities described in this thesis, $\Delta\varepsilon = \varepsilon_1 - \varepsilon_2$ is the difference between the dielectric constants of gallium phosphide (silicon) and air, and $\Delta\varepsilon^{-1} = \varepsilon_1^{-1} - \varepsilon_2^{-1}$. \mathbf{q} is the normed displacement and $\hat{\mathbf{n}}$ the vector normal to the surface S between gallium phosphide (silicon) and air. The photoelastic effect in an anisotropic medium is described by $\frac{\partial\varepsilon}{\partial x} = -\varepsilon_0 n^4 p_{ijkl} S_{kl}$, in which case the photoelastic contribution, $g_{0,pe}$, to the optomechanical coupling is

$$g_{0,pe} = -\frac{\omega_o}{2} \frac{\int \mathbf{E} (\varepsilon_0 n^4 p_{ijkl} S_{kl}) \mathbf{E}^* dV}{\int \mathbf{E} \cdot \mathbf{D} dV} \quad (2.29)$$

with \mathbf{p} being the photoelastic tensor and \mathbf{S} the strain tensor [109].

The relative magnitude of the photoelastic and moving boundary contributions depends on the frequency of the light. The photoelastic effect is significantly more dispersive, particularly near the electronic bandgap. This is a result of the photoelastic coefficients p_{ijkl} increasing towards the bandgap [110] and the fact that the effect scales with the refractive index as n^4 , which increases dramatically near the electronic bandgap. In contrast, the moving boundary effect scales roughly as n^2 .

2.5.2 Calibration tone measurement

To determine the optomechanical vacuum coupling rate g_0 experimentally, the thermomechanical radio frequency spectrum is compared to a calibration tone created by modulating the light entering the PhC with a phase modulator [111]. The power spectral density of the mechanical mode is given by

$$S_\omega(\Omega) \approx 8g_0^2 n_{th} \cdot \frac{\Omega_m^2}{(\Omega^2 - \Omega_m^2)^2 + \Gamma_m^2 \Omega_m^2} \quad (2.30)$$

and that of the calibration tone by

$$S_\omega^{cal}(\Omega) = \frac{1}{2} \Omega_{cal}^2 \beta^2 \delta(\Omega - \Omega_{cal}), \quad (2.31)$$

where Ω_m and Ω_{cal} are the frequencies of the mechanical resonance and the calibration tone, respectively, and Γ_m denotes the mechanical linewidth. $n_{th} = k_B T / \hbar \Omega_m$ is the number of phonons occupying the mechanical mode at the ambient temperature T , where k_B is Boltzmann's constant. β is the modulation depth applied to create the calibration tone. The spectrum of the transduced photocurrent of the photodiode for both signals is given by $S_V(\Omega) = |G_{V\omega}(\Omega)|^2 \cdot S_\omega(\Omega)$, where $G_{V\omega}(\Omega)$ is a frequency dependent transduction factor. Comparing the areas beneath the calibration tone, $\langle V^2 \rangle_{cal} = \frac{1}{2} \Omega_{cal}^2 \beta^2 |G_{V\omega}(\Omega_{cal})|^2$, and the thermomechanical noise peak, $\langle V^2 \rangle_m = 2g_0^2 n_{th} |G_{V\omega}(\Omega_m)|^2$, we can determine g_0 as

$$g_0 = \frac{\beta \Omega_{cal}}{2} \sqrt{\frac{1}{n_{th}} \frac{\langle V^2 \rangle_m}{\langle V^2 \rangle_{cal}}} \left| \frac{G_{V\omega}(\Omega_{cal})}{G_{V\omega}(\Omega_m)} \right|. \quad (2.32)$$

Choosing Ω_m and Ω_{cal} to differ by only a few megahertz, we can assume the transduction factor to be nearly the same, and therefore $\left| \frac{G_{V\omega}(\Omega_{\text{cal}})}{G_{V\omega}(\Omega_m)} \right| \approx 1$.

2.5.3 Optomechanically induced transparency and absorption

To observe optomechanically induced absorption (OMIA), the laser control field at frequency ω_c is blue detuned from the cavity resonance at frequency ω_o . Additional probe fields much weaker than the control field are created by phase modulating the laser. In a frame rotating at ω_o , where $\Delta_{oc} = \omega_o - \omega_c$ is the laser-cavity detuning and $\Delta_{pc} = \omega_p - \omega_c$ is the probe-control detuning for a probe frequency ω_p , the expected transmission is

$$t_p(\Delta_{pc}) = \frac{\kappa_e/2}{i(\Delta_{oc} + \Delta_{pc}) + \kappa/2 + \frac{g^2}{i(\Omega_m - \Delta_{pc}) - \Gamma_m/2}}. \quad (2.33)$$

Here, κ is the total optical decay rate, κ_e is the contribution to the decay rate from loss through the Bragg mirrors of the PhC, and $g = g_0 \sqrt{n_{\text{cav}}}$ is the pump-enhanced optomechanical coupling rate for n_{cav} intracavity photons. The electric field transmitted through the PhC contains components oscillating at the carrier and both sideband frequencies:

$$E_{\text{out}} = e^{i\omega_c t} \{ t_p(0) + t_p(\Delta_{pc}) \frac{\beta}{2} e^{i\Delta_{pc} t} + t_p(-\Delta_{pc}) \frac{\beta}{2} e^{-i\Delta_{pc} t} \} \quad (2.34)$$

where t is time, and β is the modulation depth for the probe sidebands. The signal detected at the photodiode is proportional to $|E_{\text{out}}|^2$. The component oscillating with frequency Δ_{pc} is

$$I_{\Delta_{pc}} \propto \{ |t_p(-\Delta_{pc})| \cos(\Delta_{pc} t + \varphi_-) + |t_p(\Delta_{pc})| \cos(\Delta_{pc} t + \varphi_+) \} \quad (2.35)$$

φ_- and φ_+ are the phase shifts experienced by the lower and upper sidebands, respectively. Ideally $\varphi_+ - \varphi_- = \pi$, but in practice the two sidebands acquire an additional relative phase shift [112], so φ_- is replaced by $\varphi_+ + \theta$, and φ_+ and θ are used as fit parameters. The vector network analyzer (VNA) measures the in-phase and quadrature component of the signal.

$$I = |t_p(-\Delta_{pc})| \cos(\varphi_-) + |t_p(\Delta_{pc})| \cos(\varphi_+) \quad (2.36a)$$

$$Q = |t_p(-\Delta_{pc})| \sin(\varphi_-) - |t_p(\Delta_{pc})| \sin(\varphi_+) \quad (2.36b)$$

The $|S_{21}|$ parameter is proportional to $\sqrt{I^2 + Q^2}$. Fitting the above model to the S_{21} response of the VNA, we can extract various values, including the photon enhanced coupling rate G . To determine the vacuum coupling rate $g_0 = \frac{g}{\sqrt{n_{\text{cav}}}}$, the intracavity photon number n_{cav} must be known. It can be estimated from the power leaving the cavity using $P_{\text{out}} = n_{\text{cav}} \hbar \omega_o^2 / 2Q_e$. The external optical quality factor Q_e is calculated by evaluating the transmission for a known detuning Δ_{oc} and combining it with the measured total optical quality factor Q_o [100]

$$T(\Delta_{oc}) = \frac{P_{\text{out}}}{P_{\text{in}}} = \frac{1/4Q_e^2}{(\Delta_{oc}/\omega_o)^2 + 1/4Q_o^2} \quad (2.37)$$

Because the power entering and leaving the cavity cannot be measured directly before and after the device, but only at positions separated from the cavity by various lossy components such as the grating couplers, Q_e and therefore n_{cav} can only be determined with limited accuracy. The grating coupler losses are estimated by measuring structures in which the PhC has been replaced with a simple straight waveguide.

Measurement of optomechanically induced transparency (OMIT) is analogous to measurement of OMIA, only the laser-cavity detuning is chosen instead to be $\Delta_{\text{oc}} = -\Omega_m$, namely red-detuned. Now the combined probe and control fields interfere destructively with the mechanically modulated laser light. This leads to decreased transmission at $\Delta_{\text{pc}} = \Omega_m$. In order to carry out this measurement, the input power must be set sufficiently low that the thermo-optic shift is small and the red-detuning near $\Delta_{\text{oc}} = -\Omega_m$ is stable.

2.5.4 Dynamical backaction

If the PhC is driven off resonance, dynamical backaction gives rise to an optical spring effect and amplification (or damping) of the mechanical mode [113]. We measure these effects only for blue-detuning of the laser, as the detuning can only be varied continuously on this side of the optical resonance without complications arising from thermo-optic bistability. The expected frequency shift $\delta\Omega_m$ and linewidth narrowing Γ_{opt} induced by the light field are then [113]

$$\delta\Omega_m = g_0^2 n_{\text{cav}} \left(\frac{\Delta_{\text{oc}} - \Omega_m}{\kappa^2/4 + (\Delta_{\text{oc}} - \Omega_m)^2} + \frac{\Delta_{\text{oc}} + \Omega_m}{\kappa^2/4 + (\Delta_{\text{oc}} + \Omega_m)^2} \right) \quad (2.38a)$$

$$\Gamma_{\text{opt}} = g_0^2 n_{\text{cav}} \left(\frac{\kappa}{\kappa^2/4 + (\Delta_{\text{oc}} + \Omega_m)^2} - \frac{\kappa}{\kappa^2/4 + (\Delta_{\text{oc}} - \Omega_m)^2} \right) \quad (2.38b)$$

These effects can be observed by varying the laser-cavity detuning Δ_{oc} , recording the mechanical radio frequency spectrum and evaluating the effective mechanical resonance frequency $\Omega_{\text{eff}} = \Omega_m + \delta\Omega_m$ and the effective mechanical linewidth $\Gamma_{\text{eff}} = \Gamma_m + \Gamma_{\text{opt}}$ (Γ_m is the intrinsic mechanical linewidth). Because of the thermo-optic shift of the optical resonance, it is not straightforward to determine Δ_{oc} for a given laser frequency ω_c . Therefore, we additionally recorded OMIA spectra and also measured the transmitted power. Each of these two data sets allows independent inference of the detuning. To calculate $\delta\Omega_m$ and Γ_{opt} , we used the average of the two values thus determined.

2.6 Piezoelectric effect

Materials which have a non-vanishing second-order susceptibility $\chi^{(2)}$ are piezoelectric, too. This is because both properties require a non-centrosymmetric crystal lattice. As gallium phosphide belongs to this group of materials, devices exploiting nonlinear optics or the piezoelectric effect have been developed. In the first part of the following section the fundamentals of piezoelectricity are explained following Tichý et al.[114]. For the application of microwave-

to-optical transduction, a measure of the conversion efficiency between mechanical and electrical energy in a device is required, handled in the second part of this section.

2.6.1 Direct and inverse piezoelectric effect

The direct piezoelectric effect describes the change of electric polarization in a material proportional to strain. A material, which is piezoelectric will respond to applied strain by an internal polarization. Not all materials are piezoelectric, this behavior strongly depends upon crystal symmetry. Crystals having inversion symmetry are not piezoelectric, only non-centrosymmetric crystals are. Related to the direct piezoelectric effect is the inverse piezoelectric effect, which describes the fact that a material becomes strained if an external electric field is applied to it.

Mathematically the direct and the inverse piezoelectric effect are described by

$$\mathbf{D} = \mathbf{e}\mathbf{S} + \boldsymbol{\varepsilon}_S\mathbf{E} \quad (2.39a)$$

$$\mathbf{T} = \mathbf{c}_E\mathbf{S} - \mathbf{e}^T\mathbf{E} \quad (2.39b)$$

For the direct piezoelectric effect, strain \mathbf{S} in the material as well as an external electric field \mathbf{E} will lead to an electric displacement field \mathbf{D} . In the description of the inverse effect, an applied electric field \mathbf{E} or strain in the material \mathbf{S} leads to stress \mathbf{T} . The material coefficients linking these variables are explained in Table 2.2. The subscripts denote which value is held constant for their definition. Equation 2.39a and Equation 2.39b are in the stress-charge form, as the dependent variables are the electric displacement field \mathbf{D} and the stress \mathbf{T} .

Depending on the situation it might be of interest to have the strain \mathbf{S} and the electric displacement field \mathbf{D} as dependent variables. Then the strain-charge form can be applied, as shown in Equation 2.40a and Equation 2.40b. As a consequence the material coefficients have to be changed.

$$\mathbf{D} = \boldsymbol{\varepsilon}_T\mathbf{E} - \mathbf{d}\mathbf{T} \quad (2.40a)$$

$$\mathbf{S} = \mathbf{d}^T\mathbf{E} + \mathbf{s}_E\mathbf{T} \quad (2.40b)$$

The electric field \mathbf{E} and electric displacement field \mathbf{D} are vectors, which are linked by the permittivity $\varepsilon_{ik} = \varepsilon_{r,ik} \cdot \varepsilon_0$, a rank 2 tensor. In index notation this is represented by two indices $i, k = 1, 2, 3$. Here $\varepsilon_{r,ik}$ is the relative permittivity and ε_0 the vacuum permittivity.

Stress \mathbf{T} and strain \mathbf{S} are tensors of rank 2, but due to symmetry properties, they can be reduced to six different entries. In the Voigt notation, they are written as a vector. This allows one to write the stiffness $c_{\mu\lambda}$ and the compliance $s_{\lambda\mu}$, which connect the two variables, rank-2 tensors, with $\lambda, \mu = 1, 2, \dots, 6$ (as opposed to rank-4 tensors without the Voigt notation.)

2.6. Piezoelectric effect

Property	Physical quantity	Symbol	Definition	SI unit	SI base unit
Dielectric	Electric field	E_k		N/C=V/m	kgm/(s ³ A)
	Displacement field	D_i		N/C=V/m	kgm/(s ³ A)
	Permittivity	ϵ_{ik}	$= \frac{\partial D_i}{\partial E_k}$	F/m	s ⁴ A ² kg ⁻¹ m ⁻³
	Impermittivity	β_{ki}	$= \frac{\partial E_k}{\partial D_i}$	m/F	kg ¹ m ³ s ⁻⁴ A ⁻²
	Electric field constant	ϵ_0	$= 8.854 \cdot 10^{-12}$	F/m	s ⁴ A ² kg ⁻¹ m ⁻³
Elastic	Stress	T_μ		Pa	kg/(ms ²)
	Strain	S_λ		1	
	Stiffness	$c_{\mu\lambda}$	$= \frac{\partial T_\mu}{\partial S_\lambda}$	Pa	kg/(ms ²)
	Compliance	$s_{\lambda\mu}$	$= \frac{\partial S_\lambda}{\partial T_\mu}$	1/Pa	ms ² /kg
Piezoelectric	Piezoelectric coefficient	$d_{i\mu}$	$= \frac{\partial D_i}{\partial T_\mu} = \frac{\partial S_\mu}{\partial E_i}$	C/N	As ³ /(kgm)
	Piezoelectric modulus	$e_{i\mu}$	$= \frac{\partial D_i}{\partial S_\mu} = -\frac{\partial T_\mu}{\partial E_i}$	C/m ²	As/m ²

Table 2.2 – This table includes the variables appearing in the description of the direct and inverse piezoelectric effect and the material properties linking them. The indices of the variables and material properties define the matrix notation with $i, k = 1, 2, 3$ and $\lambda, \mu = 1, 2, \dots, 6$. The table is adapted from [114, p. 60].

2.6.2 Direction and magnitude of the piezoelectric effect

The material coefficients containing information about magnitude and direction of the piezoelectric effect are the piezoelectric coefficient $d_{i,\mu}$ and the piezoelectric modulus $e_{i,\mu}$. Each tensor has $3 \times 6 = 18$ elements. Depending on the material's crystal symmetry, often only a few elements are non-zero. These elements define the direction of the piezoelectric effect. To illustrate this connection, Equation 2.39a for the direct piezoelectric effect is shown in matrix notation (Equation 2.41). Elements with the same color will correspond to one of four possible configurations of applied stress \mathbf{T} and resulting polarization \mathbf{P} . These are illustrated in Figure 2.2. Depending on crystal symmetry, combinations of the four categories are possible.

$$\begin{bmatrix} D_1 \\ D_2 \\ D_3 \end{bmatrix} = \begin{bmatrix} \varepsilon_{11} & \varepsilon_{12} & \varepsilon_{13} \\ \varepsilon_{21} & \varepsilon_{22} & \varepsilon_{23} \\ \varepsilon_{31} & \varepsilon_{32} & \varepsilon_{33} \end{bmatrix} \cdot \begin{bmatrix} E_1 \\ E_2 \\ E_3 \end{bmatrix} + \begin{bmatrix} d_{11} & d_{12} & d_{13} & d_{14} & d_{15} & d_{16} \\ d_{21} & d_{22} & d_{23} & d_{24} & d_{25} & d_{26} \\ d_{31} & d_{32} & d_{33} & d_{34} & d_{35} & d_{36} \end{bmatrix} \cdot \begin{bmatrix} T_1 \\ T_2 \\ T_3 \\ T_4 \\ T_5 \\ T_6 \end{bmatrix} \quad (2.41)$$

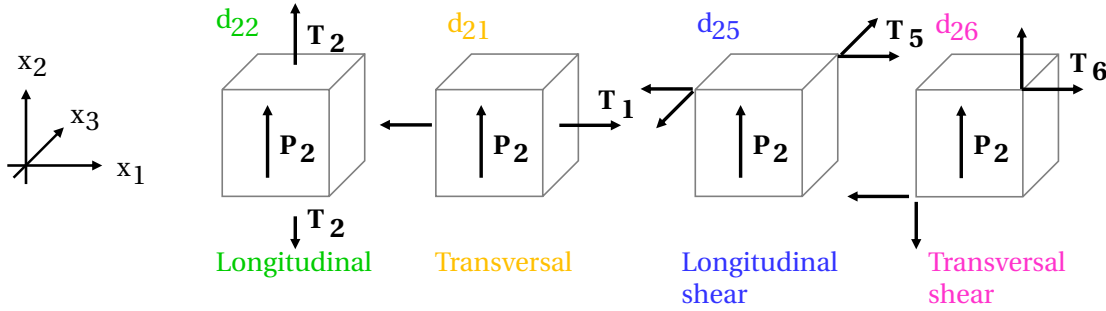


Figure 2.2 – The piezoelectric coefficient $d_{i\mu}$ corresponds to four different possible configurations of applied stress \mathbf{T} and resulting polarization \mathbf{P} (cf. [114, p. 72]). One example of the piezoelectric coefficient $d_{i\mu}$ is displayed for each category. For the inverse piezoelectric effect the configurations are analogous.

2.6.2.1 The piezoelectric coefficient of GaP

Gallium phosphide has a zincblende crystal structure. Its space group is $\bar{F}43m$. This leads to the following matrix of piezoelectric coefficients:

$$\mathbf{d}_{i\mu} = \begin{bmatrix} 0 & 0 & 0 & d_{14} & 0 & 0 \\ 0 & 0 & 0 & 0 & d_{14} & 0 \\ 0 & 0 & 0 & 0 & 0 & d_{14} \end{bmatrix} \quad (2.42)$$

There are only three identical non-zero elements, the same holds for the piezoelectric modulus $\mathbf{e}_{i\mu}$. The compliance $\mathbf{c}_{\mu\lambda}$ and the stiffness $\mathbf{s}_{\lambda\mu}$ are reduced to 12 non-zero elements with three

different values [114, p.202]. This means that we have a purely longitudinal shear piezoelectric effect. This is an important aspect for device design, as the electric field and the mechanical mode have to be placed in an appropriate configuration to achieve optimal actuation (see chapter 6).

2.6.3 Electromechanical coupling strength

To describe the efficiency of the energy conversion from an electric field to mechanical motion mediated by the piezoelectric effect, several figures of merit are known. In this section the definitions of these coefficients will be presented and the most appropriate choice for the calculation of the transduction efficiency in a microwave-to-optical transducer will be discussed.

2.6.3.1 Piezoelectric material-coupling coefficient K

The piezoelectric material-coupling coefficient K is a material property. It is defined as [115, p.54]

$$K^2 = \frac{e_{i\mu}^2}{c_{\mu\lambda}\epsilon_{ik}} = \frac{d_{i\mu}^2}{s_{\lambda\mu}\epsilon_{ik}}. \quad (2.43)$$

It is derived from the comparison of the acoustic velocity v in the medium without considering the piezoelectric properties to its actual value v^D in the presence of the piezoelectric effect: $v^D = v \cdot \sqrt{1 + K^2}$. It only depends on material parameters and is a measure for the conversion efficiency between electrical and mechanical modes in the material. The actual conversion efficiency still depends on the device design, but it is easier to build a device with a high conversion efficiency out of a material with a high K than with a low one [115, p.62].

The material coefficients K for the III-V materials GaP, GaAs and AlN are listed in Table 2.3. Considering only this figure of merit, AlN seems the preferred choice, mainly due to its high piezoelectric modulus. For devices, this material can be challenging. When sputter deposited, as for example in [51], it will be polycrystalline. This leads to high mechanical losses and additionally the direction of the piezoelectric effect can be different in the individual domains. Also the multiple non-zero components of the piezoelectric modulus lead to a mixture of configurations of mechanical displacement and electric field. This makes it difficult to electrically actuate only one specific mechanical mode and not waste electric energy to driving a multitude of them.

2.6.3.2 Effective coupling coefficient k_{eff}

A definition of the electromechanical coupling strength, that actually takes into account the device geometry by considering the distribution of the electric field and the mechanical displacement, is defined by the Berlincourt formula [117]. It relates the energy change of

Chapter 2. Theory

Material	Permittivity ϵ_r	Stiffness $c_E = c_{\mu\lambda}$ (Pa)	Piezoelectric modulus $e_{i\mu}$ (C/m ²)	Coupling coeff. K^2
GaP	9.33	$c_{11} = 1.4050 \times 10^{11}$ $c_{12} = 0.6203 \times 10^{11}$ $c_{44} = 0.7033 \times 10^{11}$	- - $e_{14} = -0.15$	3.87×10^{-3}
GaAs	12.46	$c_{11} = 1.193 \times 10^{11}$ $c_{12} = 5.999 \times 10^{10}$ $c_{44} = 5.376 \times 10^{10}$	- - $e_{14} = 0.14$	4.15×10^{-3}
AlN	9.00	$c_{33} = 5.89 \times 10^{11}$ $c_{11} = 4.1 \times 10^{11}$ $c_{12} = 1.49 \times 10^{11}$ $c_{13} = 9.9 \times 10^{10}$ $c_{44} = 1.25 \times 10^{11}$	$e_{33} = 1.55$ $e_{31} = -0.58$ $e_{15} = -0.48$	51.21×10^{-3}

Table 2.3 – Comparison of piezoelectric III-V materials. The values of GaP are the same as in Table 2.1. The material coefficients of GaAs and AlN are taken from the material database provided by the simulation software COMSOL Multiphysics [116]. The relative permittivity ϵ_r is not a tensor, as the materials in the table have cubic crystal symmetry and therefore \mathbf{P} is parallel to \mathbf{E} .

the total internal energy U to the mechanical energy U_m and the electrical energy U_e in the system. The total energy in the system is

$$U = \frac{1}{2} \int \mathbf{TS} + \mathbf{ED} \, dV. \quad (2.44)$$

Using the relations Equation 2.40a and Equation 2.40b the total energy can be divided up as $U = U_m + 2U_{\text{piezo}} + U_e$. The individual contributions are calculated as

$$U_m = \frac{1}{2} \int \mathbf{Ts}_E \mathbf{T} \, dV \quad (2.45a)$$

$$U_e = \frac{1}{2} \int \mathbf{E} \epsilon \mathbf{E} \, dV \quad (2.45b)$$

$$U_{\text{piezo}} = \frac{1}{4} \int \mathbf{T} \cdot \mathbf{d}^T \cdot \mathbf{E} + \mathbf{E} \cdot \mathbf{d} \cdot \mathbf{T} \, dV \quad (2.45c)$$

The Berlicourt formula defines the effective coupling coefficient as

$$k_{\text{eff}} = \frac{U_{\text{piezo}}}{\sqrt{U_e U_m}}. \quad (2.46)$$

2.6.4 Quantum mechanical derivation of the electromechanical coupling rate

For microwave-to-optical transduction the electromechanical coupling rate is of interest on the scale of single microwave photons and mechanical phonons. The following section follows the derivation of the corresponding electromechanical coupling rate of Zou et al. [75].

The total stress caused by the mechanical motion and the total electric field can be written as the sum of their eigenmodes:

$$\mathbf{T}(t) = \frac{1}{\sqrt{2}} \sum_m b_m \mathbf{T}^{(m)} e^{-i\Omega_m t} + \text{c.c.} \quad (2.47a)$$

$$\mathbf{E}(t) = \frac{1}{\sqrt{2}} \sum_n a_n \mathbf{E}^{(n)} e^{-i\omega_n t} + \text{c.c.} \quad (2.47b)$$

Ω_m and ω_n are the frequencies of the m -th and n -th eigenmode, b_m and a_n are quantized bosonic operators for the m -th mechanical mode and the n -th microwave cavity mode. $\mathbf{T}^{(m)}$ and $\mathbf{E}^{(n)}$ are the normalized field amplitudes of the mechanical and the electrical mode, respectively. The Hamiltonian of a piezoelectric system with the creation operator a_n^\dagger for the microwave photon and the creation operator b_m^\dagger for the phonon is given by

$$H = \sum_n \hbar\omega_n a_n^\dagger a_n + \sum_m \hbar\Omega_m b_m^\dagger b_m + \sum_{n,m} \hbar g_{mn} (a_n^\dagger + a_n)(b_m^\dagger + b_m) \quad (2.48)$$

with the coupling strength

$$g_{em} = T_{z\text{pf}} \cdot E_{z\text{pf}} \cdot \frac{1}{2\hbar} \int (\mathbf{T}^{(m)} \cdot \mathbf{d}^T \cdot \mathbf{E}^{(n)} + \mathbf{E}^{(n)} \cdot \mathbf{d} \cdot \mathbf{T}^{(m)}) dV \quad (2.49)$$

in units of the zero-point fluctuation:

$$T_{z\text{pf}} = \left(\frac{\hbar\Omega_m}{\int \mathbf{T} \cdot \mathbf{c}^{-1} \cdot \mathbf{T} dV} \right)^{1/2} \quad (2.50a)$$

$$E_{z\text{pf}} = \left(\frac{\hbar\omega_n}{\int \varepsilon_0 \varepsilon_r |\mathbf{E}|^2 dV} \right)^{1/2} \quad (2.50b)$$

They result from setting the electric and the mechanical energy to the ground state energy of mode m and n , respectively:

$$\frac{1}{2} \hbar\Omega_m = \int \mathbf{T} \cdot \mathbf{c}^{-1} \cdot \mathbf{T} dV \quad (2.51a)$$

$$\frac{1}{2} \hbar\omega_n = \int \varepsilon_0 \varepsilon_r |\mathbf{E}|^2 dV. \quad (2.51b)$$

Comparing the coupling coefficient k_{eff} (Equation 2.46) with g_{em} leads to

$$g_{em} = k_{\text{eff}} \cdot \left(\frac{\sqrt{\omega_n \Omega_m}}{2} \right). \quad (2.52)$$

This gives differing dimensions for the coupling coefficients: $[g_{em}/2\pi] = \text{Hz}$ and $[k_{\text{eff}}] = 1$. From both g_{em} and k_{eff} one can gain information about the optimal position of electric field in

relation to the mechanical displacement. For the speed of the transduction, the coupling rate g_{em} is the more useful quantity. Therefore g_{em} is used in the device design for a microwave-to-optical transducer described in chapter 6.

However, it only considers the spatial distribution of the mechanical and electrical mode in the system, and not yet the connection to an electrical circuit. For the purpose of microwave-to-optical transduction, it is though of interest to consider the electrical network the mechanical resonator is coupled to, for example a Transmon qubit. Arrangoiz-Arriola et al. [76] showed a method how to calculate the coupling of a piezoelectric resonator to a Transmon qubit. The dynamics of the electromechanical system is captured in its admittance function $Y(\omega)$. Following the method described in [76] would be the next step if the piezoelectric system should be connected to a defined microwave circuit.

2.7 Microwave-to-optical transduction

As mentioned in chapter 1, various concepts of transducing a microwave to an optical signal have been developed. In this work, microwave-to-optical transduction is envisioned as coupling a microwave resonator to a mechanical resonator, which in turn is coupled to an optical resonator. The coupling between the microwave and the mechanical resonator is achieved via the piezoelectric effect. The coupling between the optical and the mechanical resonator occurs through optomechanical coupling. This is schematically shown in Figure 2.3. The optical resonator and the microwave resonator have the frequencies ω_1 and ω_2 and the decay rates κ_1 and κ_2 . The mechanical resonator has the frequency Ω_m and the decay rate Γ_m . The optical resonator's frequency is around 200 THz. The mechanical and the microwave resonator's frequencies are chosen to be the same (around several GHz) so that the piezoelectric coupling is resonant.

A pump tone is applied to the optical resonator. It amplifies or damps the mechanical mode via optomechanical coupling depending on whether it is blue-detuned or red-detuned from the cavity resonance (see subsection 2.5.4). This determines the direction of the transduction. Quantum mechanically, the process can be described as follows: For red detuning, a phonon (Ω_m) and a pump photon ($\omega_o - \Omega_m$) combine to create a photon on resonance (ω_o) in the optical cavity. So a mechanical phonon is transduced to an optical photon. For blue detuning, a pump photon ($\omega_o + \Omega_m$) creates two new quanta, an optical photon on resonance (ω_o) and a mechanical phonon (Ω_m). A mathematical description of the transduction is given in [72]. In contrast to this off-resonant three-particle process, the electromechanical transduction is resonant. Ideally, one microwave phonon gets transduced to one mechanical phonon and vice versa. A description of the coupled system can be found in [76]. The derivation of the coupling strength has already been discussed above in subsection 2.6.3.

The efficiency of the full conversion process can be characterized by the transmission coefficients $t_{1,2} = a_{out}[\omega_{2,1}] / a_{in}[\omega_{1,2}]$ [73]. This is the ratio of the complex mode amplitude a_{in} of the field entering at one of the input ports 1 or 2 with the frequency ω_1 and ω_2 , and the field amplitude a_{out} of the successfully transduced field leaving at the other port. For the

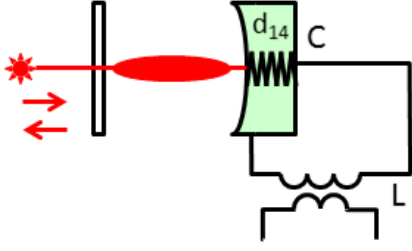


Figure 2.3 – Schematic illustrating the resonators involved in microwave-to-optical transduction. An optical cavity, represented by a Fabry-Pérot cavity, has one moving mirror. This mirror can be moved with a piezoelectric actuator. The capacitance of the microwave resonator is coupled to the piezoelectric mechanical resonator.

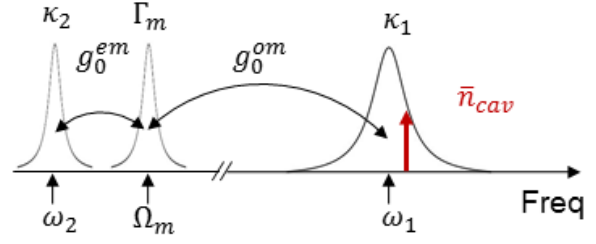


Figure 2.4 – Diagram of the resonator frequencies involved in microwave-to-optical transduction. The microwave and the mechanical resonators actually have the same frequencies of several GHz, $\omega_2 \approx \Omega_m$. (For clarity they are drawn next to each other.) The optical resonator's frequency is around $\omega_1/2\pi \approx 200$ THz. The microwave and the optical resonator each are coupled to the mechanical resonator with a coupling rate g_0^{em} and g_0^{om} , respectively. A pump tone is applied to the optical resonator, leading to an intracavity photon population \bar{n}_{cav} .

design presented in chapter 6, the input port to the optical resonator, e.g. the PhC, could be a tapered fiber next to the cavity. The input port for the microwave resonator could be a feedline coupling to the microwave resonator through a capacitance. The transduction process is bi-directional and therefore $t_1 = t_2 = t$. For a successful transduction, a number of prerequisites must be fulfilled [73]:

1. The coupling into the first and out of the last resonator must be efficient, which is quantified by the cavity coupling parameter η (see subsection 2.4.1). To assure, that a photon enters (leaves) the microwave or the optical resonator, the resonator would ideally be overcoupled.
2. The photons have to be transduced faster than the decay rate of the mechanical resonator Γ_m . In the resolved sideband limit ($\Omega_m > \kappa_1, 2$), the transduction between two cavities occurs at a rate of $\gamma_{1,2} = 4n_{1,2}^{cav} g_{om,em}^2 / \kappa_{1,2}$. For comparing this rate to the mechanical decay rate, the cooperativity is evaluated:

$$C_{1,2} = \frac{\gamma_{1,2}}{\Gamma_m} = \frac{4n_{1,2}^{cav} g_{em,om}^2}{\Gamma_m \kappa_{1,2}} \stackrel{!}{>} 1 \quad (2.53)$$

It needs to be greater than one. For the electromechanical transduction, there is no pump involved and therefore $n_2^{cav} = 1$. The transmission takes the form [73]

$$|t|^2 = \frac{4\eta_1\eta_2 C_1 C_2}{(1 + C_1 + C_2)^2} \quad (2.54)$$

and becomes maximal if $C_1 = C_2$, which means equal individual transduction rates for each cavity. At the same time, $\eta_{1,2}$ should be as close to 1 as possible, which means overcoupled, as explained before.

3. The bandwidth of the transducer is given by $\Gamma = \Gamma_m + \gamma_1 + \gamma_2$ [73, 52].
4. The amount of added noise should be minimized. To operate without added noise, the mechanical resonator should be in its ground state and operate with unity gain. As the optimization for low amount of added noise is one step further than the demonstration of successful transduction, this topic is not further discussed here. A detailed discussion can be found in [52].

3 Process development

This chapter describes the process originally developed for the fabrication of the first GaP-OI devices, as published in [23]. Some modifications and improvements made subsequently are included here as well. A scheme showing the individual steps of the fabrication process is shown in Figure 3.1. The steps are discussed in detail in the following sections.

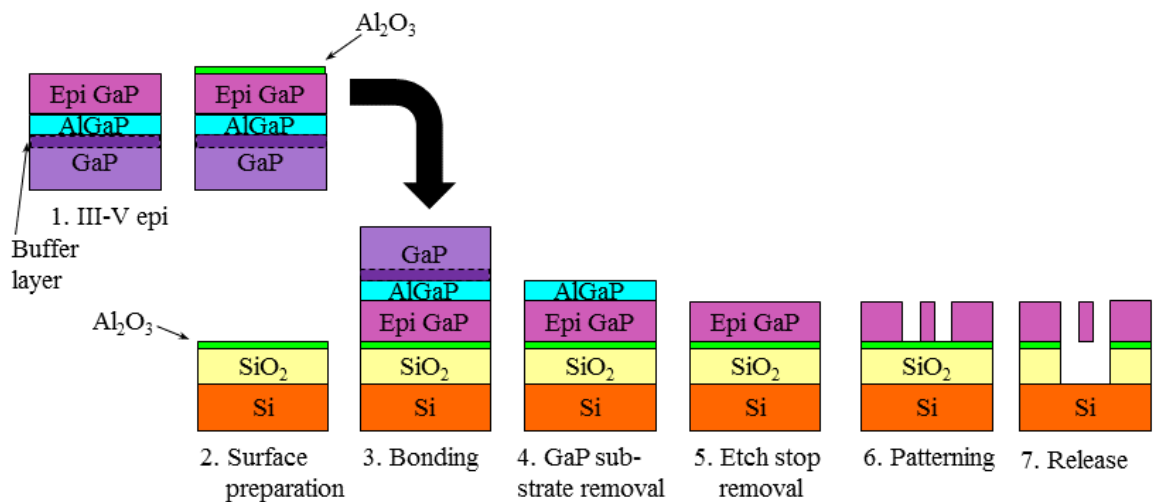


Figure 3.1 – Schematic of process flow for GaP-OI device fabrication.

3.1 Growth and direct wafer bonding

The first step in the fabrication process of GaP-OI devices is the growth of the device layer. GaP cannot be bought in the form of a thin film on an insulator, as it is the case for example for silicon and silicon-on-insulator wafers. Instead the desired GaP layer is grown on a separate substrate and afterwards wafer bonded onto an oxidized silicon wafer. As the substrate we use a 2-inch, [100]-oriented, single-side polished, nominally undoped, 400 μm -thick, GaP wafer. A GaP/Al_xGa_{1-x}P/GaP heterostructure is epitaxially grown by MOCVD. The initially

deposited 100 nm-thick homoepitaxial GaP buffer layer provides for facile nucleation of the subsequent $\text{Al}_x\text{Ga}_{1-x}\text{P}$ etch-stop layer. The $\text{Al}_x\text{Ga}_{1-x}\text{P}$ layer, also 100 nm thick, had an approximate composition of $\text{Al}_{0.36}\text{Ga}_{0.64}\text{P}$ as determined by X-ray diffraction (XRD). The lattice mismatch of 0.09% between GaP and $\text{Al}_{0.36}\text{Ga}_{0.64}\text{P}$ corresponds to a Matthews-Blakeslee critical thickness [118] of 157 nm. As the grown thickness is below this value, which should be a conservative estimate, we do not expect any influence on the quality of the following GaP device layer, which has a nominal thickness of 300 nm. All layers were deposited at a susceptor temperature of 650 °C. This layer stack, dubbed the source wafer, was bonded onto a 4 inch Si target wafer capped with 2 μm of SiO_2 prepared by thermal dry oxidation at 1050 °C, which eventually becomes the buried oxide of the GaP-OI wafer [24]. Prior to bonding, the source and target wafers were both coated with approximately 5 nm of Al_2O_3 by atomic layer deposition (ALD). Megasonic cleaning with ozone-rich deionized water before and after coating with Al_2O_3 ensured a hydrophilic surface free of organic contamination. The source and target wafer surfaces were brought into intimate contact at room temperature in ambient atmosphere to initiate the bonding followed by annealing at 300 °C for 2 hours to increase the bonding energy.

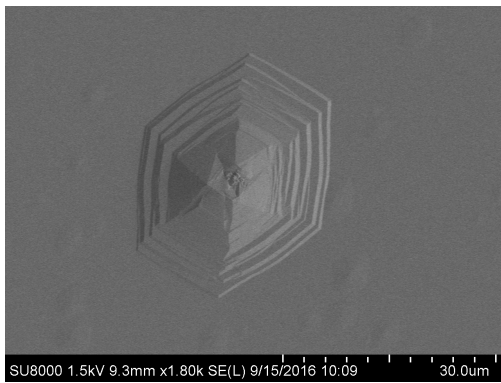
A prerequisite for successful wafer bonding is a sufficiently smooth surface (root mean square (RMS) roughness $R_q \leq 1 \text{ nm}^1$) of the wafers to be bonded. In this respect, the growth of GaP by MOCVD turned out to be challenging because, depending on the growth parameters, defects with the shape of hexagonal pyramids appear. They have a diameter up to several microns and a height up to several 100 nanometers, as illustrated in Figure 3.2(a) and Figure 3.2(b). Attempts to fully eliminate their occurrence were not successful, so instead we focused on lowering their number. The area within a radius of 10 times the height around such a defect usually does not bond. So for low enough defect density, there remains a sufficient amount of bonded wafer surface. For example in one case the defect density was as low as 470/cm² while the RMS roughness was 0.3 nm, as shown in Figure 3.2(c) and Figure 3.2(d). These numbers stem from a wafer only bonded (partially) in a second attempt (see Figure 3.2(f)). Because any characterization measurements are generally avoided before wafer bonding to reduce contamination, statistics on defect density are usually not available for successfully bonded wafers. An image of the very first successfully bonded wafer is shown in Figure 3.2(e).

3.2 Wafer thinning and selective etching of GaP

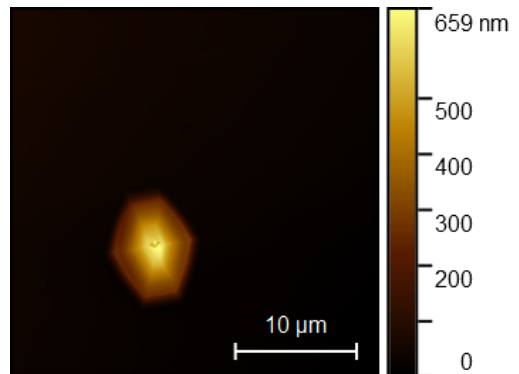
The original GaP substrate must be removed after bonding. Ideally, a single process which rapidly and selectively removes GaP, stopping on the $\text{Al}_x\text{Ga}_{1-x}\text{P}$ layer, would be used. We first present the attempts to develop a selective wet etch for this purpose. As no selectivity was achieved, the following sections treat the development of a selective dry etch with a preceding thinning of the substrate. For thinning, three different methods were employed.

¹This has not been systematically tested. Experience, also from other materials platforms used in the BRNC [119], though suggests a limit in this range.

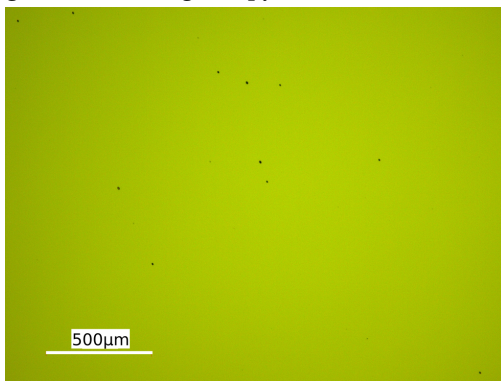
3.2. Wafer thinning and selective etching of GaP



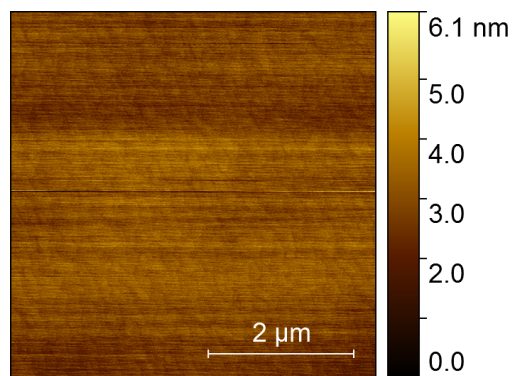
(a) The main type of defects occurring during growth are hexagonal pyramids.



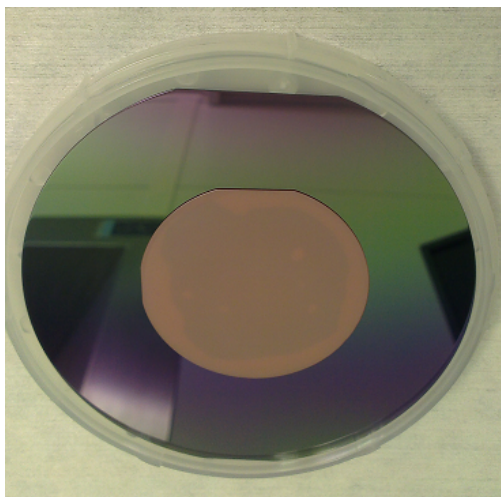
(b) Height profile of a hexagonal defect.



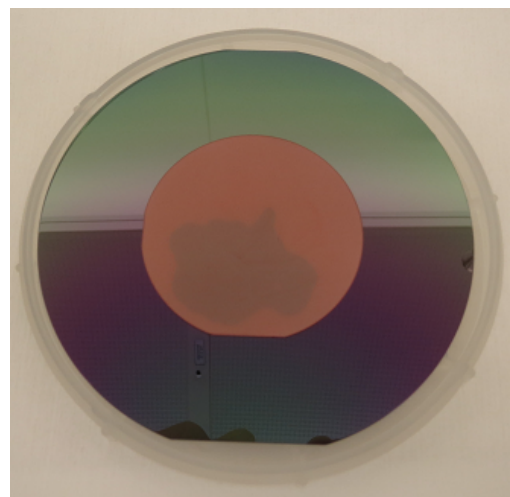
(c) In one example the defect density was as low as $470/\text{cm}^2$.



(d) The RMS roughness of the wafer was 0.29 nm.



(e) First successfully bonded wafer. The dark central region is the actually bonded area.



(f) Later attempts sometimes resulted only in partial bonding.

Figure 3.2

3.2.1 Investigation of selective wet etching of GaP in the presence of $\text{Al}_x\text{Ga}_{1-x}\text{P}$

To our knowledge, no suitable process for wet etching of GaP selectively with respect to $\text{Al}_x\text{Ga}_{1-x}\text{P}$ has been published. With the prerequisite of removing several hundred microns in a reasonable time, we tested various solutions for this purpose without success (see Table 3.1).

Etchant mixtures by volume ^a	Hotplate temperature [°C]	Etch rate of GaP [nm/min]	Etch rate of $\text{Al}_{0.18}\text{Ga}_{0.82}\text{P}$ [nm/min]
Citric acid/ H_2O_2 (1:5)		< 0.5	
Citric acid/ H_2O_2 (1:1)		< 0.5	
Citric acid/ H_2O_2 (5:1)		1.3	
Citric acid/ H_2O_2 (25:1)		1.3	
Citric acid/ H_2O_2 (10:1)	100	15	13
$\text{H}_2\text{O}_2/\text{NH}_4\text{OH}$ (1:10)	80	5	3
$\text{H}_2\text{O}_2/\text{NH}_4\text{OH}$ (1:1)	80	7	5
$\text{H}_2\text{O}_2/\text{NH}_4\text{OH}$ (10:1)	80	7	
$\text{H}_2\text{O}_2/\text{NH}_4\text{OH}$ (100:1)	80	6	5
$\text{H}_2\text{O}_2/\text{NH}_4\text{OH}$ (10:1)	100	16	8
HCl		0	> 116
HCl/ H_2O_2 (1:3)		10 ^b	
HCl/ H_2O_2 (1:1)		> 500 ^b	
HCl/ H_2O_2 (3:1)		≤ 18000 ^b	fast
HCl/ H_2O_2 (10:1)		> 1000 ^b	
HCl/ HNO_3 (3:1)		210 ^c	276
HCl/ HNO_3 (3:1)	60	1600 ^c	

Table 3.1 – Etch tests for wet etching of GaP selectively with respect to $\text{Al}_x\text{Ga}_{1-x}\text{P}$. Tests were performed with 4 mm × 4 mm, [100]-oriented, GaP and $\text{Al}_{0.18}\text{Ga}_{0.82}\text{P}$ chips with a 50 nm-thick SiO_2 mask. Tests on $\text{Al}_{0.18}\text{Ga}_{0.82}\text{P}$ were conducted only if the etching of GaP was sufficiently fast and uniform. The experiments were carried out at room temperature unless otherwise noted, in which case the temperature indicated is that of the hotplate heating the solution. In no case was adequate selectivity achieved.

^aCitric acid: 50% citric acid monohydrate, H_2O_2 : 30-31%, NH_4OH : 58-62% (28-30% NH_3), KOH: 44%, HCl: 37%, HNO_3 : 70%

^bThe high etch rates are estimates, as the etchant is consumed quickly and etching is not uniform.

^cCircular pits on surface, etching not uniform (see Figure 3.3).

3.2.2 Thinning of the GaP substrate

As no selective wet etch was found, instead we focused on the development of a selective dry-etch process. Such a selective dry-etch process is known [25], but cannot practically be used alone due to its relatively slow rate and the quantity of material to be removed. In [23] therefore a three-step procedure was employed. The first step is the thinning of the

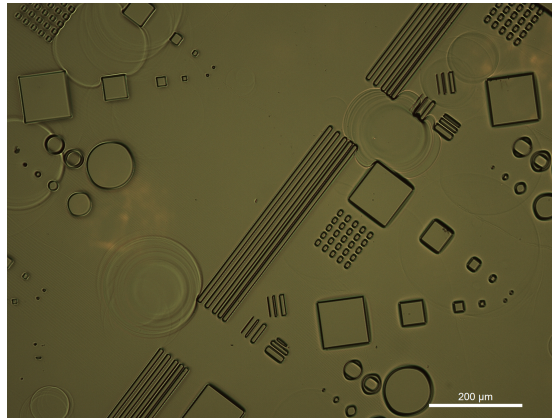


Figure 3.3 – Etching GaP with aqua regia leads to circular etch pits. The etch time was 1 min at a temperature of 60 °C.

GaP substrate to $\leq 70 \mu\text{m}$ by etching in a commercial alkaline solution of $\text{K}_3\text{Fe}(\text{CN})_6$ (Gallium Phosphide Etchant, Transene). Second, after dicing the wafer into chips, more material is removed in a fast dry-etch process. And finally a dry-etch process selective to $\text{Al}_x\text{Ga}_{1-x}\text{P}$ is employed to remove the remaining GaP substrate.

After improving the etch rate of the selective dry-etch process [120], the second step could be skipped.

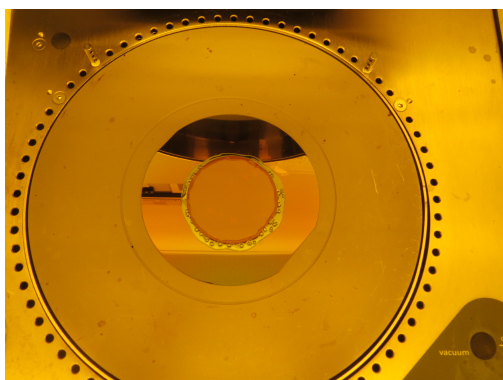
3.2.2.1 Thinning by wet etching with Gallium Phosphide Etchant

A fast method for removing the GaP substrate which can be used for large amounts of material is etching in a commercial alkaline solution of $\text{K}_3\text{Fe}(\text{CN})_6$ (Gallium Phosphide Etchant, Transene). Because {100} faces are polished by this etchant, the peak-to-peak roughness of the initially unpolished back side of the substrate was substantially reduced. To prevent etching from the wafer edges, which is faster than from the top, the edges are covered with ProTEK (Brewer Science) following the application guidelines². The maximum temperature used was 140 °C to prevent cracking of the wafer. A wafer prepared for etching is shown in Figure 3.4(a). The observed etch rate reached a maximum of 670 nm/min for the {100} face, but depended on agitation, temperature, and time in the etchant (presumably because the etchant was being consumed) and was thus hard to control and not sufficiently homogeneous. An image of the configuration of stirrer, sample holder and etchant is shown in Figure 3.4(b). In later runs, the etch rate was increased by using a sample mount to hang the bonded wafer upside-down into the etchant. This has two advantages: First, collection of particles on the surface of the GaP and the resulting masking are prevented, and second, the stir bar used to mix the solution is closer to the GaP wafer and therefore the etchant is better agitated near the etched surface.

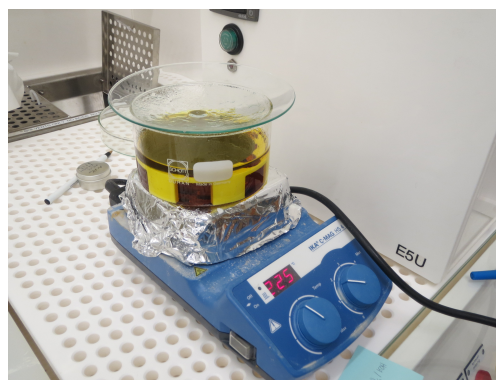
²The purpose of ProTEK is to protect surfaces from alkaline etch solutions. Two components, a primer and a coating, are typically spincoated followed by baking steps. For protecting only the wafer edges, we spread both components with a brush. If necessary, the coating was repeated. A commercial remover is available as well. We soaked the wafer in acetone followed by rinsing with acetone and isopropanol to remove the ProTEK coating.

Chapter 3. Process development

After thinning, the wafer is diced into chips approximately 7 mm × 7 mm.



(a)



(b)

Figure 3.4 – (a) Bonded wafer prepared for thinning in GaP etchant with edges covered with ProTEK. (b) Sample holder in GaP etchant. Later on this sample holder was modified to allow upside down hanging of the wafer above the stirrer.

3.2.2.2 Thinning by wafer grinding

An alternative for thinning by wet etching is wafer grinding, which provides better thickness uniformity and permits continued processing on a wafer scale. This was tested with a partially bonded wafer. Grinding was provided by the Fraunhofer institute IAF in Freiburg, Germany. The GaP was ground down to a thickness of 55 μm . The resulting wafer is shown in Figure 3.5.

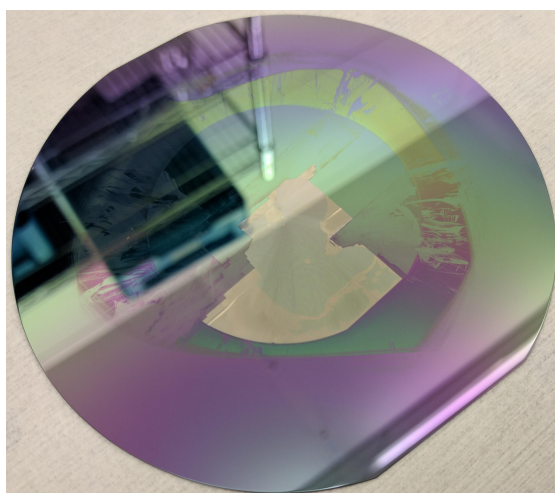


Figure 3.5 – Bonded wafer after substrate removal by grinding.

3.2.2.3 Thinning by etching with H₂ and Cl₂ in an ICP-RIE process

For the first bonded wafer, after thinning with GaP etchant, the remaining GaP substrate was further thinned to $\leq 20 \mu\text{m}$ by inductively-coupled-plasma reactive ion etching (ICP-RIE) with a mixture of H₂ and Cl₂ that etches homogeneously at a rate of $1.6 \mu\text{m}/\text{min}$. The process parameters were 20 sccm Cl₂, 20 sccm H₂, 260 V DC bias, 80 W RF power, 600 W ICP power, 5 mTorr chamber pressure, and 80 °C sample electrode temperature.

3.2.3 Selective dry etching of GaP in the presence of Al_xGa_{1-x}P

Selective etching of GaP in the presence of Al_xGa_{1-x}P was provided by the third and final step consisting of another ICP-RIE process, this time with a mixture of Cl₂ and CF₄. The only previously known selective plasma etch is a SiCl₄/SiF₄ RIE process developed by Epple et al. [25], with which a selectivity of 126:1 was achieved for GaP with respect to Al_{0.6}Ga_{0.4}P, a composition with high aluminum content. The etching action is attributed primarily to chlorine-containing species, whereas the fluorine is required for the formation of relatively nonvolatile AlF₃, which serves as an etch inhibitor. Because SiF₄ is not available in our ICP-RIE tool (Oxford Instruments PlasmaPro System 100 ICP), we investigated alternative mixtures of various chlorine and fluorine sources, namely Cl₂/SF₆, Cl₂/CF₄, Cl₂/CHF₃, SiCl₄/CHF₃ and SiCl₄/CF₄ mixtures (see Table 3.2). Only Cl₂/CF₄ and Cl₂/CHF₃ plasmas exhibited etch rates above 100 nm/min as needed for the removal of several microns within a reasonable timeframe. Optimization of the Cl₂/CF₄ process (see Table 3.4) gave the following process parameters: 7.5 sccm Cl₂, 30 sccm CF₄, 240 V DC bias, 100 W ICP power, 60 W RF power, 15 mTorr chamber pressure, and 20° sample electrode temperature (Recipe 2 in Table 3.4). GaP was etched with an etch rate of 270 nm/min. The selectivity with respect to Al_{0.36}Ga_{0.64}P for our bonded heterostructure was estimated to be approximately 120:1. This might be due to a difference in the Al_{0.36}Ga_{0.64}P interface when it is directly capped with GaP during MOCVD growth. Indeed, preliminary experiments suggest that initial etch rates may depend on past exposure of the top surface of the various GaP and Al_xGa_{1-x}P samples.

The dependence on the Al content was investigated by comparing the behavior of Al_{0.36}Ga_{0.64}P and Al_{0.18}Ga_{0.82}P when etched with recipe 2 from Table 3.4. The selectivity increased by a factor of 1.5 for the higher Al content.

This optimized recipe was used to remove the remaining GaP on top of the Al_{0.36}Ga_{0.64}P layer. It should be noted that, although it may be possible to grow an Al_xGa_{1-x}P stop layer with suitable quality that is perhaps twice as thick as that used here, improved selectivity may be even more helpful in reducing the requirements on thickness uniformity following substrate wafer thinning.

It was subsequently discovered that the combination of SiCl₄ and SF₆, which we had previously not considered, is an even better choice for selectively etching GaP in the presence of Al_xGa_{1-x}P [120] (see Table 3.3). It provides an improved selectivity (>2700:1) and an increased etch rate (>10 $\mu\text{m}/\text{min}$) and has replaced the selective dry etching with Cl₂ and CF₄ as our preferred method.

Chapter 3. Process development

Cl compound (sccm)	F compound (sccm)	DC bias [V]	Etch rate GaP [nm/min]	Etch rate AlGaP [nm/min]	Selectivity
Cl ₂ (10)	SF ₆ (40)	152	4	–	–
Cl ₂ (20)	SF ₆ (20)	170	8	–	–
Cl ₂ (7.5)	CF ₄ (30)	242	275	8	37
Cl ₂ (7.5)	CHF ₃ (30)	258	127	6	21
SiCl ₄ (7.5)	CF ₄ (30)	250	23	–	–
SiCl ₄ (7.5)	CHF ₃ (30)	250	23	–	–

Table 3.2 – Etch tests of GaP and Al_{0.18}Ga_{0.82}P with various sources of chlorine and fluorine species. They were performed with 4 mm × 4 mm GaP and Al_{0.18}Ga_{0.82}P chips with either a 50 nm- or 100 nm-thick SiO₂ mask. The experimental parameters were fixed at 100 W ICP power, 60 W RF power, 15 mTorr chamber pressure, and 20° sample electrode temperature. Etch tests of Al_{0.18}Ga_{0.82}P were carried out only for those cases where the etch rate of GaP was reasonably high.

SiCl ₄	13 sccm
SF ₆	7 sccm
ICP power	60 mTorr
RF power	300 W
DC bias	150 V
Temp	30°

Table 3.3 – Etch recipe for selective etching of GaP with respect to Al_xGa_{1-x}P.

3.2. Wafer thinning and selective etching of GaP

Recipe	Cl ₂ flow ^a (%)	CF ₄ flow ^a (%)	Pressure [mTorr]	ICP power [W]	DC bias [V]	Etch rate GaP [nm/min]	Etch rate AlGaP [nm/min]	Selec- tivity
1	11	89	15	100	243	0	0	-
2	20	80	15	100	241	257	7.5	37:1
3	29	71	15	100	238	320	11	29:1
4	20	80	15	130	242	265	8.5	31:1
5 ^b	20	80	15	130	183	208	7	30:1
6	19	81	15	180	185	4	22	0.18:1
7	12	88	15	180	244	11	11	1:1
8	25	75	15	180	238	291	11.5	25:1
9	19	71	50	100	173	4.5	20	0.22:1
10	12	88	50	130	178	2.5	3	0.83:1
11	19	71	50	130	238	8.5	17	0.5:1
12	25	75	50	130	240	93	5.5	17:1
13	25	75	50	180	180	0	0	-
14	12	88	50	180	240	7	5.5	1.3:1

Table 3.4 – Etch tests of GaP and Al_{0.18}Ga_{0.82}P with a Cl₂/CF₄ plasma. The sample electrode temperature was 20 °C for all recipes. The DC bias was targeted at either 180 V or 240 V. Etch times were generally limited to 2 min (except as indicated), because the plasma erodes the SiO₂ mask.

^aProportion of the total gas flow, which was chosen between 34.5 and 37.5 sccm.

^bEtched for 4 min.

3.3 Removal of the $\text{Al}_x\text{Ga}_{1-x}\text{P}$ etch stop layer

Once the original GaP substrate is no longer present, the $\text{Al}_{0.36}\text{Ga}_{0.64}\text{P}$ etch stop layer is easily removed by submerging the sample in concentrated HCl (37 % by weight) for 90 s, resulting in the final GaP-OI wafer. This step has the opposite selectivity of the previous substrate removal step and leaves the GaP device layer intact.

3.4 Characterization of the GaP device layer

The GaP device layer is characterized by XRD (Figure 3.6). A fit of the finite-size oscillations of the GaP (004) Bragg reflection in an omega-2-theta scan yields a GaP layer thickness of 295 nm. The full width at half maximum of the rocking curve for the GaP reflection is 80 arcsec, which corresponds to a threading dislocation density of $2 \times 10^7 \text{ cm}^{-2}$ as calculated from the model of Ayers [121] and indicates that the transferred epitaxial film is of high quality.

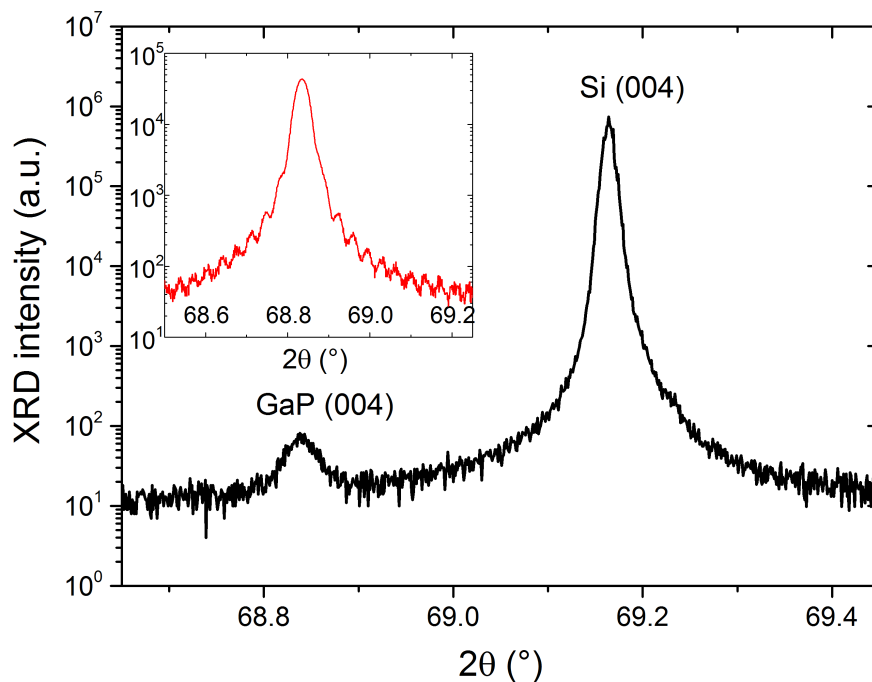


Figure 3.6 – Omega-2-theta XRD spectrum of a GaP-OI sample showing diffraction from (004) planes of GaP (left peak) and Si (right peak). The inset displays the GaP diffraction pattern on the same wafer when the diffractometer is aligned to the GaP Bragg reflection to resolve the finite-size oscillations.

3.5 Dry etch for device patterning

The patterning of devices in the top GaP layer is a critical step. Photonic devices, e.g. grating couplers, waveguides, and ring resonators, require well-defined (typically vertical) and smooth sidewalls to obtain the desired transmission properties, particularly low scattering losses. The fabrication of photonic crystal structures in addition calls for a high-resolution process capable of creating small features with a high aspect ratio and high dimensional accuracy [122, 26].

3.5.1 Possible gases for ICP-RIE etching of GaP and their effects

Most of the studies of anisotropic GaP dry-etching in the literature have focused on increasing the etch rate and maintaining a smooth top-surface morphology [123, 124, 125, 126, 127, 128, 129, 130]. In these studies, either chlorine-containing species, such as Cl_2 or BCl_3 [124, 129, 130, 131], or mixtures of H_2 and CH_4 [125, 126] or a combination of both [128] have been used. Inclusion of Ar and N_2 , gases which are expected to contribute more to physical as opposed to chemical etching, has also been investigated [124, 129, 130, 132]. The interplay of the various process parameters and gas mixture ratios is complicated, but there are some general trends. Plasma conditions generating a high concentration of chlorine atoms and ions are especially aggressive, with GaP etch rates exceeding $1.5 \mu\text{m}/\text{min}$ [129]. Etching with BCl_3 is less aggressive than with Cl_2 [129]. The sample electrode temperature has relatively little influence on etch rate and top surface morphology, but does change the sidewall profile, with lower temperatures reducing undercut and roughness, presumably due to passivation effects [128]. For sidewall passivation, CH_4 is expected to play an important role [129], but BCl_3 and N_2 may also be involved [133]. Chemically inert components, such as Ar, that contribute to the etch process in a purely physical manner, tend to increase surface roughness and should be avoided [132].

3.5.2 Process development methodology

Keeping the above points in mind, we optimized the dry-etch process in our particular ICP-RIE system (Oxford Instruments PlasmaPro System 100 ICP) starting from a base recipe comprising gas flows of H_2 (17.5 sccm), CH_4 (2.0 sccm), Cl_2 (5.0 sccm), and BCl_3 (15.0 sccm), at 600 W ICP-power, 300 V DC bias, 80°C sample electrode temperature, and 5 mTorr chamber pressure. Optimizing one parameter at a time sequentially, we varied the gas ratios, temperature, ICP power, and chamber pressure. The tests were performed with $4 \text{ mm} \times 6 \text{ mm}$ chips diced from [100]-oriented, single-side polished, nominally undoped GaP wafers. A test pattern with various slot openings as small as 20 nm (see Figure 3.7) was defined by e-beam lithography (Vistec EBPG 5200ES) using either 4% or 6% hydrogen silsesquioxane (HSQ) in 4-methylpentan-2-one from Dow Corning as a negative resist spin-coated at 6000 rpm, resulting in HSQ film thicknesses of nominally 85 nm and 150 nm, respectively. To improve the adhesion of HSQ to GaP, a thin (3 nm) layer of SiO_2 was deposited by ALD prior to spin coating. For the ICP-RIE

process, the chips were placed directly on a 100-mm Si carrier wafer backside-cooled with helium, without any affixer such as wax or grease.

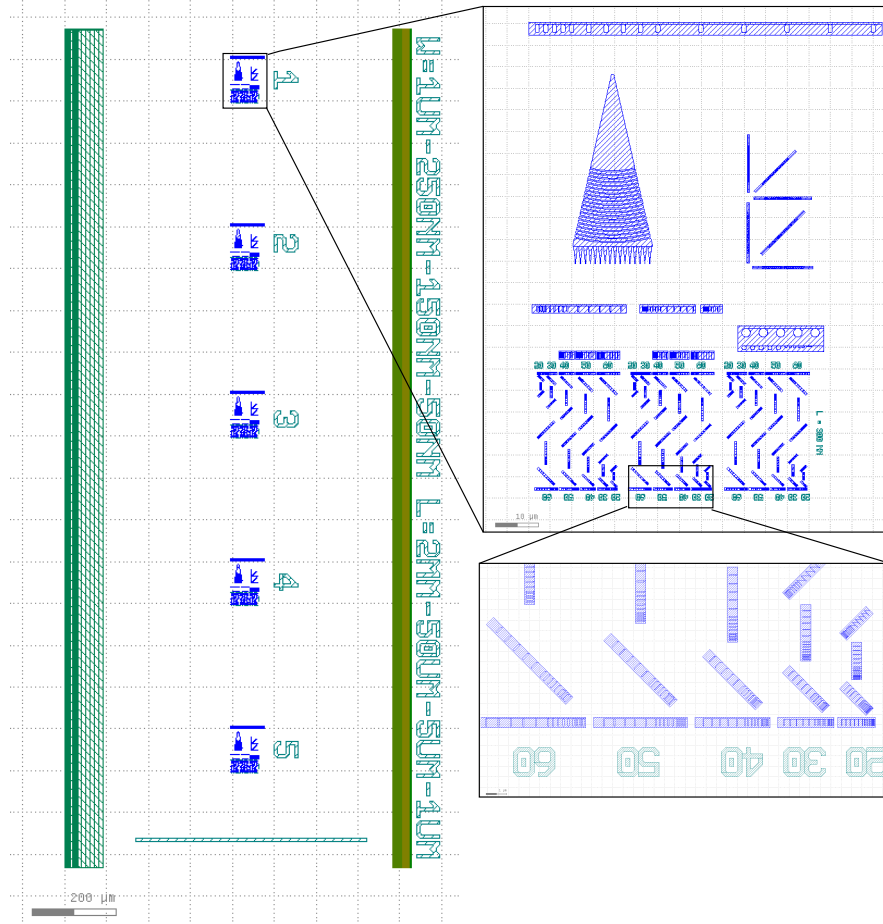


Figure 3.7 – Lithography mask for dry etch development.

3.5.3 Influence of the BCl_3 to Cl_2 ratio

As illustrated in Figure 3.8, the ratio of BCl_3 to Cl_2 has a strong influence on the GaP etch rate. For these experiments, the sum of the BCl_3 and Cl_2 flow rates was kept constant at 20 sccm, and the flow rates of H_2 and CH_4 were left unchanged. The dramatic decrease in etch rate with added BCl_3 might be due to surface passivation by BCl_3 [134] or to a reduced density of reactive chlorine-containing species in the plasma, or both. The observation of more severe sidewall roughness and increased undercutting for decreasing BCl_3 -to- Cl_2 ratio (not shown) points however to a surface passivation role for BCl_3 . An equal flow of BCl_3 and Cl_2 yields a reasonable compromise between etch rate and sidewall profile (see the scanning electron microscope (SEM) image in Fig. 3), while providing decent selectivity (5:1) with respect to HSQ and was used in the further optimization of the process as described below.

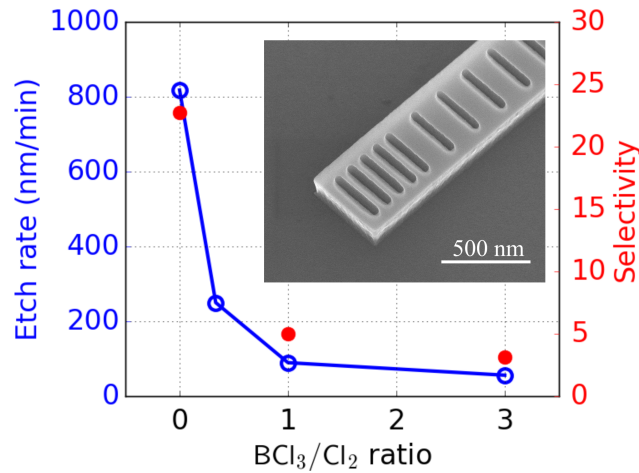


Figure 3.8 – Dependence of GaP etch rate (blue) and selectivity with respect to HSQ (red) on BCl₃-to-Cl₂ ratio. Inset: SEM image of a test pattern etched with 17.5 sccm H₂, 2.0 sccm CH₄, 10.0 sccm Cl₂, and 10.0 sccm BCl₃ for 2 min. The other parameters are as in the base recipe (see subsection 3.5.2).

3.5.4 Influence of temperature and 'high-power' recipe

Consistent with the work of Shul et al. [128], we also observed that the extent of undercut and sidewall roughness could be reduced by lowering the temperature, and at a sample electrode temperature of 20 °C, the remaining undercut could be eliminated (Figure 3.9(a)). The resultant recipe is referred to as the “high-power” recipe (Table 3.5). Further improvement of the sidewall roughness is expected to be achieved by going to even lower temperatures and adjusting the BCl₃-to-Cl₂ ratio simultaneously to maintain vertical sidewalls. For prolonged etches, the structures exhibit poorer sidewall roughness even at 20 °C, presumably due to heating of the sample. Periodically interrupting the plasma for 60 s to allow the sample to cool was found to be beneficial but left traces of the process cycling in the sidewall morphology (Figure 3.9(a)). One could also consider affixing the sample to the carrier wafer with a grease or other substance to improve thermal contact.

3.5.5 Etching of small openings

While the external sidewalls of the test structures appeared to be nearly vertical when etched with the high-power recipe, the profile inside small, high-aspect ratio openings was less satisfying. SEM images of cross-sections prepared by focused ion beam (FIB) milling with Ga ions through a test structure (Figure 3.9) revealed bowed sidewalls in the slots, where the effect is more pronounced in narrower openings. Such profile issues are common when etching narrow structures and may be caused by accumulation of negative charge near the mouths of the openings [133], leading to deflection of the impinging positive ions towards the inner

	High-power recipe	Low-power recipe
Process gases		
H ₂	17.5 sccm	14.5 sccm
CH ₄	2.0 sccm	5.0 sccm
Cl ₂	10.0 sccm	10.0 sccm
BCl ₃	10.0 sccm	10.0 sccm
RF Power	80 W	120 W
DC Bias	315 V	390 V
ICP Power	600 W	200 W
Chamber pressure	5 mTorr	5 mTorr
Temperature	20 °C	20 °C
Etch rate	80 nm/min	225 nm/min
Selectivity with respect to HSQ	4:1	11:1

Table 3.5 – Etch recipes for patterning of GaP.

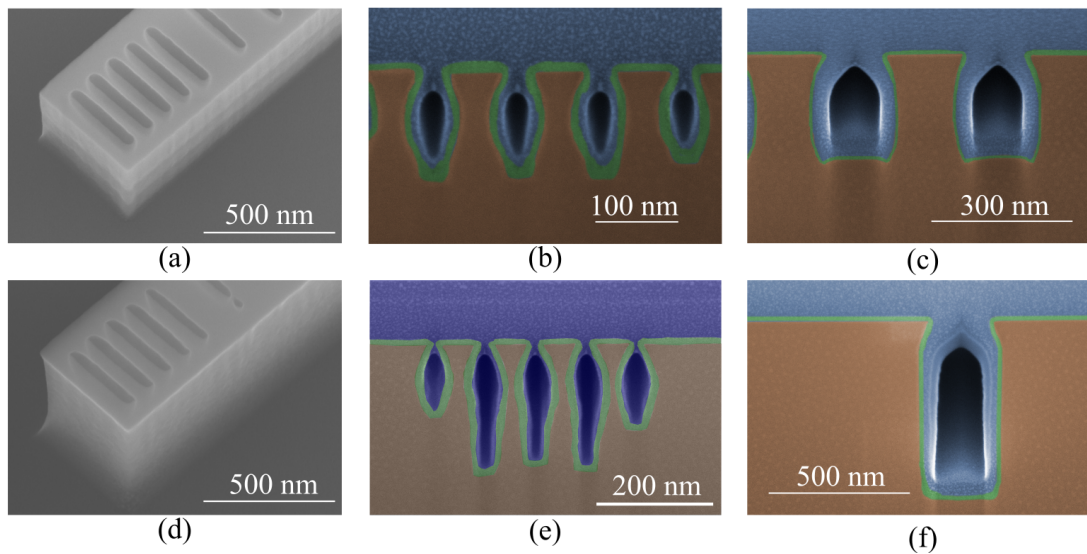


Figure 3.9 – (a) and (d) SEM images of test structures etched with the high-power recipe and low-power recipe, respectively. (b),(c),(e) and (f) False-color SEM images at 52° tilt angle of cross-sections prepared by FIB of these test structures. The GaP (brown) is covered by a thin SiO₂ layer (green), which was deposited for better contrast, and a platinum layer (blue), which was deposited to protect the devices during FIB milling. The dark regions are voids. The design width of the slots in (b) and (e) is 50 nm, in (c) and (f) it is 150 nm.

sidewalls. In addition, we also observed a reduced etch rate in high-aspect ratio openings. For nominally 50 nm-wide slots, we measured an etch rate of 30 nm/min compared to 80 nm/min outside the structure. We can compensate for this well-known phenomenon, commonly referred to as RIE lag [135], by increasing etch time, but the accompanying reduction in selectivity with respect to removal of the e-beam resist must be kept in mind. Even without the RIE lag, the selectivity with respect to HSQ is only 4:1.

To address the need for higher selectivity when etching small openings, the ICP-RIE process was further modified by adjusting the ICP power. The dependence of etch rate and selectivity on ICP power, with all other parameters of the high-power recipe left unchanged, is shown in Figure 3.10. While the GaP etch rate is essentially constant from 400 W to 600 W, we observe a significant rise in the etch rate at 200 W, a somewhat counterintuitive result given that increased ICP power is associated with a higher plasma density, which typically would increase the chemical component of etching. Several mechanisms could account for this behavior, such as a change in the plasma chemistry at higher ICP powers, leading to either creation of species that are effective at passivation or removal of species responsible for etching. For the latter possibility, sputter desorption of etchants from the surface may play a role [129].

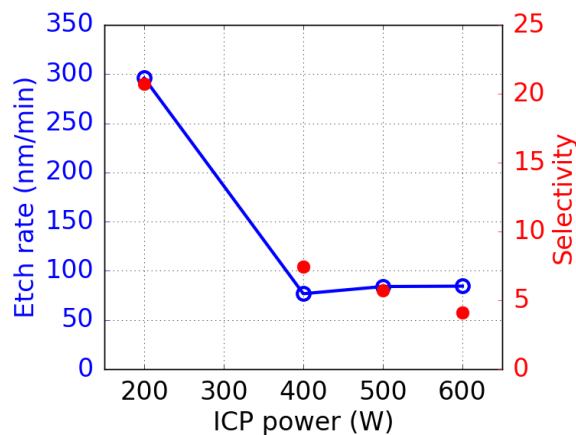


Figure 3.10 – Dependence of GaP etch rate (blue) and selectivity with respect to HSQ (brown) on ICP power.

3.5.6 Influence of pressure

One other parameter that could influence etch performance is chamber pressure. We found that an increase from 5 mTorr to 10 mTorr roughened the sidewalls and led to undercutting of the patterned structures. At lower pressure, the plasma was not stable. Therefore, a pressure of 5 mTorr was maintained.

3.5.7 Passivation with CH₄ and 'low-power' recipe

Finally, taking advantage of the known passivation behavior of CH₄ [128], the H₂-to-CH₄ ratio was reduced from the usual value of 8.75:1 to 2.9:1 in order to increase the anisotropy when etching with an ICP power of 200 W. The resulting "low-power" recipe is specified in Table 3.5. An SEM image of a test pattern fabricated with the low-power recipe (Figure 3.9(d)) indicates smooth, nearly vertical etching of the outer sidewalls for features etched over 800 nm deep. Owing to the reduced ICP power, periodic interruption of the etching to allow cooling of the sample was no longer necessary. The pronounced foot that forms at the bottom of the structures may be a consequence of the surface passivation process, as it can be reduced by cycling with an oxygen plasma. It is absent on GaP-OI substrates when the GaP is etched through to the underlying oxide (Figure 3.11). The higher selectivity with respect to HSQ (11:1) permits the use of thinner resist layers, which should improve dimensional accuracy. Except for very small openings (e.g. 50 nm width, as shown in Figure 3.9(e)), we observe a better sidewall profile than for the high-power recipe, as illustrated by the SEM image in Figure 3.9(f) of a cross-section prepared by FIB, where there is significant deviation from verticality only at the top of the opening.

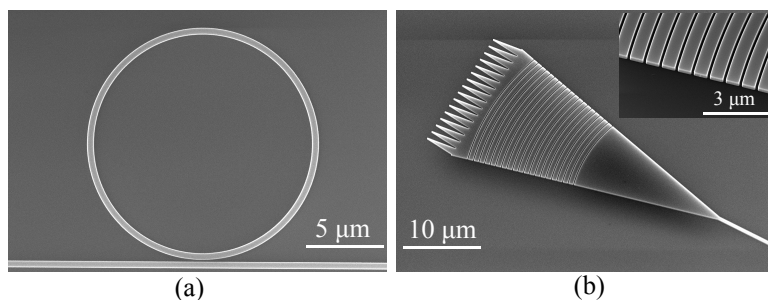


Figure 3.11 – SEM images of fabricated photonic devices. (a) Ring resonator comprising a 400 nm-wide circular waveguide with a radius of 7.5 μm and the associated 400 nm-wide bus waveguide. The gap between the ring and the bus waveguide is 160 nm. (b) Grating coupler at 30° tilt angle.

3.6 Fabrication of waveguides, ring resonators and grating couplers

A first series of device structures was fabricated on a 6 mm × 7 mm GaP-OI chip. The structures included 400 nm-wide ridge waveguides with lengths up to 2.5 mm as well as circular ring resonators, also 400 nm wide, with radii ranging from 5 μm to 15 μm and coupling gaps to the associated bus waveguide ranging from 80 nm to 240 nm (Figure 3.11(a)). Additionally, grating couplers were fabricated at the ends of the waveguides enabling local testing of the devices without end-facet polishing. Their design is described in section 4.2. The structures were defined by e-beam lithography using a pre-coating of 3 nm of SiO₂ deposited by ALD and 6% HSQ as resist. Pattern transfer was carried out with the low-power ICP-RIE recipe, as described above in section 3.5. The waveguides, ring resonators, and grating-couplers were all

fabricated in the same process step and were fully etched through to the underlying SiO₂ layer. After etching, the chip was exposed to an oxygen plasma (600 W) for 3 min. This step serves to prevent the formation of droplet-shaped residues otherwise observed on the GaP sidewalls. Finally, the HSQ was removed by submerging the chip in standard buffered oxide etchant for 10 s. An atomic force microscopy (AFM) measurement of the top device surface gives a RMS surface roughness of 0.30 nm (Figure 3.12).

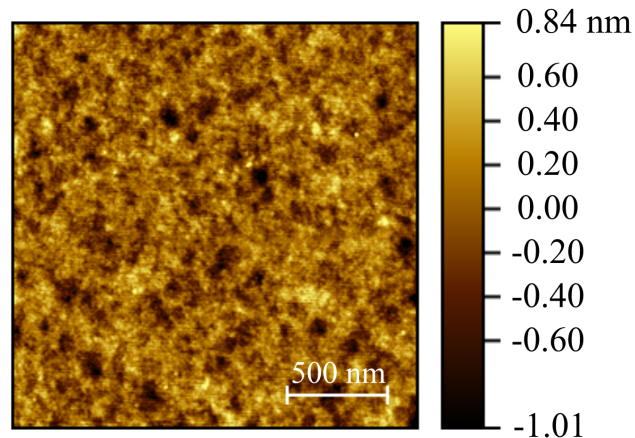


Figure 3.12 – 2 μm \times 2 μm AFM image of the GaP device layer after device fabrication. The RMS roughness is 0.30 nm.

3.7 Fabrication of freestanding devices

To create freestanding devices, e.g. PhCs, the patterned chips were coated with the positive resist AZ6612. The resist was exposed and developed to make rectangular openings around the optical cavities while leaving the input/output waveguides and grating couplers protected. Good adhesion of the photoresist is essential and is achieved via deposition of 5 nm of SiO₂ by ALD followed by treatment with hexamethyldisilazane (HMDS) before spin coating of the resist. Approximately 1.1 μm of the sacrificial buried SiO₂ layer under the devices was then removed by submerging the chip in buffered HF for 15 min. An optical microscope image of released PhCs is shown in Figure 3.13.

3.8 Fabrication of photonic crystal cavities

The fabrication of PhCs follows the steps described in the previous sections. A SEM image of a PhC thus fabricated is shown in Figure 3.14. The devices feature smooth, nearly vertical sidewalls. The latter is evident from the cross-sectional image prepared by focused-ion-beam milling in Figure 3.14(c). Faithful reproduction of the simulated design is essential, as the optical quality factor drops by 70% if the hole radii are too large by 10% (subsection 6.1.2).

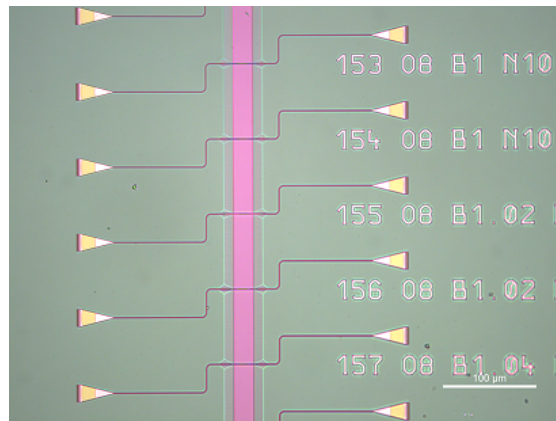


Figure 3.13 – Optical microscope image of released PhCs. The portion of the chip, where the sacrificial buried SiO₂ layer was removed, appears pink. The resulting trench is wider at its top than at the bottom. Around the waveguides, the adhesion of the photoresist was not optimal in this case, as the SiO₂ was etched next to the waveguides.

Compared to the fabrication of waveguides or ring resonators, the fabrication of PhCs is especially challenging because of the required dimension accuracy, the high aspect ratio and the requirement of a smooth surface. High dimension accuracy is achieved by carefully calibrating the e-beam lithography. If systematic deviations of the hole radii are observed, an additional bias of 5 nm is applied to the device dimensions, which leads to an increase of the area coated with HSQ. Furthermore the angle of the HSQ is influenced by the electron dose set for the e-beam. To make sure that the HSQ covers the devices during the complete dry etch process, the angle must not be too flat. Finally, the resolution for the e-beam is set to its minimum of 1 nm for the parts of the layout containing PhCs. Although this increases the writing time, it is crucial for receiving smooth holes. Additionally, in the chip layouts, the size of the holes is varied to compensate for possible over- or underetching during the dry-etch process.

Examples for faulty device fabrication are shown in Figure 3.15, where (a) shows an alignment mismatch between the write fields of the e-beam written with the fine resolution required for the PhCs and the coarse resolution for the waveguides. Figure 3.15(b) is a PhC that was written without adjusting the e-beam settings for a PhC, but keeping the same settings as for waveguides.

The high aspect ratio of the holes in the PhCs leads to a reduced etch rate in the holes during dry-etching. This can result in holes, which are not completely open and implies a required increase in etch time. Before releasing the PhCs, the unopened holes can be hard to perceive in SEM images. To check if the device layer was completely etched through, it can be helpful to check the area beneath the gratings of the grating couplers. If there are undesired remainders of the device layer and the HSQ has not been removed yet, it is possible to repeat the dry-etch process to fully open the holes. Examples for PhCs with not completely opened holes are shown in Figure 3.15(c) and (d).

Another source of processing difficulties were residues covering the surface of the PhCs,

3.8. Fabrication of photonic crystal cavities

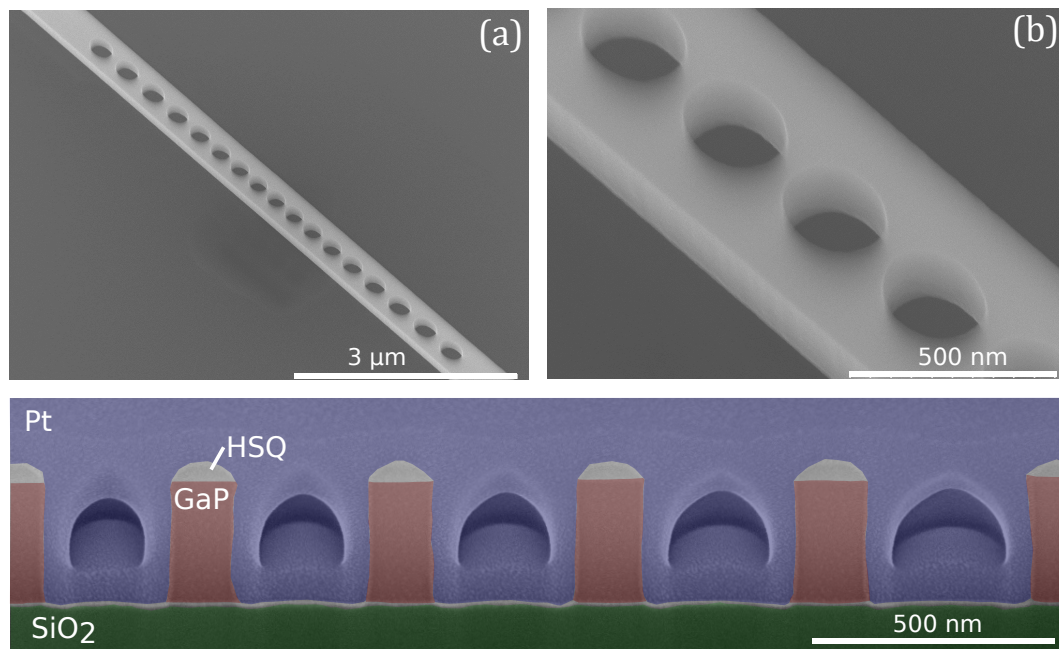


Figure 3.14 – SEM images of a fabricated 1D GaP PhC. (a) Freestanding device (beam width and height are 542 nm and 300 nm, respectively). (b) Magnification of the central part of the PhC showing smooth and straight sidewalls, even inside the holes. (c) PhC cross-section before device release prepared by focused-ion-beam milling.

especially after the release process. This seemed to be connected to multiply using the same beaker of buffered HF. Instead, fresh buffered HF should be used for the release of the PhCs.

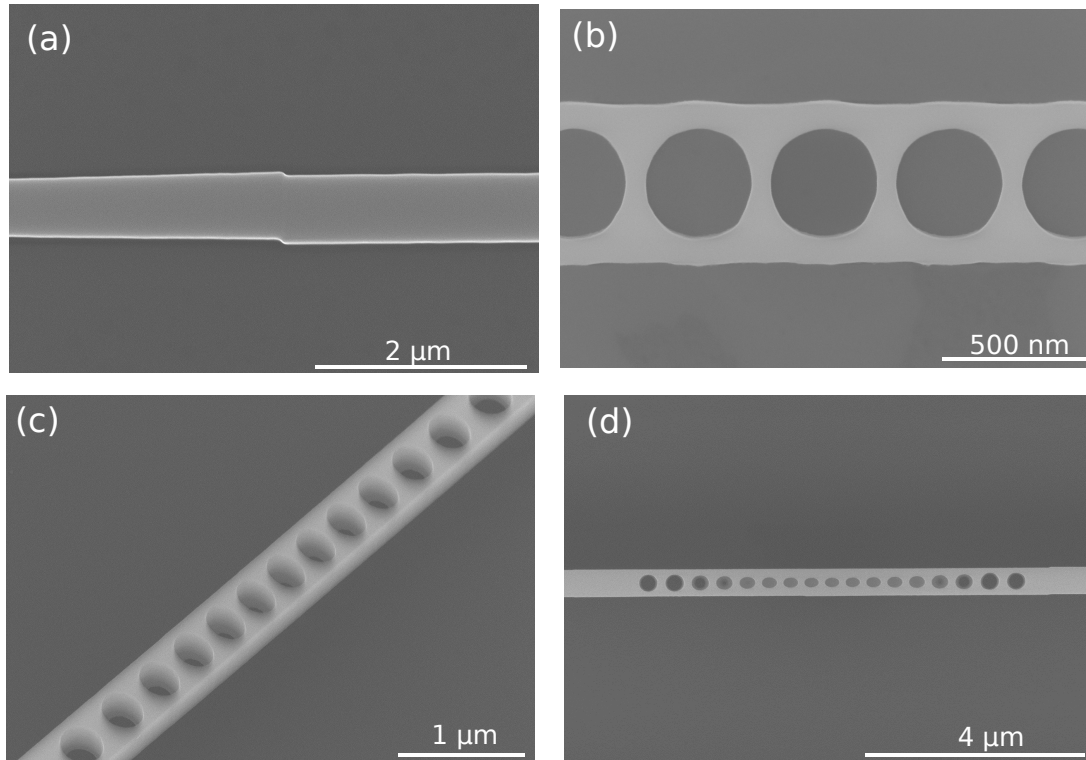


Figure 3.15 – Challenges in photonic crystal cavity fabrication. (a) Because the e-beam resolution is changed between PhCs and waveguides, an offset between the write fields can occur which is commonly known as stitching. (b) PhC written with the same settings for the e-beam as used for a waveguide. (c) and (d) PhCs with not completely opened holes.

3.9 Chip layout

This section provides an example of a chip layout used for a 7 mm × 7 mm GaP-OI chip containing PhCs. The layouts for nonlinear optics and silicon photonics are comparable. They are designed with IPKISS [136], a photonic circuit design package. A typical chip layout is shown in Figure 3.16. The red area is the actual chip area. The actual write field is smaller; it is limited by requirements of chip handling and alignment markers. Because a photonic crystal chip involves two lithography steps, one e-beam and one optical lithography step, alignment markers (the orange patterns on the left-hand and right-hand sides of the chip) are needed to align the two steps. In this case, the layout has five columns, the four on the left contain devices with PhCs, the right one contains ring resonators. Each of the photonic crystal devices is positioned in the center of a waveguide with an S-bend. The S-bend has two functions:

First, it reduces the light that travels from one cleaved fiber to the other without entering the device and second, the S-bend serves as a filter that preferentially transmits transverse electric (TE) polarized as opposed to transverse magnetic (TM) polarized light, as the bending losses are higher for the TM mode. The photonic crystal devices are crossed by long, vertical trenches. These trenches are created by openings in the photomask used for exposing the positive photoresist applied in device release (see section 3.7). Each column of photonic crystals is divided into blocks of devices with identical hole number. Within each block, the size of the holes is varied to compensate for possible over- or underetching. At the beginning of each block, there is one waveguide without a PhC. This serves as a reference to determine the grating coupler performance and also for alignment of the cleaved fibers used when measuring the devices. At the lower end of each column, there are two devices which are meant for investigations with the SEM in the course of fabrication. Exposure to the electron beam of the SEM can alter the structure, for example, through deposition of carbon, which influences further processing. Instead the 'SEM test devices' are imaged.

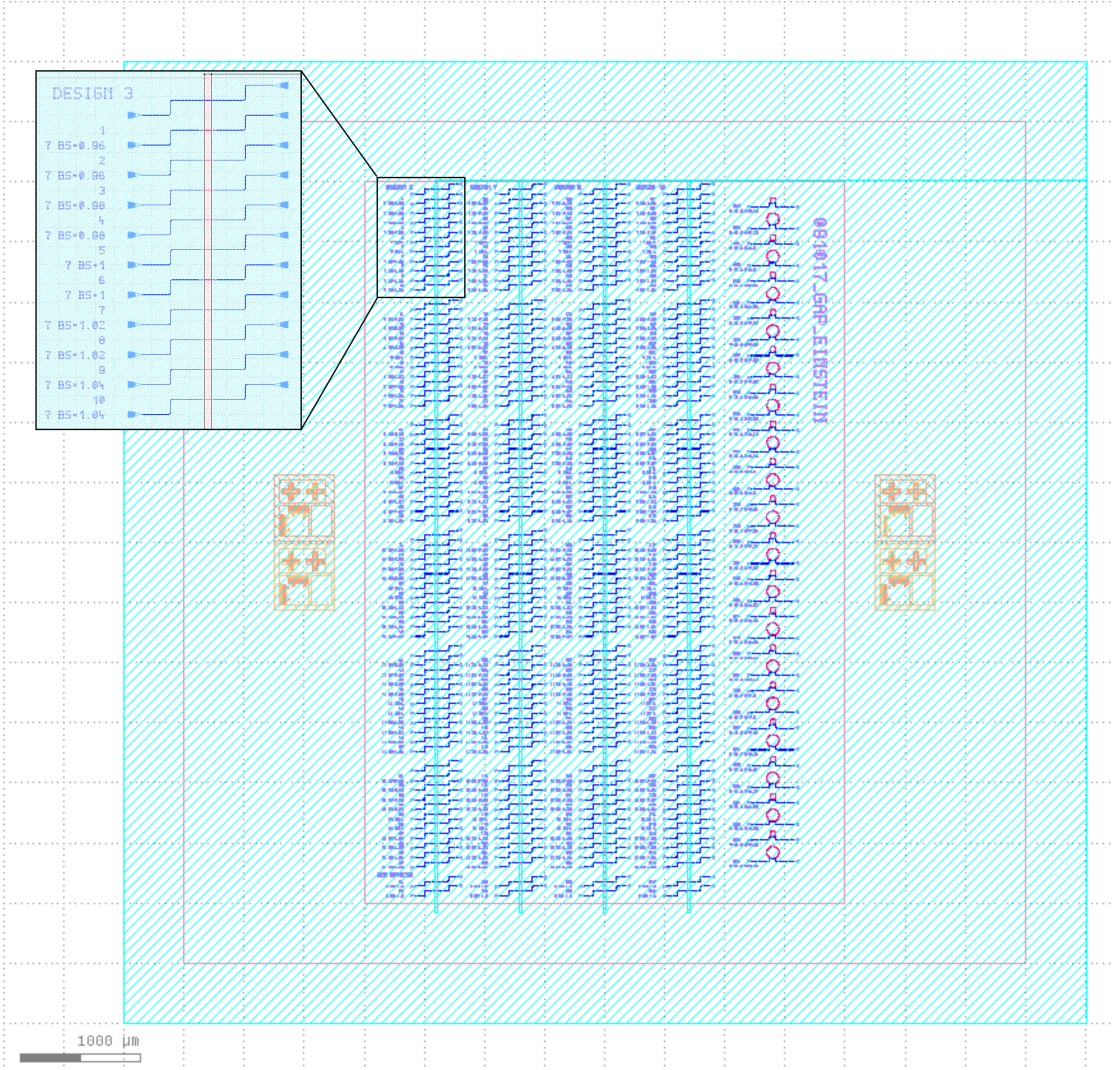


Figure 3.16 – Typical chip layout of a 7 mm × 7 mm GaP-OI chip with photonic crystal cavities.

4 Design of GaP devices for nonlinear optics

For the integration of photonic devices, some essential components have are necessary: First, single mode waveguides for either TE or TM polarization are required in order to route the light on chip. As GaP has a higher refractive index ($n_0 > 3$) than the surrounding air or the SiO₂ the light can be confined in rectangular ridge waveguides, due to total internal reflection at the boundaries to the substrate and air. Second, a means to couple light on and off the chip is required. Several methods are known to accomplish this, for example tapered fibers [137, 138], butt or end-firecoupling[139], tapered waveguides [140, 141] and grating couplers[142]. Fully etched grating couplers are employed in our group for the ease of fabrication and measurement, but at the expense of coupling efficiency (see Appendix E for a comparison of different grating coupler types and their predicted and achieved coupling efficiencies). Third, for many applications optical resonators are required (section 2.4). To explore the nonlinear optical properties of GaP, in this work ring resonators are employed. For frequency comb generation, cross-sectional dimensions of the waveguides comprising the resonators must be chosen to provide overall anomalous dispersion, as described in the last part of the chapter.

4.1 Waveguides

For the purposes of the devices studied here, we would like to assure that the waveguides used support a single TE mode. The number of guided modes is determined by the dimensions of the waveguide. The group refractive index of the waveguide is also inferred from the dimensions and is an important value, as it influences certain device properties, such as the FSR of the ring resonators.

4.1.1 Single mode waveguides

The cross-section of the waveguide is a rectangle as this is what can most easily be fabricated. When choosing its height and width, we consider the height of the other components fabri-

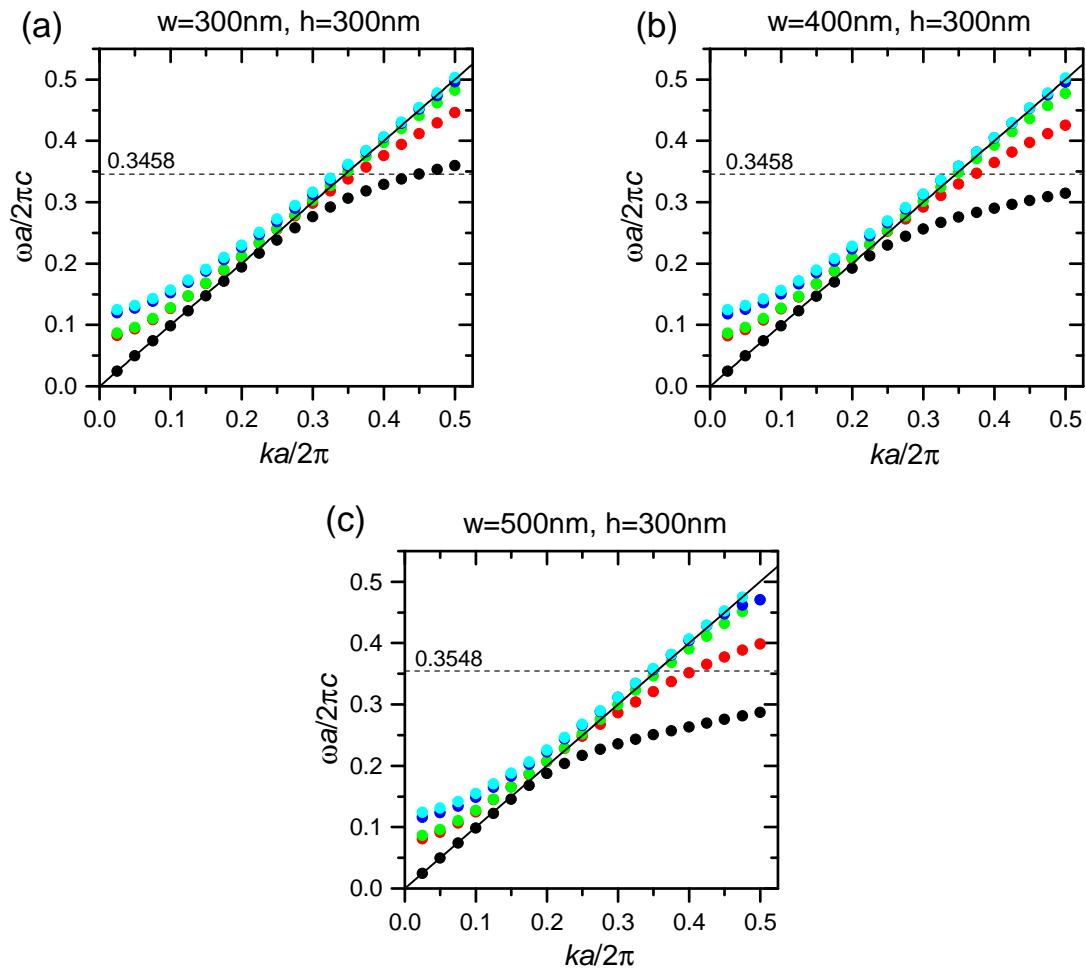


Figure 4.1 – Simulated band structures for a waveguide made of GaP on SiO_2 surrounded by air. The height is 300 nm for every simulation, the widths are (a) 300 nm, (b) 400 nm and (c) 500 nm. For a width of 500 nm, the waveguide is almost multimode for a wavelength of 1550 nm.

cated in the same etch step as the waveguides, as this keeps the process steps to a minimum. For the PhCs used for optomechanics, the optimal height is 300 nm (see section 6.1), so this sets the height of the waveguides for the chips containing PhCs. To figure out the maximum width of the waveguide for which it is single mode, the band structure for various widths is calculated with the mode solver MPB [143]. The solver computes the energies of the eigenmodes depending on the k-vector, the results are shown in Figure 4.1 in units of the cell size $a = 550$ nm. A mode with a vacuum wavelength of $\lambda = 1550$ nm has an energy of 0.3458, which is marked by a horizontal dashed line in each of the plots. The black line, which corresponds to $\omega = ck$, is the light line. It separates the energies of the modes that are guided ($\omega < ck$) from the modes leaking into air ($\omega > ck$). For a single mode waveguide, there should be only one guided mode for the wavelength of $\lambda = 1550$. As can be seen from Figure 4.1 for waveguide widths of 300 nm, 400 nm and 500 nm, there is always one strongly guided mode (black dots). The second mode (red dots) is a weakly guided mode for $\lambda = 1550$ for all the simulated widths. Finally, 400 nm is chosen for the waveguide width.

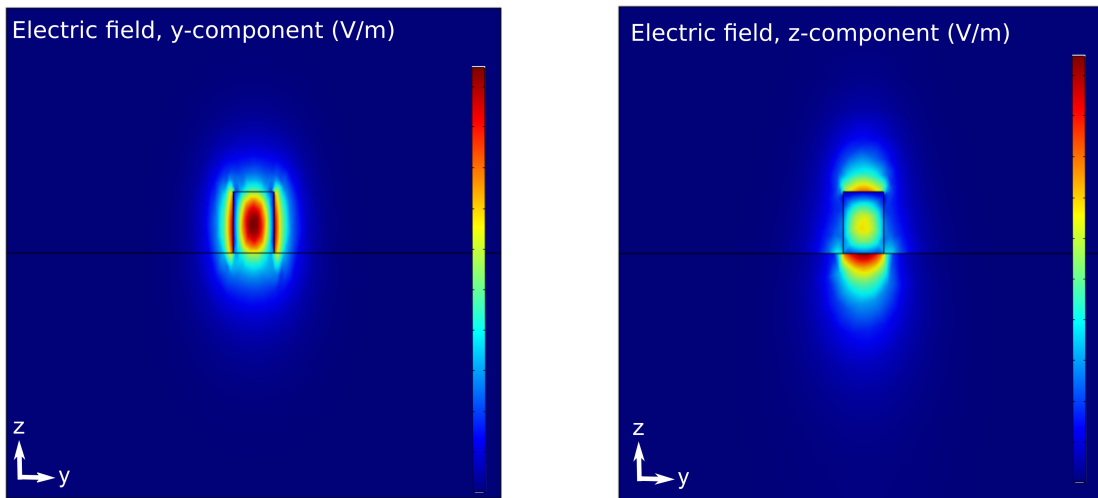
For the ring resonators used for frequency comb generation this is changed, as there the dispersion is important, which is controlled by the waveguide width (see section 4.3). Also the bus waveguides used for the ring resonators were different, as the coupling between bus waveguide and ring resonator depends on the width of both. For the devices used in [89] the bus waveguides had a width of 550 nm.

4.1.2 Group index

For the calculation of the free spectral range of the ring resonators, we need to know the group refractive index n_g . It can be calculated from the change of the effective refractive index n_{eff} with the vacuum wavelength λ_0 (see Equation 2.12). Therefore n_{eff} is inferred for different values of λ_0 using numerical simulations with COMSOL Multiphysics [116]. From the slope in Figure 4.2(c) and the effective refractive index $n_{\text{eff}}(1550 \text{ nm}) = 1.3975$ the group refractive index $n_g(1550 \text{ nm}) = 3.9995$ is calculated.

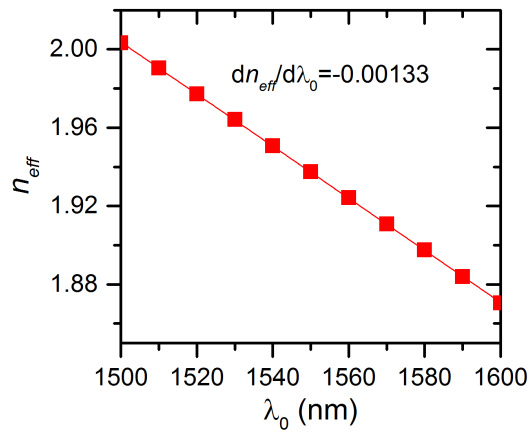
4.2 Grating couplers

Focusing grating couplers located at the ends of the waveguides enable testing of individual devices without end-facet polishing. The gratings are designed by considering two equations [144]. With the first (Equation 4.1a), the so called grating equation, the angle φ_c into which light of wavelength λ will be diffracted for a certain diffraction order m and grating period Λ can be determined. n_c is the refractive index of the cladding, n_{eff} the effective refractive index of the guided wave (see section 4.1). The second equation gives the condition for constructive interference of light diffracted from individual grating lines (Equation 4.1b). q is the number of the grating line, z is the co-ordinate in the propagation direction of the mode, y is the coordinate in the plane of the grating coupler perpendicular to z . The resulting grating



(a) Mode profile of the fundamental TE mode.

(b) Mode profile of the fundamental TM mode.



(c) Numerically simulated dependence of n_{eff} on λ_0 .

Figure 4.2 – Numerical simulations for the calculation of the group refractive index n_g . The mode profile of the fundamental TE mode was simulated for a GaP on SiO₂ waveguide with the dimensions $w=400$ nm and $h=300$ nm. The effective refractive index n_{eff} was inferred for different wavelengths. The slope is used to calculate the group refractive index n_g .

consists of elliptical grating lines with a common focal point.

$$n_{\text{eff}} = n_c \cos \varphi_c + m\lambda / \Lambda \quad (4.1a)$$

$$q\lambda = zn_c \cos \varphi_c - n_{\text{eff}} \sqrt{y^2 + z^2} \quad (4.1b)$$

Equation 4.1b is only valid for shallow gratings, as it assumes that n_{eff} is the same in the waveguide and the coupler region. For fully-etched gratings, such as those we use, a correction term must be added to the right side of (Equation 4.1b), namely:

$$r(q)\Delta n_{\text{eff}} = q\lambda \frac{-ze_a \sqrt{y^2 + z^2} + y^2 + z^2}{y^2 + (1 - e_a^2)z^2} \Delta n_{\text{eff}} \quad (4.2a)$$

$$e_a = \frac{n_c \cos \varphi_c}{n_{\text{eff}}} \quad (4.2b)$$

The effective refractive index in the grating region depends on the duty cycle (DC) of the grating and is inferred from numerical simulation of the mode profile in one grating line. Equation 4.1a and Equation 4.1b with the correction do not define a unique geometry; they can be satisfied by several combinations of DC and Λ .

The grating coupler design used here for GaP-OI consists of 19 curved lines of GaP and is designed with either a periodicity of 764 nm and a duty cycle of 80% or a periodicity of 728 nm and a duty cycle of 85%. The couplers have a length of 35 μm and are designed for nearly vertical coupling (10 degree at 1550 nm). Sub-wavelength-sized wedges are incorporated opposite the waveguide to reduce reflections [145].

4.3 Ring resonators

As mentioned in subsection 2.4.3.1 for frequency comb generation, a small anomalous group velocity dispersion (GVD) is desired to achieve phase matching and enable broad combs. An anomalous GVD means $\beta_2 < 0$, which is equivalent to $D_2 > 0$ (see subsection 2.4.3.1, i.e. Equation 2.23). The GVD can be simulated numerically, where the material dispersion is included through the Sellmeier equation [146, 147]. The simulation was carried out for various waveguide widths of an uncladded waveguide of thickness $h = 300$ nm. The result is shown in Figure 4.3. As our targeted wavelength of operation for the pump laser is 1550 nm, a width of $w = 500$ nm was chosen, because the region of anomalous GVD is centered around approximately this wavelength.

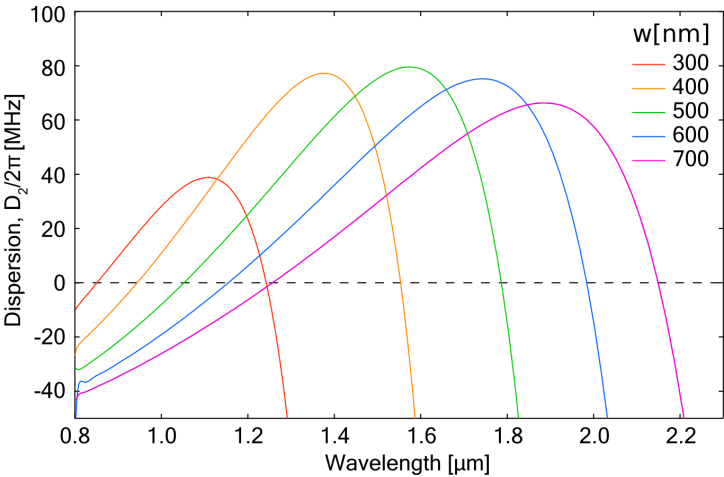


Figure 4.3 – Simulated resonator dispersion for various waveguide widths for an uncladded waveguide of thickness $h = 300$ nm and variable width w .

5 Nonlinear optics

Due to its non-centrosymmetric crystal structure, GaP has a non-vanishing second-order nonlinearity. Furthermore, its large third-order nonlinearity, high refractive index and wide band gap make GaP an interesting material for integrated nonlinear photonics. Having established the capability of fabricating integrated GaP photonic devices, we explored the nonlinear properties of GaP are explored. The results are presented in this chapter. First, basic building blocks required for integrated photonics, such as waveguides, grating couplers and ring resonators are fabricated and characterized. The ring resonators exhibit second- and third-harmonic generation, and a precision measurement of the Kerr coefficient n_2 at near infrared wavelengths is made. By engineering the waveguide's GVD to be anomalous, Kerr frequency comb formation is observed for the first time in GaP waveguide resonators. This allows to observe frequency comb formation. In combination with the $\chi^{(2)}$ nonlinearity, frequency doubled combs are simultaneously generated. Finally, in cladded devices, the combination of SRS and FWM leads to Raman-shifted frequency combs.

5.1 Experimental setup

A schematic of the apparatus used for transmission measurements and higher-harmonic generation is shown in Figure 5.1 (a). All measurements were performed in air at atmospheric pressure with the chip resting on an aluminum block held at 20.0 °C, as measured with an integrated thermistor, and controlled with a Peltier element. Continuous-wave infrared light from a tunable external-cavity laser (Photonetics Tunics-Plus) was directed through a cleaved single-mode optical fiber into the input grating coupler of the device under test (DUT). For characterization of the resonances of ring resonators, the laser light was first passed through a fast wavelength meter (Yenista CT400 Optical Component Tester). A fiber polarization controller (FPC) was used to align the polarization of the light with the TE design orientation of the grating couplers. Light emitted from the output grating coupler on the other side of the device was collected with another cleaved single-mode optical fiber, which was connected to a power meter (EXFO IQ 1600), either directly or through a fiber beam splitter (FBS), for monitoring and recording of transmission spectra. For measurements of second- and third-harmonic

generation, an optical spectrometer (Ocean Optics USB2000) was used, where the second cleaved fiber was positioned either over the output grating coupler or directly above the ring resonator to collect the scattered light. The latter configuration was necessary for observation of the third-harmonic, as it is absorbed by the GaP, and in any case, the grating couplers were not designed for the harmonic wavelengths, nor are the harmonics efficiently coupled from the ring to the bus waveguide. For characterization of the power dependence of harmonic generation, an erbium-doped fiber amplifier (EDFA), a bandpass filter, and a variable optical attenuator (VOA) were introduced between the tunable laser and the FPC.

The measurement setup used for frequency comb generation and the determination of the Kerr coefficient is shown in Figure 5.1(b). The arrangement for coupling light in and out of the resonators is the same as for the previous setup. As higher input powers were required for comb generation, the pump laser was passed through a 2-W erbium-doped fiber amplifier (BkTel) before entering the device. After the device, the transmitted light is passed through a near-infrared optical spectrum analyzer.

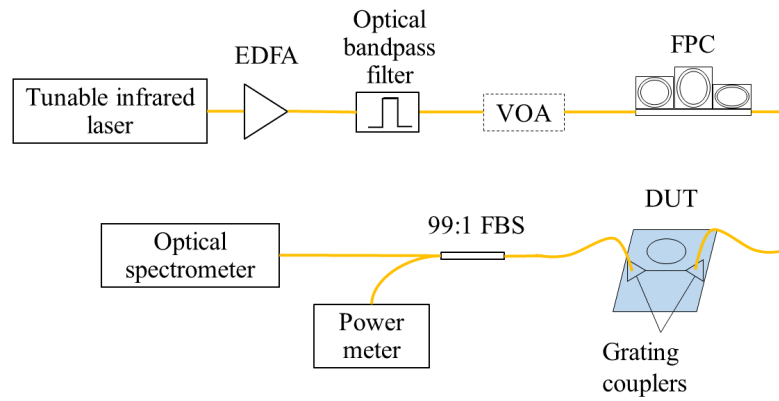
For the measurement of the Kerr coefficient, the resonator was probed by two fields ("pump" and "probe") generated by separate tunable diode lasers (Photonetics Tunics). The fields were combined before the resonator on a fiber beam splitter. Before combining, the pump field was passed through an fiber-coupled intensity modulator. At the resonator output, the combined field was split into two paths. On one path, the output field was directed to the monitor port of the wavelength meter. On the other path, the pump field is stripped using a fiber Bragg grating and the filtered probe field was monitored with a high-speed photoreceiver. The pump intensity modulator was driven by the output port of a vector network analyzer. The input port of the network analyzer was connected to the output of the probe photoreceiver.

5.2 Characterization of waveguides and grating couplers

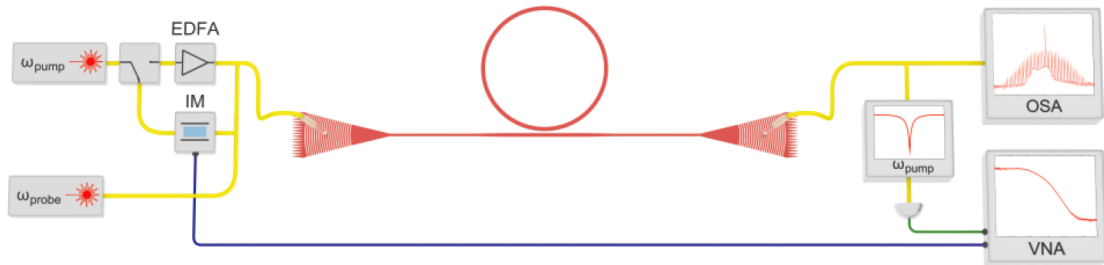
The first fabricated GaP-OI chip contained waveguides with grating couplers at the end and waveguide coupled ring resonators. In this and the next section, the results measured with these first GaP-OI devices are presented. Some of them, as for example the optical quality factors of the ring resonators, could be improved tremendously in future generations.

To give an impression of the fabrication yield for the first chip, we provided statistics and performance values for the first chip with GaP-OI devices. Of the 88 devices patterned in GaP on the first chip, 82 (93%) showed transmission. The grating couplers exhibited a Gaussian-shaped transmission profile (Figure 5.2(a)) that was red shifted with respect to the design wavelength of 1550 nm presumably because of deviations from design dimensions in the fabricated structures. However, when the input and output optical fibers were aligned at an angle of 20° to the chip normal instead of the 10° design angle, the center wavelength was at 1553 nm and the maximum efficiency per coupler was measured to be -4.8 dB or 33.5%. The average coupling efficiency was 6.6 ± 0.4 dB. In principle, the losses could differ between the input and output grating couplers; we have assumed that they are identical and taken half

5.2. Characterization of waveguides and grating couplers



(a) Measurement apparatus used for transmission measurements of waveguides and ring resonators, as well as harmonic generation.



(b) Measurement setup used for frequency comb characterization and the modulation transfer measurement for determination of the Kerr coefficient.

Figure 5.1 – Schematics of the experimental setups.

of the total loss occurring between the two cleaved fibers. For comparison, the best grating couplers fabricated with the GaP-on-diamond system developed by others achieve efficiencies of -7.7 dB [22]. Silicon focusing grating couplers with a design similar to that described here, i.e. fully etched with no cladding, have more than 10 dB loss per coupler [18], presumably to some extent because of the higher index contrast. Highly optimized, partially etched and cladded focusing grating couplers in silicon can however have a coupling efficiency approaching -1 dB [148]. With the same techniques as used for silicon, it should be possible to improve the transmission of the GaP grating couplers.

For waveguide lengths up to 2200 μm , variations in the grating coupler losses dominate over losses in the waveguides. In other words, the propagation loss is not significant compared to the scatter in the measured transmission and would require significantly longer waveguides to be determined. From the Q factors observed for the ring resonators in [23] (see below) we can however estimate an upper bound of 8 dB/cm for the propagation loss using Equation 2.13b and Equation 2.13a. This could be improved in later devices to 1.2 dB/cm [89].

5.3 Characterization of ring resonators

In this section the ring resonators used for two different measurements are described. At the beginning, measurements on second- and third harmonic generation were carried out with the first fabricated devices. For frequency comb generation a later generation of ring resonators was used.

5.3.1 Ring resonators used for second- and third harmonic generation

Figure 5.2(b) displays the transmission spectrum of a ring resonator comprising a 400 nm-wide circular waveguide with a radius $r = 15\mu\text{m}$ evanescently coupled to a 400 nm-wide bus waveguide through a 240-nm coupling gap. The observation of a single family of resonances is consistent with the small cross-section of the waveguide supporting only the fundamental TE-polarized mode. We attribute the splitting of some of the resonances into double resonances (not visible in Figure 5.2) to coupling with counter propagating modes excited by backscattering from imperfections in the waveguide such as surface roughness. From finite element simulations at $\lambda = 1550\text{ nm}$, $n_{\text{eff}} = 1.9375$ and $n_g = 3.9995$ are inferred (see subsection 4.1.2 and section 2.4), which leads to $\text{FSR}/2\pi = 0.80\text{ THz}$ (equivalent to 6.3 nm at this wavelength). The measured free spectral range for the device in Figure 5.2(b) is 0.83 THz.

Fitting a Lorentzian function to a resonance, as shown in Figure 5.2(c), allows one to infer the quality factor. The best measured devices from the first GaP-OI chip have loaded quality factors of $Q = 20000$. The periodic background ripple is due to interference between reflections from the grating couplers and can be modelled with an Airy function, which is the typical description of the sum of the longitudinal mode profiles of a Fabry-Pérot cavity [149]. The optical quality factors are slightly better than the values reported for GaP-on-diamond devices (which however have a smaller radius) [22] but still much lower than what has been achieved

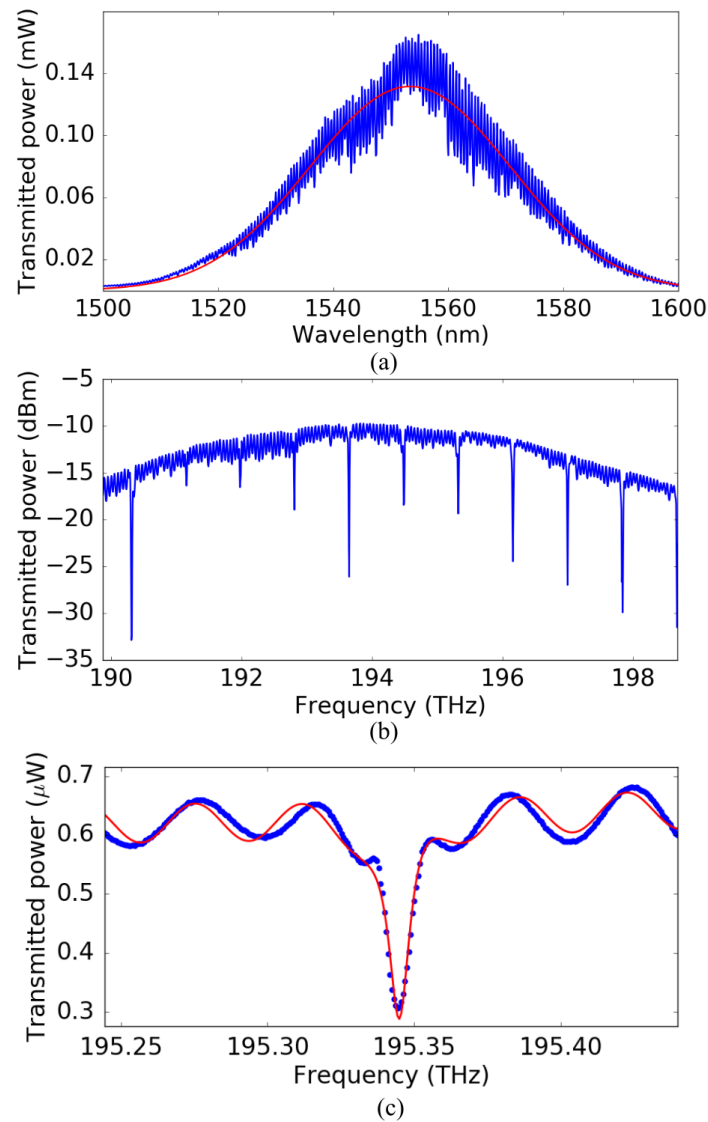


Figure 5.2 – Transmission spectra through a grating coupler and a ring resonator of the first device generation. (a) Transmission through two grating couplers with a period of 764 nm and a duty cycle of nominally 80% connected by a 550 μ m-long waveguide measured with 1.17 mW input power and the input and output optical fibers at an angle of 20 degree to normal. The maximum coupling efficiency is -4.8 dB as obtained by fitting a Gaussian function (red). (b) Transmission spectrum of a ring resonator with a radius of 15 μ m. (c) Transmission spectrum of a device with a radius of 15 μ m near one particular resonance with quality factor of $Q = 20000 \pm 900$. The oscillating background is due to reflections between the grating couplers.

for GaP-on-AlGaP microdisks using resist reflow to reduce sidewall roughness [17].

5.3.2 Ring resonators used for frequency comb generation

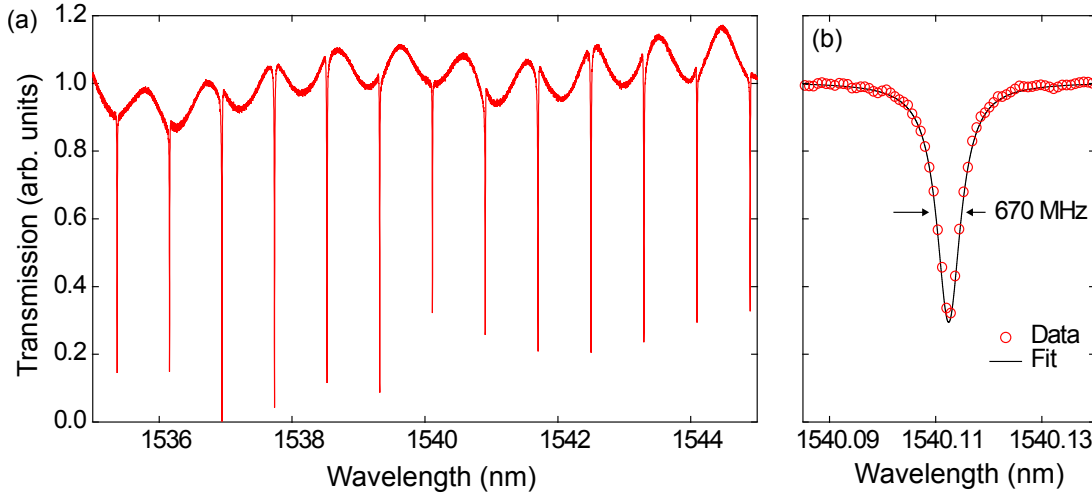


Figure 5.3 – (a) Transmission spectrum of a ring resonator cladded with SiO_2 used for frequency comb generation. (b) Fit of the central peak to a Lorentzian with a linewidth of 0.67 GHz, corresponding a loaded Q of 3×10^5 .

In a device with sufficiently high $\chi^{(3)}$ and optical quality factor Q , Kerr frequency combs can be generated by cascaded FWM (see subsection 2.1.5). Because the threshold for parametric oscillation decreases quadratically with the reciprocal of Q (see Equation 2.10), a principal goal is the improvement of the ring resonator's quality factor. The transmission through a near-critically coupled device cladded with SiO_2 is shown in Figure 5.3. The measured loaded quality factor is $Q = 3 \times 10^5$, which corresponds to an intrinsic quality factor of $Q_i = 6 \times 10^5$ for a wavelength in the telecommunications C-band. The corresponding linear propagation loss, $\alpha = 1.2$ dB/cm, was calculated using Equation 2.13b and Equation 2.13a and is attributed to sidewall roughness. This propagation loss is on par with state-of-the-art AlGaAs [31] and Si [150] waveguides of similar dimensions.

5.4 Second- and third-harmonic generation

The non-centrosymmetric crystal structure of GaP implies that it has a non-vanishing second-order susceptibility ($\chi^{(2)}$), which leads to nonlinear optical effects, e.g. second-harmonic generation (SHG) (see section 2.1). A spectrum of the light gathered with the output fiber positioned above a ring resonator taken while pumping at 1539 nm with 3.7 mW injected into the device (i.e. after the input grating coupler) is shown in Figure 5.4. In addition to the strong second-harmonic signal observed at 770 nm, third-harmonic generation (THG) is detected around 513 nm (inset in Figure 5.4). The third-harmonic light is visible to the human eye, as

5.4. Second- and third-harmonic generation

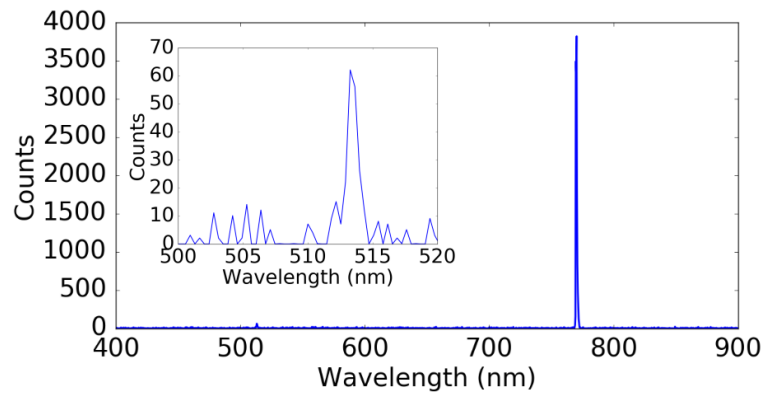
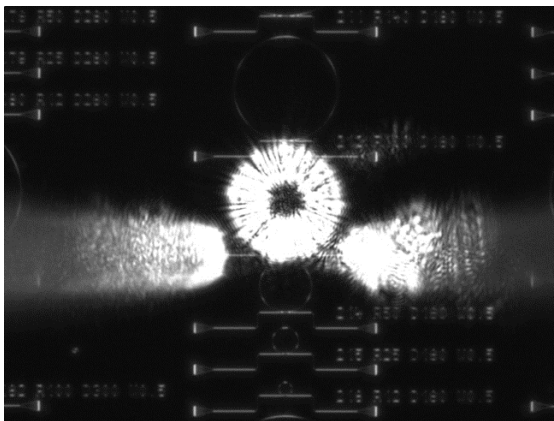
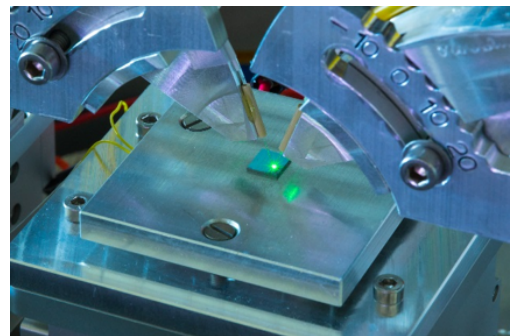


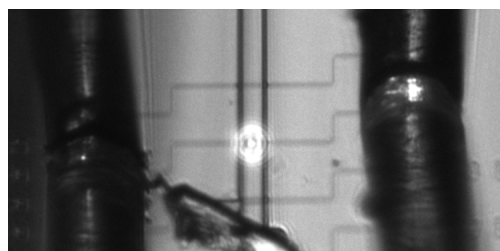
Figure 5.4 – Spectrum of the diffracted light collected with the output fiber positioned above a ring resonator with 3.7 mW entering the device and an integration time of 5 s. The peak at 770 nm is the SHG signal. At 513 nm (inset), the THG signal is observed.



(a) Grayscale image recorded with the alignment camera showing the second-harmonic light generated in a ring resonator as viewed from directly above the device.



(b) Camera image of the third-harmonic light (green) scattered from a ring resonator.



(c) Grayscale image recorded with the alignment camera showing the second-harmonic light generated in a PhC, taken at an oblique angle with respect to the chip surface.

Figure 5.5 – Grayscale images of second-harmonic generation for a ring resonator (a) and a PhC (c) and camera image of the green third harmonic scattered by a ring resonator (b). Visible on all three images are the cleaved fiber tips used to couple light in and out of the grating couplers

its wavelength is in the green. It can be seen with the naked eye while measuring. A camera image showing the scattered THG light is shown in Figure 5.5 (b). In addition to detection with the spectrometer, the second harmonic can also be observed with the camera used to align the samples during measurement. Images of the second-harmonic light produced in a ring resonator and in a PhC are presented in Figure 5.5 (a) and (c), respectively. Because an unknown fraction of the total generated second-harmonic light is collected, we cannot quantify the conversion efficiency. SHG has been previously reported at low input powers in 2D PhCs and waveguides made of GaP [9, 151]. To our knowledge this is the only report of THG in a GaP microcavity other than a brief mention in a previous study of GaP microdisks, where no data was shown [16].

The dependence of the second-harmonic intensity on the input power at the fundamental

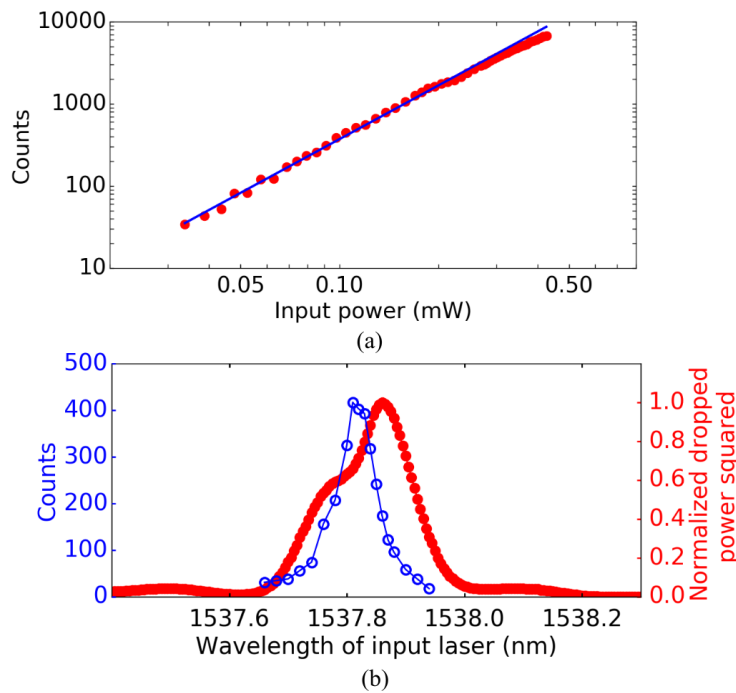


Figure 5.6 – (a) Logarithm of the intensity of the second harmonic as a function of the logarithm of the power entering the bus waveguide of the ring resonator. A linear fit (solid line) gives a slope of 2.17 ± 0.02 . This confirms the quadratic dependence of SHG on input power. (b) Second-harmonic intensity as a function of input wavelength (blue) as measured with the output fiber above the ring resonator. A transmission measurement at the fundamental wavelength has been inverted, squared and rescaled (red).

wavelength for a resonance at 1537.67 nm is shown in Figure 5.6(a). A linear fit of the logarithmically plotted data confirms the second-order nature of the process. The slight deviation from quadratic behavior is attributed to a small thermo-optic shift of the resonance frequency [152]. Indeed, at higher input powers, we observe a significant thermo-optic displacement of the resonances to longer wavelengths, as is typical of such devices and as has already been reported for GaP microdisks [16, 17]. The dependence of the second-harmonic intensity on

5.5. Measurement of the Kerr coefficient with a modulation-transfer technique

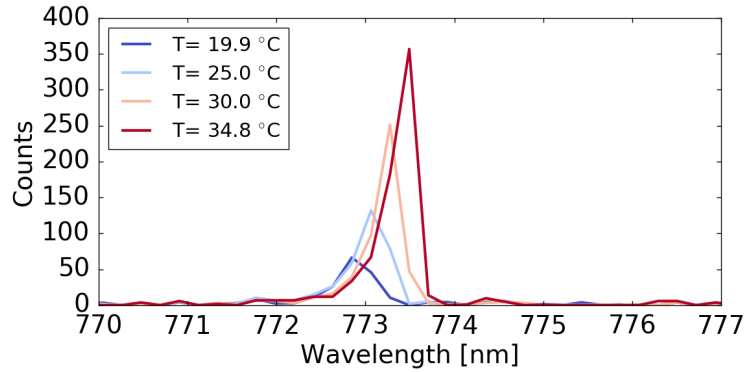


Figure 5.7 – Temperature dependence of the second-harmonic spectrum. With increasing temperature, the resonance shifts to higher wavelength and the efficiency increases.

the input wavelength is shown in Figure 5.6(b). The SHG signal was detected with the cleaved fiber positioned above the ring resonator. The square of the inverted transmitted power (i.e. the power dropped into the ring) measured separately is overlaid on the plot. The observed resonance is split; there are therefore two unresolved peaks in the dropped power spectrum. The difference in shape of the two signals may be due to the resonance at the second-harmonic wavelength having a different splitting and quality factor than the fundamental resonance. The peak of the second harmonic is slightly blue-shifted with respect to the resonance at the pump wavelength, which can be attributed to dispersion and the consequent misalignment of the resonances at the second-harmonic frequency with respect to those at the fundamental frequency. This misalignment can be compensated by thermally tuning the resonance frequencies to more fully take advantage of resonant enhancement [16, 153]. Specifically, the thermo-optic effect causes both resonances to move to higher wavelength with increasing temperature but at different rates, as the thermo-optic coefficient is wavelength dependent. The second-harmonic and fundamental resonances can therefore be tuned with respect to each other to increase the degree of resonant enhancement, as has been demonstrated in detail by Guo et al. in AlN ring resonators [153]. We observe similar temperature dependence of the SHG efficiency, as illustrated in Figure 5.7. Here, the temperature reported is that of the sample holder as controlled by the Peltier element.

5.5 Measurement of the Kerr coefficient with a modulation-transfer technique

The efficiency of all third-order nonlinear processes depends on the third-order susceptibility $\chi^{(3)}$, which is related to the Kerr coefficient n_2 (Equation 2.6). To determine n_2 experimentally, we measured the waveguide nonlinear parameter $\gamma_{\text{NL}} = \omega n_2 / A_{\text{eff}}$, with A_{eff} being the effective area of the waveguide mode. Multiplied with the guided power P this gives the nonlinear propagation constant $\beta_{\text{NL}} = \gamma_{\text{NL}} P$ [94]. We employ a modulation-transfer technique that allows discrimination of the Kerr effect from the much larger thermally induced frequency shift

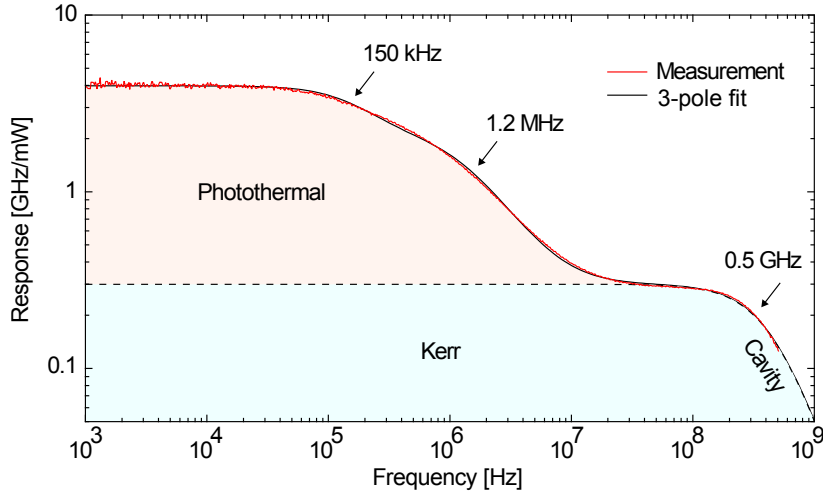


Figure 5.8 – Power-frequency response of a 50- μm -radius ring resonator. Plateaus at 0-10 kHz and 0.1-0.5 GHz are due to the photothermal and Kerr effect, respectively. Roll-off at 0.5 GHz is due to the finite cavity response time.

by exploiting the different time scales of the responses [154]. The corresponding measurement setup is shown in Figure 5.8(a). An intensity-modulated pump field was injected into the cavity on resonance and a detuned probe field was used to record the frequency response of an adjacent cavity mode, as illustrated in Figure 5.8. At sufficiently high frequencies, the response of the probe mode is dominated by the Kerr effect

$$\delta\omega_{\text{probe}}(\Omega) \approx \frac{8\eta Qc}{V_{\text{eff}}} \frac{n_2}{n_g^2} \delta P_{\text{pump}}(\Omega). \quad (5.1)$$

Here, $V_{\text{eff}} = 2\pi r A_{\text{eff}}$ is the effective resonator mode volume with the effective mode area A_{eff} (Equation 2.7), n_g is the waveguide group index, Ω is the modulation frequency and P_{pump} is the injected pump power. $\eta \in \{0, 1\}$ is the cavity coupling parameter (see subsection 2.4.1). Normalizing the response curve to the DC photothermal frequency shift, we infer $\gamma_{\text{NL}} = 2.4(6) \times 10^2 \text{ W}^{-1} \text{ m}^{-1}$ and $n_2 = 1.1(3) \times 10^{-17} \text{ m}^2/\text{W}$. somewhat lower values for n_2 have been obtained using less direct pulsed measurements [155, 156]. An alternative method to estimate n_2 makes use of the threshold for generation of frequency combs described in section 5.7.

5.6 Confirmation of the simulated group velocity dispersion

In section section 4.3, the expected group velocity dispersion was presented for waveguides of 300 nm height and varying width. A width of 500 nm was found to be optimal for achieving an anomalous GVD at 1550 nm as required for frequency comb generation. To confirm this model, ring resonators were patterned with waveguide width varied from 400 to 650 nm. Measurements of the free spectral range $D_1/2\pi$ were then carried out (see Figure 5.9) as a

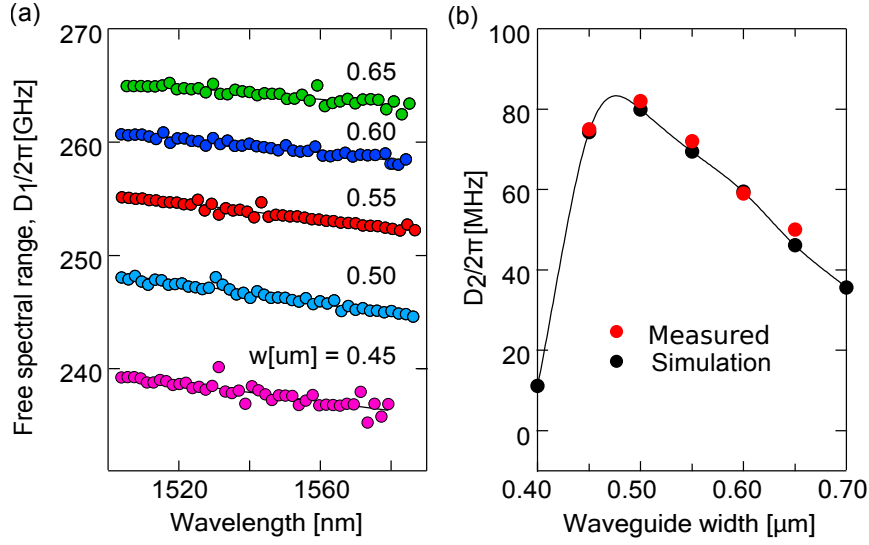


Figure 5.9 – (a) Measured free spectral range versus wavelength for a 50- μm -radius ring resonator with various for different waveguide widths. (b) Comparison of measured and simulated dispersion.

function of wavelength. The dispersion D_2 derived from D_1 (Equation 2.21) was found to be in good agreement simulations (see section 4.3).

5.7 Frequency comb generation

The onset of parametric oscillation in a 50- μm radius, 550-nm-wide ring resonator is shown in Figure 5.10(a). Sideband generation was observed at a threshold power of ≈ 3 mW, here for a near-critically coupled mode at 1560 nm with $Q \approx 2 \times 10^5$ (Figure 5.10(b)). Similar measurements were carried out for modes with $Q = (0.7 - 2.5) \times 10^5$ by varying the operating wavelength and bus-waveguide separation (Figure 5.10(c)). Comparing this set of measurements to Equation 2.10, we infer $n_2 \approx 1.2(5) \times 10^{-17} \text{m}^2/\text{W}$, within the error of the value inferred from the response measurement. The value for n_2 was obtained from the average and standard deviation of the 16 measurements shown in Figure 5.10(c). For each measurement, the resonance extinction ratio was used to infer η from the transmitted signal at resonance $T = (1 - 2\eta)^2$. An effective area of $A_{\text{eff}} = 0.2 \mu\text{m}^2$ was assumed based on finite element simulation (compare Figure 4.2), this value being a good approximation for TE_{00} modes of 500 and 550-nm-wide waveguides (both used in the measurement set). A group index of $n_g = 3.8$ was used based on measurements of the free spectral range (shown in Figure 5.9).

Using input powers greater than P_{th} , broadband frequency comb generation was observed in numerous devices. An example is shown in Figure 5.11(a), in which the input power was fixed at 1 W and the laser-cavity detuning was incrementally reduced. Typical behavior is shown: Initially sub-combs separated by multiple free spectral ranges are formed (consistent

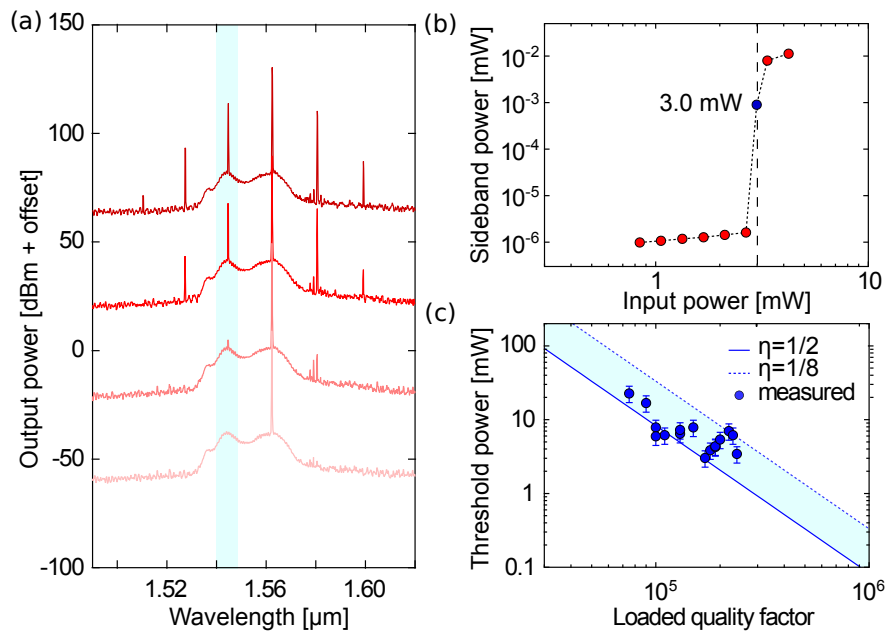


Figure 5.10 – Onset and power threshold for frequency comb generation. (a) Optical spectrum of the cavity output field as a function of input power. Parametric oscillation (spontaneous FWM) is observed above a threshold value P_{th} . (b) Power in the left primary sideband versus input power, revealing $P_{th} \approx 3$ mW for a $Q \approx 2 \times 10^5$ device. (c) Measurements of P_{th} versus Q for various devices, compared to Equation 2.10.

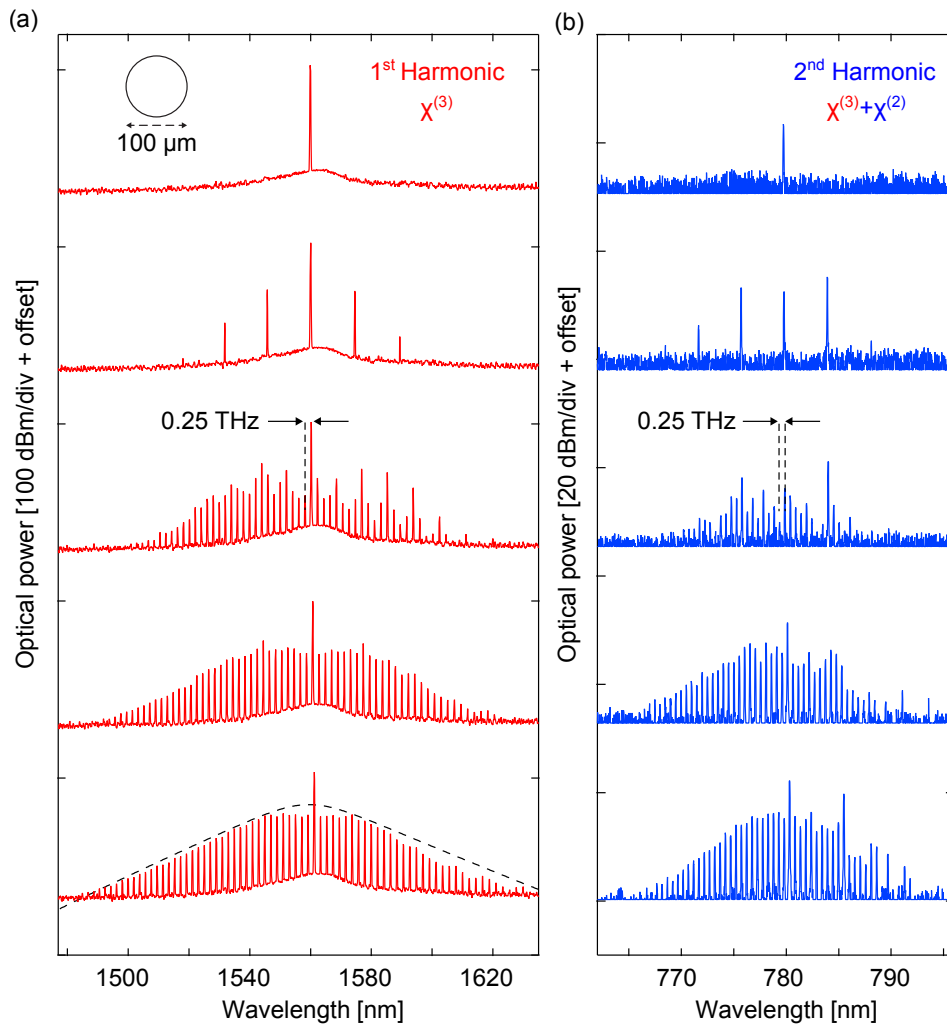


Figure 5.11 – (a) Frequency comb generation in a 50- μm -radius ring resonator. From top to bottom, the laser power is fixed and the laser-cavity detuning is incrementally reduced. A sech-squared function (dashed black) is overlaid on the last spectrum. (b) Simultaneous measurements of frequency-doubled combs on the same device.

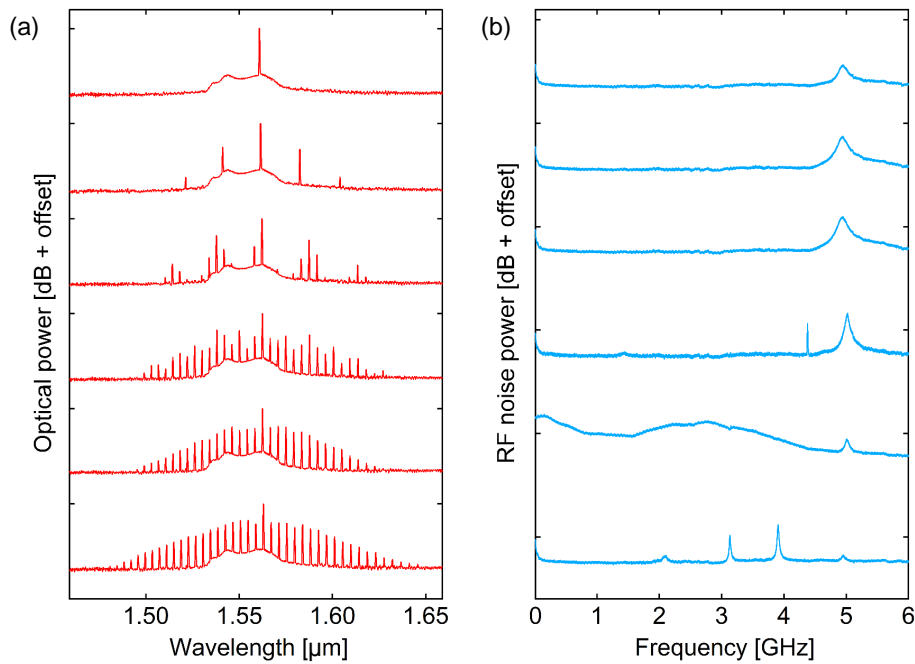


Figure 5.12 – Radiofrequency noise spectrum of GaP-OI frequency comb. (a) Optical power spectrum of the output field of a $R = 25 \mu\text{m}$ ring resonator pumped by a $\sim 1 \text{ W}$ input field at $1.56 \mu\text{m}$. Sub-combs form and merge as laser-resonator detuning is decreased, as in Figure 5.11. (b) Radiofrequency noise spectrum of same field, recorded by direct detection on a fast photodiode (JDSU RX10) and analyzed with a digital spectrum analyzer (Signal Hound). Elevated noise occurring as subcombs merge is evidence that the comb state is not coherent.

with phase matching for the far-detuned pump [103]). At smaller detunings, interleaving of sub-combs results in a "full" comb with a characteristic sech-squared envelope, here with a 3 dB width of 1.4 THz, limited by the large magnitude of the resonator dispersion [157].

The sech-squared-shaped frequency comb observed for multiple devices is suggestive of a coherent (soliton) comb state [157]. To test this hypothesis, the comb light was analyzed for radio frequency (RF) intensity noise, its absence being a necessary (but not sufficient) condition for soliton formation. To measure RF intensity noise, the comb light was directed to a fast photodetector and the photosignal was analyzed with a spectrum analyzer (Signal Hound BB60C). Evolution of the RF noise spectrum of a 0.5 THz comb is shown in Figure 5.12. As the sub-combs merge, a large noise excess appears below 6 GHz (note that the persistent 5 GHz peak is intrinsic to the laser). Further increasing the pump power reduces the noise to a set of discrete frequencies. Similar behavior was observed in multiple devices. This can be taken as evidence that the combs we observe are not fully coherent [103]. A possible reason for the resistance to soliton formation is perturbation of the cavity dispersion due to mode splitting [158].

5.8 Frequency-doubled combs

In tandem with FWM, the $\chi^{(2)}$ polarizability of GaP enables frequency combs generated in the C-band (≈ 1550 nm) to be simultaneously doubled to visible wavelengths (≈ 780 nm). Frequency-doubled combs produced in tandem with the primary combs in Figure 5.11(a) are shown in Figure 5.11(b). As visible light is not efficiently coupled from ring to bus waveguide, for these measurements the output fiber was positioned above the ring. An auxiliary high-resolution visible OSA (Yogogawa AQ7373) was used, revealing as many as 50 comb lines (limited by the OSA sensitivity) for the smallest laser-cavity detuning .

5.9 Raman combs

It is well known that SRS competes with FWM in waveguides with normal or weak dispersion [98]. We observe this effect in waveguide resonators which are cladded in silica, which reduces D_2 by an order of magnitude and displaces the center of the anomalous window to 1650 nm. FWM and SRS in a 100-GHz cladded racetrack resonator with $Q = 2 \times 10^5$ is shown in Figure 5.13(a),(b). For a subset of modes, broadband (> 200 nm) frequency combs centered at the pump wavelength are generated by FWM. For others, FWM is preceded by efficient Raman lasing (20 dBm threshold, 10% conversion efficiency) with a Stokes frequency of 12 THz. The selectivity between FWM and SRS, and the absence of SRS in resonators with smaller radii, is likely due to the narrowness of the Raman transition, inherent to the crystalline material. Independent Raman spectroscopy of a GaP wafer (Figure 5.13(c)) confirms that the transition at 12 THz is less than 100 GHz wide.

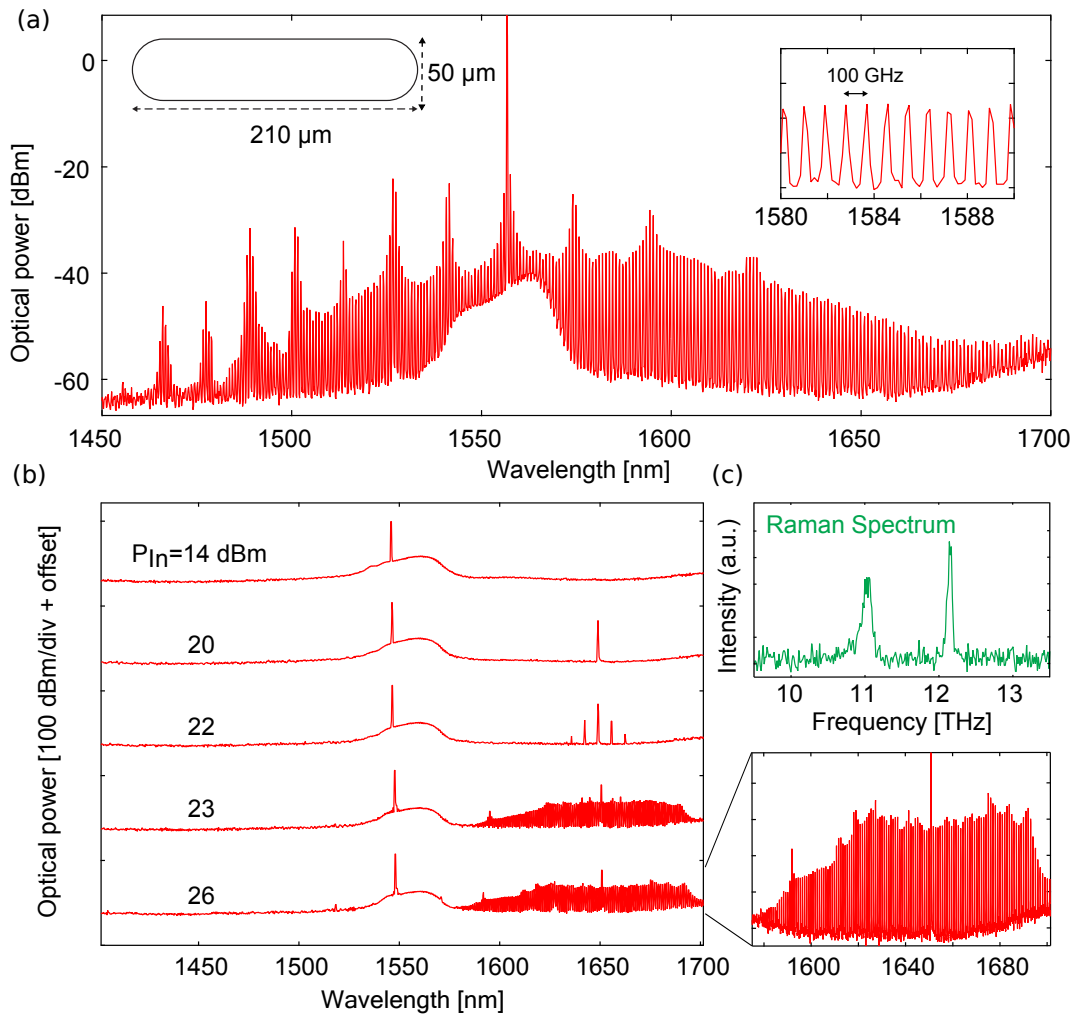


Figure 5.13 – Measurement of cladded racetrack resonators. (a) Broadband frequency comb generated in a resonator with an FSR of 100 GHz. (b) Raman-shifted frequency comb observed on a different mode of the same device. (c) Raman spectrum of the GaP wafer.

6 Design of GaP devices for optomechanics and microwave-to-optical transduction

In the first part of this section, the design of PhCs is optimized for a high optomechanical coupling rate and optical quality factor at the example of the design presented in [159]. In the second part, the piezoelectric actuation of a GaP PhC is studied with the goal of developing a microwave-to-optical transducer. Therefore the mechanical losses are minimized while maximizing the electromechanical coupling rate.

6.1 Design of photonic crystal cavities

The PhC consists of a freestanding GaP beam patterned with elliptical holes. The hole radii increase quadratically with hole number from the center of the device outward, followed by a set of identical holes, as illustrated in Figure 6.1(a). In this way, gradual mode matching is achieved between the center of the cavity and the Bragg-mirror outer portion of the structure. To attain a design which supports co-localized optical and mechanical modes with a high optomechanical coupling rate, numerical simulations with the finite-element solver COMSOL Multiphysics [116] were performed. The COBLYA algorithm [160], which is part of the NLOPT package [161], was employed varying those dimensions of the PhC indicated in Figure 6.1(b) for a GaP layer thickness of 300 nm and maximizing the fitness, defined as $F = g_0 \cdot Q_o$ (with Q_o capped at 1.5×10^6 to avoid unrealistic values) [162]. Both moving boundary and photoelastic contributions (see Equation 2.28 and Equation 2.29) to the optomechanical coupling rate were considered, where the long axis of the PhC is oriented in the [110] crystal direction. The best structure found (ellipse radii r_a and r_b and unit cell size a shown in Figure 6.1(a) and $w = 542$ nm) has an optical quality factor $Q_o > 1.4 \times 10^6$ and a mode volume of $0.0971 (\lambda_{\text{vac}}/n^3)$ at $\lambda_{\text{vac}} = 1493$ nm. The mechanical breathing mode, for which the displacement profile is shown in Figure 6.1(c), is calculated to have a frequency of $\Omega_m/2\pi = 2.84$ GHz, an effective mass of $m_{\text{eff}} = 8.6 \times 10^{-13}$ g, and an optomechanical coupling rate of $g_0/2\pi = 760$ kHz. The photoelastic contribution ($g_{\text{pe}}/2\pi = 725$ kHz) dominates the moving boundary contribution of the same sign ($g_{\text{mb}}/2\pi = 35$ kHz) because the motion-induced strain profile overlaps well with the regions of high electric field (compare Figure 6.1(d) and (e)).

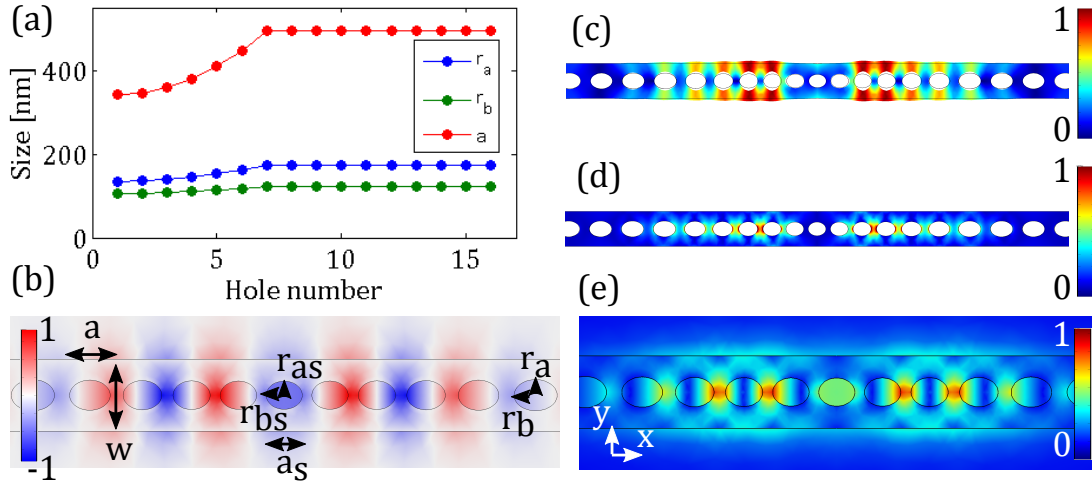


Figure 6.1 – Optimized device design as obtained from numerical finite-element simulations. (a) Dimensions of elliptical holes and unit cell. (b) y-component of the electric field. The overlaid outline of the device structure is labeled with the dimensions optimized in the finite-element simulations. (c) Displacement profile of the optimized mechanical breathing mode at 2.84 GHz. (d) Principal strain for the breathing mode. (e) Magnitude of the electric field. The images in (b) – (e) are all for a plane passing through the middle of the PhC and the color scales are normalized.

6.1.1 Photoelastic coefficients of GaP

For the calculation of the photoelastic contribution g_{pe} to the optomechanical coupling rate g_0 , the photoelastic coefficients need to be known. We use the following photoelastic coefficients: $p_{11} = -0.23$, $p_{12} = -0.13$ and $p_{44} = -0.10$ [90]. These coefficients were measured for a vacuum wavelength of $\lambda = 632.8$ nm. It should be remarked that there are further publications treating the photoelastic coefficients of GaP [163], but none presenting results at our design wavelength of $\lambda = 1550$ nm. Because the dispersion of the photoelastic effect for wavelengths far from the bandgap is expected to be small, these coefficients should provide a reasonable estimate of the magnitude of the photoelastic contribution to the optomechanical coupling. Nevertheless, to evaluate the validity of these numbers, we additionally considered published piezooptic coefficients [164], as these can be combined with elastic stiffness coefficients to calculate the photoelastic coefficients [90]. We extrapolated the model given in [164], which was used to analyze piezooptic data over the range $\lambda = 460$ to 1240 nm, and found that the predicted values $p_{12} - p_{11} = 0.10$ and $p_{44} = -0.08$ for $\lambda = 1550$ nm are consistent with the photoelastic coefficients in [90].

6.1.2 Simulation of design tolerances

To estimate the required fabrication accuracy, parameter sweeps in the COMSOL Multiphysics simulation are performed for the waveguide thickness, the ellipse radii and the waveguide width. The evaluated device properties are the optical and the mechanical resonance frequency, the optical quality factor, the optomechanical coupling rate and the fitness $F = g_0 \cdot Q_o$ (with Q_o capped at 1.5×10^6 to avoid unrealistic values). The results shown in Figure 6.2 indicate that the design is quite robust with respect to fabrication inaccuracies. The mechanical and the optical resonance frequency as well as the optical quality factor are affected most by the ellipse radii. Increasing the radii by 10 % (15 nm) leads to a drop of the quality factor by 70 %. Nevertheless, even then the simulated quality factor still exceeds one million. The optomechanical coupling rate g_0 exhibits a more complex dependence on the swept parameters; for the range of simulated values the variation is around ± 100 kHz.

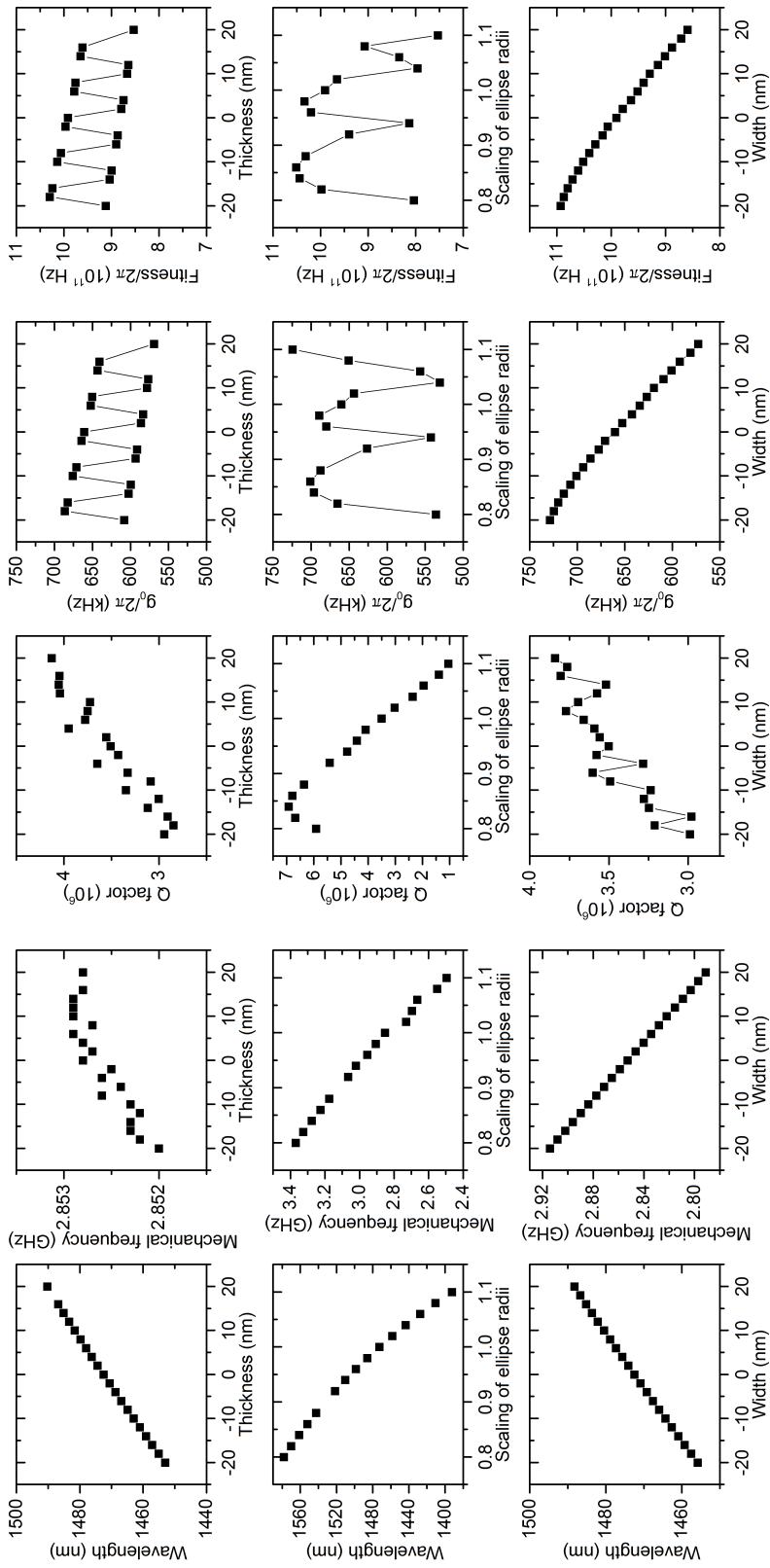


Figure 6.2 – Results of parameter sweeps performed in simulation of the optomechanical properties with the finite-element solver COMSOL Multiphysics, where the waveguide thickness, the hole radii and the waveguide width were varied. Here, scaling of the ellipse radii is relative to the radii of the optimal design as shown in Figure 6.1 (a).

6.2 Optimization of the piezoelectric coupling

To find a device design for efficient actuation of the mechanical mode via the piezoelectric effect, the electromechanical coupling strength g_{em} is evaluated for various device geometries with the finite element method solver COMSOL Multiphysics [116]. g_{em} is defined as described in subsection 2.6.4 by Equation 2.49. The implementation of a COMSOL simulation considering piezoelectric coupling is explained in Appendix D.

6.2.1 Conditions for efficient actuation

To piezoelectrically actuate a mechanical mode in a nanoscale photonic device, certain boundary conditions must be considered during device design. First of all, the design must be fabricable. For example achievable alignment accuracy, device dimensions and the number of required process steps must be considered. For the design optimization presented in this chapter, only designs which are fabricable in our opinion were considered.

Secondly, the crystal orientation with respect to the applied electric field must be chosen correctly. Thirdly, the electrodes must be sufficiently far from any optical field that absorption of the light is avoided. These last two points are discussed in more detail in the following sections.

6.2.1.1 Device orientation with respect to the GaP crystal lattice

For setting up the numerical simulation of the piezoelectric actuation of the mechanical mode, it is important to choose the correct device orientation with respect to the GaP crystal lattice. As shown in subsection 2.6.2.1, the piezoelectric effect in GaP causes a longitudinal shear motion. This means that the electric potential must be applied perpendicular to the mechanical motion, and the maximum displacement will be along the diagonals of the crystal lattice. As our goal is to actuate the breathing mode, the diagonals should be along the beam. Therefore we set the orientation of the coordinate system in the simulation to align our device with the [110] direction. For our GaP wafers, the [110] direction is parallel to the flat, as illustrated in Figure 6.3.

6.2.1.2 Distance between electrodes and optical mode

An important constraint for the positioning of the electrodes is the need to avoid absorption of light. We therefore perform simulations of the optical eigenmode and evaluate the quality factor for two conceptually different device designs: For one, the electrodes are located on one side of the cavity in direct contact with the GaP beam (see Figure 6.4(a)). For the other the electrodes are above and below the center of the cavity but separated by a gap from the beam (see Figure 6.4(c)). The resulting relation between optical quality factor and electrode position is shown in Figure 6.4(b) and Figure 6.4(d). For the first configuration, it can be seen, that at a

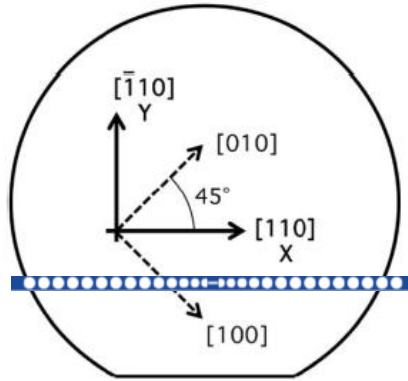


Figure 6.3 – Desired GaP device orientation for piezoelectric actuation with respect to the crystal lattice.

distance of approximately $4\ \mu\text{m}$ from the center, the electrodes no longer disturb the optical mode and the quality factor reaches the value expected for a device without electrodes. For the second configuration, the electrodes should be laterally separated from the beam by $0.7\ \mu\text{m}$ to preserve the optical quality factor. These results are taken into account for the further device optimization.

6.2.2 Configuration with electrodes on the photonic crystal cavity

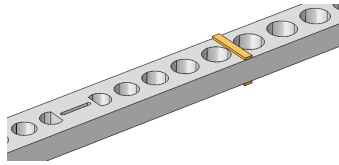
6.2.2.1 Initial device design

Fabrication of device with two electrodes in contact with the PhC is challenging as it requires one electrode be directly below the GaP beam. However, the simulations show that it might be worth the effort.

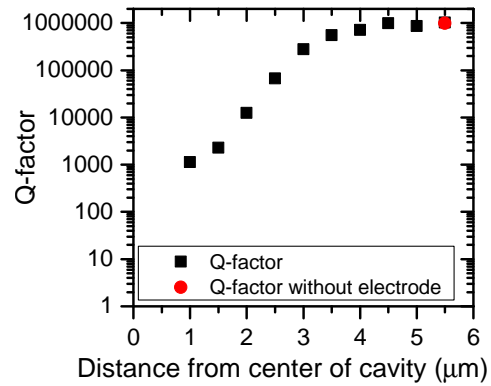
The initial device design at the beginning of our optimization process is shown in Figure 6.5(a). The electrodes are positioned at one end of the beam, one on top of it, the other below. In this model, we omit the feed line for the top electrode, as it is not expected to change the outcome of the simulations. In the following paragraph, we point out certain weaknesses of this device design to motivate the improvements presented in the following section.

In addition to achieving a high electromechanical coupling strength g_{em} , it is important to minimize the mechanical loss (compare with Figure 6.5(b)). It is evaluated by simulating the mechanical eigenmode. An example is shown in Figure 6.5(c) and Figure 6.5(d). The mechanical flux $\vec{P} = -\mathbf{T} \times \vec{v}$ out of the beam into the substrate is evaluated, where T is the stress tensor, and \vec{v} the velocity vector [165, p.166]. In Figure 6.5(b), the mechanical energy flux through the contact area between beam and pad as a function of the length of the beam on the pad has been calculated (the length between the pads is kept constant). It is obvious that **the larger the contact area between the beam and the substrate, the more mechanical energy leaks out of the beam and into the substrate**. This leakage should be avoided, as

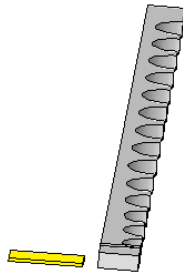
6.2. Optimization of the piezoelectric coupling



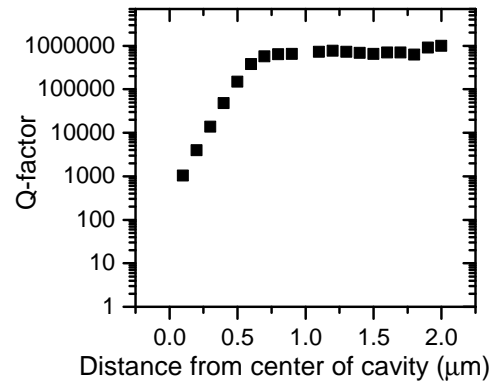
(a) Slotted photonic crystal cavity model made of Si with a top electrode of gold. The slot does not change the conclusion about the position of the electrodes for devices with a central hole, as used later for piezoelectric actuation.



(b) Simulated quality factor versus distance of the electrodes from the center of the cavity for the configuration with the electrodes in direct contact with the beam.



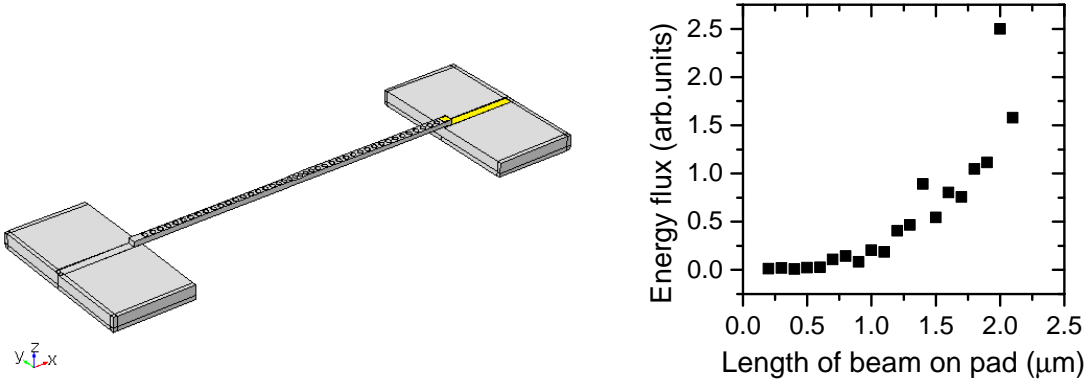
(c) Model of a PhC with a central hole. The first electrode is next to the beam, the second is not considered for this simulation, because it is at least $1\ \mu\text{m}$ below the beam.



(d) Simulated quality factor versus distance of the electrodes from the center of the cavity for the configuration with the electrodes separated laterally from the beam.

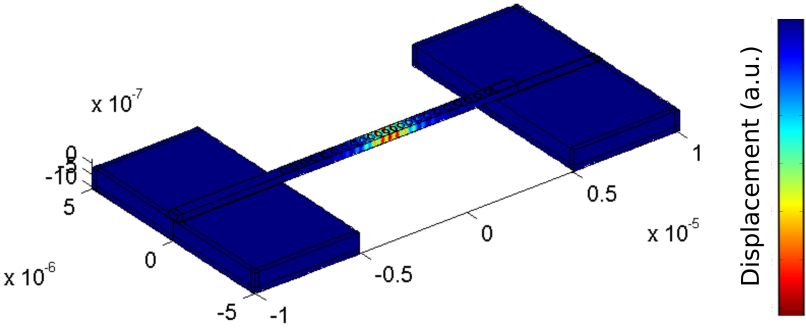
Figure 6.4 – Sweep of the electrode position for electrodes in contact with the beam and electrodes separated laterally from the beam and resulting change in quality factor.

Chapter 6. Design of GaP devices for optomechanics and microwave-to-optical transduction

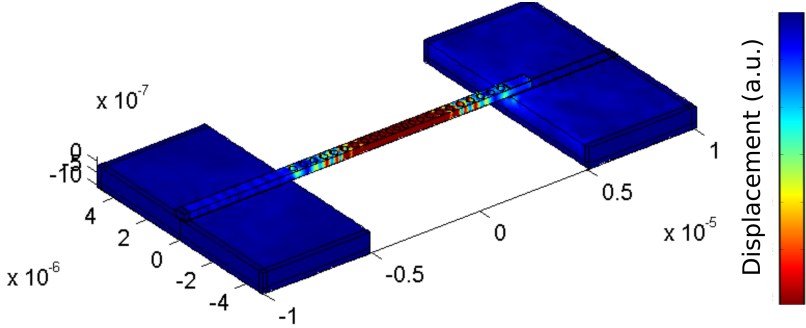


(a) Model for the simulation of actuation with the electrodes (yellow) at one end of the beam.

(b) Mechanical energy flux through the contact area between beam and pad on the right side versus contact area.



(c) Resonantly actuated breathing mode of the initial device design.



(d) Same figure as (c), but with the colorscale adjusted so that the leakage of mechanical energy into the substrate is apparent.

Figure 6.5 – Evaluation of the coupling strength for the device design where the electrodes are at one end of the GaP beam.

any energy loss channel makes the piezoelectric actuation inefficient and leads to a loss of information in signal transduction.

Another lesson which we have learned from the initial device design is that the **electrodes at the end of the beam lead to clamping of the mechanical mode**. Like for a jump rope, where the two ends are fixed by hands, antinodes will be fixed at the clamping points. As the electromechanical coupling strength is basically an overlap integral of the electric field and the mechanical displacement (compare Equation 2.49), this will reduce g_{em} .

Another potential challenge is that the piezoelectric actuation may drive modes other than the breathing mode. If the beam is rather long, a propagating wave is launched by the piezoelectric actuation that in the end couples to the breathing mode, which is a stationary mode. Much of the mechanical motion just runs through the center of the device and is reflected at the other end of the beam¹. The **necessity of coupling two mechanical modes to actually drive the breathing mode creates another loss channel**, as coupling between two modes is almost never perfect. Many of the prominent examples for piezoelectric actuation of an optomechanical system have this disadvantage [51, 54, 53]. Especially designs with interdigital transducers (IDTs) never get around coupling two mechanical modes, as the dimensions of IDTs lead to quite extended surface acoustic waves that eventually need to be coupled to a narrow photonic crystal waveguide. Reflection and transmission at the interface is governed by the ratio of the mechanical impedance, which is given by $Z_m = \rho v$, where ρ is the material density and v is the sound velocity [165, p.24]. This formula holds for the boundary between two half-spaces. For a boundary between two bars, the cross-sectional area A of the bar enters the formula: $Z_{m,b} = A\rho v$. A mechanical impedance mismatch will lead to reflections at the interfaces and therefore inefficient coupling. Possible positions for such an impedance mismatch for the PhCs are the contacts of the beam to the pads. It therefore is of interest to actuate the mechanical breathing mode directly on the freestanding part of beam instead of on the pad.

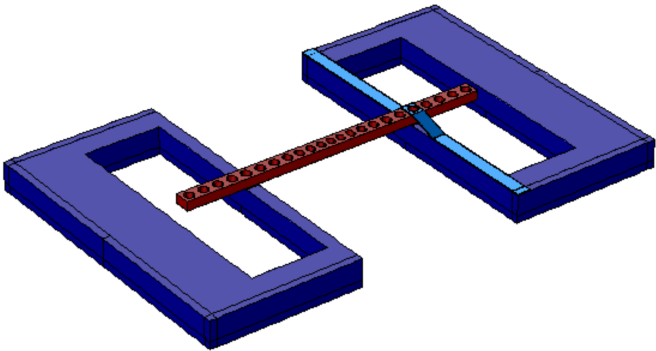
An optimized device design that avoids coupling of mechanical modes, clamping caused by the electrodes and mechanical energy loss at the contact area between beam and substrate is presented in the next section.

6.2.2.2 Optimized device design

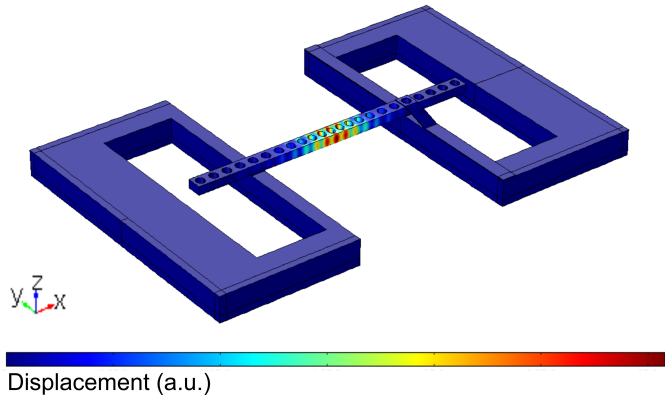
The optimized device design is shown in Figure 6.6(a). The breathing mode for this design is shown in Figure 6.6(b) and (c). Compared to the initial design, it was altered to have overhanging, freestanding ends of the photonic crystal beam. Furthermore the device was shortened to the length required to achieved a sufficiently high optical quality factor. The electrodes are no longer at the end but but have been moved towards the center of the beam. The reasons for these changes are explained in the following sections.

¹For this reason it is important to include the full beam in the simulations. In contrast, for optomechanical simulations, it is possible to take advantage of symmetry and simulate only one eighth of the device, which reduces calculation time (see Appendix C).

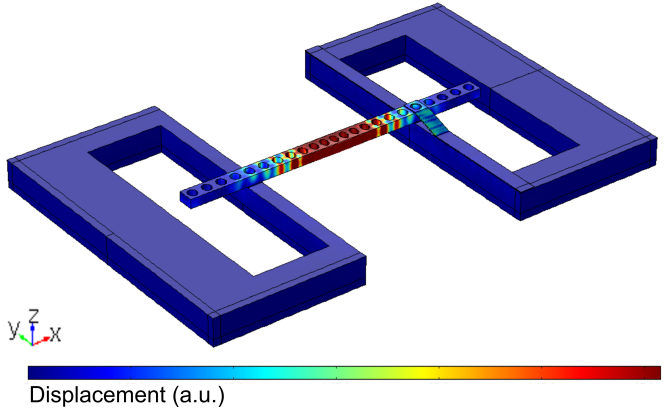
Chapter 6. Design of GaP devices for optomechanics and microwave-to-optical transduction



(a) Optimized device design with the GaP PhC (red), electrodes (light blue) and substrate (dark blue).



(b) Breathing mode of the optimized device design.



(c) Same mode as in (b) but with a color scale adjusted to show the displacement towards the end of the beam.

Figure 6.6 – Optimized device design for the piezoelectric actuation of the breathing mode of a GaP PhC.

Direct actuation of the breathing mode

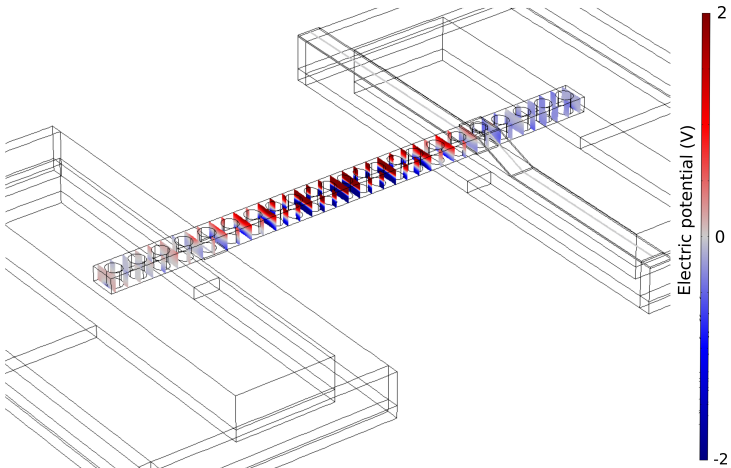
For direct actuation, the breathing mode must overlap with the externally applied electric field. Ideally, the region of overlap is the region of largest displacement, as this will maximize g_{em} (see subsection 2.6.4). This is not possible though, because the optical mode is also localized in the center of the structure and the electrodes would lead to absorption. From Figure 6.4(b) we know though that we can place the electrodes at a distance of $4\ \mu\text{m}$ from the center without disturbing the optical mode. Furthermore, we want to place the electrodes at an antinode of the mechanical mode in order to have the maximum possible displacement between the electrodes. These antinodes can be conveniently visualized by looking at the electric polarization of the GaP beam created by the displacement of the mechanical eigenmode (see Figure 6.7(a)). Then the position and dimensions of the electrodes can be adjusted, in order to match the electric polarization created by the displacement to the electric polarization of the externally applied electric field. Then the position and dimensions of the electrodes should match the position and extent of the antinodes. The optimized position of the electrodes and the mechanical displacement are shown in Figure 6.8.

Avoiding clamping with an overhang

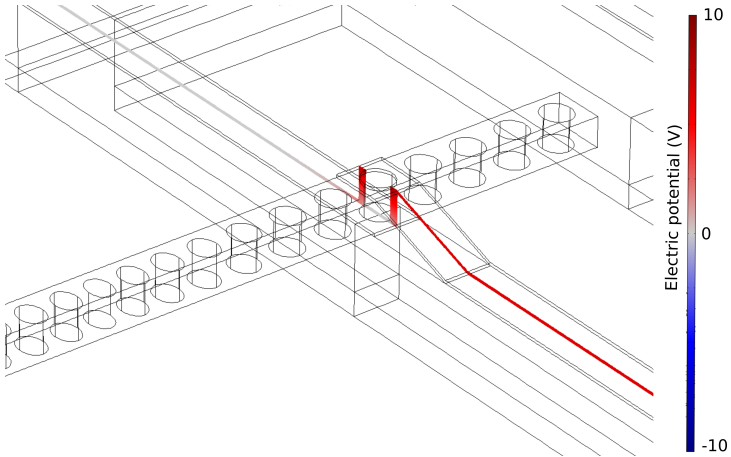
To appreciate the effect of the overhang, the design in Figure 6.9(a) can be compared to Figure 6.7(a). Both figures show the electric potential resulting from the direct piezoelectric effect for the mechanical breathing mode. In Figure 6.9(a), the electrode is so wide that it prohibits mechanical motion of the beam. In contrast in Figure 6.7(a), there is motion on both sides of the electrodes and also between the electrodes. The design Figure 6.7(a) therefore leads to a higher electromechanical coupling rate g_{em} . The dependence of g_{em} on the electrode width is shown in Figure 6.9(b).

Small anchoring points perpendicular to the plane of mechanical displacement

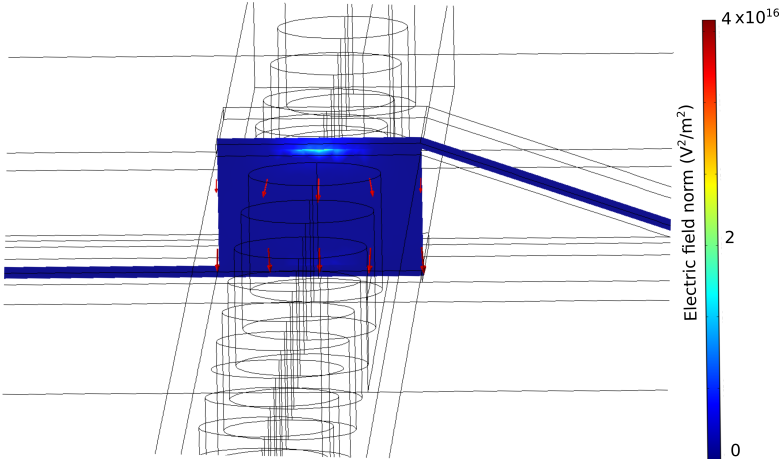
In the previous section, the outward energy flux for the initial device design has been shown to depend on the contact area between the beam and the substrate (see Figure 6.5(b)). The outward energy flux for the optimized devices design is displayed in Figure 6.10. Starting at an electrode width of approximately $5a$, where a is again the photonic crystal unit cell size, the outward energy flow increases. Therefore it is reasonable to keep the size of the electrodes and the contact area to the substrate small. We note that the very first data point in Figure 6.10 indicates energy flow in the opposite direction, i.e. into the device, which is unphysical and is attributed to a calculation inaccuracy. The effect of the anchoring direction is evident from a comparison to the device design of Bochmann et al. [51], which is shown in Figure 6.11. The device is made of AlN. The electrodes are on the bottom and top surfaces of the beam and extend over the pad, which is also made of AlN. The anchoring is not below the beam as in our design but at the end of the beam to the pad, which leads to losses from the mechanical motion propagating into the pad. The energy flux represented by the vectors in Figure 6.11 clearly shows the energy transport into the pad. As a comparison, Figure 6.12 shows the displacement and the energy flux in the optimized device design. The energy flux is mainly along the beam and not in the direction of the anchoring point below the beam, and thus energy loss into the



(a) Electric potential created by the direct piezoelectric effect due to the breathing mode's strain in the GaP beam.



(b) Externally applied electric potential, which should match the potential created by the mechanical eigenmode (see (a)).



(c) Electric field distribution (vectors) and electric field strength corresponding to the electric potential from (b).

Figure 6.7 – Matching the applied electric potential to the potential created by the direct piezoelectric effect.

6.2. Optimization of the piezoelectric coupling

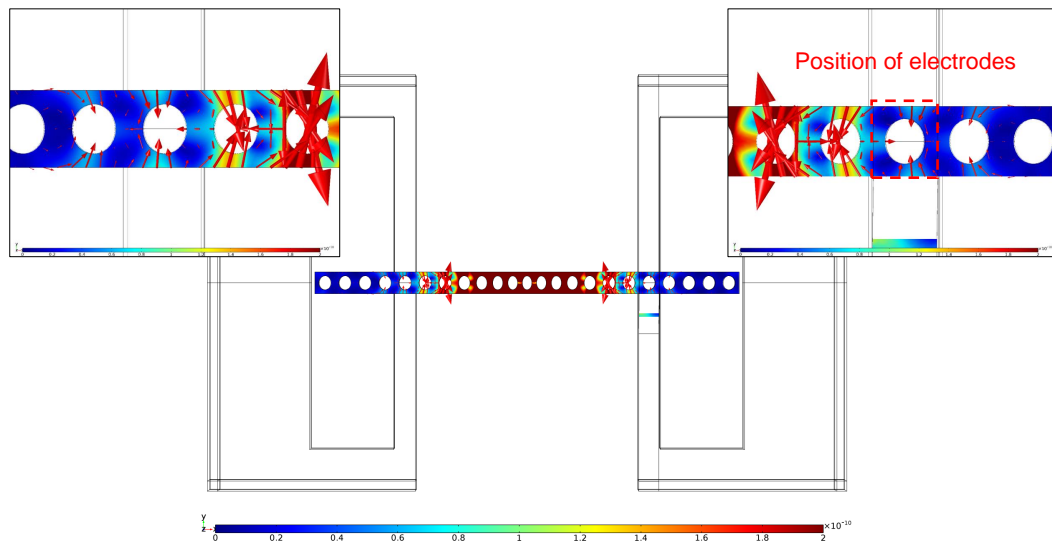
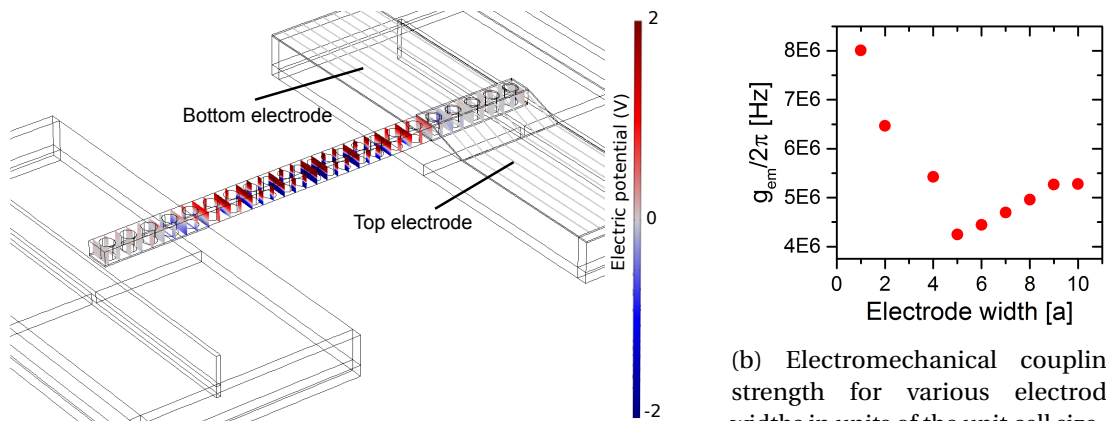


Figure 6.8 – Optimized electrode position at an antinode of the eigenmode. The electrodes are not explicitly shown, their position is marked with a red dashed box, where they are positioned above and below the beam. The color and the vectors denote the displacement of the beam.



(a) Mechanical eigenmode of a design with an electrode as wide as 5 holes of the PhC. The structure is clearly clamped in the region of the electrodes, as no electric potential resulting from mechanical displacement is visible.

(b) Electromechanical coupling strength for various electrode widths in units of the unit cell size a . The illustration in (a) corresponds to $a = 5$. For smaller electrodes, the coupling strength increases as the clamping is reduced.

Figure 6.9 – Effect of clamping by the electrodes on the electromechanical coupling strength.

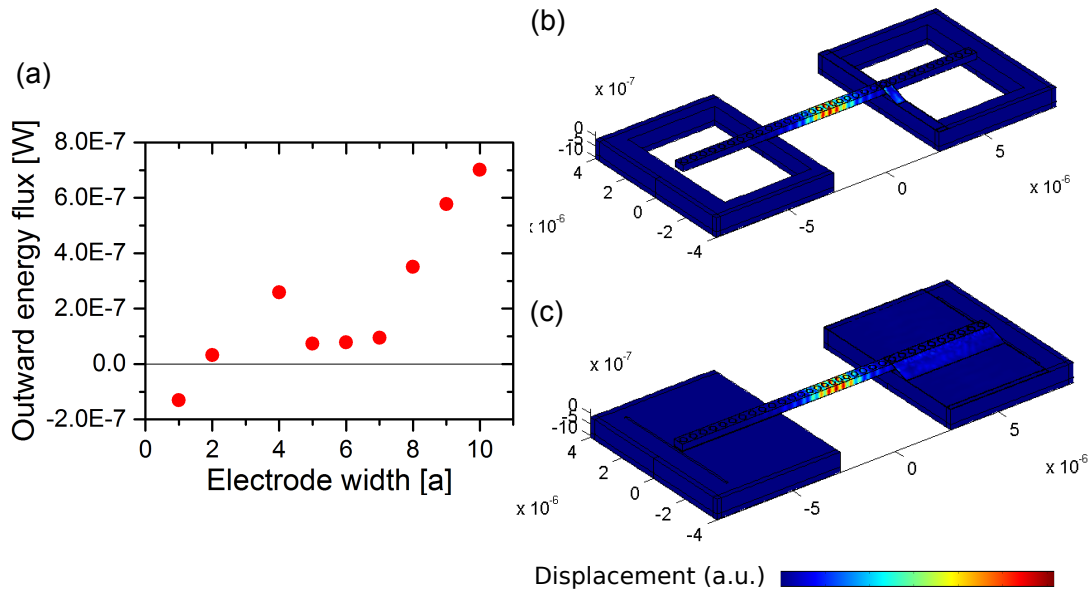


Figure 6.10 – (a) Outward energy flux depending on electrode width and therefore contact area to the substrate for the optimized device design. (b) Actuated mechanical mode for an electrode width of a and (c) for an electrode width of $10a$.

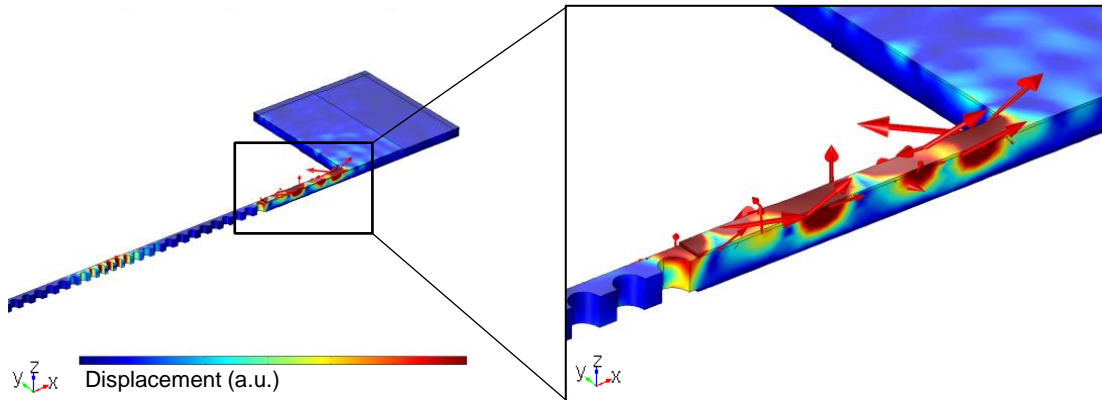


Figure 6.11 – Mechanical displacement and energy flux (vectors, cycle average) for the device design published by Bochmann et al. [51] with electrical actuation. The device is made of AlN. The electrodes are on the bottom and top surfaces of the beam and extend over the pad. The anchoring is not below the beam as in our design but at the end of the beam to the pad, which leads to losses from the mechanical motion propagating into the pad.

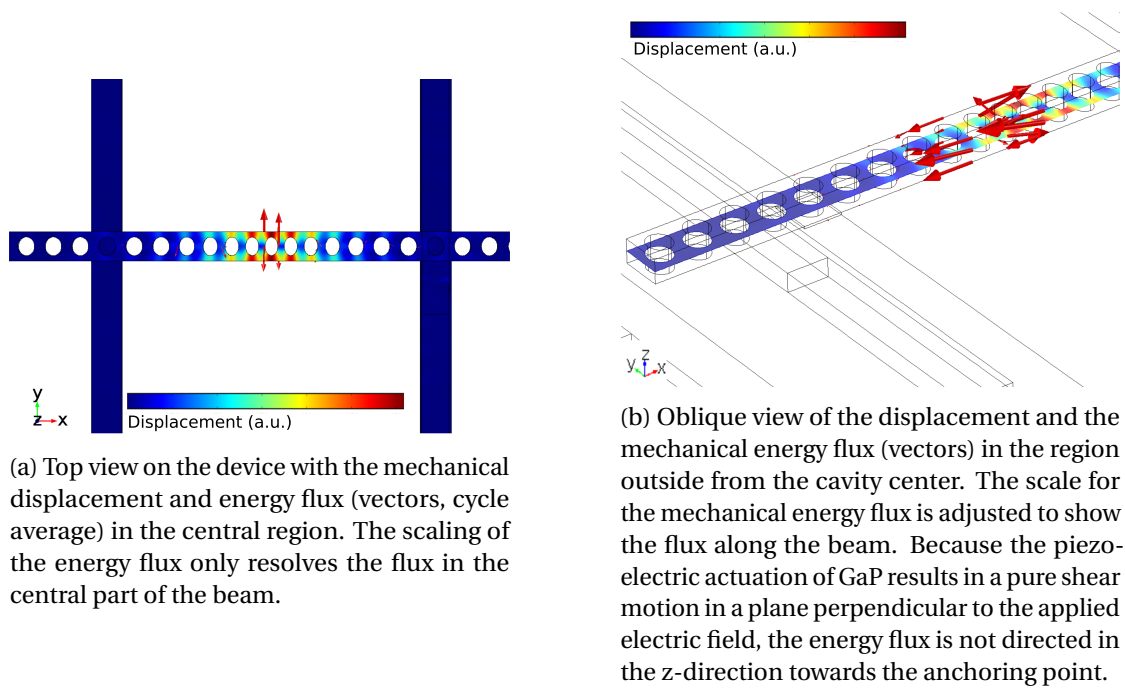


Figure 6.12 – Mechanical displacement and energy flux for the piezoelectrically actuated breathing mode of the optimized device design.

substrate is prevented. Keeping the mechanical energy flux mainly within a plane is possible for GaP PhCs because piezoelectric actuation of GaP produces only longitudinal shear motion, which is restricted to the plane perpendicular to the applied electric field. In contrast, with AlN, which has three different directions of piezoelectric actuation (longitudinal, transversal and transversal shear), a devices design that avoids actuation of mechanical modes in a certain direction is hardly possible.

Electromechanical coupling strength

The electromechanical coupling strength finally achieved with the optimized design is greater than 10 MHz, as can be seen in Figure 6.13. Here, g_{em} has been calculated as a function of electrode position which has been varied in steps of one unit cell width a . It turns out, that the closer the electrodes are to the center of the device, the larger g_{em} is, as one would expect from the displacement field being larger towards the center of the device. This is reasonable, as towards the center of the beam the the displacement field grows. However, the electrodes cannot be placed in the center of the beam, as the minimum possible distance is given by the onset of optical absorption by the metal electrodes (compare with subsection 6.2.1.2). There is a trade-off between further increasing the coupling strength g_{em} by moving the electrode closer to the center and sacrificing optical quality factor Q_o . As the cooperativities $C_{em} \propto g_{em}^2$ and $C_{om} \propto Q_o$, it might be beneficial to place the electrodes even closer to the center than the $4\mu\text{m}$ inferred in subsection 6.2.1.2, and so further increase g_{em} while decreasing Q_o .

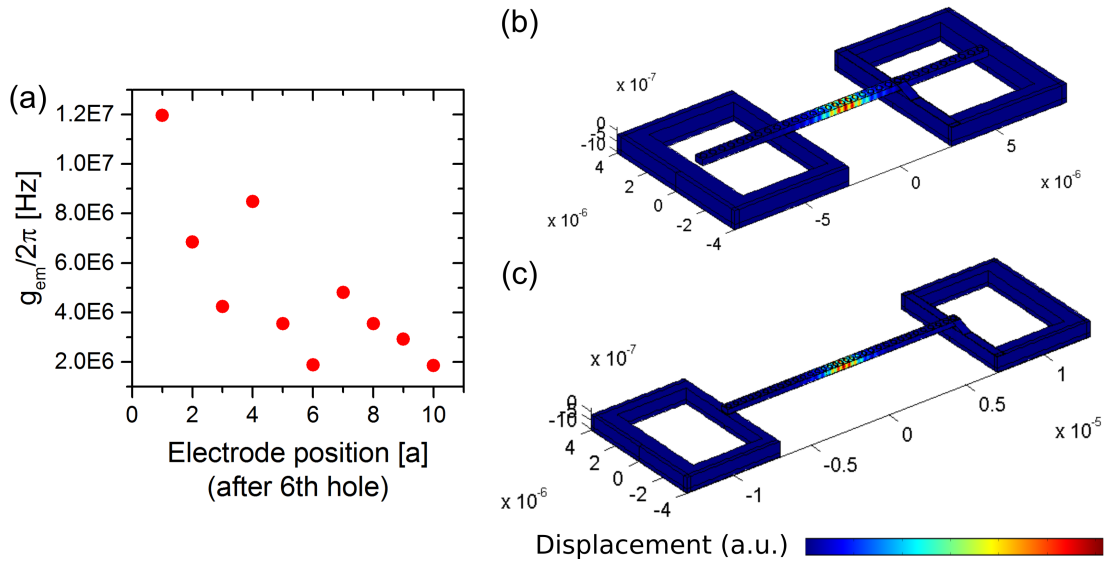


Figure 6.13 – (a) Electromechanical coupling strength depending on electrode position. The closer the electrodes are to the center of the cavity, the larger g_{em} is. (b) Actuated mode for the position a and (c) for the position $10a$, where a is the unit cell width.

6.2.3 Configuration with electrodes separated laterally from the photonic crystal cavity

Piezoelectric actuation of the mechanical breathing mode, requires an electric field component perpendicular to the surface of the GaP layer. As seen in the previous chapter, this configuration can be achieved by placing electrodes above and below the beam. Another possible configuration is a pair of electrodes where one is displaced to the side from the center of the beam and the other is below the beam in the trench created for the release of the PhC (see Figure 6.14(a)). A similar configuration has been used to piezoelectrically actuate disc resonators made of AlN [55] and theoretically discussed for the actuation of an AlN beam by Zou et al. [75].

We have simulated a related design for the actuation of a GaP PhC. A cross-section through the device at a position 480 nm from the center of the beam is shown in Figure 6.14(b). Two electrodes with a thickness of 30 nm and a width of 1 μm are positioned on the underlying SiO_2 , one electrode 1 μm to the side and the other electrode 1 μm below the GaP beam. The distances between the electrodes and the PhC are chosen to provide an easily fabricated configuration, but other choices may be possible. With the model configuration we can nevertheless obtain a first estimate of the achievable electromechanical coupling strength. The mechanical mode of interest is the breathing mode, which in this case has a frequency of 3.55 GHz.

We calculate the electromechanical coupling rate g_{em} as described in subsection 2.6.4 for various distances of the bottom electrode to the PhC. The change of the electrode distance changes the direction of the electric field and therefore g_{em} as shown in Figure 6.15(a). The coupling strength varies between 5 and 25 MHz. The mechanical displacements correspond-

6.2. Optimization of the piezoelectric coupling

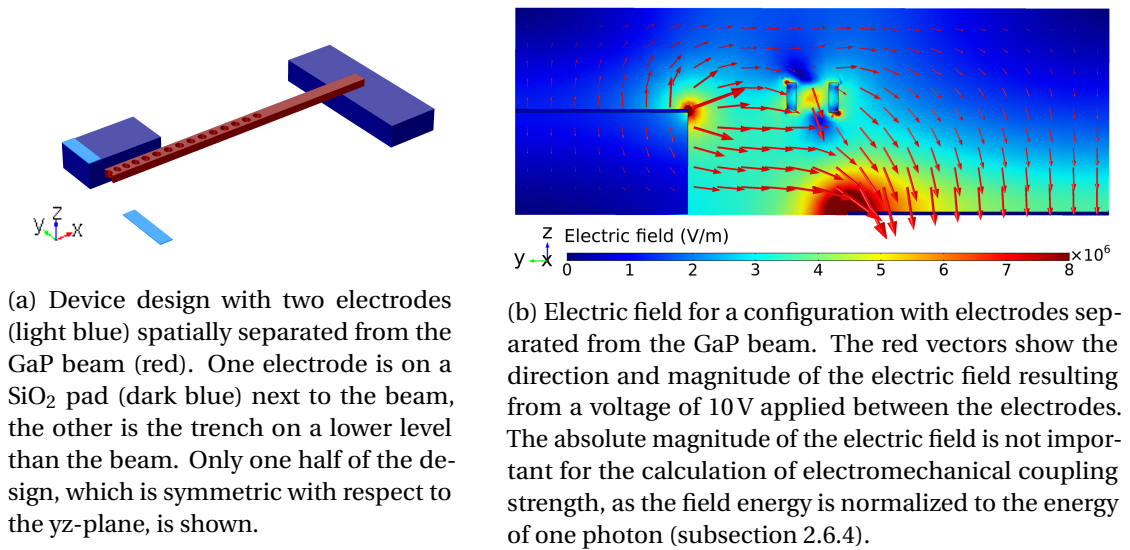


Figure 6.14 – Electric field for a configuration with electrodes separated laterally from the PhC: One electrode is located below the beam and the other one next to it.

ing to the closest and the furthest simulated distance are shown in Figure 6.15 (b) and (c). Surprisingly, the achievable coupling strength is even higher than that for the design investigated in subsection 6.2.2 despite the fact that much of the electric field is dropped in air and therefore the overlap of the mechanical and electrical modes is not particularly high. Also the direction of the electric field is not well aligned with the z-axis, the direction of electric polarization resulting from the mechanical eigenmode due to the direct piezoelectric effect. The order of magnitude of g_{em} for the configuration with separated electrodes matches however the results obtained for a similar design in Zou et al. [75]. The configuration with laterally separated electrodes still has to be further investigated. Due to the angle of the electric field, other out-of-plane mechanical modes might be excited, which then would be in competition with the desired breathing mode.

6.2.4 Expected performance of a microwave-to-optical transducer

The figures of merit for microwave-to-optical transduction are introduced in section 2.7 and are evaluated for the developed designs in this paragraph. The simulated electromechanical coupling strength $g_{em} > 10$ MHz is for both designs far greater than the optomechanical coupling strength and also the product of the linewidths involved in the electromechanical transduction is smaller than those of the optomechanical transduction, so the electromechanical cooperativity C_{em} will be greater than the optomechanical cooperativity C_{om} . Here, for the electromechanical coupling the single-photon cooperativity $C_{0,em}$ is decisive, because for the resonant transduction there is no pump involved and $n_{cav} = 1$. For the optomechanical transduction the multiphoton cooperativity C_{om} is considered. As the efficiency of the microwave-to-optical transduction is basically limited by the lower of the two cooperativities

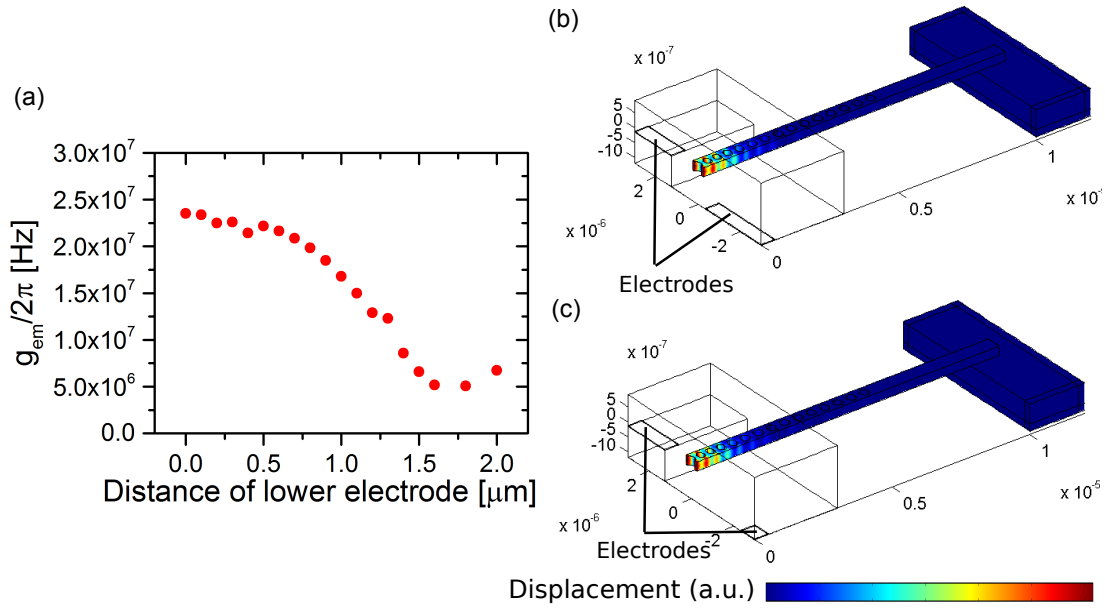


Figure 6.15 – Electromechanical coupling strength depending on lower electrode distance. (a) Electromechanical coupling strength depending on the distance of the lower electrode from the beam. The closer the electrode is to the PhC, the larger g_{em} is. (b) Actuated mode for the electrode directly below the beam and (c) for the an electrode distance of 2 μm .

(see Equation 2.54), the piezoelectric actuation of the mechanical mode is not expected to be the limiting factor. Instead, the optomechanical transduction and the quality factors of the optical and mechanical mode should be the focus of improvement. The expected device performance is summarized in Table 6.1. The value for g_{em} stems from simulations. The value for the quality factor Q_e and the linewidth κ_e of the superconducting resonator have been achieved for devices fabricated in the BRNC, and also in published works on the topic [166]. Only Q_m is an estimate based on the performance of Si devices [167], as the low-temperature behavior of GaP mechanical resonators has not yet been measured in vacuum at cryogenic temperatures. Both parts of the transducer, the optomechanical and the electromechanical, should be able to achieve cooperativities above 1. The next step is therefore the fabrication of photonic crystal nanobeam cavities with integrated electrodes and the experimental testing of the piezoelectric actuation.

6.2. Optimization of the piezoelectric coupling

Parameter	Expected performance
$g_{em}/2\pi$ [Hz]	$> 10^7$
$g_{om}/2\pi$ [Hz]	$\sim 10^6$
Q_o	10^5
Q_e	$> 10^5$
Q_m	10^4
$\Omega_m/2\pi$ [Hz]	$\sim 3 \times 10^9$
$\omega_e/2\pi$ [Hz]	$= \Omega_m$
$\omega_o/2\pi$ [Hz]	$\sim 200 \times 10^{12}$
$\kappa_m/2\pi$ [Hz]	3×10^5
$\kappa_e/2\pi$ [Hz]	3×10^4
$\kappa_o/2\pi$ [Hz]	2×10^9
$C_{0,em}$	4.4×10^4
$C_{0,om}$	6.7×10^{-3}
n_{cav}	10^4
C_{om}	67

Table 6.1 – Expected performance of the microwave-to-optical transduction.

7 Optomechanics with one-dimensional GaP photonic crystal cavities

7.1 Experimental setup

The measurement apparatus used for optical and mechanical characterization of our PhCs is presented in Figure 7.1. For ease of interrogation, the PhCs are connected to waveguides terminated with grating couplers designed for a nominal input/output coupling angle 10° from vertical (see section 4.2 and section 5.2). Continuous-wave, TE-polarized, infrared light from a tunable external cavity laser (Photonetics Tunics-Plus) is directed through a cleaved single-mode optical fiber into the input grating coupler. Light transmitted through the device is gathered with a second single-mode fiber positioned over the output grating coupler. A portion of the collected light is split off with a fiber beam splitter (FBS) to a power meter (EXFO IQ 1600) to monitor the power level. For measurements of the thermomechanical radio frequency spectrum, the transmitted light is amplified by an erbium-doped fiber amplifier (EDFA, JDS Uniphase MAP Amplifier) followed by a bandpass filter (BPF, JDS Uniphase TB3) and sent to an optical receiver consisting of a fast photodiode with a built-in transimpedance amplifier (JDS Uniphase MAP Receiver RX10). The transduced photocurrent from the photodiode is evaluated with an electrical spectrum analyzer (HP8563A). For measurements of optomechanically induced absorption and transparency, the laser output was phase modulated with an electro-optic modulator (EOM, Thorlabs 10 GHz LN65S-FC) before entering the device, for which a frequency generator (HP 8341A Synthesized Sweeper 0.01 - 20 GHz) delivered the radio frequency input signal, and a vector network analyzer (HP8510B) monitored the frequency dependent response of the device.

7.2 Optical spectroscopy

By fitting a Lorentzian function to the transmission spectrum of a PhC, we obtain the optical quality factor (see subsection 2.4.1). The highest quality factor measured, $Q_o = 111000 \pm 2000$, is for a device with 12 holes on each side (Figure 7.2(a)) and is close to the intrinsic quality factor Q_i , as is apparent from Figure 7.2(b). With increasing number of holes, the coupling

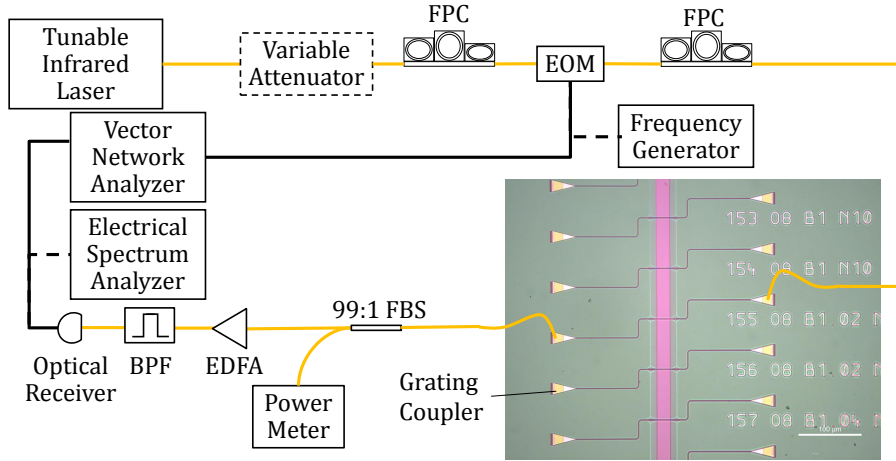


Figure 7.1 – Schematic of the measurement apparatus. FPC denotes a fiber polarization controller. In the optical microscope image, the pink stripe is where $\approx 1.1 \mu\text{m}$ of the underlying SiO_2 layer has been removed by wet etching to release the PhCs.

rate to the attached waveguides decreases, the external quality factor Q_e becomes larger than Q_i , and the measured quality factor $Q = (1/Q_e + 1/Q_i)^{-1}$ approaches Q_i . The typical power dependence of the transmission spectrum of a PhC is shown in Figure 7.2(c), in this case for a device with 11 holes on each side. With increasing intracavity photon number, the optical resonance shifts to lower frequency (Figure 7.2(e)) due to both the thermo-optic and Kerr effect, where the former most likely dominates [89]. For many experiments in optomechanics, it is desirable to reduce this shift as much as possible, as it can severely constrain the ability to independently control laser detuning with respect to the cavity resonance for high intracavity energy levels. Heating due to absorption also limits the lowest attainable temperature in cryogenic experiments. A plot of the quality factors (Figure 7.2(d)) obtained from these same power-dependent spectra reveals an increase with input power, implying a decrease in the internal optical losses. Two general regimes are observed, one at the lowest powers where the quality factor changes rapidly with increasing power, and a second in which the quality factor increases gradually and eventually plateaus. A similar increase in quality factor with input power has been reported previously for GaP microdisks [17] and tentatively attributed to the presence of saturable absorbers. For TPA, as occurs with silicon [168], the opposite, namely a decrease of quality factor with increasing power is expected.

The absence of TPA makes us interested in comparing the absorption losses of GaP devices to devices of materials showing TPA, for example silicon [97]. Therefore in order to obtain a more quantitative measure of the thermo-optic effect, we analyze the dependence of the optical resonance frequency on the power dissipated in the cavity $P_d = \kappa_i U_{\text{cav}}$ (Figure 7.2(e)) [101, 102], the derivative of which we define as the thermal susceptibility $\chi_{\text{th}} = \frac{\partial \omega}{\partial P_d}$ (see subsection 2.4.2.1).

Taking a linear fit of the higher power portion of the plot of Figure 7.2(e), we estimate $\chi_{\text{th}}/2\pi = -0.9 \text{ THz/mW}$ for this particular device, the magnitude of which we consider an

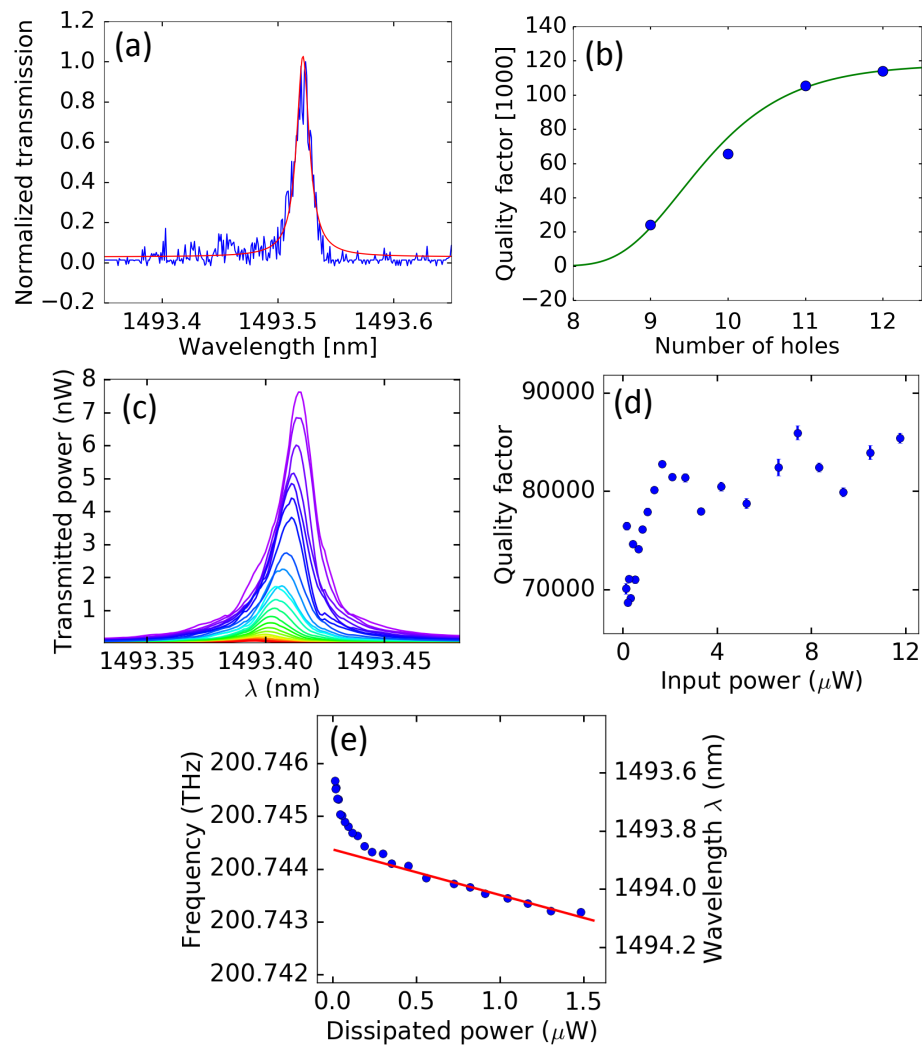


Figure 7.2 – Analysis of optical transmission measurements. (a) Spectrum of a PhC with the highest measured optical quality factor $Q_o = 1.11(2) \times 10^5$. (b) Dependence of the measured Q_o on the number of holes on each side of the PhC. The green line is a guide to the eye. (c) Transmission spectra of a device with 11 holes on each side for input powers ranging from $0.079 \mu\text{W}$ to $7.7 \mu\text{W}$. (d) Increase of the optical quality factor with input power. (e) Dependence of the resonance frequency on dissipated power P_d .

upper limit given that the quality factor has not yet plateaued at these power levels. Using Equation 2.18, we can calculate the fraction of the intrinsic loss rate of the cavity that comes from absorption and leads to heating of the device κ_{abs} .

We therefore determine $\beta(\omega_o) = -0.00683$ THz/K directly by measuring the optical resonance frequency as a function of sample temperature at low intensity, where there is no significant thermo-optic shift due to the transmitted laser light. Specifically, the temperature of the aluminum block on which the sample chip was mounted was varied with a Peltier element and measured with an integrated thermistor. The results are shown in Figure 7.3 for the resonance at $\lambda_{\text{vac}}=1494$ nm of the device used for the measurements shown in Figure 7.2. A linear fit of the data gives a slope of -0.00683 THz/K.

We then have $\kappa_{\text{abs}}R_{\text{th}} = 0.28$ THz K/mW. Comparable devices made of silicon [18] have $\kappa_{\text{abs}}R_{\text{th}} = 1.2$ to 1.6 THz K/mW. The thermal resistance R_{th} of a PhC made of GaP relative to that of a PhC made of Si can be estimated by considering the thermal resistivity k of the respective materials and the cross-sectional area $A = w \cdot h$ of the beams, where w and h are the beam width and height, respectively. For the GaP device, $w = 542$ nm, $h = 300$ nm and $k_{\text{GaP}} = 110$ WK/m, whereas for the Si devices considered, $w = 550$ nm, $h = 220$ nm and $k_{\text{Si}} = 150$ WK/m. For a simple rectangular beam of length l , $R_{\text{th}} = l/kA$, which gives a ratio of 1.0 for the values of R_{th} for the Si beam versus the GaP beam assuming the same length. The presence of holes in the PhC of course alters the thermal conductivity, but given the closely related designs and similar beam lengths, we expect R_{th} for the GaP and Si devices to be nearly the same. We conclude that κ_{abs} is at least a factor of 5 smaller in the GaP PhCs for power levels where the optical quality factor has leveled off.

Making use of this result and Equation 2.19, we can as well estimate the frequency shift $\partial\omega$ caused by the absorbed light. For the silicon devices used in this comparison, $\beta(\omega_o) = -0.0070$ to -0.0076 THz/K, differing by only about 10% from $\beta(\omega_o)$ for the GaP device. Assuming again that R_{th} is also similar for the Si and GaP devices, the resonance frequency shift $\partial\omega$ for a given intracavity energy U_{cav} should also be at least a factor of 5 smaller in the GaP device. The above conclusions hold when the circulating power in the cavity is sufficient for the quality factor to have reached a steady value. For the GaP device examined here, this corresponds to less than a thousand intracavity photons, well below the level used in many optomechanics experiments. We also note that the same general behavior as shown in Figure 7.2(c) – (e) was observed for several other devices, i.e. the data shown is representative. Measurement in a nitrogen atmosphere did not have an effect.

7.3 Thermomechanical radio frequency spectrum

Thermal fluctuations of the mechanical modes of the GaP PhC lead to phase modulation of the transmitted light. The resulting thermomechanical radio frequency spectrum is obtained by evaluating the transduced photocurrent of the fast photodiode used to detect the light with an electrical spectrum analyzer. An example is shown in Figure 7.4 for a device with 10 holes on each side. The various mechanical eigenmodes of the PhC produce Lorentzian-shaped

7.4. Optomechanical vacuum coupling rate

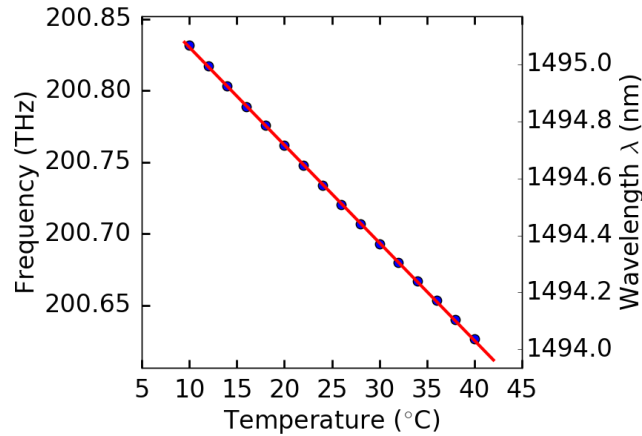


Figure 7.3 – Optical resonance frequency as a function of sample temperature. The shift is due to a combination of the thermo-refractive effect and thermal expansion. A linear fit (red line) gives a slope of -0.00683 THz/K.

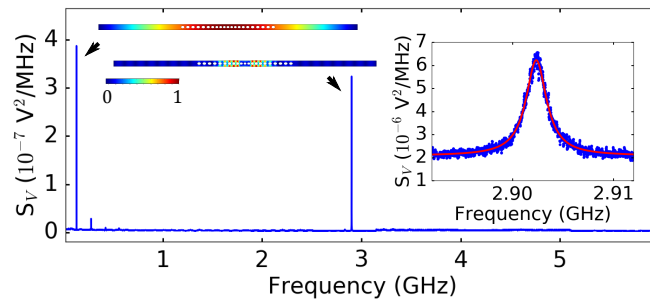


Figure 7.4 – Power spectral density of a device with 10 holes on each side. The two dominant modes are the accordion mode at 130 MHz and the breathing mode at 2.902 GHz; their simulated displacement profile is depicted next to the respective resonance, where the color scale gives the normalized displacement. An expanded view of the breathing mode resonance is shown in the inset.

resonances, where the amplitude is proportional to the optomechanical vacuum coupling rate g_0 . The breathing mode for which the device design was optimized is found at 2.902 GHz. Another strongly coupled mode is observed at 130 MHz and is assigned on the basis of the numerical simulations to an accordion mode, in which the nanobeam stretches longitudinally such that all holes are displaced symmetrically with respect to the center of the device (see the color-coded images in Figure 7.4).

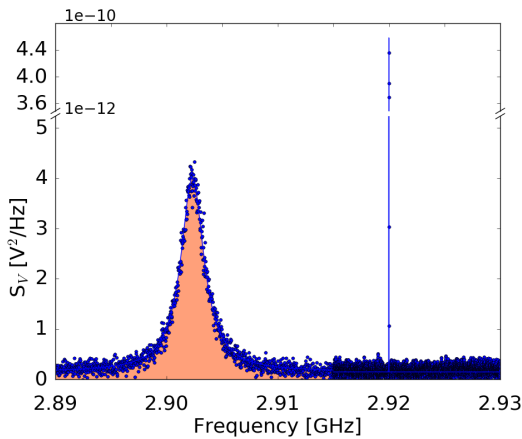
7.4 Optomechanical vacuum coupling rate

To quantify the optomechanical vacuum coupling rate g_0 , two independent measurements are performed. In the first, a calibration-tone measurement, a thermomechanical radio frequency spectrum is recorded while phase modulating the laser light entering the optical

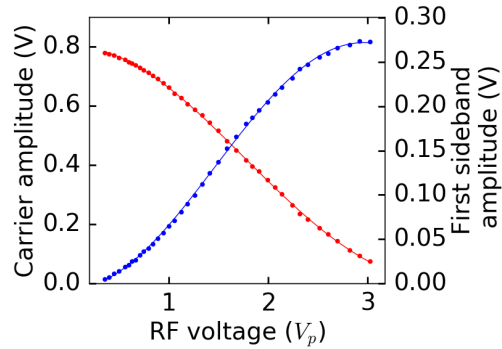
cavity at a frequency near that of the mechanical resonance and with a known modulation depth. Comparing the area under the peak corresponding to the mechanical breathing mode with that under the calibration tone peak (see subsection 2.5.2) gives a coupling rate of $g_0/2\pi = 370 \pm 40$ kHz [111]. The according measurement is shown in Figure 7.5(a).

To ascertain the modulation depth $\beta = V_p/V_\pi \cdot \pi$ of the calibration tone, where V_p is the amplitude of the radio frequency voltage applied to the phase modulator, the half-wave voltage V_π of the modulator must be known. Measurement of V_π is accomplished by setting the radio frequency drive signal to 2.9 GHz and varying V_p . The light transmitted through the phase modulator is guided to a scanning Fabry-Pérot interferometer (Thorlabs SA210-12B), with which the carrier and the sideband signals are resolved. The carrier amplitude as a function of V_p can be described as $A_0 = a(J_0(\pi V_p/V_\pi))^2$ and the first sideband amplitude as $A_1 = a(J_1(\pi V_p/V_\pi))^2$, where J_0 and J_1 are Bessel functions of the first kind and a is a scaling factor. A fit of these functions to the measured carrier and sideband amplitudes (see Figure 7.5(b)) yields a half-wave voltage $V_\pi = 5.09 \pm 0.02$ V, in agreement with the vendor specifications ($4.5 \text{ V} < V_\pi < 6.5 \text{ V}$ for 3 GHz).

The second method exploits optomechanically induced absorption (OMIA) [169, 72]. The



(a) Power spectral density of the mechanical resonance (left peak) and the calibration tone (right peak). An optomechanical vacuum coupling rate of $g_0/2\pi = 370 \pm 40$ kHz is inferred.



(b) Measured amplitude of the carrier (red dots) and first-order sidebands (blue dots) created by modulation of the laser light at 1550 nm with a phase modulator driven at 2.9 GHz and amplitude V_p . The lines are fits to the data and give a half-wave voltage $V_\pi = 5.09 \pm 0.02$ V.

Figure 7.5 – Calibration tone measurement to determine the optomechanical vacuum coupling rate.

measurement is explained in subsection 2.5.3. The expected transmission is evaluated by routing the transduced photocurrent of the photodiode to the response port of the VNA and performing an S_{21} measurement. A coarse sweep of the modulation frequency over 10 GHz maps out the optical resonance of the PhC, as shown in Figure 7.6(a) for the same device as used for the calibration-tone measurement above. A finer sweep around the maximum of the S_{21} signal (Figure 7.6(b)) reveals an enhanced transmission window caused by constructive interference of the light mechanically modulated in the cavity — in this case at $\Omega_m/2\pi =$

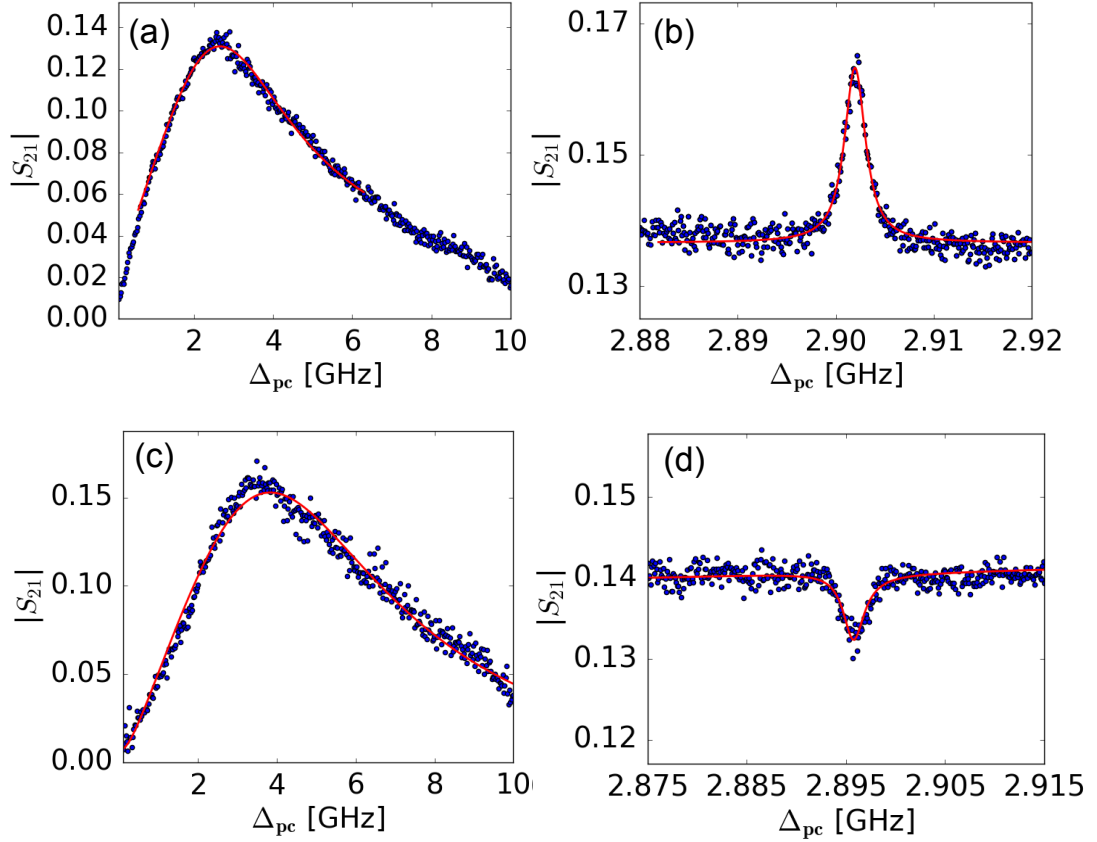


Figure 7.6 – Measured VNA traces (blue dots) fitted as explained in subsection 2.5.3 (red lines). (a) and (b) Measurement with the laser control frequency blue-detuned from the optical resonance. OMIA appears in (b) as an enhanced transmission peak at the mechanical resonance frequency Ω_m on top of the broader optical resonance delineated in (a). (c) and (d) Measurement with the laser control frequency red-detuned from the optical resonance. OMIT causes a dip (d) in the transmission at the mechanical resonance frequency on top of the optical resonance in (c).

2.902 GHz — and the probe and control fields at frequency-matched detuning. A fit of the expected transmission profile (see Equation 2.33) allows one to infer $g = \sqrt{n_{\text{cav}}} \cdot g_0$ [162, 112]. With knowledge of the optical power entering and leaving the grating couplers, the average grating-coupler losses, and the laser-cavity detuning Δ_{oc} , the intracavity photon number n_{cav} can be estimated (see Equation 2.17). For the measurement shown in Figure 7.6(a) and (b), $n_{\text{cav}} = 2100 \pm 700$. Averaging over several measurements with different detunings Δ_{oc} gives $g_0/2\pi = 680 \pm 320$ kHz, in agreement with the result obtained in the calibration-tone experiment, albeit with greater uncertainty.

Because the calibration-tone method does not require knowledge of the intracavity photon number, which is difficult to precisely estimate in our experiment, we believe it provides a more reliable value for g_0 than the OMIA technique. The measured coupling rate differs

from the simulated value by approximately a factor of two. This may be due to fabrication inaccuracies (see subsection 6.1.2) or an incorrect estimate of the photoelastic coefficients (see subsection 6.1.1).

7.5 Optomechanically induced transparency

Measurement of optomechanically induced transparency (OMIT) is analogous to measurement of OMIA, only the laser-cavity detuning is chosen instead to be $\Delta_{oc} = -\Omega_m$, namely red-detuned. Now the combined probe and control fields interfere destructively with the mechanically modulated laser light. This leads to decreased transmission at $\Delta_{pc} = \Omega_m$ (Figure 7.6(c) and (d)). In order to carry out this measurement, the input power must be set sufficiently low that the thermo-optic shift is small and the red-detuning near $\Delta_{oc} = -\Omega_m$ is stable. This is usually not possible at room temperature with silicon PhCs, for example, because of the large thermo-optic effect. OMIT has however been shown at room temperature for PhCs made of diamond [170] and Si_3N_4 [171], which like GaP have a wide electronic bandgap and therefore weak TPA. Diamond has the additional advantage of high thermal conductivity further mitigating heating [172]. When performing the OMIT measurement, the optical quality factor of the device of interest had degraded, presumably due to some photo-induced reaction. Because the device was no longer in the resolved-sideband regime, the laser input power was lower, and $|\Delta_{oc}| > \Omega_m$, the OMIT dip is quite shallow compared to the magnitude of the OMIA peak (see Figure 7.6).

7.6 Dynamical backaction

If the PhC is driven off resonance, dynamical backaction gives rise to an optical spring effect and amplification (or damping) of the mechanical mode [113]. We measure these effects only for blue-detuning of the laser, as the detuning can only be varied continuously on this side of the optical resonance without complications arising from thermo-optic bistability. The expected frequency shift $\delta\Omega_m$ and linewidth narrowing Γ_{opt} induced by the light field can be calculated with Equation 2.38a and Equation 2.38b, respectively.

These effects can be observed by varying the laser-cavity detuning Δ_{oc} , recording the mechanical radio frequency spectrum and evaluating the effective mechanical resonance frequency $\Omega_{eff} = \Omega_m + \delta\Omega_m$ and the effective mechanical linewidth $\Gamma_{eff} = \Gamma_m + \Gamma_{opt}$ (Γ_m is the intrinsic mechanical linewidth). Because of the thermo-optic shift of the optical resonance, it is not straightforward to determine Δ_{oc} for a given laser frequency ω_c . Therefore, we additionally recorded OMIA spectra and also measured the transmitted power. Each of these two data sets allows independent inference of the detuning (see next section). To calculate $\delta\Omega_m$ and Γ_{opt} , we used the average of the two values thus determined. The results, which demonstrate the presence of both the optical spring effect and parametric amplification, are displayed in Figure 7.7(a) and (b). The red curves show the expected backaction according to Equation 2.38a and Equation 2.38b with $g_0/2\pi = 400$ kHz taken from the calibration tone measurement (sec-

tion 7.4) and $\kappa/2\pi = 3.15$ GHz taken from the optical transmission profile (section 7.2). For this particular experiment, the intracavity photon number was estimated from the measured power leaving the cavity to be $n_{\text{cav}} = 10000\delta \pm 3300$ on resonance and assumed to have a Lorentzian distribution with detuning corresponding to the optical resonance. The model yields an intrinsic mechanical linewidth of $\Gamma_m/2\pi = 3.12$ MHz and an intrinsic mechanical frequency of $\Omega_m/2\pi = 2.9023$ GHz. The corresponding mechanical quality factor $Q_m \approx 930$ is of the expected magnitude for a crystalline material at room temperature and atmospheric pressure.

If the detuning Δ_{oc} is kept constant and instead the intracavity photon number is varied, the mechanical frequency and linewidth change linearly with n_{cav} , which is shown in Figure 7.7(c) and (d). Constant detuning was obtained by adjusting Δ_{oc} to maximize the height of the OMIA peak. Because this implies a detuning of $\Delta_{\text{oc}} = \Omega_m$, the optical spring effect is expected to be negligible [113]. The intercepts of the linear fits to the mechanical linewidth and mechanical frequency give an intrinsic mechanical decay rate of $\Gamma_m/2\pi = 3.13 \pm 0.06$ MHz and an intrinsic mechanical frequency $\Omega_m/2\pi = 2.90 \pm 0.03$ GHz, respectively, consistent with the values obtained from the detuning-dependent measurements.

At even higher input power, the linewidth of the mechanical resonance narrows extremely as the regime of mechanical lasing (also called self-sustained oscillations) [173, 174, 175] is reached. The transition into this regime is shown in Figure 7.7(e), where the detuning has been kept constant at $\Delta_{\text{oc}} \approx \Omega_m$ while increasing the power. The lowest observed input power threshold to achieve mechanical lasing was $20 \mu\text{W}$ for a device with 10 holes on each side. Achieving mechanical lasing indicates that our system attains a photon-enhanced cooperativity $C = n_{\text{cav}}(4g_0^2)/\Gamma\kappa > 1$ [113]. This is an important threshold: the transduction between light and mechanics is faster than the mechanical decoherence rate [113], which is a prerequisite for quantum state transfer protocols. Furthermore, the observation of these regenerative oscillations implies that, for an equal detuning on the red side, the temperature of the mechanical mode could be reduced by a factor of two [176].

Interestingly, the total amount of light reaching the photodiode drops in the transition to mechanical lasing. The cause of this behavior becomes apparent when the transmitted power is examined in the time domain with a high-speed oscilloscope (Tektronix CSA 8000 Communications Signal Analyzer). The amplitude changes from an almost constant value to a signal oscillating strongly at the mechanical frequency (see Figure 7.7(f)). The non-sinusoidal shape is a consequence of operating under conditions where optomechanical backaction becomes nonlinear [175, 177], which also leads to a reduction in the average detected power. The nonlinearity is also evident in the mechanical radio frequency spectrum (see Figure 7.7(g)), where harmonics of the mechanical mode up to the fourth order (limited by the photodiode) are observed.

7.6.1 Determination of laser detuning for evaluation of dynamical backaction

Whenever laser light passes through the PhC, the thermo-optic effect causes a shift of the optical resonance, which depends on the intracavity energy, as shown in Figure 7.8(a). As the

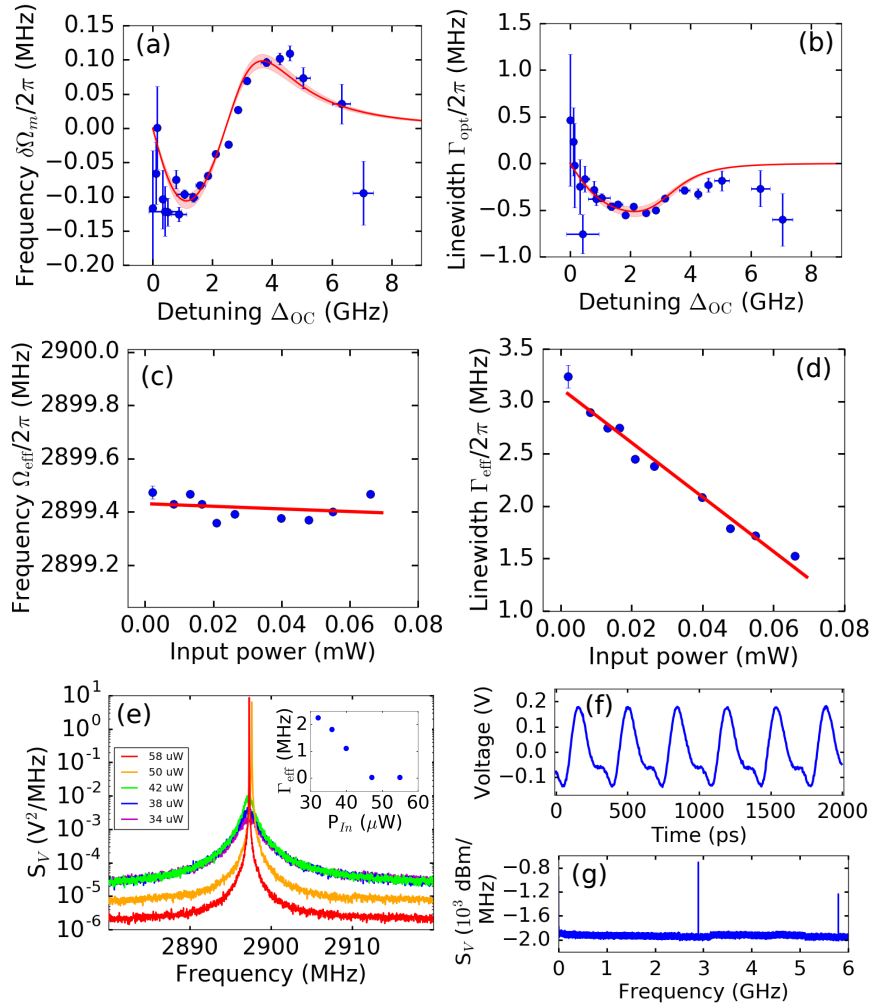


Figure 7.7 – Dynamical backaction measurements. (a) and (b) Detuning-dependent spring effect and parametric amplification (blue dots are measured data; red line is the model, where the shaded area accounts for an uncertainty in g_0 of ± 20 kHz). (c) and (d) Power-dependent spring effect and parametric amplification (blue dots are measured data; red line is the prediction from the model). (e) Extreme linewidth narrowing of the mechanical resonance with increasing input power, where the inset shows the effective linewidth Γ_{eff} obtained from a Lorentzian fit of the spectra. (f) Time-resolved transmission signal for 77 μ W input power showing oscillations at a frequency of 2.91 GHz, which matches the mechanical resonance frequency. The non-sinusoidal shape is due to the optomechanical backaction becoming nonlinear. Because of the 10-GHz bandwidth of the photodiode, the trace is effectively low-pass filtered at this frequency. (g) Radio frequency spectrum showing the fundamental mechanical resonance and its first harmonic, indicating nonlinear backaction.

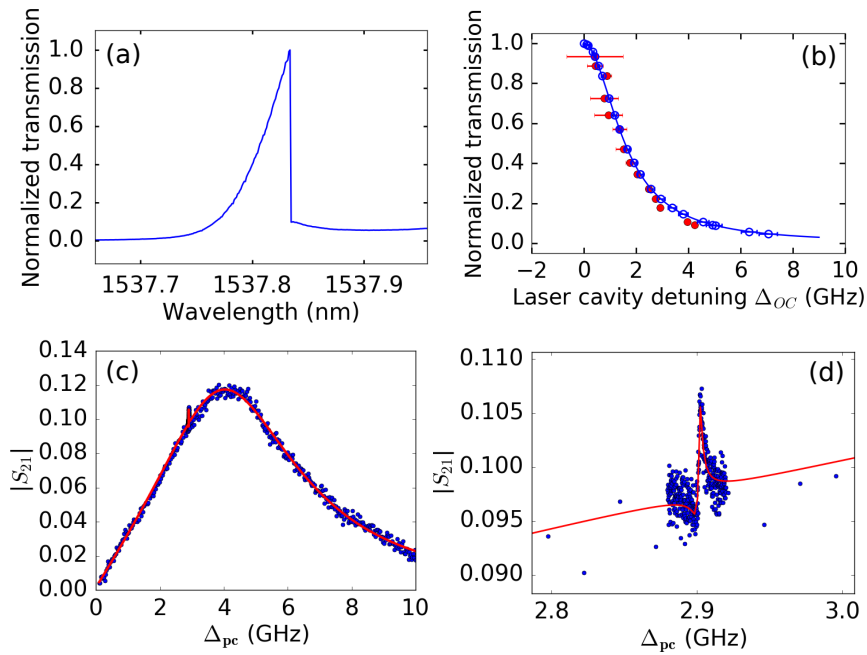


Figure 7.8 – Determination of the laser-cavity detuning for the dynamical backaction measurements. (a) Transmission profile of the device used for measurement of dynamical backaction with $21 \mu\text{W}$ input power. Due to the thermo-optic shift, the position of the optical resonance changes while sweeping the laser wavelength, producing a triangular transmission profile. (b) Plot of detuning inferred from transmission (blue open circles) assuming a Lorentzian profile with the linewidth $\kappa/2\pi = 3.15 \text{ GHz}$ (blue line) and from fits of OMIA traces (red closed circles). (c) and (d) Example of a measured OMIA trace (blue dots) with fit to Equation 2.33 (red line), where (d) is a magnification of the area around the OMIA peak in (c).

laser frequency is varied, the optical resonance frequency will change, and the detuning of the laser with respect to the cavity Δ_{oc} is not obvious. To determine the detuning, as is required to evaluate the optical spring effect and parametric amplification, two methods were applied. In the first, the transmitted optical power is recorded for each thermomechanical radio frequency spectrum taken. Assuming a Lorentzian transmission profile and using the known values for maximum transmitted optical power and optical linewidth, a detuning can be assigned to each transmitted power value. The resulting dependence of detuning on transmitted power is shown in Figure 7.8(b) with blue open circles. For the second method, in addition to the thermomechanical radio frequency spectra, we recorded a VNA trace as described for the measurements of OMIA. Its shape strongly depends on the detuning (see Figure 7.8(c) and (d) for an example), and fitting Equation 2.33 to the data gives the detuning Δ_{oc} . This method does not work for very large or very small detuning, as the OMIA peak is then no longer visible. The results are plotted as red solid circles in Figure 7.8(b) and overlap well with the values obtained from the first method. For the further evaluation of dynamical backaction, the average of the two data sets was used.

8 Optomechanics with slotted one-dimensional silicon photonic crystal cavities

The work presented on optomechanics with gallium phosphide devices in the previous chapters was motivated by the experiences made with silicon PhCs. As silicon is an established material in the nanomechanical photonic crystal community [167, 178] as well as in nanophotonics, fabrication methods are quite advanced and complex structures can be fabricated [179]. This led to the idea of building a slotted 1D PhC [18], with a high quality-factor-to-mode-volume ratio. The benefit of this device design for optomechanics was investigated in this thesis. The principles and experiments are often the same as for the optomechanical devices made of GaP (see section 2.5, chapter 6 and chapter 7).

8.1 Exploiting the slot effect

Displacement of a dielectric interface in a photonic cavity leads to a change in the cavity's optical eigenfrequencies, the so-called moving boundary effect. The magnitude of the frequency shift depends on the spatial distribution of both the optical and mechanical modes. Increased electric field energy in the region of greatest mechanical motion is generally expected to enhance the contribution of the moving boundary effect to the overall optomechanical coupling [178]. To this end, structures incorporating a slot are particularly interesting. Because of the requirement for continuity of the normal component of the electric displacement field across a dielectric boundary, an abrupt change in the normal component of the electric field occurs in slot structures [180] – an effect that has been exploited, for example, to substantially increase the confinement of light in slotted waveguides [181]. For electric fields perpendicular to the slot axis, the maximum is directly at the surface of the slot wall, from where it decays exponentially towards the middle of the slot. Narrow slots are therefore preferable for maintaining a high electrical field throughout the slot.

With these considerations in mind, we have chosen to investigate a 1D photonic crystal nanobeam cavity with a central slot, as shown in Figure 8.1. It comprises a freestanding waveguide with a sequence of holes forming Bragg mirrors on either side of the cavity. The unit cell of the periodic holes is scaled linearly in terms of length and hole radius for the five holes closest to the slot so as to ensure a gradual matching of the mode profile between the

Bragg mirrors and the slot region, which in turn yields a high optical quality factor [182, 183]. Such a 1D photonic crystal nanobeam cavity supports multiple optical modes, the highest frequency mode being symmetric with an antinode of the electric field in the center of the structure. The next mode is antisymmetric with a node of zero electric field in the middle of the device [18]. As the optical cavity modes are confined primarily to the slot region, a mechanical mode overlapping well with the electric field is the in-plane breathing mode involving lateral opening and closing of the slot. In principle, optomechanical coupling can be achieved with both optical modes, but for a large moving boundary contribution, the first mode with an antinode in the middle has greater net overlap with the mechanical breathing mode.

In contrast to our previous work [18], the slot is terminated before the first hole on either side of the cavity in order to increase the mechanical resonance frequency of the breathing mode to several gigahertz. The distance between the first two holes corresponds to roughly half the effective wavelength of the central portion of the structure, so the first nodes in the electric field fall at the crosspieces closing off the first holes. This is also the location of the "joint" for the mechanical breathing mode, the region of greatest strain. Often the sign of the photoelastic contribution to the optomechanical coupling rate is the opposite of that of the moving boundary contribution, leading to at least a partial cancellation of the effects. In this case, however, the region of most strain is where the electric field is small and the photoelastic and moving boundary contributions have the same sign. The result is a relatively high overall optomechanical coupling rate dominated by the moving boundary contribution, for which the mechanical frequency is high enough to be in the resolved side-band regime.

The final design has a simulated mode volume of $V = 0.017(\lambda_{\text{vac}}/n)^3$, which is close to the mode volume published in [18] with a theoretical optical quality factor $Q = 1.6 \times 10^6$, which corresponds to $Q/V = 9.7 \times 10^7$. The simulated electric field distribution is shown in Figure 8.1(a) and (b). The very low effective mass $m_{\text{eff}} = 103$ fg leads to a high mechanical resonance frequency of $\Omega_m/2\pi = 2.69$ GHz. We show the simulated displacement in Figure 8.1(c) and the associated strain in Figure 8.1(d). Analysis of the numerical simulations predicts a vacuum coupling rate of $g_0/2\pi = 342$ kHz. Notably, the moving boundary contribution, $g_{0,\text{mb}}/2\pi = 294$ kHz, is approximately six times larger than the photoelastic contribution, $g_{0,\text{pe}}/2\pi = 47$ kHz.

8.2 Device design

The device design is initially optimized for a high optical quality factor using finite-difference time-domain simulations [184] carried out with the freely available software package MEEP [185]. To optimize the mechanical properties as well, simulations are performed with the finite element mode solver COMSOL Multiphysics [116]. Both the photoelastic effect and the moving boundary effect are considered for the calculation of the overall optomechanical coupling rate $g_0 = g_{0,\text{pe}} + g_{0,\text{mb}}$ (see subsection 2.5.1). A Nelder-Mead algorithm is applied to optimize the geometry of the structure for the fitness function $F = g_0 \min(Q_o, Q_{\text{lim}})$ [162]. Q_{lim} is an upper limit for the optical quality factor that prevents the optimization algorithm from considering unreasonably high values calculated by COMSOL. The design produced

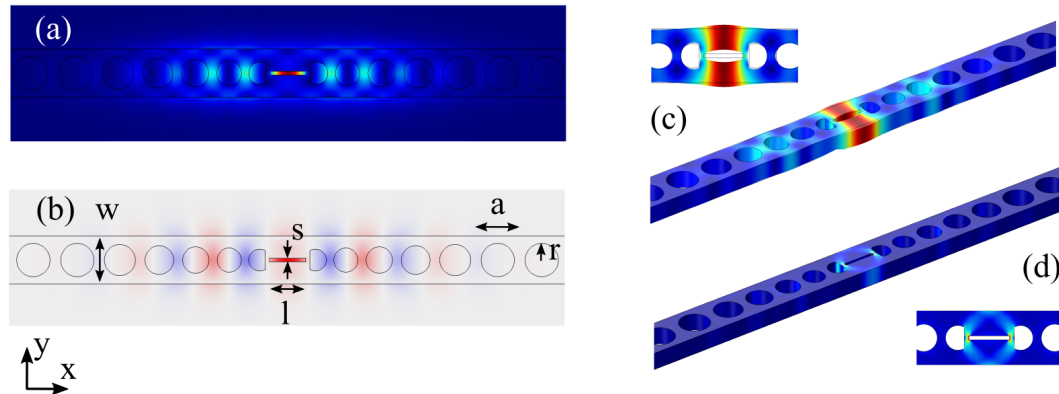


Figure 8.1 – (a) and (b) Cross-sections through the central portion of the PhC taken from a finite element simulation of the electric field of the highest frequency cavity mode with an antinode in the slot. (a) Total magnitude of the electric field, increasing from blue to red. (b) E_y component of the electric field (red and blue correspond to opposite signs). The simulations indicate that the electric field amplitude for this mode is strongly enhanced in the slot. (c) Displacement field from a finite-element simulation of the in-plane mechanical breathing mode at 2.69 GHz. The displacement overlaps spatially with the region of maximum electric field shown in (a). (d) Distribution of the first principal strain for the breathing mode. The region of greatest strain is nearly identical to the location of the first node in the electric field.

by the optimization algorithm is scaled so as to provide an optical resonance frequency of approximately $\omega_o/2\pi = 193.5$ THz, which corresponds to $\lambda_{\text{vac}} = 1550$ nm. The resulting design has the following dimensions: The holes have a nominal period of $a = 500$ nm, with waveguide width $w = 542$ nm, waveguide thickness $h = 220$ nm, slot width $s = 40$ nm, and slot length $l = 408$ nm. While the periodic hole radius is given by $r = 0.378a$, the five holes closest to the slot are linearly tapered in both radius and spacing to 65.6% of their nominal value (Figure 8.1(b)).

8.3 Fabrication

The fabrication process, as shown in Figure 8.2, is similar to that previously published [18]. We first pattern the negative resist 4% HSQ (80-nm thickness) on silicon-on-insulator (SOI) chips with a top-silicon thickness of 220 nm and a 3 μm buried oxide layer using 100-keV e-beam lithography (Vistec EBPG 5200ES). Inductively-coupled-plasma reactive-ion etching (Oxford Plasmalab System 100 ICP) with HBr/ O_2 chemistry [186] is employed to transfer the pattern into the top silicon. For device release, broadband ultraviolet photolithography with the positive resist AZ ECI 3027 is used to create openings around the devices while protecting the rest of the chip. Device release is subsequently accomplished by submerging the chip in a mixture of one part concentrated HF ($\geq 48\%$) and five parts standard 7:1 buffered oxide

Chapter 8. Optomechanics with slotted one-dimensional silicon photonic crystal cavities

etchant (for rapid etching without compromising resist adhesion) for 195 seconds to remove approximately 1.1 μm of the sacrificial buried-oxide layer under the devices.

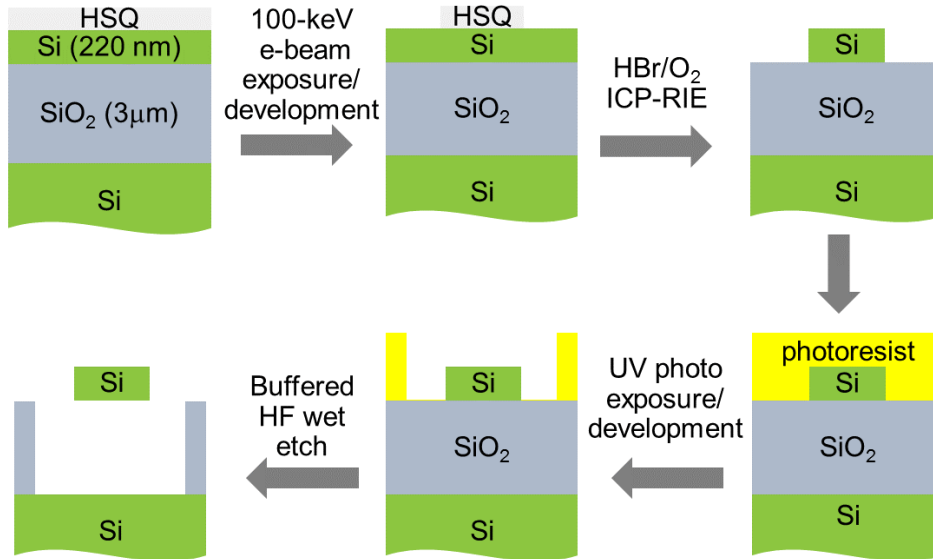


Figure 8.2 – Schematic of the fabrication process for freestanding silicon devices on SiO₂.

Scanning electron microscope (SEM) images of the resulting structure are shown in Figure 8.3. Design dimensions are accurately reproduced in the fabricated devices (typical deviations are ≤ 10 nm as measured by scanning electron microscopy) with low surface roughness, although there is some deviation from the desired vertical sidewalls, particularly the outer waveguide sidewalls. The most critical dimension in our design however is the slot width. Simulations indicate that a deviation of 5 nm from the target value can reduce the optical quality factor by 80%, which poses a considerable challenge given typical process fluctuations. To meet this stringent requirement, we fabricate structures with a range of nominal slot widths. Slots of length ≤ 100 nm or width ≤ 30 nm cannot be reliably opened by dry etching, and a 40-nm slot width represents a lower limit for reproducible device fabrication in our process.

The number of holes on each side of the slot is also varied between eight and 11. A higher number of holes decreases the rate of loss of intracavity photons to the attached waveguides, but it also lowers the rate of coupling into the cavity. The chip layout also includes input and output ridge waveguides with a length of several hundred microns connected to each device, at the ends of which focusing grating couplers are located to enable individual testing of the devices as previously described [18]. Here, however, we integrate the PhCs into one arm of a Mach-Zehnder interferometer formed by two directional couplers connected with two waveguides (Figure 8.4). The directional coupler on the input side of the PhC is designed to send 90% of the light into the cavity and 10% through the waveguide without a cavity. The directional coupler on the output side is a 50:50 splitter.

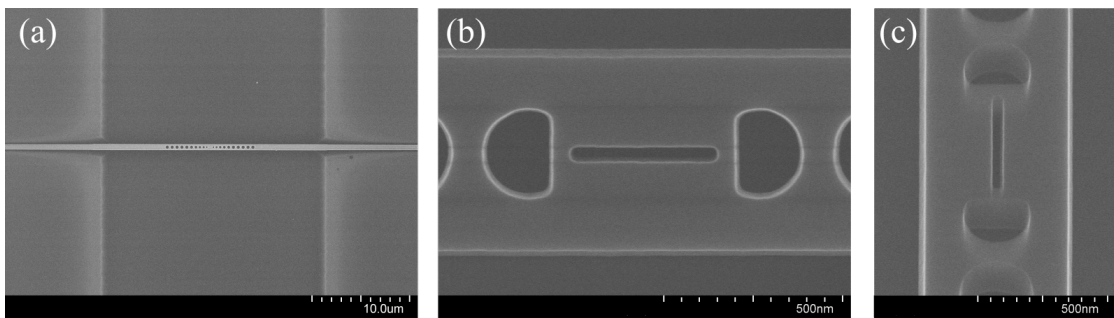


Figure 8.3 – Scanning electron microscope images of the freestanding photonic crystal nanobeam cavity on a silicon-on-insulator (SOI) wafer with a 40-nm slot. (a) Full device with nine holes on either side of the cavity. The center of the structure, where the cavity is located, is freestanding. The connected waveguides rest on the SiO₂ substrate. (b) The central portion of the PhC. (c) View down the slot at 30° tilt. Note the almost perfectly straight inner sidewalls of the slot.

8.4 Measurement setup

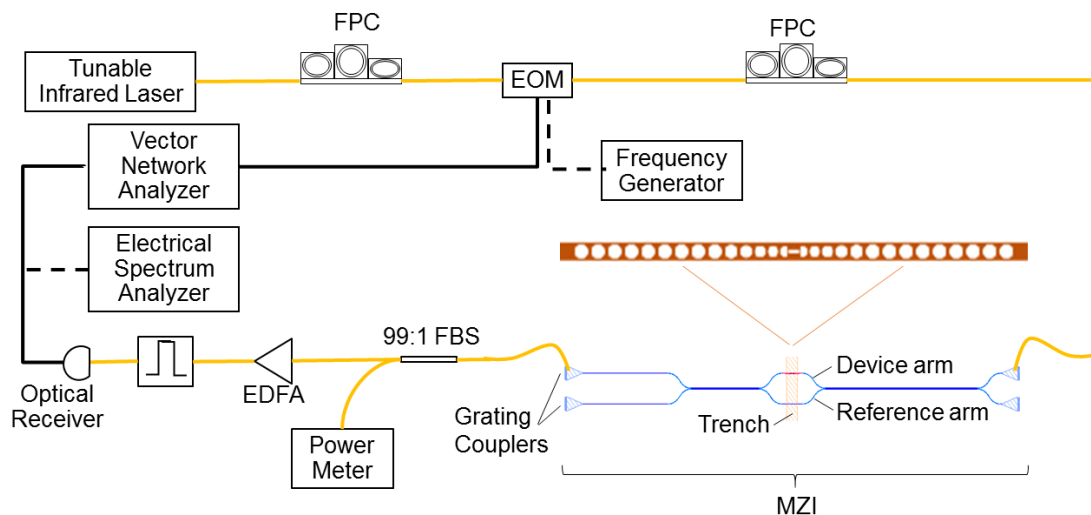


Figure 8.4 – Schematic of the experimental apparatus for characterization of the photonic crystal nanobeam cavities. See text for definition of abbreviations.

A schematic of the measurement apparatus is shown in Figure 8.4. All measurements are performed in air at atmospheric pressure with the sample chip resting on an aluminum block held at 20.0 °C as measured with an integrated thermistor and controlled with a Peltier element. Continuous-wave infrared light (New Focus Velocity 6328 external-cavity tunable diode laser, linewidth kHz) is directed through a cleaved single-mode fiber into a grating coupler at one input of the Mach-Zehnder interferometer (MZI). A fiber polarization controller (FPC) aligns the polarization of the light with the TE design orientation of the grating couplers. The PhC is located in one arm of the interferometer, permitting homodyne signal detection: The light in

Chapter 8. Optomechanics with slotted one-dimensional silicon photonic crystal cavities

the reference arm interferes with the light of the device arm. The resulting signal is collected with a second cleaved single-mode fiber at one output of the MZI. Measured in this way, the MZI produces an amplification of the signal transmitted through the photonic crystal. The integrated MZI in principle offers the possibility to perform balanced homodyne detection, in which case both outputs would be measured simultaneously, however for the data presented here, this technique has not been utilized.

Depending on the type of measurement made, the light is then routed in various ways. Simple transmission spectra (subsection 8.5.1) are recorded using a power meter (EXFO IQ 1600). The same power meter is also employed for power monitoring, for which a small part of the transmitted signal is coupled out through a fiber beam splitter (FBS). For measurement of mechanical resonances, the output light is first amplified with an erbium-doped-fiber amplifier (EDFA) (JDS Uniphase MAP EDFA) followed by a narrow bandpass filter (JDS Uniphase MAP Tunable Filter TB3) and then detected with a fast photodiode (JDS Uniphase MAP Receiver RX10) connected to an electrical spectrum analyzer (HP8563A). Calibration-tone measurements are performed by introducing an electro-optic phase modulator (EOM) (Thorlabs 10 GHz LN65S-FC) after the light source. A frequency generator (HP 8341A Synthesized Sweeper 0.01 - 20 GHz) provides the radio-frequency (RF) input signal for the modulator. Finally, for the observation of optomechanically induced absorption, the RF input signal is instead generated with a vector network analyzer (HP8510B), which also analyzes the signal from the fast photodiode.

8.5 Device characterization

The optical and mechanical properties as well as the coupling between the two are characterized for the fabricated PhCs. Therefore measurements of the transmission, the thermomechanical noise spectrum and OMIA are performed.

8.5.1 Optical transmission

A typical optical transmission spectrum for a device with ten holes on each side of the cavity is shown in Figure 8.5. From a Lorentzian fit we obtain an optical quality factor of $Q_o = 8.8 \times 10^4$ for this device. The slightly distorted shape of the resonance is due to the underlying interference pattern caused by the Mach-Zehnder interferometer.

8.5.2 Thermomechanical radio-frequency spectra

Determination of the mechanical resonances of a device is accomplished by detecting the RF modulation spectrum of light transmitted through the PhC. The Brownian thermal motion of the mechanical modes modulates the intracavity light. The resulting intensity modulation of the output light leads to Lorentzian resonances in the power spectral density S_V of the transduced photocurrent produced by the fast photodiode, as illustrated in Figure 8.6. Here

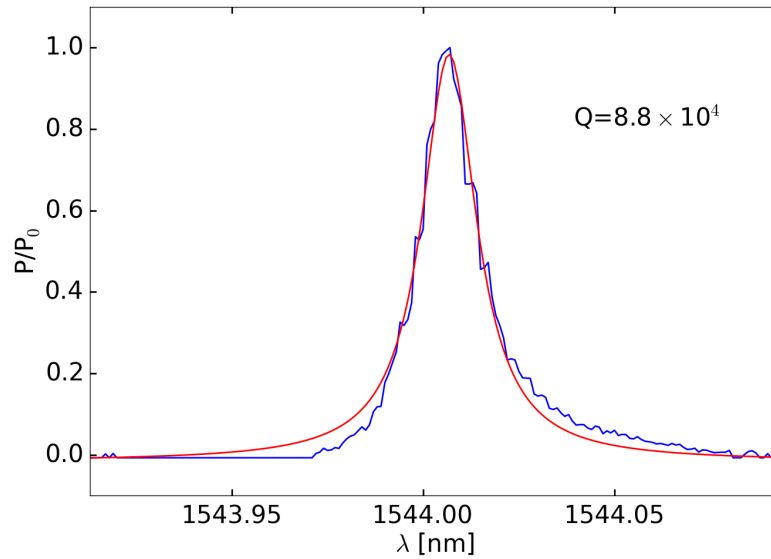


Figure 8.5 – Measured optical transmission spectrum of a device with ten holes on each side (blue). A Lorentzian fit (red) yields a calculated optical quality factor of $Q_o = 8.8 \times 10^4$.

transduced photocurrent refers to the voltage measured at the output of the transimpedance amplifier attached to the photodiode. Each resonance peak corresponds to a different mechanical mode. The mode with the highest amplitude at $\Omega_m/2\pi = 2.69$ GHz is assigned to the breathing mode and matches well the simulated frequency of 2.694 GHz. The inset in Figure 8.6 shows a magnification of this resonance. The linewidth of $\Gamma_m/2\pi = 6.4$ MHz corresponds to a mechanical quality factor of $Q_m = 417$. Comparable 1D PhCs without a central slot typically exhibit a higher quality factor for the breathing mode [187, 188, 171, 112]. While in some cases this might be due to the use of different materials, such as strained silicon nitride, we suspect the discrepancy is more likely attributable to the presence of the slot altering the isolation of the mechanical mode, as we have seen similarly low quality factors in other slotted designs. The laser frequency in this off-resonance measurement can only be blue detuned from the cavity resonance because of heating of the device as a result of two-photon absorption and the concomitant thermo-optical shift to lower cavity frequency. Optomechanical backaction in this case leads to an amplification of the mechanical mode and therefore to a slight decrease of the mechanical linewidth [188]. The intrinsic mechanical quality factor is presumably smaller than the above value. In addition to the resonances shown in Figure 8.6, there are further less pronounced mechanical resonances up to frequencies as high as $\Omega_m/2\pi = 6.04$ GHz.

8.5.3 Optomechanical coupling rate

To quantify the optomechanical vacuum coupling rate g_0 , two independent measurements are performed. In the first, a calibration-tone measurement, the thermomechanical noise

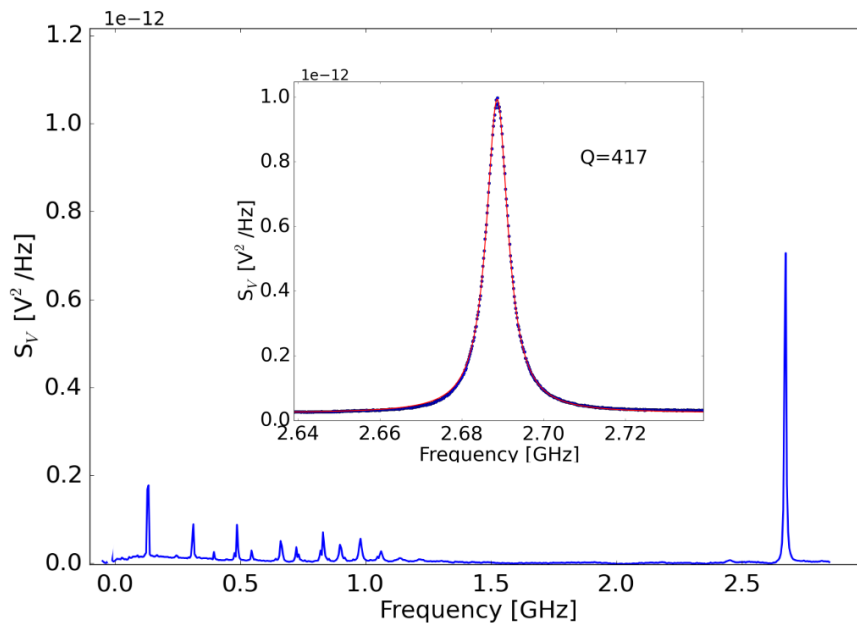


Figure 8.6 – Power spectral density after the transimpedance amplifier of the fast photodiode. Each resonance peak corresponds to a mechanical mode that couples optomechanically to the light trapped in the cavity. The most prominent peak is the breathing mode at $\Omega_m/2\pi = 2.69$ GHz. The inset shows a magnification of this resonance peak.

spectrum is compared to a sideband created by phase modulating the laser light entering the cavity. In the second, the transmission spectrum resulting from OMIA is used to infer the optomechanical coupling rate g . With knowledge of the intracavity photon number n_{cav} , the vacuum coupling rate g_0 can then be calculated.

8.5.3.1 Calibration tone measurement

The optomechanical vacuum coupling rate can be determined by taking advantage of the fact that the PhC transduces laser frequency fluctuations and cavity frequency fluctuations in the same way. Following the method described by Gorodetsky et al. [111], we determine g_0 by comparing the power spectral density resulting from the thermomechanical cavity frequency fluctuation with that produced by a calibration tone. Details of the derivation of g_0 from this measurement are given in subsection 2.5.2. The measured power spectral density is shown in Figure 8.7. The broad Lorentzian peak is the mechanical resonance, the narrow peak the calibration tone. The calibration tone's width and shape are given by the filter function of the spectrum analyzer, which in this case was a Gaussian function. Comparing the areas under the peaks leads to $g_0/2\pi = 310 \pm 47$ kHz for a device with nine holes on each side of the cavity.

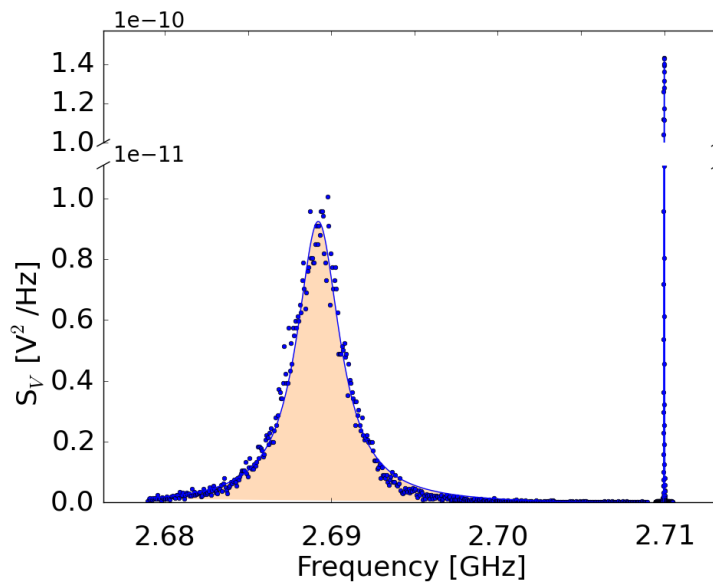


Figure 8.7 – Determination of g_0 by comparing the thermomechanical cavity frequency fluctuation with a calibration tone, generated by phase modulating the input laser field. The left peak is the Lorentzian mechanical resonance resulting from the thermal motion of the optical cavity. The right peak is the Gaussian calibration tone.

8.5.3.2 Calibration of the phase modulator

For the calibration-tone measurement of the optomechanical coupling rate, the modulation depth $\beta = V_p/V_\pi \cdot \pi$ must be known, which requires precise determination of the half-wave voltage V_π of the electro-optic phase modulator. V_p is the amplitude of the RF signal applied at the RF input of the EOM. Measurement of V_π is accomplished by setting the RF drive signal to 2.9 GHz and varying V_p . Light at 1550 nm transmitted through the modulator is passed through a scanning Fabry-Pérot interferometer (Thorlabs SA210-12B), where the detected signal is resolved into carrier and sidebands. The carrier amplitude as a function of RF power can be described as $A_0 = a \cdot (J_0(\pi V_p/V_\pi))^2$ and the first sideband amplitude as $A_1 = a \cdot (J_1(\pi V_p/V_\pi))^2$, where J_0 and J_1 are Bessel functions of the first kind and a is a scaling factor (Figure 8.8). Fitting the amplitudes of the carrier and sidebands gives $V_\pi = 5.26 \pm 0.07$. This value is in agreement with the specifications of the vendor.

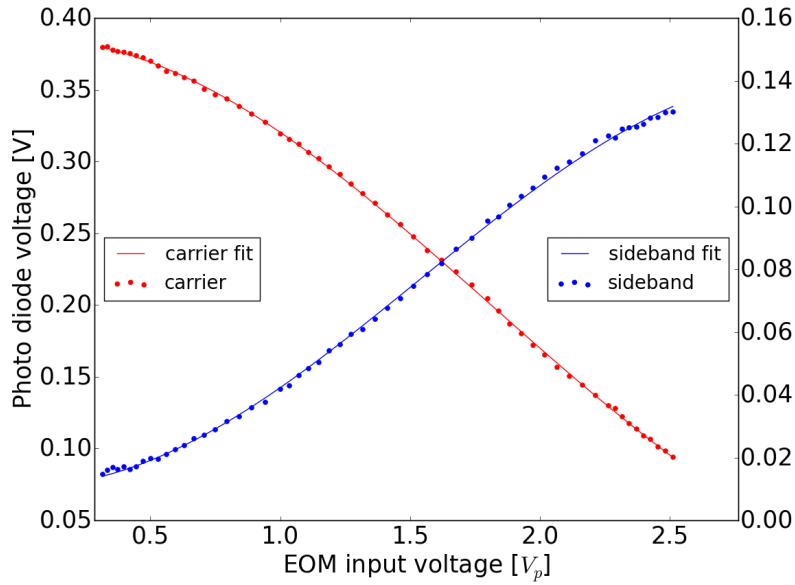


Figure 8.8 – Measured amplitude of the carrier (red dots) and first sideband (blue dots) as a function of the input voltage at the EOM. Lines are fits of Bessel functions of the first kind to the data.

8.5.3.3 Optomechanically induced absorption

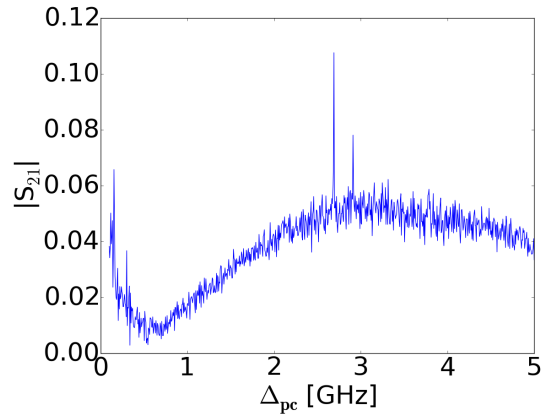
Optomechanically induced absorption (OMIA) is indicative of a coherent interaction of the mechanical motion and the laser field entering the cavity. To observe this behavior, the laser field at frequency ω_c , which we call the control field, is blue detuned from the cavity resonance ω_o . An additional probe field, much weaker than the control field, is created by phase modulating the laser. This leads to two sidebands, of which only the lower frequency one enters the optical cavity to any significant extent, as the upper one is far from resonance. The control

field is modulated by the thermal motion of the cavity itself. The lower sideband created by the mechanical motion at $\omega_c - \Omega_m$ interferes constructively with the intracavity probe field, if the probe-control detuning $\Delta_{pc} = \omega_c - \omega_p$ coincides with the mechanical resonance frequency Ω_m . This leads to an enhanced transmission signal. The mathematical description of the expected transmission profile and the method used to infer the optomechanical vacuum coupling rate g_0 from this measurement are described in subsection 2.5.3.

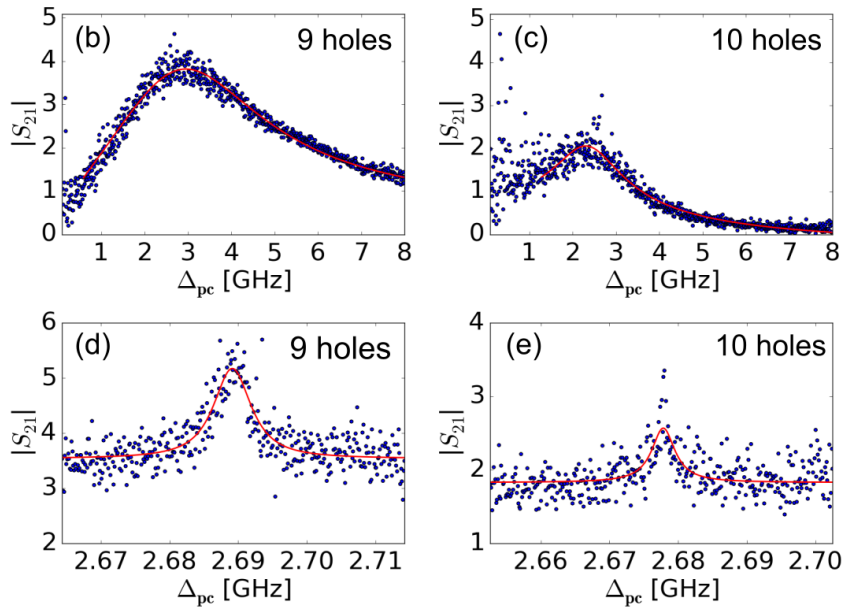
Typical OMIA signals are presented in Figure 8.9. Transmission versus two-photon detuning Δ_{pc} is shown in Figure 8.9(a) for a device with nine holes on each side of the cavity. The background is given by the transmission profile of the optical resonance. The two spikes are produced by OMIA at two different mechanical resonances, one at $\Omega_m/2\pi = 2.69$ GHz and the other at $\Omega_m/2\pi = 2.92$ GHz. Data for the same measurement but with a larger range for the two-photon detuning are displayed in Figure 8.9(b). Due to the limited number of points recordable by the VNA, the OMIA peaks are not resolved in this measurement, but the full cavity transmission profile is visible. The transmission profile is narrower and more symmetric for a device with ten holes on each side of the cavity (Figure 8.9(c)). Indeed, the asymmetry of the signal is expected to decrease with decreasing κ/Ω_m [112]. Figure 8.9(d) and (e) show a zoom-in of the transmitted signal on the OMIA peak. To reduce the number of fitting parameters necessary to describe the complete transmission profile, we first fit the cavity resonance to the $|S_{21}|$ data shown in Figure 8.9(b) and (c) [162] with g set to zero in the expression for $t(\Delta_{pc})$ (see Equation 2.33). The values extracted for κ and Δ_{oc} are then used to fit the OMIA peak to the data of Figure 8.9 (d) and (e). For the measurements presented here, $\Delta_{oc} \approx -\Omega_m$, which is consistent with the symmetric shape of the OMIA peak [72]. We obtain the following results for the nine-hole device: $Q_o = 5.2 \times 10^4$, $\kappa/2\pi = 3.9$ GHz and $g_0/2\pi = 600 \pm 300$ kHz. For the ten-hole device, $Q_o = 1.2 \times 10^5$, $\kappa/2\pi = 1.6$ GHz and $g_0/2\pi = 900 \pm 600$ kHz. In principle, no significant difference is expected in the coupling rate g_0 for these two devices, as the number of holes extends well beyond the region where the breathing mode is localized. However, there may be some variation due to imperfections in fabrication.

8.5.3.4 Dependence of optomechanical coupling rate on slot width

A better understanding of the optomechanical coupling potentially achievable with a slotted PhC is obtained from simulations of devices with various central slot widths. Figure 8.10 shows the optomechanical vacuum coupling rate g_0 for designs optimized as described in section 8.2. Only designs with optical quality factors above 1.0×10^6 were considered. The results clearly indicate that devices with slot widths less than 40 nm would exhibit higher values of g_0 , if they could be successfully fabricated. The turning point at 40 nm corresponds to a change in the relative magnitude of g_{mb} and g_{pe} : for slot widths ≤ 40 nm, the moving boundary contribution g_{mb} dominates; for slot widths > 40 nm, the photoelastic contribution g_{pe} is greater in the optimized structure.



(a) The two spikes are OMIA signals with the broad background given by the cavity transmission profile.



(b) and (c) Same measurement as in (a) with increased range for Δ_{pc} . The measurements were taken for devices with different numbers of holes on each side of the cavity as indicated. The OMIA spikes are not resolved because of the limited number of sampling points. (d) and (e) Measurement at higher resolution of the transmitted signal over the window of induced absorption.

Figure 8.9 – Measured transmission signal $|S_{21}|$ versus two-photon detuning Δ_{pc} .

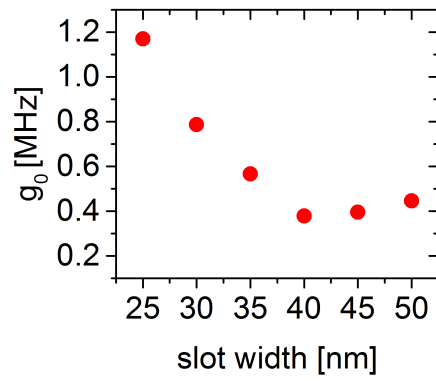


Figure 8.10 – Simulated optomechanical coupling rates for optimized designs of varying slot width.

9 Summary and outlook

In this work a new platform for integrated GaP-on-insulator devices was introduced. Several new process steps have been demonstrated: direct wafer bonding of a GaP/ $\text{Al}_x\text{Ga}_{1-x}\text{P}$ /GaP heterostructure to a SiO_2 -on-Si wafer; a GaP substrate removal procedure involving a combination of wet and dry etching, where the key step is a final Cl_2/CF_4 ICP-RIE process that stops selectively on the $\text{Al}_x\text{Ga}_{1-x}\text{P}$ sacrificial layer (this process has meanwhile been further improved by changing to a $\text{SiCl}_4/\text{SF}_4$ gas mixture [120]) and two alternative ICP-RIE recipes employing $\text{H}_2/\text{CH}_4/\text{Cl}_2/\text{BCl}_3$ plasmas that allow device patterning of high aspect-ratio devices with relatively smooth, nearly vertical, outer sidewalls. Building blocks for integrated photonic circuits have been realized, such as waveguides, grating couplers with losses below 5 dB, and ring resonators.

The ability to work with full GaP-on- SiO_2 wafers makes this approach inherently higher yield and more versatile than the liftoff-and-transfer method previously employed for GaP-on-diamond devices [15, 21, 22]. It is also more robust with respect to further processing and allows more direct integration than bonding methods employing polymers [7, 32, 45]. Indeed, this GaP-OI technology platform is expected to enable both new device architectures for GaP and their integration into photonic and electronic circuits. For example, the various device concepts utilizing photonic crystal structures, which to-date have been demonstrated as isolated, free-standing devices interrogable only with free-space optics such as high-numerical aperture microscope objectives or tapered fibers, could instead be connected directly with other on-chip elements via waveguides. Devices operating in the visible spectrum, for example, spectrometers or structures which couple to atoms [189], quantum dots or NV centers [21], could be similarly integrated.

We exploited the new GaP-OI platform to fabricate waveguide resonators for nonlinear optics and 1D PhCs for optomechanics. The waveguide resonators were used for second- and third-harmonic generation as well as frequency comb generation. Operating in the telecommunication wavelengths, propagation losses as low as 1.2 dB/cm were observed for single-mode strip waveguides with effective areas of $0.2\ \mu\text{m}^2$. Exploiting precision control over sidewall dimensions, waveguides were dispersion engineered to support efficient four-wave mixing. Resonators formed from these waveguides were found to exhibit parametric oscillation with as

little as 3 mW injected power, followed by formation of broadband (> 100 nm) frequency combs with comb spacing ranging from 100 GHz to 250 GHz, depending on resonator geometry. In conjunction with pump-probe measurements, a direct measurement of the Kerr coefficient of GaP was made at optical wavelengths: $n_2 = 1.1(5) \times 10^{-17} \text{ m}^2/\text{W}$. Also observed were frequency-doubled combs and Raman-shifted frequency combs. Looking forward, various applications of GaP-on-insulator nonlinear photonics seem promising. Microresonators could be designed with a second bus waveguide for efficient collection and out-coupling of the SHG signal [153], and, eventually, on-chip frequency conversion of integrated emitters could be explored. Reduction of waveguide sidewall roughness and enhanced dispersion engineering might allow soliton comb formation, mid-IR frequency combs, and ultra-broadband supercontinuum generation. The large transparency window of GaP ranging from 0.6 to 11 μm makes GaP especially appealing, because it enables applications in the visible and near infrared where many nonlinear materials are unusable due to absorption [3]. Furthermore, second harmonic combs are of interest for achieving a fully-stabilized comb through self-referencing. This technique usually requires an additional second-order nonlinear element, which could be avoided with GaP because of simultaneous second-harmonic generation and frequency comb generation [190, 191].

The 1D GaP PhCs have been optimized for optomechanics and were used for first demonstration of cavity optomechanics with PhCs made of GaP. We have developed and fabricated a PhC design that permits coupling of an optical mode with a measured quality factor as high as $Q_o = 1.1 \times 10^5$ (linewidth $\kappa/2\pi = 1.8$ GHz) to a stationary mechanical mode with a frequency of 2.902 GHz. The optomechanical coupling, occurring at a rate of $g_0/2\pi=400$ kHz, gives rise to effects such as OMIA and dynamical backaction, which we have characterized and compared to theoretical models. Observation of OMIT is also possible at room temperature because of a weak thermo-optic shift, in contrast to the situation with comparable devices made of silicon. Because the devices are sideband-resolved, efficient amplification of the mechanical mode by the optical pump is achieved, manifesting itself in the form of mechanical lasing at high input powers. This implies a multiphoton cooperativity $C > 1$ for our devices, which is a prerequisite for quantum transduction and efficient cooling. That the wide electronic bandgap of GaP reduces two-photon absorption at typical telecommunication wavelengths is demonstrated by measuring power-dependent transmission spectra. We thus confirm that GaP is a good choice for applications requiring high intracavity photon numbers while maintaining a stable optical resonance frequency.

A question that could not be fully resolved within the scope of this work is the apparent existence of saturable absorbers in the GaP, which lead to an initial increase in optical quality factor with increasing power. Also, the gradual degradation of the optical device properties over time is not yet fully understood. We have some indication from our work on ring resonators that a protective coating, such as a few nanometers of Al_2O_3 , may thwart the deterioration, suggesting some sort of photooxidation as the underlying cause. Answers to both questions require more extensive study.

Alternative designs for PhCs fabricated of silicon have been studied, in which the moving boundary effect dominates over the photoelastic effect in determining the optomechanical

coupling rate. Specifically, a slot was introduced at the center of the PhC to locally enhance the electric field. In simulations, it was discovered that, with slot widths ≤ 30 nm, coupling strengths of $g_0/2\pi > 1$ MHz are achievable. Fabrication in silicon of such structures is however challenging; only slots with widths ≥ 40 nm could be opened. Nevertheless, we were able to realize slotted PhCs with optical quality factors as high as $Q = 8.8 \times 10^4$, in which a mechanical mode with a resonance frequency of 2.7 GHz couples to the optical mode with a rate of $g_{0,om}/2\pi = 310$ kHz. The slotted design is useful for materials that do not have a significant photoelastic effect, for example AlN. Furthermore, these slotted PhCs should exhibit minimal inherent dispersion, especially when the optical resonance frequency is far from the electronic bandgap, as the highly dispersive photoelastic contribution ($\sim n^4$) is minimized. The small mode volume combined with the electric field maximum being located outside of the silicon offers an interesting opportunity for experiments involving coupling to an additional mechanical resonator. For example, one could investigate the mechanical motion of carbon nanotubes, nanowires or even atoms placed in or near the slot, where they would interact strongly with the optical mode of the cavity and, in turn, couple to mechanical modes of the silicon.

In contrast to silicon, GaP is non-centrosymmetric. We propose using the consequent piezoelectric properties of GaP to develop a microwave-to-optical transducer with an intermediate mechanical resonator. For that purpose, the 1D PhC optimized for optomechanical coupling would be connected to a superconducting electric circuit by creating an electric field across the beam with two electrodes on or close to the beam. The direct and inverse piezoelectric effects would then lead to transduction of mechanical motion into an electric potential and vice versa. In simulations, the electromechanical coupling was maximized for two different approaches: one with electrodes attached to the beam and one with electrodes separated by a gap from PhC. For both device designs we predict coupling strengths $g_{em}/2\pi > 10$ MHz. The achievable single photon cooperativity $C_{0,em}$ would be above 10^4 , assuming a mechanical resonator with $Q_m \approx 10^4$ and an electrical resonator with $Q_e \approx 10^5$, both of which have been demonstrated experimentally [167, 166]. The next steps for realizing these concepts are the incorporation of electrodes into the fabrication process for our GaP PhCs. The scheme envisioned for fabricating the bottom or backside electrode is shown in Figure 9.1. For the top electrode, an air bridge might be required, as described for example in Chen et al. [192]. Superconducting microwave resonators made of Nb are currently under development in our team, and the first results have been obtained.

The final goal would be to integrate the microwave-to-optical transducer with superconducting quantum circuits used for quantum computing [50]. The transduction of quantum information in the optical domain would enable sending qubits at room temperature, which could be used to link several quantum computers or provide their remote control via the so called blind quantum computing protocol. Linking of two quantum computers could increase available qubits for computations by connecting existing, smaller quantum computers. Blind quantum computing could give end-users secure remote access to quantum computers hosted by providers.

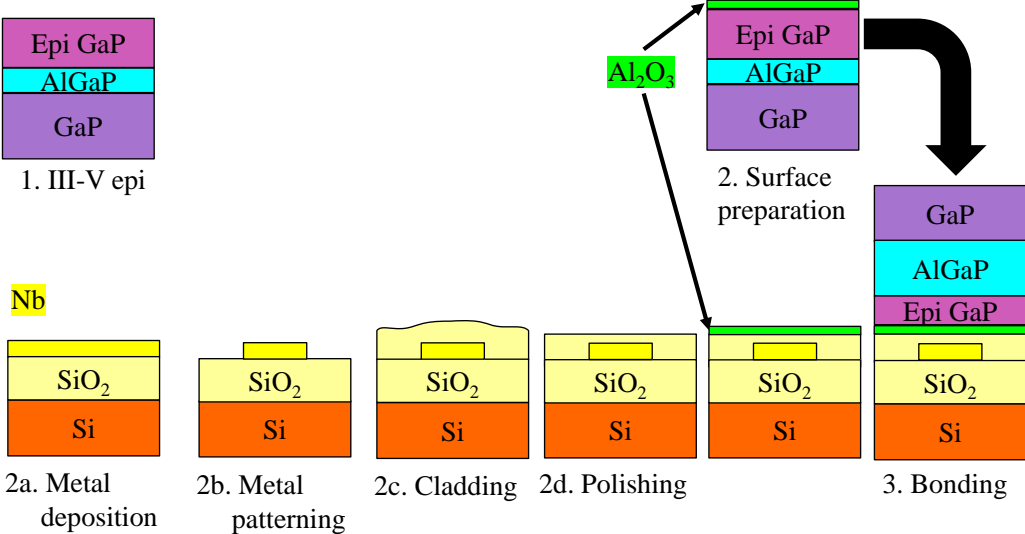


Figure 9.1 – Envisioned fabrication scheme for the bottom electrode. A superconducting metal, in this example Nb, is deposited on the oxidized silicon wafer. After patterning the electrodes, they are cladded with SiO₂, which is planarized in the next step. The wafer is then bonded as usual.

A Processing manual GaP photonic devices

In Table A.1, the exact processing steps conducted in the BRNC for the fabrication of freestanding PhCs made with 7 mm × 7 mm GaP-OI chips are provided. For details of the substrate removal from the bonded wafers, refer to chapter 3.

Process step	Description
Adhesion layer	deposit 3 nm of SiO ₂ by ALD
HSQ deposition	<ul style="list-style-type: none"> • warm vial containing 6% HSQ to room temperature for at least 5 min • dehydrate substrate for 10 min at 180 °C • spin coat HSQ for 5 s at 500 rpm, 60 s at 6000 rpm, acceleration 2000 rpm/s
e-beam writing	electron beam exposure with 7300 μC/cm apply 5 nm bias for PhCs
HSQ development	<ul style="list-style-type: none"> • mix 10 ml AZ351B with 30 ml H₂O • put the chip for 5 min into the mixture and agitate to prevent the formation of bubbles on the chip • add 50 ml H₂O, wait for 30 s • rinse beaker under running water for at least 5 min • rinse chip with acetone, isopropanol (IPA) • blow-dry with N₂
ICP dry etch	low power recipe as in Table 3.5 <ul style="list-style-type: none"> • condition chamber for 20 min • calibrate etch rate with GaP chip with SiO₂ hardmask • etch chip until GaP layer is completely removed in regions not covered by HSQ (check with SEM before HSQ removal)
O ₂ plasma	600 W, 500 sccm O ₂ for 3 min with chip on watch glass
HSQ removal	<ul style="list-style-type: none"> • dip sample for 10 s in BHF(7:1) • rinse in water • blow-dry with N₂

Appendix A. Processing manual GaP photonic devices

Adhesion layer	deposit 5 nm SiO ₂ with ALD
Photoresist deposition	<ul style="list-style-type: none">• dehydration bake for 5 min 150 °C• apply HMDS• spin coat AZ6612 for 40 s at 4000 rpm, acceleration 1000 rpm/s• pre-bake for 1 min at 110 °C
Exposure	expose for 3.1 s with 13 mW/cm ²
Development	<ul style="list-style-type: none">• mix developer AZ400K with H₂O, ratio 1:4• put chip for 30 s into mixture• rinse for 2 min in water• blow-dry with N₂
Etch SiO ₂ in HF	<ul style="list-style-type: none">• put chip in fresh BHF(7:1) in a Teflon beaker for 15 min• rinse in water• blow-dry with N₂
Mask removal	<ul style="list-style-type: none">• put chip in acetone for 2 min• rinse with IPA• blow dry with N₂
O ₂ plasma	600 W, 500 sccm O ₂ for 3 min with chip on watch glass

Table A.1 – Process flow for GaP-OI devices starting from GaP-OI substrate.

B Processing manual Si photonic devices

In Table B.1, the exact processing steps conducted in the BRNC for the fabrication of freestanding PhCs made with $2\text{ cm} \times 2\text{ cm}$ SOI chips are provided. The recipes are published in Seidler et al. [18, 26]. The description described for the processing of $2 \times 2\text{ cm}^2$

Process step	Description
HSQ deposition	<ul style="list-style-type: none"> • warm vial containing 4% HSQ to room temperature for at least 5 min • dehydrate substrate for 10 min at 180°C • spin coat HSQ for 5 s at 500 rpm, 60 s at 6000 rpm, acceleration 4000 rpm/s
E-beam writing	electron beam exposure with $7300\text{ }\mu\text{C}/\text{cm}$ apply 5 nm bias for PhCs
HSQ development	<ul style="list-style-type: none"> • mix 10 ml AZ351B with 30 ml H_2O • put the chip for 5 min into the mixture and agitate to prevent the formation of bubbles on the chip • add 50 ml H_2O, wait for 30 s • rinse beaker under running water for at least 5 min • rinse chip with acetone, IPA • blow-dry with N_2
ICP dry etch	<ul style="list-style-type: none"> • HBr/O_2 chemistry [26] • condition chamber until plasma is stable (this can take up to one hour) <ul style="list-style-type: none"> • affix chip to carrier wafer with Apiezon (Apiezon®T, M& I Materials) • place strips of aluminum foil over two opposite corners of the chip and cover them with polyimide tape (Kapton®) [26]
Removal of Kapton tape residues	clean carrier wafer and backside of chip (use Q-tip) with Hexan

Appendix B. Processing manual Si photonic devices

HSQ removal	<ul style="list-style-type: none"> • dip sample for 10 s in BHF • rinse in water • blow-dry with N₂
O ₂ plasma	600 W, 500 sccm O ₂ for 3 min with chip on watch glass
Photoresist deposition	<ul style="list-style-type: none"> • dehydration for 5 min 180 °C • apply HMDS • spin coat AZ ECI3027 for 40 s at 4000 rpm, acceleration 2000 rpm/s • pre-bake 90 s at 90 °C
Exposure	expose for 22 s with 13 mW/cm ²
Post-bake	post-bake 1 min at 110 °C
Development	<ul style="list-style-type: none"> • put chip for 50 s in AZ726 M/F (undiluted) • rinse for 2 min in water • blow-dry with N₂
Hard-bake	hard-bake 5 min at 180 °C
O ₂ plasma	200 W, 500 sccm O ₂ for 1 min with chip on metal plate
Etch SiO ₂	<ul style="list-style-type: none"> • prepare 1:5 HF (≥ 48%): BHF(7:1) • mix well before etching • submerge chip for 3 min 15 s (prevent any agitation) • rinse in water for at least 2 min • blow-dry with N₂
Mask removal	<ul style="list-style-type: none"> • NMP soak on hotplate at 140 °C • rinse with acetone, IPA • blow-dry with N₂
O ₂ plasma	600 W, 500 sccm O ₂ for 3 min with chip on watch glass

Table B.1 – Process flow for Si-on-insulator devices.

C Simulation of optomechanical coupling with COMSOL

To simulate the optomechanical properties of the 1D PhCs the finite element solver COMSOL Multiphysics [116] is used. The program enables simulation of various physical properties, depending on which modules are in use. To simulate the optical properties of the PhCs, we use the Wave Optics module. For the mechanical properties, the MEMS module is employed. To determine the eigenmodes, eigenfrequency studies are performed. This is done consecutively; one eigenfrequency study is carried out for the optical eigenmode, another for the mechanical eigenmode. In each case, the eigenfrequency and a quality factor are determined, the latter being the imaginary part of the eigenfrequency. The quality factors can be deduced from the simulations, however they should be properly interpreted: Not all loss channels influencing the quality factors of mechanical and optical modes are included in a simple simulation. Optical quality factors might be compromised by surface roughness, which is usually not considered in simulations. Additional mechanical damping can result from imperfections in the crystal lattice and surface states, which are often referred to as two-level systems, air damping, clamping loss or losses to bulk modes. Mechanical quality factors were therefore not considered in the optimization of the PhC design. Optical quality factors are expected to be around a factor ten in reality.

Symmetry of the model

The physical boundary conditions for the electromagnetic waves study and the solid mechanics study are set independently. For the optical mode, symmetry considerations are included in the model, by defining mirror planes as perfect magnetic conductors and perfect electric conductors. A perfect magnetic conductor sets the tangential component of the magnetic field to zero and imposes antisymmetry for electric fields. A perfect electric conductor sets the tangential component of the electric field to zero and imposes mirror symmetry for electric fields. In this way the simulated optical eigenmodes is defined as having either a node or antinode at the center of the photonic crystal. Importantly, symmetry reduces the size of the model, which helps to reduce computation time. For example, by using three orthogonal mirror plans, we reduce the model size and, in turn, the computation time by a factor of eight.

Appendix C. Simulation of optomechanical coupling with COMSOL

For the mechanical mode, symmetry is just set but choosing a boundary and declaring it to be a symmetry plane. Additionally, fixed boundaries are chosen, which represent the attachment of the device to the substrate. This method of attachment or fixing to the substrate is valid as long as no loss or coupling between mechanical modes is simulated. If the losses into the bulk are important, the fixed boundary needs to be set to a more remote location.

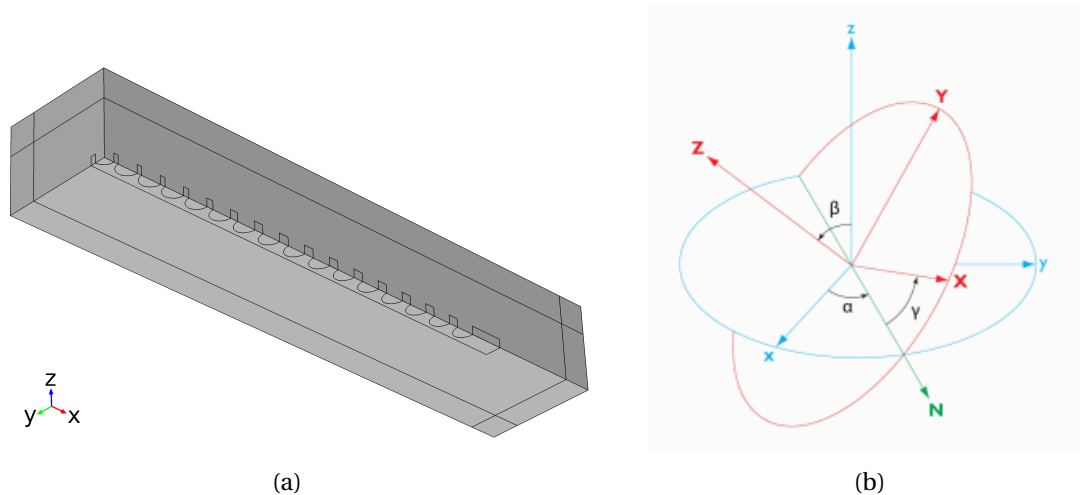


Figure C.1 – (a) COMSOL model of 1D PhC. Due to symmetry, only one eighth of the structure needs to be simulated. (b) Euler angles used to define the device orientation with respect to the crystal lattice with COMSOL.

Anisotropic material properties and crystal orientation

For mechanics the relation between stress and strain for specific crystal orientations is given by the elastic modulus. This can be entered into COMSOL, if it is not included in the material database. For both Si and GaP, the elastic properties are anisotropic, so it is important to set the model to "Anisotropic" and be aware of whether Voigt or standard notation is used. This is important for Si as well as for GaP. The correct orientation of the device with respect to the crystal lattice must also be considered (compare subsection 6.2.1.1). The alignment of the device can be changed by applying a rotated coordinate system. For GaP this means a rotation about $\alpha = 45^\circ$, as our devices are aligned along the [110] direction of the crystal lattice (see Figure C.1(b)).

Boundary conditions

To reflect the quasi infinite environment of the PhC and prevent any back reflection of scattered electromagnetic fields, a perfectly matched layer (PML) is used on the outside faces on all sides of the model. Within the PML, the coordinate system is scaled, leading to a decay of all

fields.

Mesh

The choice of an appropriate mesh is decisive for achieving correct simulation results. COMSOL offers various possibilities for organizing the mesh. The one used most is a tetrahedral mesh, as shown in Figure C.2. To keep computation time to the minimum necessary to achieve physically reasonable results, it makes sense to choose a different resolution for different parts of the model, depending on how accurate the results in each region need to be. For the PhCs, setting the mesh size to "Fine" for the complete device led to a reasonable scaling of the mesh by COMSOL, so the mesh was not further modified. So no further modification was applied. The physical plausibility of the results should be tested by refining the mesh and checking whether the simulation results change. The results will converge for finer meshes but at the same time computation time will go up, so that an optimum must be found.

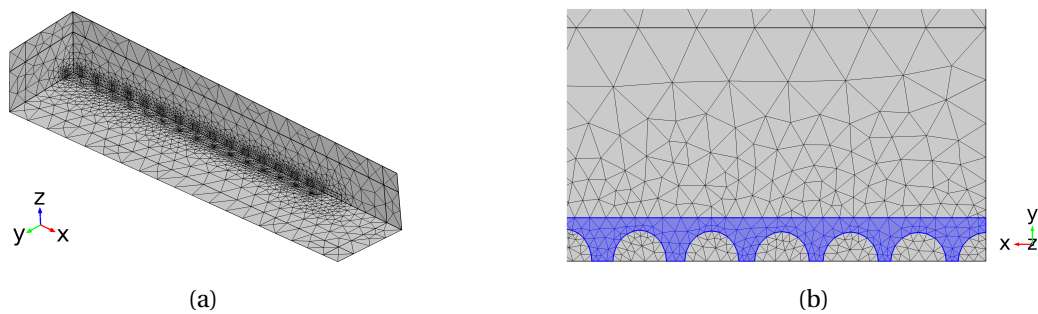


Figure C.2 – Meshed model of an eighth of a PhC.

Calculation of the optomechanical coupling strength

To predict the mechanical and optical behavior, two eigenfrequency studies are done, one only considering electromagnetic waves, the other considering solid mechanics. Only one optical eigenfrequency is evaluated. Because the mode spacing is quite wide, an initial guess of 193.5 THz for the eigenmode usually leads to the desired optical mode. For the mechanical mode, at least 20 eigenfrequencies are evaluated. The desired mechanical mode is then selected afterwards by inspecting the mode profile of the mode. If a breathing mode is desired, it makes sense to pick the mode with the highest center displacement. It is important to have the two eigenfrequency searches as steps in the same study. This ensures that the mesh is the same for both calculations. The settings for retaining the results of the optical eigenfrequency study after the mechanical eigenfrequency search are shown in Figure C.3.

To calculate the moving-boundary and the photoelastic contributions to the optomechanical

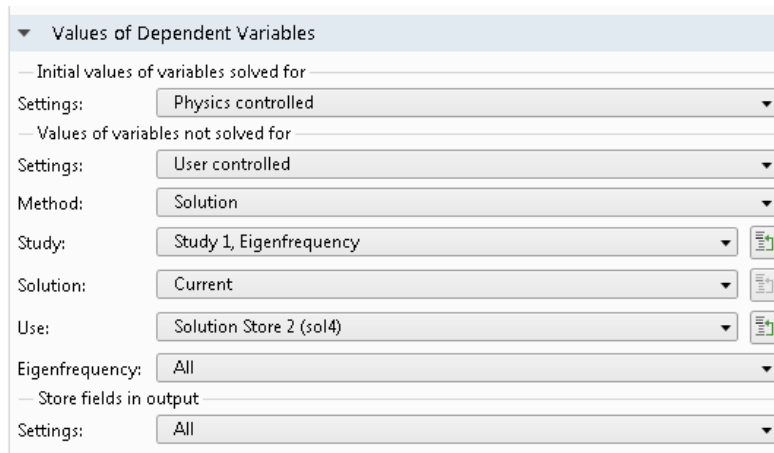


Figure C.3 – Settings for retaining the solution of the optical eigenfrequency study.

vacuum coupling rate, Equation 2.28 and Equation 2.29 need to be evaluated in COMSOL. Both have the same volume integral in the denominator. The former has a surface integral in the numerator, the latter another volume integral. These integrals can be evaluated directly within COMSOL. For a volume integral, the integration volume must be defined. For a surface integral, all relevant surfaces must be set. In each case, the integrand can be entered with MATLAB scripting. All relevant characteristics of the eigenmodes, e.g. displacement, electric field distribution or mechanical strain can be extracted from the results of the numerical simulation. The only drawback is that vectors, as for example $\mathbf{T}^{(m)} \cdot \mathbf{d}^T \cdot \mathbf{E}^{(n)}$ (see Equation 2.49) cannot be entered directly into COMSOL but have to be entered component wise (vector products or scalar products are not evaluated). The combination of numerator and denominator into Equation 2.28 and Equation 2.29 was done within a MATLAB script accessing the COMSOL model via LiveLink for MATLAB. Livelink allows on the one hand complete control over all settings of a model through MATLAB commands. On the other hand, results from simulation can be exported and further treated in MATLAB scripts.

The same method was employed to calculate the effective mass (see Equation 2.26). Here, the maximum displacement of the mechanical mode must be determined, which can also be done within COMSOL through a Global Evaluation.

Optimization of the PhC design for optomechanics

Figure C.4 illustrates the structure of the MATLAB routine used for the optimization of the PhC design. The design is described by a set of parameters, which are illustrated in Figure 6.1(b) and the additional parameters for the waveguide thickness t and length l . For the optimization, the parameters t and l are fixed, as t is given by the device layer thickness obtained from material growth and l does not matter for the simulation. The free parameters are w , a_s , r_{as} , r_{bs} , r_a and r_b . All parameters are defined relative to the unit cell size a . As the solutions of the eigenvalue problem are scale invariant, we can shift the solution's eigenfrequency to the

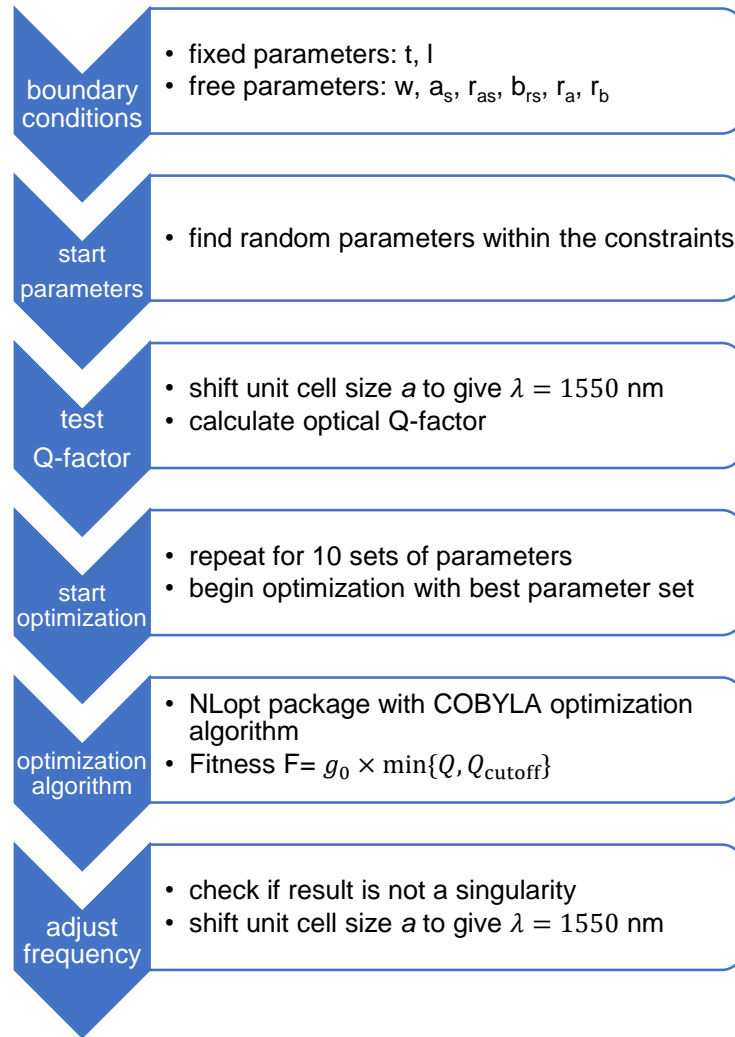


Figure C.4 – Structure of the program used for PhC design optimization.

desired frequency by scaling the complete design, which means adapting a .

The goal of the MATLAB routine is to find the set of parameters that leads to the best fitness $F = g_0 \times \min\{Q_o, 1.5 \times 10^6\}$. The quality factors are capped at 1.5×10^6 , to prevent considering results resulting from numerical errors. Before the actual optimization is started, the initial parameters and the parameter constraints have to be defined. The constraints are not necessary, but help to reduce computation time. They are inferred from experience with previous PhC designs. The initial parameters are chosen in various steps. First a set of random parameters within the constraints is generated. In the next step, the eigenfrequency of the design based on those parameters is calculated and then adjusted to 193.5 THz, which corresponds to a wavelength of 1550 nm, by changing the unit cell size a . Then the current optical quality factor Q_o is calculated. This procedure is repeated for 10 different sets of start parameters. The actual optimization algorithm is started with the most promising result.

The optimization algorithm is part of the package NLOpt [161]. The specific algorithm in use is the COBYLA (Constrained Optimization By Linear Approximations) algorithm [160]. This is only one possible choice of optimization algorithm. It was chosen because it does not require a derivative and accepts parameter constraints. Furthermore, COBYLA found solutions for as many as six parameters. The algorithm requires a set of start parameters, parameter constraints, a fitness function and breaking conditions. The breaking conditions were set to a runtime of two hours or 120 function calls.

Upon completion of the optimization, we check whether the solution is a singularity by performing parameter sweeps to ensure the continuity of the solution landscape. Finally, the eigenfrequency is again adjusted by scaling the unit cell size a .

This procedure is repeated 10 to 15 times, as the global maximum for the fitness is not always found. Additionally, some local maxima might be more attractive than the global maximum due to appealing combinations of coupling strength, geometric properties, mechanical eigenfrequency etc.

D Simulation of electromechanical coupling with COMSOL

Setup of the simulation

For simulating the electromechanical coupling in a GaP PhC, only the MEMS module is used. With the MEMS module, both solid mechanics and electrostatics can be simulated. To calculate the electromechanical coupling strength the displacement profile of the mechanical eigenmode and the electric field distribution between the electrodes are required. For the electrostatic properties, the photonic crystal beam, the electrodes and, if required, the surrounding air are included in the simulation. One of the electrodes is defined as ground, the other as a terminal, and the beam made of GaP is marked as piezoelectric material. In contrast, for the mechanical properties, the beam and the electrodes as well as the substrate are considered, with the bottom face of the substrate designated as being a fixed boundary. Also here GaP is designated as a piezoelectric material. To include the piezoelectric interaction, the multiphysics option "piezoelectric effect" is chosen, which links the two physics domains of solid mechanics and electrostatics within the software.

The treatment of the crystal orientation, the mesh, the symmetry and the anisotropic material properties is the same as for the simulation of the optomechanical coupling (see Appendix C)

Calculation of the electromechanical coupling strength

The actual simulation is done in two steps. First, an eigenfrequency study is performed to find the mechanical eigenmode. In the second step, a frequency domain study is used to actuate the beam, whereby an alternating voltage is applied. The terminal type is set to "voltage" and the amplitude of the applied voltage is set. From the frequency study, the resulting distribution of the electrical field and the mechanical displacement are obtained. To calculate the electromechanical coupling rate, Equation 2.49 needs to be evaluated, which requires the calculation of three volume integrals. The integration can be done directly within COMSOL. The integrals are then combined as in Equation 2.49 using MATLAB.

E Fully etched grating couplers with a Gaussian mode profile

In this thesis, an effort was made to improve the grating coupler design that is conventionally used in our research group. The purpose of a grating coupler is to couple light between a fiber facet and an integrated waveguide. The principle design rules for the couplers presented in section 4.2 lead to a combination of duty cycle DC and grating period Λ that depend on the wavelength λ , the coupling angle φ_c and the effective refractive index n_{eff} of the grating. A top view of such a coupler is shown in Figure E.1. The wedge-shaped teeth at the end of the structure serve to reduce back reflections. The design is made for fully etched grating couplers, which means that the guiding material is completely etched through to the underlying lower-refractive-index material. For the SOI wafers used for the fabrication of the silicon PhCs in chapter 8, this would mean a grating height of 220 nm. There are known methods on how to

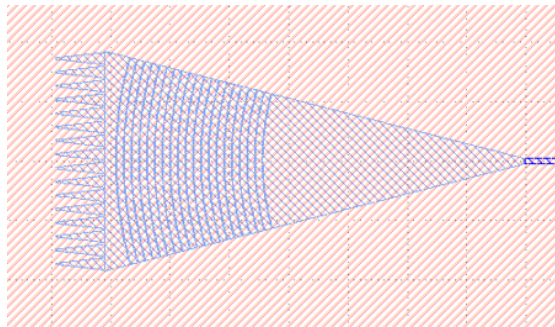


Figure E.1 – Grating coupler design applied in our research group.

improve the grating coupler efficiency. For example, partially etched grating couplers, where the grating teeth are not fully etched into the device layer, increase the coupling efficiency, as they reduce backreflection from the grating coupler [193, p.55]. A cladding also helps to increase coupling efficiency, if its refractive index fulfills $n_{\text{air}} < n_{\text{clad}} < n_{\text{grat}}$. Furthermore, losses due to diffraction from the grating toward the bottom side of the chip can be mitigated by including a bottom reflector in the device design. A method based on changing the grating design was presented by Waldhäusl et al. [194]. To improve the coupling efficiency, they eliminated higher grating orders by introducing an irregular grating with varying grating depth.

Appendix E. Fully etched grating couplers with a Gaussian mode profile

So the emission profile of the grating matches the Gaussian field distribution emitted from a fiber. Another way to achieve this emission pattern is to vary the duty cycle across the grating [142]. A summary of efficiencies attained with various techniques is listed in Table E.1. The designs are all for SOI wafers. The last two examples were fabricated in the BRNC.

Source	Structure	Measured efficiency	Simulated efficiency
[142, 195]	basic grating	31%	37%
	basic grating, cladding	34%	44%
	basic grating, bottom reflector		79%
	Gaussian, cladding, bottom reflector		92%
[196]	basic grating	12.6 %	
	basic grating, cladding	20%	

Table E.1 – Performance of published grating coupler designs. All designs are for partial etch in SOI wafers.

Improving the focusing grating coupler design

Because the fabrication process of the silicon PhCs requires high dimensional accuracy, the number of etch steps affecting the device layer is kept at a minimum. Instead of partially etched gratings, we use fully etched gratings, which require one less etch step. We also avoid using a cladding, which would have to be removed in the region of the PhCs and would involve another process step potentially affecting the PhCs. We aim therefore for fully etched couplers with a Gaussian emission profile. A suitable design has already been published [197] but not yet tested experimentally. The design was optimized in a way that the duty cycle and the period of the innermost grating grooves were individually adapted while leaving the outer grooves uniformly periodic. Changing more than the five innermost grooves did not lead to further improvement in the coupling efficiency, which was 38.7%.

To test the performance of these "Gaussian" couplers, a test series of devices was fabricated.

groove #	1	2	3	4	5+
period [nm]	721.6	656.0	716.8	774.9	775.5
duty cycle	0.836	0.846	0.790	0.720	0.717

Table E.2 – Parameters for grating couplers simulated by Spieser et al.[197] for a transmitted field with a Gaussian profile.

For comparison we included a number of conventional grating couplers on the same chip.

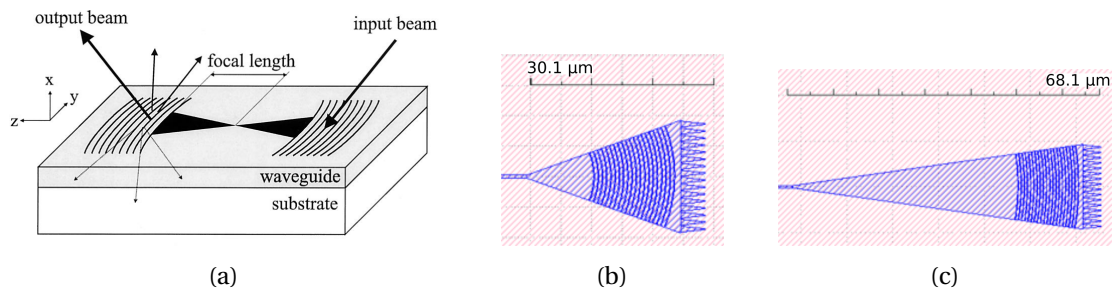


Figure E.2 – Considerations for the improvement of the grating coupler design. (a) Schematic of the transmission through grating couplers embedded in a slab waveguide [194]. For a ridge waveguide, the focal point of the grating can be placed at various positions in of before the attached waveguide. (b),(c) The length of the grating coupler determines its opening angle and the distance of the grating from the focal point.

The following additional questions concerning the grating coupler design were also addressed:

- Where should the focal point of the focusing grating couplers lie with respect to the connected waveguide?
- Do the teeth at the end of the couplers make a difference?
- How long should the grating coupler be, or equivalently, what is the optimum distance between the grating and the focal point?
- Should the end of the coupler be rounded to match the grating profile instead of being flat?

The fabricated chip therefore included four different designs:

1. Gaussian couplers with varying lengths
2. Conventional couplers with varying lengths
3. Conventional couplers with an offset of the focal point position
4. Conventional couplers without teeth and with round ends

For the Gaussian devices a second version of the dimensions was included in the tests to compensate for possible overetching by 5 nm during dry etching. For the conventional couplers, three combinations of duty cycle DC and period Λ that had performed well on a previous test chip (see Table E.3) were tested. This also gives the reference point for potential improvements.

Evaluation of the transmission measurements

To evaluate the performance of the various grating couplers, the transmission through a pair of them connected with a straight waveguide with a length of 400 μm was measured. The light

Appendix E. Fully etched grating couplers with a Gaussian mode profile

Design number	Period [nm]	Duty cycle	Loss per coupler [dB]	Coupling efficiency
1	666	0.85	-7.8	16.6
2	704	0.80	-8.3	14.8
3	694	0.80	-8.14	15.4

Table E.3 – Performance of conventional fully etched grating couplers fabricated of SOI in the BRNC.

from a tunable infrared laser was coupled through a cleaved single-mode fiber into the input grating coupler. The transmitted light was gathered with a second cleaved single-mode fiber and sent to a power meter.

A clear statement could immediately be made regarding the ends of the grating couplers: Whether the ends were flat, rounded, or terminated with wedge-shaped teeth had no noticeable influence on coupling efficiency or the appearance of interference fringes due to reflection between couplers at opposite ends of the connecting waveguide.

Length of the grating couplers

To answer the question, whether the length of the grating coupler, that is the distance from the grating to the waveguide, matters, the device length is plotted versus the coupling efficiency of a single coupler for the conventional coupler designs and the Gaussian couplers (see Figure E.3). Independent of device design, the optimum length seems to be around 50 μm , however the coupling efficiency changes by only 5% over the range of tested lengths.

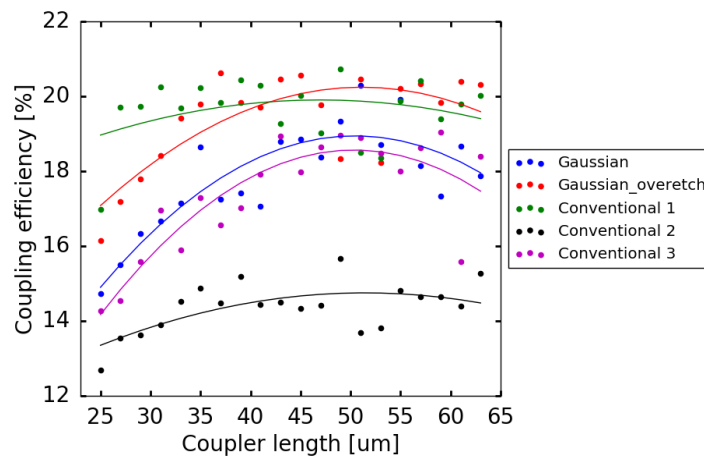


Figure E.3 – Grating coupler efficiency versus coupler length.

Position of focal point with respect to waveguide

From the evaluation of the coupler transmission as a function of offset in position of the grating's focal point (see Figure E.4), it seems that the current conventional position with no offset seems ideal, because for two of the three design there is a transmission maximum. Again, the variation in coupling efficiency over the measured offset range is small, only about 3%. It seems that this parameter is not critical.

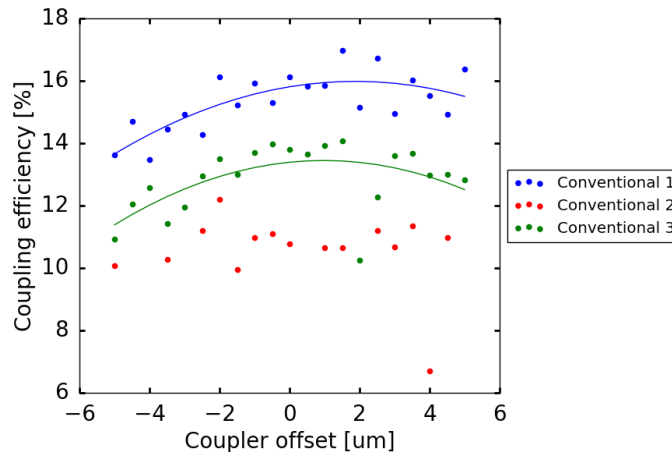


Figure E.4 – Grating coupler efficiency versus focal point position.

Overall coupling efficiency

The Gaussian couplers as well as design 1 of the conventional couplers (see Table E.3) achieved up to 21% coupling efficiency per coupler. The transmission profiles for these two coupler designs are shown in Figure E.5. For an uncladded grating, this coupling efficiency is a good result and an improvement compared to the starting reference devices (compare Table E.3). The performance of the Gaussian couplers is not bad but below the simulated coupling efficiency of 38.7%. One explanation might be the differing alignment of the fiber with respect to the grating coupler on the input and the output side of the device. Only if they are symmetric, will the maximum transmission be achieved. The measured coupling efficiency depends upon the cleaved fibers and their alignment at least as much as on the grating geometry. A method to overcome this is measuring in reflection, as then input and output alignment are automatically identical and therefore no signal will be lost due to incorrect alignment.

From the transmission profiles of the Gaussian and the conventional gratings shown in Figure E.5, another advantage of the Gaussian profile becomes clear: The interference fringes are much smaller for a Gaussian grating. We believe that the two conventional gratings form Bragg reflectors, creating a resonant cavity between the couplers. Presumably the non-periodic structure of the Gaussian gratings is responsible for drastically reducing this effect.

Appendix E. Fully etched grating couplers with a Gaussian mode profile

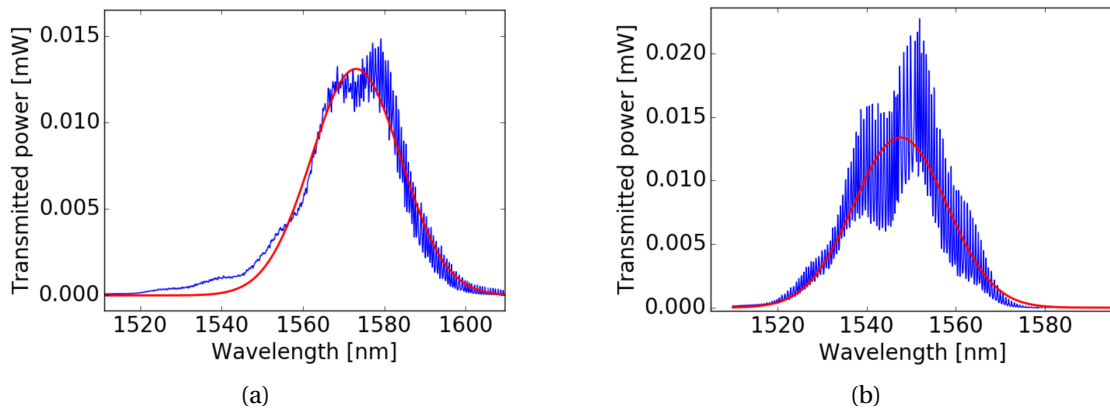


Figure E.5 – Transmission profile of the optimized grating couplers, (a) Gaussian coupler and (b) conventional grating.

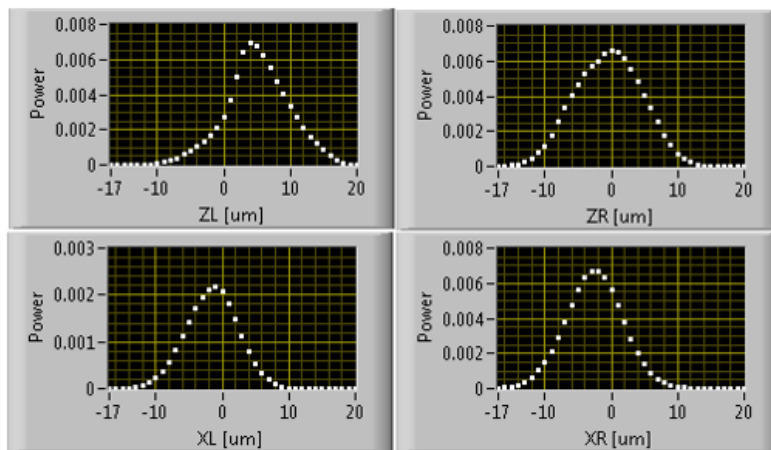


Figure E.6 – Transmission through a pair of couplers connected by a waveguide when tuning the left and right fiber position along (top) and perpendicular (bottom) to the coupler.

Conclusion

The grating coupler efficiency of the conventional couplers was improved by 5%. Furthermore the Gaussian couplers were tested, but their coupling efficiency was not found to be an improvement compared to the conventional design. However, the interference fringes in the transmission spectrum are much smaller for the Gaussian design. This study revealed how important the proper alignment of the cleaved fibers above the grating couplers is. As a consequence, the fiber mounts were modified: Instead of fixing the fiber cores with a scotch tape in a trench, a syringe needle is mounted in the trench and the cleaved fiber pushed through it (see Figure E.7). In this way we ensure that the fibers on the input and output side have the same angle with respect to the grating coupler.

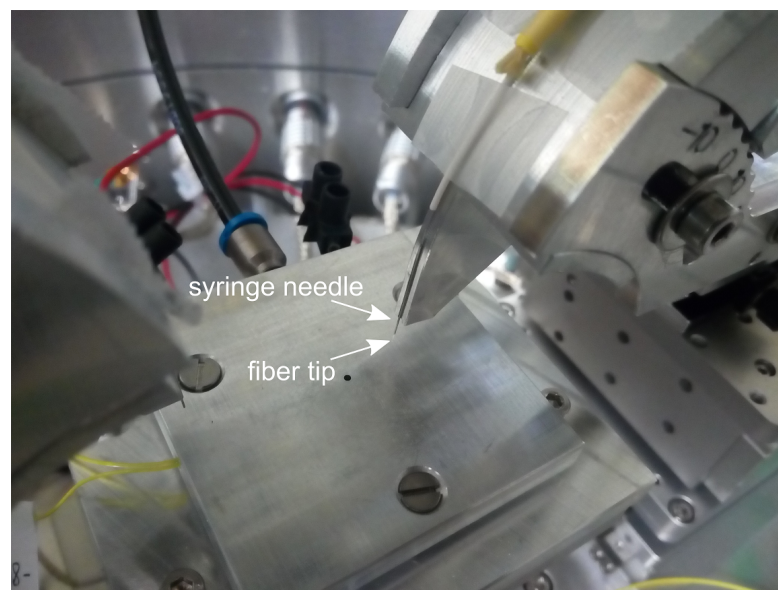


Figure E.7 – Improved design of fiber mount. A syringe needle tip is glued on the tip of the mount and the fiber is fed through the needle, allowing accurate alignment of the fiber.

F Coplanar waveguide resonators made of Nb

As a next step towards microwave-to-optical transduction, superconducting microwave resonators need to be combined with the PhCs to enable the piezoelectric actuation of the mechanical mode. An impressive example, where a bulk resonator made of AlN was coupled to a superconducting microwave resonator made of NbTiN, was published in Han et al. [198]. The system reached the strong-coupling regime with a cooperativity of $C > 2000$ and a mechanical quality factor of $Q = 7.5 \times 10^5$. Other materials besides NbTiN that can be used for superconducting microresonators are listed in Table F.1.

material	T_c [K]	B_c [T]
TiN	3.4	5
Al	1.2	0.01
In	3.4	0.03
NbTiN	16	13
Nb	9.25	0.2

Table F.1 – Superconducting materials and their transition temperature T_c and critical magnetic field B_c considered for electrode implementation with the PhCs. The values are taken from [199](Al and In), [200] (TiN), [201](NbTiN) and [202, 199](Nb).

For our purpose, it is firstly of interest that the electrodes can be fabricated in the BRNC and secondly, that $T_c > 3K$ as this is the temperature that can be reached with our cryostat (Variable Temperature Insert (VTI)-Cryostat). Therefore we cannot use Al despite its wide use in the community of superconducting quantum circuits. Indium would be an interesting alternative, as metal-metal bonding is possible with this material, providing a simple technique for including a bottom electrode in the wafer bonding procedure [203]. As indium tends to diffuse into other materials, it is not allowed to be processed in the BRNC. The expected quality of NbTiN fabricated in the BRNC is not very high, because there is no dedicated tool for the sputter process. This leaves TiN or Nb as possibilities for the electrodes. We choose Nb to perform initial tests to confirm superconductivity.

Device fabrication

Two different types of Nb devices were fabricated: For four-point measurements used to confirm superconductivity, four pads connected by a thin bar were required. Subsequently, coplanar waveguide resonators on intrinsic silicon were prepared. The fabrication of both types of devices is explained in this paragraph.

Nb deposition by magnetron sputtering

We deposited Nb deposited by magnetron sputtering (von Ardenne, CS320S) on oxidized silicon wafers for devices made for the four-point measurements and on an intrinsic silicon wafer for coplanar waveguide resonators. The various recipes for sputtering of Nb in the literature all involve DC sputtering at room temperature and with DC sputtering. The chamber pressure ranges from 3 to 20 μbar and the applied voltage is between 150 V and 410 V¹. Lower chamber pressure is generally better, as then there is usually less contamination. The argon flow, which can be set on the tool in the BRNC, is not mentioned in the recipes found in the literature. For initial tests, we chose 20 sccm. The final recipe employed for the devices is shown in Table F.2. A sputter time of 120 s lead to a layer thickness of 66 nm. For the coplanar waveguide resonators, a thicker layer is desired. Therefore the sputter time was increased to 364 s, which gave to a layer thickness of 166 nm. To remove the native oxide on the intrinsic silicon wafers used for the resonators, an inverse sputter etch was applied for 2 min prior to the deposition of the Nb. Figure F.1 shows AFM and SEM images of the deposited Nb films. Nb forms columnar grains of varying size, depending on sputtering gas (Ar) pressure, power, deposition time and substrate temperature [204]. The grain size can have an influence on the critical temperature. The RMS surface roughness was around 3 nm for the 66-nm films and 2.6 nm for the 166-nm films.

Parameter	Value
Presputter time [s]	180
DC power [W]	250
Sputter pressure [μbar]	10
Ar flow [sccm]	20
Temperature [$^{\circ}\text{C}$]	20
Current [A]	0.97
Voltage [V]	275

Table F.2 – Process parameters for Nb magnetron sputtering.

¹The voltage cannot be set directly on our magnetron sputter tool. Instead, the power is set and the resulting voltage and current are read off during the process. The current is expected to be around 1 A.

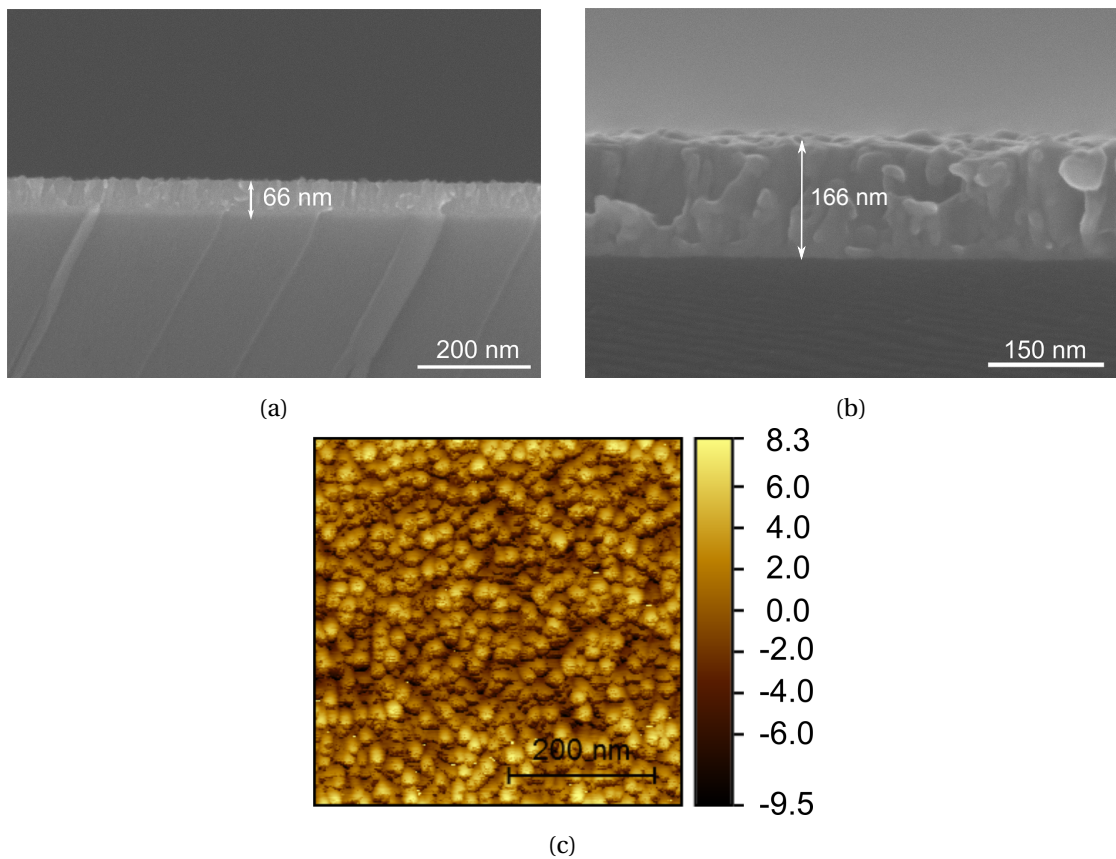


Figure F.1 – Magnetron sputtered Nb films. (a) SEM image of a cleaved Nb film sputtered on an oxidized silicon wafer with a sputter time 120 s and a thickness of 66 nm. (b) Nb film sputtered on intrinsic silicon with a sputter time of 364 s and a thickness of approximately 160 nm. (c) AFM image of a 500 nm × 500 nm region of the sample shown in (a) with a RMS-surface roughness of 3 nm.

Device patterning

Different resists were used for the fabrication of the devices for the four-point measurement and the coplanar waveguide resonators. The former were defined by spin coating HSQ6 (5s at 500 rpm, 60 s at 6000 rpm, acceleration 2000 rpm/s). For the resonators, the positive photoresist AZ6612 was used instead of HSQ. Devices were subsequently dry-etched with an ICP-RIE process using a mixture of Cl₂ and Ar. The etch rate was determined to be 180 nm/min. The HSQ was removed by submerging the sample into dilute HF (5%). In a previous test, Nb was not found to etch in HF. Optical microscope images of the final devices are shown in Figure E2.

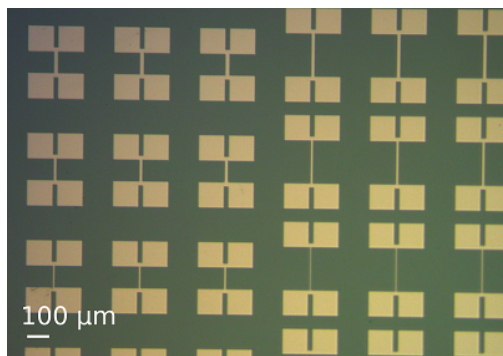
The removal of the photoresist after etching of the resonators turned out to be rather difficult. Various cycles in different solvents such as Acetone, dimethyl sulfoxide (DMSO) or N-methyl-2-pyrrolidone (NMP) left remnants of the resist on the Nb. Finally, an O₂ plasma etch in the RIE tool for 2 min at 100 W removed the residues. Such O₂ plasma treatments should in generally be avoided, as Nb is known to form undesired oxides. An alternative for future samples is to use of an SiO₂ hardmask photolithographically patterned onto the Nb film prior to etching, which would prevent direct contact of photoresist and metal.

Parameter	Value
Temperature [°C]	30
Pressure [mTorr]	3
Cl ₂ flow [sccm]	10
Ar flow [sccm]	30
DC bias [V]	300
RF power [W]	100
ICP power [W]	500

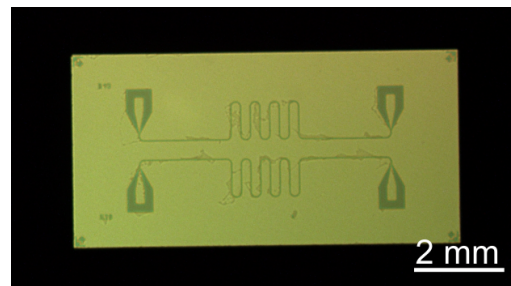
Table F.3 – ICP-RIE process for Nb etching.

Confirming superconductivity with four-point probe measurements

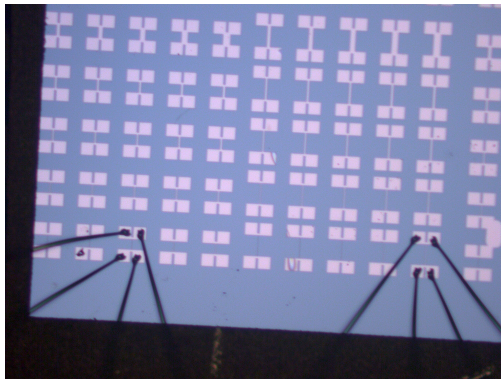
For measurements with a dip stick in our cryostat (VTI-Cryostat), the chips were glued onto a sample holder, which consisted of two pieces, a frame and a bottom plate. The frame has multiple copper contacts to which individual devices were wire bonded enabling connection to the circuitry of the experiment Figure E2 (c). Afterwards the carrier was mounted onto the dip stick and put into the cryostat. To test for superconductivity, the temperature was decreased and a four-point probe measurement was performed: A current is applied between two pads on different ends of the beam. The electric potential is measured across the two remaining pads. This allows determination of the electrical resistance, which is done at various temperatures. An example for such a measurement is shown in Figure E3(a). Once the temperature drops below the critical temperature T_c , the resistance goes to zero. In this case, a critical temperature of $T_c = 7.7$ K could be inferred, which is much lower than the values reported in the literature. The reason is presumably a measurement inaccuracy due to the



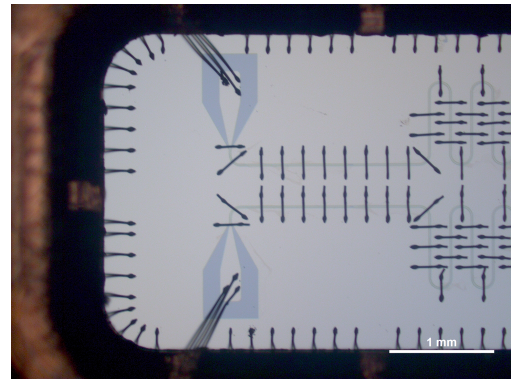
(a)



(b)



(c)



(d)

Figure F2 – Optical microscope images of fabricated Nb devices. (a) Devices for four-point measurements and (b) diced chip (4 mm × 8 mm) with two coplanar waveguide resonators. The imperfections in the Nb film visible in the image are due to residues from the photoresist. (c) and (d) Chips mounted into sample holders with wire-bonded devices allowing connection with the circuitry of the experiment.

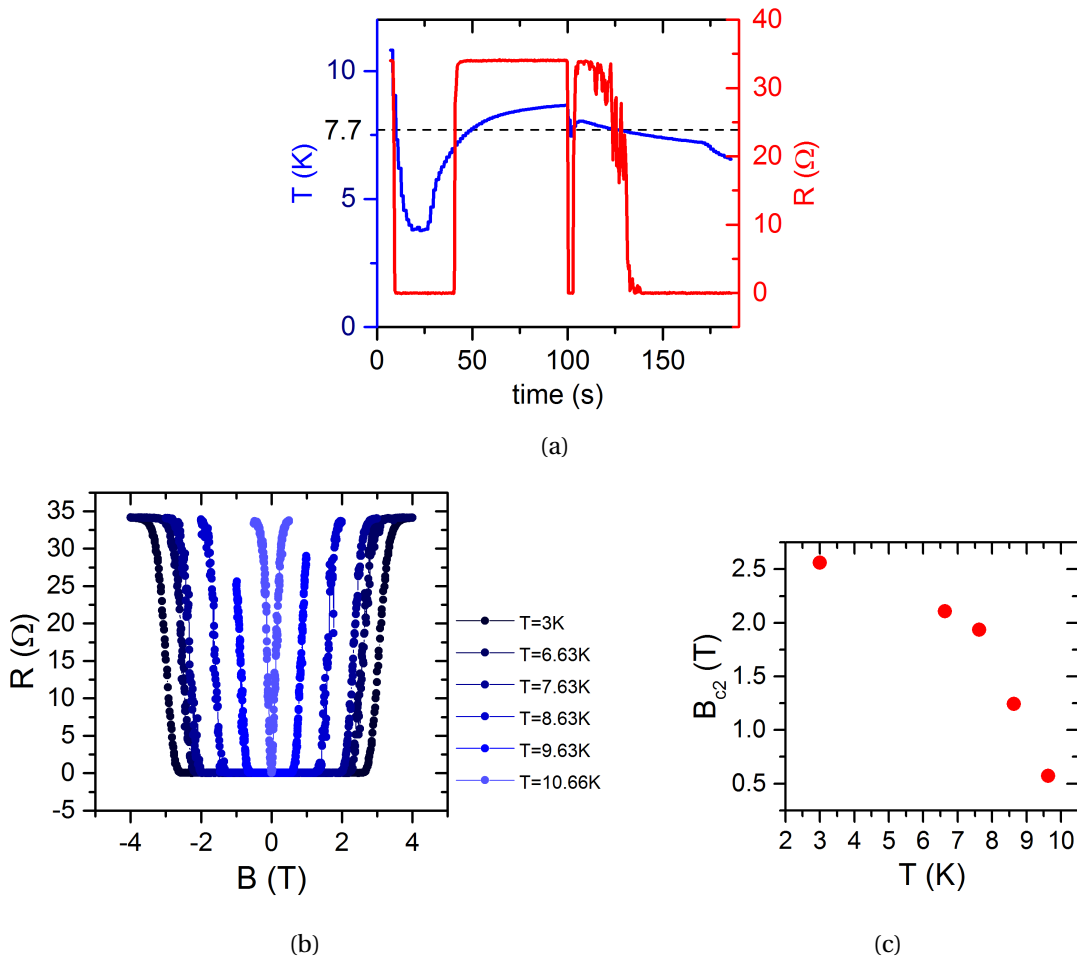


Figure E3 – Four terminal sensing measurement for determining the critical temperature and the critical magnetic field for Nb electrodes. (a) Temperature variation in the cryostat plotted together with the measured resistance R . (b) Magnetic field sweep for various temperatures T . The jump in resistance corresponds to breakdown of superconductivity and occurs at the critical field B_{c2} for a given temperature T . (c) Dependence of the critical field B_{c2} on temperature.

position of the thermistor on the dip stick, which is different from the sample position. Another method to infer the critical temperature is to measure the critical field $B_{c2}(T)$, for which superconductivity breaks down for a type II superconductor. In this case, a sweep of the magnetic field strength is performed for at a fixed temperature T and the transitions from normal conductivity to superconductivity are recorded (see Figure E3)(b). The dependence of the critical field on temperature is given by $B_{c2}(T) = B_{c2|T=0}(1 - (\frac{T}{T_c})^2)$. Although there are too few data points for a precise fit, the estimated x-intercept of the data is around 10 K. This number is slightly higher than the values given in literature.

Coplanar waveguide resonators

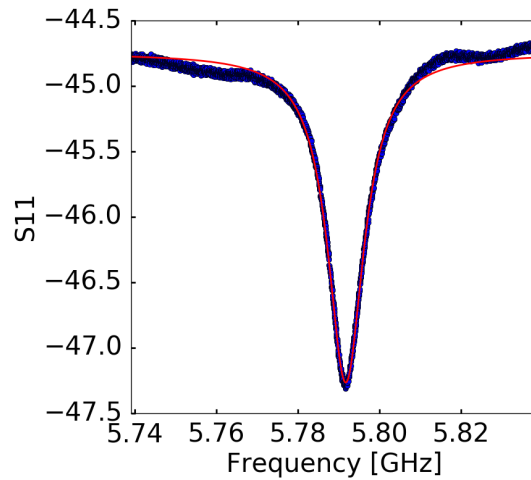


Figure E4 – Response curve of a Nb coplanar waveguide resonator in a reflection measurement. The quality factor is around $Q = 500$.

For the transduction of microwave to optical qubits, superconducting resonators are needed. After confirming the superconductivity of the Nb layers deposited in the BRNC, the next step is the fabrication of coplanar waveguide resonators [166]. The design of such a resonator is shown in Figure E2(b). Its resonance frequency is determined by the resonator length and its loaded quality factor by its capacitive coupling to input and output transmission lines. The characterization is performed in a dilution refrigerator, which reaches temperatures in the low mK range. The sample is mounted in a copper housing and the two resonators on the chip are wire bonded to the frame of the housing (see Figure E2(d)). Numerous air bridges connecting the ground planes on the two sides of the resonator prevent stray fields. After cooling down the sample, a reflection measurement is performed on each of the sample inputs. Unfortunately, only one measurement showed a clear resonance. The resonance frequency is 5.79 GHz. The measured quality factor is $Q = 500$. From the depth of the resonance dip an intrinsic quality factor of $Q_i = 1840$ is inferred. This is far less than the expected quality factor, which can easily reach several hundred thousands [205, 206]. Also, the frequency deviates from the expected design frequency of 7 GHz. As the measurement was the first of its kind to be conducted in

Appendix F. Coplanar waveguide resonators made of Nb

this setup, it needs to be repeated after testing samples with known properties to confirm the correct operation of the setup.

Bibliography

- [1] E. F. Schubert, "History of light-emitting diodes," in *Light-emitting diodes*. Cambridge: Cambridge University Press, 2006, ch. 1, pp. 1–26.
- [2] M. Pilkuhn and L. M. Foster, "Green luminescence from solution-grown junctions in GaP containing shallow donors and acceptors," *IBM Journal of Research and Development*, vol. 10, no. 2, pp. 122–129, 1966.
- [3] J. Václavík and D. Vápenka, "Gallium Phosphide as a material for visible and infrared optics," in *EPJ Web of Conferences*, vol. 48, 2013, pp. 1–4.
- [4] Oomlout, "5mm Green LED," 2009. [Online]. Available: https://commons.wikimedia.org/wiki/File:5mm{}_Green{}_LED.jpg
- [5] Semiconductor Wafer Inc., "GaP wafer." [Online]. Available: <http://www.semiwafer.com/images>
- [6] H. Mori, M. Ogasawara, M. Yamamoto, and M. Tachikawa, "New hydride vapor phase epitaxy for GaP growth on Si," *Appl. Phys. Lett.*, vol. 51, no. 16, pp. 1245–1247, 1987.
- [7] H. Emmer, C. T. Chen, R. Saive, D. Friedrich, Y. Horie, A. Arbabi, A. Faraon, and H. A. Atwater, "Fabrication of Single Crystal Gallium Phosphide Thin Films on Glass," *Scientific Reports*, vol. 7, no. 1, p. 4643, 2017.
- [8] K. Rivoire, A. Faraon, and J. Vučković, "Gallium phosphide photonic crystal nanocavities in the visible," *Applied Physics Letters*, vol. 93, p. 063103, 2008.
- [9] K. Rivoire, A. Kinkhabwala, F. Hatami, W. T. Masselink, Y. Avlasevich, K. Müllen, W. E. Moerner, and J. Vučković, "Lithographic positioning of fluorescent molecules on high-Q photonic crystal cavities," *Applied Physics Letters*, vol. 95, no. 123113, 2009.
- [10] D. Englund, B. Shields, K. Rivoire, F. Hatami, J. Vučković, H. Park, and M. D. Lukin, "Deterministic Coupling of a Single Nitrogen Vacancy Center to a Photonic Crystal Cavity," *Nano Lett.*, vol. 10, pp. 3922–3926, 2010.
- [11] X. Gan, N. Pervez, I. Kyriassis, F. Hatami, and D. Englund, "A high-resolution spectrometer based on a compact planar two dimensional photonic crystal cavity array," *Applied Physics Letters*, vol. 100, no. 231104, 2012.

Bibliography

- [12] K. Rivoire, Z. Lin, F. Hatami, W. T. Masselink, and J. Vučković, “Second harmonic generation in gallium phosphide photonic crystal nanocavities with ultralow continuous wave pump power,” *Optics Express*, vol. 17, no. 25, pp. 22 609–22 615, 2009.
- [13] G. Shambat, K. Rivoire, J. Lu, F. Hatami, and J. Vučković, “Tunable-wavelength second harmonic generation from GaP photonic crystal cavities coupled to fiber tapers,” *Optics Express*, vol. 18, no. 12, pp. 12 176–84, 2010.
- [14] K. Rivoire, Z. Lin, F. Hatami, and J. Vučković, “Sum-frequency generation in doubly resonant GaP photonic crystal nanocavities,” *Applied Physics Letters*, vol. 97, no. 043103, 2010.
- [15] P. E. Barclay, K.-M. Fu, C. Santori, and R. G. Beausoleil, “Hybrid photonic crystal cavity and waveguide for coupling to diamond NV-centers,” *Optics Express*, vol. 17, no. 12, pp. 9588–9601, 2009.
- [16] D. P. Lake, M. Mitchell, H. Jayakumar, L. F. Dos Santos, D. Curic, and P. E. Barclay, “Efficient telecom to visible wavelength conversion in doubly resonant gallium phosphide microdisks,” *Applied Physics Letters*, vol. 108, no. 031109, 2016.
- [17] M. Mitchell, A. C. Hryciw, and P. E. Barclay, “Cavity optomechanics in gallium phosphide microdisks,” *Applied Physics Letters*, vol. 104, no. 141104, 2014.
- [18] P. Seidler, K. Lister, U. Drechsler, H. Rothuizen, J. Hofrichter, and T. Stöferle, “Photonic crystal nanobeam cavities with an ultrahigh quality factor-to-modal volume ratio,” *Optics Express*, vol. 21, no. 26, pp. 32 468–32 483, 2013.
- [19] R. Riedinger, S. Hong, R. A. Norte, J. A. Slater, J. Shang, A. G. Krause, V. Anant, M. Aspelmeyer, and S. Gröblacher, “Non-classical correlations between single photons and phonons from a mechanical oscillator,” *Nature*, vol. 530, no. 7590, pp. 313–316, 2016.
- [20] P. E. Barclay, K. M. C. Fu, C. Santori, and R. G. Beausoleil, “Chip-based microcavities coupled to nitrogen-vacancy centers in single crystal diamond,” *Applied Physics Letters*, vol. 95, no. 191115, 2009.
- [21] N. Thomas, R. J. Barbour, Y. C. Song, M. L. Lee, and K. M. C. Fu, “Waveguide-integrated single-crystalline GaP resonators on diamond,” *Optics Express*, vol. 22, no. 11, pp. 13 555–13 564, 2014.
- [22] M. Gould, S. Chakravarthi, I. R. Christen, N. Thomas, S. Dadgostar, Y. Song, M. L. Lee, F. Hatami, and K.-M. C. Fu, “Large-scale GaP-on-diamond integrated photonics platform for NV center-based quantum information,” *Journal of the Optical Society of America B*, vol. 33, no. 3, p. B35, 2016.
- [23] K. Schneider, P. Welter, Y. Baumgartner, H. Hahn, L. Czornomaz, and P. Seidler, “Gallium phosphide-on-silicon dioxide photonic devices,” *Journal of Lightwave Technology*, vol. 36, no. 14, pp. 2994–3002, 2018.

- [24] L. Czornomaz, N. Daix, P. Kerber, K. Lister, D. Caimi, C. Rossel, M. Sousa, E. Uccelli, and J. Fompeyrine, "Scalability of Ultra-thin-body and BOX InGaAs MOSFETs on Silicon," in *Proc. of the European Solid-State Device Research Conference (ESSDERC)*, no. 6, Bucharest, Romania, 16 - 20 September 2013, 2013, pp. 143–146.
- [25] J. H. Epple, C. Sanchez, T. Chung, K. Y. Cheng, and K. C. Hsieh, "Dry etching of GaP with emphasis on selective etching over AlGaP," *Journal of Vacuum Science and Technology B: Microelectronics and Nanometer Structures Processing, Measurement, and Phenomena*, vol. 20, no. 6, p. 2252, 2002.
- [26] P. Seidler, "Optimized process for fabrication of free-standing silicon nanophotonic devices," *Journal of Vacuum Science and Technology B, Nanotechnology and Microelectronics: Materials, Processing, Measurement, and Phenomena*, vol. 35, no. 3, p. 031209, 2017.
- [27] A. Martin, D. Sanchez, S. Combri , A. de Rossi, F. Raineri, S. Combri , A. de Rossi, and F. Raineri, "GaInP on oxide nonlinear photonic crystal technology," *Optics Letters*, vol. 42, no. 3, p. 599, 2017.
- [28] Y. Ueno, V. Ricci, and G. I. Stegeman, "Second-order susceptibility of Ga_{0.5}In_{0.5}P crystals at 1.5 μm and their feasibility for waveguide quasi-phase matching," *J.Opt.Soc.Am.B*, vol. 14, no. 6, pp. 1428–1436, 1997.
- [29] S. Combri , Q. V. Tran, A. De Rossi, C. Husko, and P. Colman, "High quality GaInP nonlinear photonic crystals with minimized nonlinear absorption," *Applied Physics Letters*, vol. 95, no. 22, pp. 1–4, 2009.
- [30] M. Dinu, F. Quochi, and H. Garcia, "Third-order nonlinearities in silicon at telecom wavelengths," *Applied Physics Letters*, vol. 82, no. 18, pp. 2954–2956, 2003.
- [31] M. Pu, L. Ottaviano, E. Semenova, and K. Yvind, "Efficient frequency comb generation in AlGaAs-on-insulator," *Optica*, vol. 3, no. 8, pp. 8–11, 2016.
- [32] U. D. Dave, B. Kuyken, F. Leo, S.-P. Gorza, S. Combrie, A. De Rossi, F. Raineri, and G. Roelkens, "Nonlinear properties of dispersion engineered InGaP photonic wire waveguides in the telecommunication wavelength range," *Optics Express*, vol. 23, no. 4, p. 4650, 2015.
- [33] B. J. M. Hausmann, I. Bulu, V. Venkataraman, P. Deotare, and M. Loncar, "Diamond nonlinear photonics," *Nature Photonics*, vol. 8, no. 5, pp. 369–374, 2014.
- [34] C. Xiong, W. Pernice, K. K. Ryu, C. Schuck, K. Y. Fong, T. Palacios, and H. X. Tang, "Integrated GaN photonic circuits on silicon (100) for second harmonic generation," *Optics Express*, vol. 19, no. 11, p. 10462, 2011.
- [35] D. Munk, M. Katzman, O. Westreich, M. B. Nun, Y. Lior, N. Sicron, Y. Paltiel, and A. Zadok, "Four-Wave Mixing in GaN Waveguides," in *CLEO*, vol. 1, 2018.

Bibliography

- [36] H. Jung, C. Xiong, K. Y. Fong, X. Zhang, and H. X. Tang, "Optical frequency comb generation from aluminum nitride microring resonator," *Optics Letters*, vol. 38, no. 15, p. 2810, 2013.
- [37] X. Ji, F. A. S. Barbosa, S. P. Roberts, A. Dutt, J. Cardenas, Y. Okawachi, A. Bryant, A. L. Gaeta, and M. Lipson, "Ultra-low-loss on-chip resonators with sub-milliwatt parametric oscillation threshold," *Optica*, vol. 4, no. 6, p. 619, 2017.
- [38] L. Razzari, D. Duchesne, M. Ferrera, R. Morandotti, S. Chu, B. E. Little, and D. J. Moss, "CMOS-compatible integrated optical hyper-parametric oscillator," *Nature Photonics*, vol. 4, no. 1, pp. 41–45, 2010.
- [39] J. Li, H. Lee, T. Chen, and K. J. Vahala, "Low-pump-power, low-phase-noise, and microwave to millimeter-wave repetition rate operation in microcombs," *Physical Review Letters*, vol. 109, no. 23, pp. 1–5, 2012.
- [40] X. Lu, J. Y. Lee, S. Rogers, and Q. Lin, "Optical Kerr nonlinearity in a high-Q silicon carbide microresonator," *Optics Express*, vol. 22, no. 25, p. 30826, 2014.
- [41] A. S. Barker and M. Ilegems, "Infrared lattice vibrations and free-electron dispersion in GaN," *Physical Review B*, vol. 7, no. 2, pp. 743–750, 1973.
- [42] J. Miragliotta and D. Wickenden, "Optical third-harmonic studies of the dispersion in $\chi(3)$ for gallium nitride thin films on sapphire," *Physical Review B*, vol. 50, no. 20, pp. 960–964, 1994.
- [43] W. Ching and M.-Z. Hang, "Calculation of optical excitations in cubic semiconductors. III. Third-harmonic generation," *Phys. Rev. B*, vol. 47, no. 15, pp. 9479–9491, 1993.
- [44] W. C. Hurlbut, K. L. Vodopyanov, P. S. Kuo, M. M. Fejer, and Y. S. Lee, "Multi-photon absorption and nonlinear refraction of GaAs in the mid-infrared," *Optics Letters*, vol. 32, no. 6, pp. 668–670, 2006.
- [45] L. Ottaviano, M. Pu, E. Semenova, and K. Yvind, "Low-loss high-confinement waveguides and microring resonators in AlGaAs-on-insulator," *Optics Letters*, vol. 41, no. 17, p. 3996, 2016.
- [46] E. Hecht, *Optics*, 4th ed. San Francisco: Addison Wesley, 2016.
- [47] C. Kittel, *Introduction to Solid State Physics*, 8th ed. New York: John Wiley, 1986.
- [48] J. Koch, T. M. Yu, J. Gambetta, A. A. Houck, D. I. Schuster, J. Majer, A. Blais, M. H. Devoret, S. M. Girvin, and R. J. Schoelkopf, "Charge-insensitive qubit design derived from the Cooper pair box," *Physical Review A - Atomic, Molecular, and Optical Physics*, vol. 76, no. 4, pp. 1–19, 2007.

- [49] H. Paik, D. I. Schuster, L. S. Bishop, G. Kirchmair, G. Catelani, A. P. Sears, B. R. Johnson, M. J. Reagor, L. Frunzio, L. I. Glazman, S. M. Girvin, M. H. Devoret, and R. J. Schoelkopf, "Observation of high coherence in Josephson junction qubits measured in a three-dimensional circuit QED architecture," *Physical Review Letters*, vol. 107, no. 24, pp. 1–5, 2011.
- [50] S. Pirandola and S. L. Braunstein, "Physics: Unite to build a quantum Internet," *Nature*, vol. 532, no. 7598, pp. 169–171, 2016.
- [51] J. Bochmann, A. Vainsencher, D. D. Awschalom, and A. N. Cleland, "Nanomechanical coupling between microwave and optical photons," *Nature Physics*, vol. 9, pp. 712–176, 2013.
- [52] R. W. Andrews, R. W. Peterson, T. P. Purdy, K. Cicak, R. W. Simmonds, C. A. Regal, and K. W. Lehnert, "Bidirectional and efficient conversion between microwave and optical light," *Nature Physics*, vol. 10, pp. 321–326, 2014.
- [53] K. C. Balram, M. I. Davanço, J. D. Song, and K. Srinivasan, "Coherent coupling between radiofrequency, optical and acoustic waves in piezo- optomechanical circuits," *Nature Photonics*, vol. 10, pp. 346–352, 2016.
- [54] A. Vainsencher, K. J. Satzinger, G. A. Peairs, and A. N. Cleland, "Bi-directional conversion between microwave and optical frequencies in a piezoelectric optomechanical device," *Applied Physics Letters*, vol. 109, no. 033107, pp. 322–323, 2016.
- [55] K. Y. Fong, L. Fan, L. Jiang, X. Han, and H. X. Tang, "Microwave-assisted coherent and nonlinear control in cavity piezo-optomechanical systems," *Physical Review A - Atomic, Molecular, and Optical Physics*, vol. 90, no. 5, pp. 1–5, 2014.
- [56] L. Li, T. Schröder, E. H. Chen, H. Bakhru, and D. Englund, "One-dimensional photonic crystal cavities in single-crystal diamond," *Photonics and Nanostructures - Fundamentals and Applications*, vol. 15, pp. 130–136, 2015.
- [57] T. Bağcı, A. Simonsen, S. Schmid, L. G. Villanueva, E. Zeuthen, J. Appel, J. M. Taylor, A. Sørensen, K. Usami, A. Schliesser, and E. S. Polzik, "Optical detection of radio waves through a nanomechanical transducer," *Nature*, vol. 507, no. 7490, pp. 81–85, 2014.
- [58] M. Winger, T. D. Blasius, T. P. M. Alegre, S. Meenehan, J. Cohen, and S. Stobbe, "A chip-scale integrated cavity-electro-optomechanics platform," *Optics Express*, vol. 19, no. 25, pp. 24 905–24 921, 2011.
- [59] P. B. Dieterle, M. Kalaei, J. M. Fink, and O. Painter, "Superconducting Cavity Electromechanics on a Silicon-on-Insulator Platform," *Phys. Rev. Appl.*, vol. 6, no. 014013, pp. 1–9, 2016.
- [60] J. M. Fink, M. Kalaei, A. Pitanti, R. Norte, L. Heinzle, K. Srinivasan, and O. Painter, "Quantum electromechanics on silicon nitride nanomembranes," *Nature Communications*, vol. 7, no. 12396, pp. 1–10, 2016.

Bibliography

- [61] I. Moaddel Haghighi, N. Malossi, R. Natali, G. Di Giuseppe, and D. Vitali, “Sensitivity-Bandwidth Limit in a Multimode Optoelectromechanical Transducer,” *Physical Review Applied*, vol. 9, no. 3, p. 34031, 2018.
- [62] M. Tsang, “Cavity quantum electro-optics,” *Phys.Rev. A*, vol. 81, no. 063837, pp. 1–5, 2010.
- [63] M. Tsang, “Cavity quantum electro-optics. II . Input-output relations between traveling optical and microwave fields,” *Phys.Rev.A*, vol. 84, no. 043845, pp. 1–8, 2011.
- [64] A. Rueda, F. Sedlmeir, M. C. Collodo, U. Vogl, B. Stiller, G. Schunk, D. V. . Strekalov, C. Marquardt, J. M. Fink, O. Painter, G. Leuchs, and H. G. L. Schwefel, “Efficient microwave to optical photon conversion : an electro-optical realization,” *Optica*, vol. 3, no. 6, pp. 597–604, 2016.
- [65] C. Javerzac-Galy, K. Plekhanov, N. R. Bernier, L. D. Toth, A. K. Feofanov, and T. J. Kippenberg, “On-chip microwave-to-optical quantum coherent converter based on a superconducting resonator coupled to an electro-optic microresonator,” *Physical Review A*, vol. 94, no. 5, pp. 1–5, 2016.
- [66] L. Fan, C.-L. Zou, R. Cheng, X. Guo, X. Han, Z. Gong, S. Wang, and H. X. Tang, “Superconducting cavity electro-optics: a platform for coherent photon conversion between superconducting and photonic circuits,” *arxiv*, vol. 1805.04509, pp. 1–17, 2018.
- [67] M. Hafezi, Z. Kim, S. L. Rolston, L. A. Orozco, B. L. Lev, and J. M. Taylor, “Atomic interface between microwave and optical photons,” *Physical Review A*, vol. 85, no. 020302, pp. 1–5, 2012.
- [68] X. Gao, Z.-Q. Yin, and T. Li, “High-speed quantum transducer with a single-photon emitter in an atomically thin resonator,” *arxiv*, vol. 1712.09245, pp. 1–12, 2017.
- [69] R. Hisatomi, A. Osada, Y. Tabuchi, T. Ishikawa, A. Noguchi, R. Yamazaki, K. Usami, and Y. Nakamura, “Bidirectional conversion between microwave and light via ferromagnetic magnons,” *Physical Review B*, vol. 93, no. 17, pp. 1–13, 2016.
- [70] L. A. Williamson, Y. H. Chen, and J. J. Longdell, “Magneto-optic modulator with unit quantum efficiency,” *Physical Review Letters*, vol. 113, no. 20, pp. 1–5, 2014.
- [71] T. P. Purdy, R. W. Peterson, P. L. Yu, and C. A. Regal, “Cavity optomechanics with Si_3N_4 membranes at cryogenic temperatures,” *New Journal of Physics*, vol. 14, no. 115021, pp. 1–17, 2012.
- [72] A. Safavi-Naeini, T. P. Mayer Alegre, J. Chan, M. Eichenfield, M. Winger, Q. Lin, J. T. Hill, D. E. Chang, and O. Painter, “Electromagnetically induced transparency and slow light with optomechanics,” *Nature*, vol. 472, pp. 69–73, 2011.

- [73] F. Lecocq, J. B. Clark, R. W. Simmonds, J. Aumentado, and J. D. Teufel, "Mechanically Mediated Microwave Frequency Conversion in the Quantum Regime," *Physical Review Letters*, vol. 116, no. 4, p. 043601, 2016.
- [74] P. Arrangoiz-Arriola, E. A. Wollack, M. Pechal, J. D. Witmer, J. T. Hill, and A. H. Safavi-Naeini, "Coupling a superconducting quantum circuit to a phononic crystal defect cavity," *arxiv*, vol. 1804.03625, pp. 1–9, 2018.
- [75] C.-I. Zou, X. Han, L. Jiang, and H. X. Tang, "Cavity piezomechanical strong coupling and frequency conversion on an aluminum nitride chip," *Phys.Rev.A*, vol. 94, no. 1, p. 013812, 2016.
- [76] P. Arrangoiz-Arriola and A. H. Safavi-Naeini, "Engineering interactions between superconducting qubits and phononic nanostructures," *Physical Review A*, vol. 94, no. 6, pp. 1–8, 2016.
- [77] K. C. Balram, M. I. Davanço, B. R. Ilic, J. H. Kyhm, J. D. Song, and K. Srinivasan, "Acousto-Optic Modulation and Optoacoustic Gating in Piezo-Optomechanical Circuits," *Physical Review Applied*, vol. 7, no. 2, pp. 1–9, 2017.
- [78] M. Miura, H. Murata, Y. Shiro, and K. Iishi, "Ionicity scale and piezoelectricity of crystals with zinblende- and wurtzite-type structure," *Journal of Physics and Chemistry of Solids*, vol. 42, no. 10, pp. 931–936, 1981.
- [79] G. Arlt and P. Quadflieg, "Piezoelectricity in III-V compounds with a phenomenological analysis of the piezoelectric effect," *Physics Status Solidi B*, vol. 25, no. 1, pp. 323–330, 1968.
- [80] E. Bernardini, V. Fiorentini, and D. Vanderbilt, "Spontaneous polarization and piezoelectric constants of III-V nitrides," *Physical Review B - Condensed Matter and Materials Physics*, vol. 56, no. 16, pp. R10 024–R10 027, 1997.
- [81] S. Y. Davydov, "Evaluation of physical parameters for the group III nitrides: BN, AlN, GaN, and InN," *Semiconductors*, vol. 36, no. 1, pp. 41–44, 2002.
- [82] R. Leijssen and E. Verhagen, "Strong optomechanical interactions in a sliced photonic crystal nanobeam," *Scientific Reports*, vol. 5, no. 15974, pp. 1–10, 2015.
- [83] L. Merrill, "Behavior of the AB-type compounds at high pressures and high temperatures," *Journal of Physical and Chemical Reference Data*, vol. 6, no. 4, pp. 1205–1252, 1977.
- [84] V. N. Bessolov, T. T. Dedegkaev, A. N. Efimov, N. F. Kartenko, and Y. P. Yakovlev, "Lattice constants of GaP, Al_xGa_{1-x}P and AlP crystals," *Sov. Phys. Solid State*, vol. 22, p. 1652, 1980.
- [85] M. B. Panish and H. C. Casey, "Temperature dependence of the energy GaP in GaAs and GaP," *Journal of Applied Physics*, vol. 40, no. 1, pp. 163–167, 1969.

Bibliography

- [86] W. Bond, "Measurement of the refractive indices of several crystals," *Journal of Applied Physics*, vol. 36, pp. 1674–1677, 1965.
- [87] Y. K. Yogurtçu, A. J. Miller, and G. A. Saunders, "Pressure dependence of elastic behaviour and force constants of GaP," *Journal of Physics and Chemistry of Solids*, vol. 42, no. 1, pp. 49–56, 1981.
- [88] M. M. Choy and R. L. Byer, "Accurate second-order susceptibility measurements of visible and infrared nonlinear crystals," *Physical Review B*, vol. 14, no. 4, pp. 1693–1706, 1976.
- [89] D. J. Wilson, K. Schneider, S. Hoenl, M. Anderson, T. J. Kippenberg, and P. Seidler, "Gallium Phosphide Nonlinear Photonics," *arxiv*, vol. 1808.03554, pp. 1–13, 2018.
- [90] B. Mytsyk, N. Demyanyshyn, and O. Sakkaruk, "Elasto-optic effect anisotropy in gallium phosphide crystals," *Applied Optics*, vol. 54, no. 28, pp. 8546–8553, 2015.
- [91] R. W. Boyd, *Nonlinear Optics*, 3rd ed. Oxford: Elsevier, 2008.
- [92] B. E. A. Teich and M. C. Saleh, "Nonlinear optics," in *Fundamentals of Photonics*. New York: Wiley, 1992, ch. 21, pp. 873–917.
- [93] R. W. Boyd, *Nonlinear Optics*, 2nd ed. Rochester, New York, USA: Elsevier, 2003.
- [94] G. P. Agrawal, *Nonlinear fiber optics*, 3rd ed., P. L. Kelley, I. P. Kaminow, and G. P. Agrawal, Eds. San Diego, CA, USA, London: Academic Press, 2001.
- [95] T. J. Kippenberg, S. M. Spillane, and K. J. Vahala, "Kerr-nonlinearity optical parametric oscillation in an ultrahigh-Q toroid microcavity," *Physical Review Letters*, vol. 93, no. 8, pp. 18–21, 2004.
- [96] Y. K. Chembo and N. Yu, "Modal expansion approach to optical-frequency-comb generation with monolithic whispering-gallery-mode resonators," *Physical Review A*, vol. 82, no. 3, pp. 1–18, 2010.
- [97] T. Carmon, Lan Yang, and K. Vahala, "Dynamical thermal behavior and thermal self-stability of microcavities," (*CLEO*). *Conference on Lasers and Electro-Optics, 2005.*, vol. 12, no. 20, pp. 4742–4750, 2004.
- [98] B. Min, L. Yang, and K. Vahala, "Controlled transition between parametric and Raman oscillations in ultrahigh-Q silica toroidal microcavities," *Applied Physics Letters*, vol. 87, no. 18, pp. 1–3, 2005.
- [99] M. Aspelmeyer, F. Marquardt, and T. J. Kippenberg, "Cavity optomechanics," *Reviews of Modern Physics*, vol. 86, no. 4, pp. 1391–1452, 2014.
- [100] J. D. Joannopoulos, S. G. Johnson, J. N. Winn, and R. D. Meade, *Photonic crystals - Molding the flow of light*, 2nd ed. Princeton and Oxford: Princeton University Press, 2008.

- [101] M. Borselli, T. J. Johnson, and O. Painter, “Beyond the Rayleigh scattering limit in high-Q silicon microdisks: theory and experiment,” *Optics Express*, vol. 13, no. 5, pp. 1515–1530, 2005.
- [102] M. H. P. Pfeiffer, J. Liu, A. S. Raja, T. Morais, B. Ghadiani, and T. J. Kippenberg, “Probing the loss origins of ultra-smooth Si₃N₄ integrated photonic waveguides,” *arxiv*, vol. 1802.08315, 2018.
- [103] T. Herr, K. Hartinger, J. Riemensberger, C. Y. Wang, E. Gavartin, R. Holzwarth, M. L. Gorodetsky, and T. J. Kippenberg, “Universal formation dynamics and noise of Kerr-frequency combs in microresonators,” *Nature Photonics*, vol. 6, no. 7, pp. 480–487, 2012.
- [104] A. A. Savchenkov, A. B. Matsko, W. Liang, V. S. Ilchenko, D. Seidel, and L. Maleki, “Kerr combs with selectable central frequency,” *Nature Photonics*, vol. 5, no. 5, pp. 293–296, 2011.
- [105] I. Favero and K. Karrai, “Optomechanics of deformable optical cavities,” *Nature Photonics*, vol. 3, pp. 201–205, 2009.
- [106] M. Wu, A. C. Hryciw, C. Healey, D. P. Lake, H. Jayakumar, M. R. Freeman, J. P. Davis, and P. E. Barclay, “Dissipative and Dispersive Optomechanics in a Nanocavity Torque Sensor,” *Physical Review X*, vol. 4, no. 021052, pp. 1–11, 2014.
- [107] S. G. Johnson, M. Ibanescu, O. Skorobogatiy, D. Weisberg, and J. Joannopoulos, “Perturbation theory for Maxwell’s equations with shifting material boundaries,” *Physical Review E*, vol. 65, no. 066611, 2002.
- [108] P. T. Rakich, P. Davids, and Z. Wang, “Tailoring optical forces in waveguides through radiation pressure and electrostrictive forces,” *Optics Express*, vol. 18, no. 14, pp. 14 439–14 453, 2010.
- [109] A. Yariv and P. Yeh, *Optical waves in crystals: Propagation and control of laser radiation*. Wiley-Blackwell, 1984.
- [110] D. K. Biegelsen, “Photoelastic tensor of silicon and the volume dependence of the average gap,” *Physical Review Letters*, vol. 32, no. 21, pp. 1196–1199, 1974.
- [111] M. L. Gorodetsky, A. Schliesser, G. Anetsberger, S. Deleglise, and T. J. Kippenberg, “Determination of the vacuum optomechanical coupling rate using frequency noise calibration,” *Optics Express*, vol. 18, no. 22, pp. 23 236–23 246, 2010.
- [112] K. E. Grutter and M. Davanço, “Si₃N₄ Nanobeam Optomechanical Crystals,” *IEEE Journal on Selected Topics in Quantum Electronics*, vol. 21, no. 4, p. 2700611, 2015.
- [113] M. Aspelmeyer, T. J. Kippenberg, and F. Marquardt, *Cavity Optomechanics*, M. Aspelmeyer, F. Marquardt, and T. J. Kippenberg, Eds. Berlin Heidelberg: Springer, 2014.

Bibliography

- [114] J. Tichý, J. Erhart, E. Kittinger, and J. Přívratská, *Fundamentals of Piezoelectric Sensorics*, 1st ed. Berlin-Heidelberg: Springer-Verlag Berlin Heidelberg, 2010.
- [115] K.-y. Hashimoto, Ed., *Bulk acoustic wave filters for communications*. Norwood, MA: Artech House, 2009.
- [116] "COMSOL Multiphysics® v. 5.3." Stockholm, Sweden. [Online]. Available: www.comsol.com
- [117] D. A. Berlincourt, D. R. Curran, and H. Jaffe, "Piezoelectric and Piezomagnetic Materials and Their Function in Transducers," in *Physical Acoustics*. New York: Academic Press, 1964, ch. 3, pp. 169 – 270.
- [118] J. W. Matthews and A. E. Blakeslee, "Defects in Epitaxial Multilayers I. Misfit Dislocations," *Journal of Crystal Growth*, vol. 27, pp. 118–125, 1974.
- [119] L. Czornomaz, "Hybrid InGaAs / SiGe technology platform for CMOS applications," Ph.D. dissertation, University of Grenoble Alpes, France, 2016.
- [120] S. Hönl, H. Hahn, Y. Baumgartner, L. Czornomaz, and P. Seidler, "Highly selective dry etching of GaP in the presence of $\text{Al}_x\text{Ga}_{1-x}\text{P}$ with a $\text{SiCl}_4/\text{SF}_6$ plasma," *Journal of Physics D: Applied Physics*, vol. 51, p. 185203, 2018.
- [121] J. Ayers, "The measurement of threading dislocation densities in semiconductor crystals by X-ray diffraction," *Journal of Crystal Growth*, vol. 135, pp. 71–77, 1994.
- [122] K. Schneider and P. Seidler, "Strong optomechanical coupling in a slotted photonic crystal nanobeam cavity with an ultrahigh quality factor-to-mode volume ratio," *Optics Express*, vol. 24, no. 13, pp. 13 850–13 865, 2016.
- [123] J. W. Lee, C. J. Santana, C. R. Abernathy, S. J. Pearton, and F. Ren, "Wet chemical etch solutions for $\text{Al}_x\text{Ga}_{1-x}\text{P}$," *Journal of the Electrochemical Society*, vol. 143, no. 1, pp. L1–L3, 1996.
- [124] J. W. Lee, J. Hong, E. S. Lambers, C. R. Abernathy, S. J. Pearton, W. S. Hobson, and F. Ren, "Plasma Etching of III-V Semiconductors in BCl_3 Chemistries: Part I: GaAs and Related Compounds," *Plasma Chemistry and Plasma Processing*, vol. 17, no. 2, pp. 155–167, 1997.
- [125] S. J. Pearton, W. S. Hobson, C. R. Abernathy, F. Ren, T. R. Fullowan, A. Katz, and A. P. Perley, "Dry etching characteristics of III-V semiconductors in microwave BCl_3 discharges," *Plasma Chemistry and Plasma Processing*, vol. 13, no. 2, pp. 311–332, 1993.
- [126] S. Pearton, J. Lee, E. Lambers, and C. Abernathy, "Comparison of Dry Etching Techniques for III-V Semiconductors in $\text{CH}_4/\text{H}_2/\text{Ar}$ Plasmas," *Journal of The Electrochemical Society*, vol. 143, no. 2, pp. 752–758, 1996.

- [127] S. J. Pearton, J. W. Lee, E. S. Lambers, J. R. Mileham, C. R. Abernathy, W. S. Hobson, F. Ren, and R. J. Shul, "High microwave power electron cyclotron resonance etching of III-V semiconductors in CH₄/H₂/Ar," *Journal of Vacuum Science and Technology B: Microelectronics and Nanometer Structures*, vol. 14, no. 1, p. 118, 1996.
- [128] R. J. Shul, A. J. Howard, C. B. Vartuli, P. A. Barnes, and W. Seng, "Temperature dependent electron cyclotron resonance etching of InP, GaP, and GaAs," *Journal of Vacuum Science and Technology A: Vacuum, Surfaces and Films*, vol. 14, no. 3, pp. 1102–1106, 1996.
- [129] R. J. Shul, G. B. McClellan, R. D. Briggs, D. J. Rueger, S. J. Pearton, C. R. Abernathy, J. W. Lee, C. Constantine, and C. Barrat, "High-density plasma etching of compound semiconductors," *Journal of Vacuum Science and Technology A: Vacuum, Surfaces, and Films*, vol. 15, no. 3, p. 633, 1997.
- [130] J. W. Lee, J. Hong, E. S. Lambers, C. R. Abernathy, and S. J. Pearton, "Cl₂-Based Dry Etching of GaAs, AlGaAs, and GaP," *Journal of The Electrochemical Society*, vol. 143, no. 6, pp. 2010–2014, 2010.
- [131] G. Smolinsky, R. P. Chang, and T. M. Mayer, "Plasma etching of III-V compound semiconductor materials and their oxides," *Journal of Vacuum Science and Technology*, vol. 18, no. 1, p. 12, 1981.
- [132] S. H. Yang and P. R. Bandaru, "An experimental study of the reactive ion etching (RIE) of GaP using BCl₃ plasma processing," *Materials Science and Engineering B: Solid-State Materials for Advanced Technology*, vol. 143, no. 1-3, pp. 27–30, 2007.
- [133] C. Welch, "Nanoscale Etching in Inductively Coupled Plasmas," 2011. [Online]. Available: <http://www.oxfordplasma.de/pla{ }news/wh{ }paper/OIPT-NanoscaleEtchingofICPPlasmas2011.pdf>
- [134] D. L. Flamm and V. M. Donnelly, "The Design of Plasma Etchants," *Plasma Chemistry and Plasma Processing*, vol. 1, no. 4, pp. 317–363, 1981.
- [135] H. Jansen, M. de Boer, R. Wiegerink, N. Tas, E. Smulders, C. Neagu, and M. Elwenspoek, "RIE lag in high aspect ratio trench etching of silicon," *Microelectronic Engineering*, vol. 35, no. 1-4, pp. 45–50, 1997.
- [136] W. Bogaerts, M. Fiers, M. Sivilotti, and P. Dumon, "The IPKISS Photonic Design Framework," in *Optical Fiber Communication Conference*, Anaheim, CA, USA, 2016, pp. 1–3.
- [137] J. C. Knight, G. Cheung, F. Jacques, and T. A. Birks, "Phase-matched excitation of whispering-gallery-mode resonances by a fiber taper," *Optics Letters*, vol. 22, no. 15, p. 1129, 1997.
- [138] M. Cai, O. Painter, and K. J. Vahala, "Observation of Critical Coupling in a Fiber Taper to a Silica-Microsphere Whispering-Gallery Mode System," *Phys.Rev.Lett.*, vol. 85, no. 1, pp. 74–77, 2000.

Bibliography

- [139] P. Karioja and D. Howe, "Diode-laser-to-waveguide butt coupling," *Applied Optics*, vol. 35, no. 3, pp. 404–416, 1996.
- [140] T. G. Tiecke, K. P. Nayak, J. D. Thompson, T. Peyronel, N. P. de Leon, V. Vuletić, and M. D. Lukin, "Efficient fiber-optical interface for nanophotonic devices," *Optica*, vol. 2, no. 2, pp. 70–75, 2014.
- [141] T. Alder, A. Stöhr, R. Heinzlmann, and D. Jäger, "High-efficiency fiber-to-chip coupling using low-loss tapered single-mode fiber," *IEEE Photonics Technology Letters*, vol. 12, no. 8, pp. 1016–1018, 2000.
- [142] D. Taillaert, P. Bienstman, and R. Baets, "Compact efficient broadband grating coupler for silicon-on-insulator waveguides," *Optics Letters*, vol. 29, no. 23, p. 2749, 2004.
- [143] S. G. Johnson and J. D. Joannopoulos, "Block-iterative frequency-domain methods for Maxwell's equations in a planewave basis," *Optics Express*, vol. 8, no. 3, pp. 173–190, 2001.
- [144] R. Waldhausl, B. Schnabel, E.-B. Kley, and A. Brauer, "Efficient focusing polymer waveguide grating couplers," *Electronics Letters*, vol. 33, no. 7, pp. 623–624, 1997.
- [145] S. Assefa, S. Shank, W. Green, M. Khater, E. Kiewra, C. Reinholm, S. Kamlapurkar, A. Rylyakov, C. Schow, F. Horst, H. Pan, T. Topuria, P. Rice, D. M. Gill, J. Rosenberg, T. Barwicz, M. Yang, J. Proesel, J. Hofrichter, B. Offrein, X. Gu, W. Haensch, J. Ellis-Monaghan, and Y. Vlasov, "A 90nm CMOS Intergated Nanophotonics Technology for 25Gbps WDM Optical Communications Applications," in *Proc. of 2012 IEEE International Electron Devices Meeting (IEDM)*. San Francisco, CA, USA 10 - 13 December 2012: IEEE, 2012, pp. 809–811.
- [146] Marcuse D., *Light transmission optics*. New York: Van Nostrand Reinhold, 1982.
- [147] J. Wei, J. M. Murray, J. O. Barnes, D. M. Krein, P. G. Schunemann, and S. Guha, "Temperature dependent Sellmeier equation for the refractive index of GaP," *Optical Materials Express*, vol. 8, no. 2, pp. 485–490, 2018.
- [148] A. Mekis, S. Gloeckner, G. Masini, A. Narasimha, T. Pinguet, S. Sahni, and P. De Dobbeleere, "A grating-coupler-enabled CMOS photonics platform," *IEEE Journal on Selected Topics in Quantum Electronics*, vol. 17, no. 3, pp. 597–608, 2011.
- [149] N. Ismail, C. C. Kores, D. Geskus, and M. Pollnau, "Fabry-Pérot resonator: spectral line shapes, generic and related Airy distributions, linewidths, finesses, and performance at low or frequency-dependent reflectivity," *Optics Express*, vol. 24, no. 15, p. 16366, 2016.
- [150] A. G. Griffith, R. K. Lau, J. Cardenas, Y. Okawachi, A. Mohanty, R. Fain, Y. H. D. Lee, M. Yu, C. T. Phare, C. B. Poitras, A. L. Gaeta, and M. Lipson, "Silicon-chip mid-infrared frequency comb generation," *Nature Communications*, vol. 6, pp. 1–5, 2015.

- [151] K. Rivoire, S. Buckley, F. Hatami, and J. Vučković, “Second harmonic generation in GaP photonic crystal waveguides,” *Applied Physics Letters*, vol. 98, no. 263113, 2011.
- [152] S. Mariani, A. Andronico, A. Lemaître, I. Favero, S. Ducci, and G. Leo, “Second-harmonic generation in AlGaAs microdisks in the telecom range,” *Optics Letters*, vol. 39, no. 10, pp. 3062–5, 2014.
- [153] X. Guo, C. Zou, and H. Tang, “Second-harmonic generation in aluminum nitride microrings with 2500 % W conversion efficiency,” *Optica*, vol. 3, no. 10, p. 1126, 2016.
- [154] H. Rokhsari and K. J. Vahala, “Observation of Kerr nonlinearity in microcavities at room temperature,” *Optics Letters*, vol. 30, no. 4, p. 427, 2005.
- [155] F. Liu, Y. Li, Q. Xing, L. Chai, M. Hu, C. Wang, Y. Deng, Q. Sun, and C. Wang, “Three-photon absorption and Kerr nonlinearity in undoped bulk GaP excited by a femtosecond laser at 1040 nm,” *Journal of Optics*, vol. 12, no. 9, 2010.
- [156] A. Martin, S. Combrié, A. de Rossi, G. Beaudoin, I. Sagnes, and F. Raineri, “Nonlinear gallium phosphide nanoscale photonics [Invited],” *Photonics Research*, vol. 6, no. 5, p. B43, 2018.
- [157] T. Herr, V. Brasch, J. D. Jost, C. Y. Wang, N. M. Kondratiev, M. L. Gorodetsky, and T. J. Kippenberg, “Temporal solitons in optical microresonators,” *Nature Photonics*, vol. 8, no. 2, pp. 145–152, 2014.
- [158] T. Herr, V. Brasch, J. D. Jost, I. Mirgorodskiy, G. Lihachev, M. L. Gorodetsky, and T. J. Kippenberg, “Mode spectrum and temporal soliton formation in optical microresonators,” *Physical Review Letters*, vol. 113, no. 12, pp. 1–6, 2014.
- [159] K. Schneider, P. Welter, Y. Baumgartner, S. Hönl, H. Hahn, D. Wilson, L. Czornomaz, and P. Seidler, “Optomechanics with one-dimensional gallium phosphide photonic crystal cavities,” *to be published*, 2019.
- [160] M. J. D. Powell, “A direct search optimization method that models the objective and constraint functions by linear interpolation,” in *Advances in Optimization and Numerical Analysis*, S. Gomez and J. Hennart, Eds. Dordrecht: Springer, 1994, pp. 51–67.
- [161] S. G. Johnson, “The NLOpt nonlinear-optimization package.” [Online]. Available: <http://ab-initio.mit.edu/nlopt>
- [162] J. Chan, A. H. Safavi-Naeini, J. T. Hill, S. Meenehan, and O. Painter, “Optimized optomechanical crystal cavity with acoustic radiation shield,” *Appl. Phys. Lett.*, vol. 101, no. 081115, 2012.
- [163] R. W. Dixon, “Photoelastic properties of selected materials and their relevance for applications to acoustic light modulators and scanners,” *Journal of Applied Physics*, vol. 38, no. 13, pp. 5149–5153, 1967.

Bibliography

- [164] F. Canal, M. Grimsditch, and M. Cardona, "Piezobirefringence in GaP and InP," *Solid State Communications*, vol. 29, no. 2, pp. 523–526, 1979.
- [165] J. Achenbach, *Wave propagation in elastic solids*, 1st ed. Amsterdam: North-Holland, 1980.
- [166] M. Göppl, A. Fragner, M. Baur, R. Bianchetti, S. Filipp, J. M. Fink, P. J. Leek, G. Puebla, L. Steffen, and A. Wallraff, "Coplanar waveguide resonators for circuit quantum electrodynamics," *Journal of Applied Physics*, vol. 104, no. 11, 2008.
- [167] J. Chan, T. P. M. Alegre, A. H. Safavi-Naeini, J. T. Hill, A. Krause, S. Groeblacher, M. Aspelmeyer, and O. Painter, "Laser cooling of a nanomechanical oscillator into its quantum ground state," *Nature*, vol. 478, pp. 89–92, 2011.
- [168] P. E. Barclay, K. Srinivasan, and O. Painter, "Nonlinear response of silicon photonic crystal micresonators excited via an integrated waveguide and fiber taper," *Optics Express*, vol. 13, no. 3, pp. 801–820, 2005.
- [169] S. Weis, R. Rivière, S. Deléglise, E. Gavartin, O. Arcizet, A. Schliesser, and T. J. Kippenberg, "Optomechanically induced transparency," *Science*, vol. 330, pp. 1520–1523, 2010.
- [170] M. J. Burek, J. D. Cohen, S. M. Meenehan, N. El-Sawah, C. Chia, T. Ruelle, S. Meesala, J. Rochman, H. A. Atikian, M. Markham, D. J. Twitchen, M. D. Lukin, O. Painter, and M. Lončar, "Diamond optomechanical crystals," *Optica*, vol. 3, no. 12, p. 1404, 2016.
- [171] M. Davanço, S. Ates, Y. Liu, and K. Srinivasan, " Si_3N_4 optomechanical crystals in the resolved-sideband regime," *Applied Physics Letters*, vol. 104, no. 041101, 2014.
- [172] P. Rath, S. Khasminkaya, C. Nebel, C. Wild, and W. H. P. Pernice, "Diamond-integrated optomechanical circuits," *Nature Communications*, vol. 4, pp. 1690–1699, 2013.
- [173] V. B. Braginsky, S. E. Strigin, and S. P. Vyatchanin, "Parametric oscillatory instability in Fabry-Perot (FP) interferometer," *Phys. Lett. A*, vol. 287, pp. 331–338, 2001.
- [174] T. J. Kippenberg, H. Rokhsari, T. Carmon, A. Scherer, and K. J. Vahala, "Analysis of Radiation-Pressure Induced Mechanical Oscillation of an Optical Microcavity," *Physical Review Letters*, vol. 95, p. 033901, 2005.
- [175] T. Carmon, H. Rokhsari, L. Yang, T. J. Kippenberg, and K. J. Vahala, "Temporal behavior of radiation-pressure-induced vibrations of an optical microcavity phonon mode," *Physical Review Letters*, vol. 94, no. 22, pp. 2–5, 2005.
- [176] T. J. Kippenberg and K. J. Vahala, "Cavity Optomechanics," *Optics Express*, vol. 15, no. 25, pp. 17172–17205, 2007.
- [177] S. Etaki, F. Konschelle, Y. M. Blanter, H. Yamaguchi, and H. S. J. Van Der Zant, "Self-sustained oscillations of a torsional SQUID resonator induced by Lorentz-force back-action," *Nature Communications*, vol. 4, pp. 1803–1805, 2013.

- [178] M. Eichenfield, R. Camacho, J. Chan, K. J. Vahala, and O. Painter, “A picogram- and nanometre-scale photonic-crystal optomechanical cavity,” *Nature*, vol. 459, pp. 550–556, 2009.
- [179] A. H. Safavi-Naeini, J. T. Hill, S. Meenehan, J. Chan, S. Gröblacher, and O. Painter, “Two-Dimensional Phononic-Photonic Band Gap Optomechanical Crystal Cavity,” *Physical Review Letters*, vol. 112, no. 153603, pp. 1–5, 2014.
- [180] J. T. Robinson, C. Manolatou, L. Chen, and M. Lipson, “Ultrasmall mode volumes in dielectric optical microcavities,” *Physical Review Letters*, vol. 95, no. 14, pp. 1–4, 2005.
- [181] V. R. Almeida, Q. Xu, C. A. Barrios, and M. Lipson, “Guiding and confining light in void nanostructure,” *Optics Letters*, vol. 29, no. 11, p. 1209, 2004.
- [182] P. Lalanne and J. P. Hugonin, “Bloch-Wave Engineering for High-Q, Small-V Microcavities,” *IEEE Journal of Quantum Electronics*, vol. 39, no. 11, pp. 1430–1438, 2003.
- [183] C. Sauvan, G. Lecamp, P. Lalanne, and J. P. Hugonin, “Modal-reflectivity enhancement by geometry tuning in Photonic Crystal microcavities,” *Optics Express*, vol. 13, no. 1, p. 245, 2005.
- [184] A. Taflov and S. C. Hagness, *Computational Electrodynamics- The Finite-Difference Time-Domain Method*, 3rd ed. Norwood, MA: Artech House, 2005.
- [185] A. F. Oskooi, D. Roundy, M. Ibanescua, P. Bermel, J. D. Joannopoulos, and S. G. Johnson, “Meep : A flexible free-software package for electromagnetic simulations by the FDTD method,” *Computer Physics Communications*, vol. 181, pp. 687–702, 2010.
- [186] T. Wahlbrink, T. Mollenhauer, Y. M. Georgiev, W. Henschel, J. K. Efavi, H. D. B. Gottlob, M. C. Lemme, H. Kurz, J. Niehusmann, and P. H. Bolivar, “Highly selective etch process for silicon-on-insulator nano-devices,” in *Microelectronic Engineering*, vol. 78-79, no. 1-4, 2005, pp. 212–217.
- [187] K. C. Balram, M. Davanço, J. Y. Lim, J. D. Song, and K. Srinivasan, “Moving boundary and photoelastic coupling in GaAs optomechanical resonators,” *Optica*, vol. 1, no. 6, pp. 414–420, 2014.
- [188] M. Eichenfield, J. Chan, R. M. Camacho, K. J. Vahala, and O. Painter, “Optomechanical crystals,” *Nature*, vol. 461, no. 7269, pp. 78–82, 2009.
- [189] A. González-Tudela, C.-L. Hung, D. E. Chang, J. I. Cirac, and H. J. Kimble, “Subwavelength vacuum lattices and atom–atom interactions in two-dimensional photonic crystals,” *Nature Photonics*, vol. 9, no. 5, pp. 320–325, 2015.
- [190] S. Miller, K. Luke, Y. Okawachi, J. Cardenas, A. L. Gaeta, and M. Lipson, “On-chip frequency comb generation at visible wavelengths via simultaneous second- and third-order optical nonlinearities,” *Opt. Express*, vol. 22, no. 22, pp. 26 517–26 525, Nov 2014.

Bibliography

- [191] H. Jung, R. Stoll, X. Guo, D. Fischer, and H. X. Tang, "Green, red, and ir frequency comb line generation from single ir pump in aln microring resonator," *Optica*, vol. 1, no. 6, pp. 396–399, Dec 2014.
- [192] Z. Chen, A. Megrant, J. Kelly, R. Barends, J. Bochmann, Y. Chen, B. Chiaro, A. Dunsworth, E. Jeffrey, J. Mutus, P. O'Malley, C. Neill, P. Roushan, D. Sank, A. Vainsencher, J. Wenner, T. C. White, A. N. Cleland, and J. M. Martinis, "Fabrication and Characterization of Aluminum Airbridges for Superconducting Qubit Circuits," *Bulletin of the American Physical Society*, vol. 59, no. 1, p. M36.12, 2014.
- [193] D. Taillaert, "Grating couplers as Interface between Optical Fibres and Nanophotonic Waveguides," Ph.D. dissertation, University Gent, 2005.
- [194] R. Waldhäusl, B. Schnabel, P. Dannberg, E.-B. Kley, A. Bräuer, and W. Karthe, "Efficient Coupling into Polymer Waveguides by Gratings," *Applied Optics*, vol. 36, no. 36, pp. 9383–9390, 1997.
- [195] D. Taillaert, F. Van Laere, M. Ayre, W. Bogaerts, D. Van Thourhout, P. Bienstman, and R. Baets, "Grating couplers for coupling between optical fibers and nanophotonic waveguides," *Japanese Journal of Applied Physics, Part 1: Regular Papers and Short Notes and Review Papers*, vol. 45, no. 8 A, pp. 6071–6077, 2006.
- [196] J. Hofrichter, W. M. J. Green, F. Horst, S. Assefa, M. Yang, B. Offrein, and Y. Vlasov, "Grating couplers as optical probe pads in a standard CMOS process," *8th IEEE International Conference on Group IV Photonics*, pp. 127–129, 2011.
- [197] M. Spieser, "Numerical optimizers for nanophotonic devices," Ph.D. dissertation, ETH Zurich, 2014.
- [198] X. Han, C. L. Zou, and H. X. Tang, "Multimode Strong Coupling in Superconducting Cavity Piezoelectromechanics," *Physical Review Letters*, vol. 117, no. 12, pp. 1–6, 2016.
- [199] J. Eisenstein, "Superconducting elements," *Reviews of Modern Physics*, vol. 26, no. 3, pp. 277–291, 1954.
- [200] U. S. Pracht, M. Scheffler, M. Dressel, D. Kalok, C. Strunk, and T. I. Baturina, "Direct observation of the superconducting gap in thin film of titanium nitride using terahertz spectroscopy," *Phys. Rev. B*, vol. 86, no. 184503, pp. 2–6, 2012.
- [201] C. M. Yen, L. E. Toth, Y. M. Shy, D. E. Anderson, and L. G. Rosner, "Superconducting Hc-Jc and Tc measurements in the NbTiN, NbHfN, and NbSVN ternary systems," *Journal of Applied Physics*, vol. 38, no. 5, pp. 2268–2271, 1967.
- [202] D. K. Finnemore, T. F. Stromberg, and C. A. Swenson, "Superconducting properties of high-purity niobium," *Physical Review*, vol. 149, no. 1, pp. 231–243, 1966.

- [203] E. Klein, C. Gossler, O. Paul, U. T. Schwarz, and P. Ruther, “High-yield indium-based wafer bonding for large-area multi-pixel optoelectronic probes for neuroscience,” *Proceedings of the IEEE International Conference on Micro Electro Mechanical Systems (MEMS)*, pp. 452–455, 2017.
- [204] S. Bose, P. Raychaudhuri, R. Banerjee, P. Vasa, and P. Ayyub, “Mechanism of the size dependence of the superconducting transition of nanostructured Nb,” *Physical Review Letters*, vol. 95, no. 14, pp. 3–6, 2005.
- [205] L. Frunzio, A. Wallraff, D. Schuster, J. Majer, and R. Schoelkopf, “Fabrication and characterization of superconducting circuit QED devices for quantum computation,” *IEEE Transactions on Applied Superconductivity*, vol. 15, no. 2, pp. 860–863, 2005.
- [206] R. Barends, J. J. Baselmans, J. N. Hovenier, J. R. Gao, S. J. Yates, T. M. Klapwijk, and H. F. Hoofters, “Niobium and tantalum high Q resonators for photon detectors,” *IEEE Transactions on Applied Superconductivity*, vol. 17, no. 2, pp. 263–266, 2007.

Abbreviations

1D one-dimensional.

2D two-dimensional.

AFM atomic force microscopy.

$\text{Al}_x\text{Ga}_{1-x}\text{P}$ aluminum gallium phosphide.

ALD atomic layer deposition.

BRNC Binnig and Rohrer Nanotechnology Center.

FSR free spectral range.

FWM four-wave mixing.

GaP gallium phosphide.

GaP-OI gallium phosphide-on-insulator.

GVD group velocity dispersion.

HMDS hexamethyldisilazane.

HSQ hydrogen silsesquioxane.

ICP-RIE inductively-coupled-plasma reactive ion etching.

IDTs interdigital transducers.

IPA isopropanol.

MOCVD metalorganic chemical vapor deposition.

OMIA optomechanically induced absorption.

OMIT optomechanically induced transparency.

Abbreviations

PhC photonic crystal cavity.

PhCs photonic crystal cavities.

PMMA poly(methyl methacrylate).

RIE reactive ion etching.

RMS root mean square.

SEM scanning electron microscope.

SOI silicon-on-insulator.

SRS stimulated Raman scattering.

TE transverse electric.

TM transverse magnetic.

TPA two-photon absorption.

XRD X-ray defraction.

KATHARINA SCHMEING

In der Breiti 1
8047 Zürich

E-mail	katharina.schneider89@gmx.de
Phone	+41 (78) - 8404157
Date of birth	20/02/1989
Place of birth	Freiburg i. Br.
Nationality	german

Education

since 10/2014	Doctoral student at IBM Research GmbH, Rüschlikon, Switzerland Photonics and Quantum Technology department Topic: Exploration of the optomechanical properties of 1D photonic crystal cavities made of silicon or gallium phosphide for applications in sensing and quantum technology
9/2011 - 06/2014	Technical University Munich (TUM), Germany M. Sc. Physics (Condensed Matter Physics), final grade: 1,4
05/2013 - 04/2014	Master Thesis at the Max-Planck-Institute for Quantumoptics, Garching, Germany Quantum Dynamics Group directed by Prof. Gerhard Rempe Topic: Single-Photon Transistor based on Rydberg Blockade
09/2011 - 02/2012	Zhejiang University, Hangzhou, P.R. China Student Research assistant at the Institute of Condensed Matter Phy- sics in the group of Prof. Fanlong Ning (Research Focus: Unconventio- nal Superconductors) Task: Construction of a model superconductor levitating train
10/2008 - 08/2011	Technical University Munich (TUM), Germany, B.Sc. Physics, final gra- de 2,6
05/2011 - 07/2011	Bachelor Thesis at the Max-Planck-Institute for Quantumoptics, Gar- ching, Germany Attosecond Physics Group directed by Prof. Dr. Ferenc Krausz Group of Prof. Reinhard Kienberger (TUM, MAP-Cluster) Topic: Installation of a measurement-system for single-shot carrier- envelope phase measurement of few-cycle laser pulses
1999 - 2008	Schwarzwaldgymnasium Triberg, degree: Abitur (1,0)

Awards

- 10/2008 - 06/2014 Study Scholarship of the Hans-Böckler-Stiftung
- 10/2018 1st poster prize at the EPFL Physics Day with the poster "Optomechanics with one-dimensional gallium phosphide photonic crystal cavities"

Publications

- D. Tiarks, S. Baur, K. Schneider, S. Dürr and G. Rempe: Single-photon transistor using a Förster resonance, *Phys. Rev. Lett.* **113**, 053602, 2014.
- K. Schneider, P. Seidler: Strong optomechanical coupling in a slotted photonic crystal cavity with an ultrahigh quality factor-to-mode volume ratio, *Opt. Exp.* **24** (13), 13850-13865, 2016.
- K. Schneider, P. Welter, Y. Baumgartner, S. Hönl, H. Hahn, Lukas Czornomaz, Paul Seidler: Optomechanics with one-dimensional gallium phosphide photonic crystal cavities, *Proc. SPIE* **10359**, 2017.
- K. Schneider, P. Welter, Y. Baumgartner, H. Hahn, L. Czornomaz, and P. Seidler: Gallium phosphide-on-silicon dioxide photonic devices, *Journ. of Lightw. Techn.* **36** (14), 2994-3002, 2018.
- D. J. Wilson, K. Schneider, S. Hönl, M. Anderson, T. J. Kippenberg, and P. Seidler: Gallium phosphide nonlinear photonics, preprint arXiv:1808.03554 [physics.app-ph], 2018.

Internships

- 09/2009 - 04/2011 Academic Course of the German National Academic Foundation Working group „Learn to walk“, directed by Prof. Johann Reger and PD André Seyfahrt
Topic: Research on the human walk, design and construction of a walking robot
- 09/2010 Max-Planck-Institut for Quantumoptics, Garching, Attosecond Physics Group directed by Ferenc Krausz
Task: Construction of a laser beam stabilization, quality measurement of Anti-Chirp-Mirrors with a Michelson-Interferometer, assistance to groups dealing with Attosecond Imaging
- 08/2009 Junior Research group „Advanced Technologies in Radiation Therapy“, directed by Prof. Dr. Jan Wilkens as part of the „Munich Centre For Advanced Photonics“
Task: Programming a simulation for determining the radiation dosage for tumor treatment with proton radiation.

Additional qualifications

Languages	German (native) English (fluent) French (good) Chinese (basic)
Programming	Python (good) Matlab (good) Labview (good) Mathematica (basics)
EDV	Comsol, LaTeX, MS Office, Origin
Laboratory	Nanofabrication, Cleanroom work, Photonic chip design, Optical and electrical characterization, Laser physics, Ultracold gases, Vacuum technology, Feedback control techniques

Associations & Interests

Albisfoxes Handball	Active handball player
Social commitment	Language partnership with chinese speaking students
Hobbys	Handball, hiking, reading

Zurich, 4th November 2018

